Thermal-driven flow and coastal processes in shallow water

By

Ying-Tien Lin

A dissertation submitted in partial fulfillment
of the requirements for the degree of

Doctor of Philosophy

(Civil and Environmental Engineering)

at the
University of Wisconsin-Madison

2012

Date of final oral examination: 2/3/2012

The dissertation is approved by the following members of the Final Oral Committee:

Chin H. Wu. Professor, Professor, Civil and Environmental Engineering
Dante Fratta. Professor, Associate Professor, Civil and Environmental Engineering
Kenneth W. Potter. Professor, Professor, Civil and Environmental Engineering
Steven P. Loheide. Professor, Associate Professor, Civil and Environmental Engineering
King-Jau Samuel Kung. Professor, Professor, Soil Science

Acknowledgements

First and foremost, I wish to express my greatest appreciation to my advisor, Professor Chin Wu who encourages and inspires me all along to go through the Ph.D. life. His advice and guidance has kept me moving forward. I am profoundly grateful to Professor Dante Fratta for his patience and enthusiasm to train me from a layman to become an expert in geophysics. In addition, I want to thank Professor John Hoopes for his motivation and financial support for the first three years when I started my Ph.D research in Madison. I would also like to thank my thesis committee members, Professors Steven Loheide II, Kenneth Potter, and King-Jau Kung, for their valuable assistances, comments, and suggestions for my research.

Funding was provided from Wisconsin Coastal Management Program, Anna Grant Birge Memorial Award, Nortek student equipment grant, US Environmental Protection Agency, Wisconsin Department of Natural Resources, Civil and Environmental Engineering Department. I am grateful for their support in my Ph.D study.

My special thanks go to Mr. Dave Harring and Brian Hess for brilliant craftsmanship on maintaining my experiment apparatus, facilities and instruments. Without their help, I could not conduct my field measurements very smoothly. In addition, many, many thanks to my field crew: Craig Schuettpelz, Josh Anderson, Erica Hagen, Lauren Seabury, Nick Janous, Bill Roznik, Hoilai Tseung, Khurram Khan, John Reimer, Yvonne Hsieh, Sen Yan, for helping me to safely and enjoyable collect all of the data included in this thesis. Last, but certainly not least, I am grateful to my fellow Environmental Fluid Mechanics and Water Resources graduate students for all of their support and aid.

No words can describe how much the friendship I made during my stay at Madison mean to me. I sincerely thank my friends for accompanying, encouraging, and enjoying life together in Madison: Kent Shen, Elise Wu, Sarah Lin, Hsiang-Kuo Tang, Jiun-Yi Tsai, Chin-Ya Huang, and may others.

Most importantly, my family deserves my sincerest thanks for their unconditional and endless love in these years. Their belief and never-ending support help me overcome difficulties and make this endeavor wonderful.

TABLE OF CONTENTS

Page

Abstract

In shallow water, between land and open water, physical processes over a sloping bottom are usually complicated and have significant impacts on human activities and aquatic ecosystems. The study considers thermal-driven circulation that is generated from heterogeneous horizontal temperature distributions, and sediment transport processes that occur around coastal structures. Theoretical derivations and field measurements are completed to understand the physical mechanisms of thermal-driven circulations and of sediment transport processes, respectively.

First, a theoretical understanding of thermal-driven flow within emergent vegetation is developed over diurnal cycles. During the daytime, across a sloping bottom, uniform incoming solar radiation creates warmer water in shallow regions and colder water in deep regions. The difference in horizontal temperature leads to pressure gradient and generates circulation from shallow to deep waters along the water surface and uphill near the sloping bottom. At night, the processes and the circulation patterns are reversed. In shallow water, abundant vegetation imposes inherent drag on the flow and can alter the heat distribution in the water body. Two models are included, one with a uniform distribution of solar radiation over the water column (unstratified), and one in which solar radiation decays exponentially with depth (stratified). A small bottom slope is assumed and asymptotic solutions are developed to elucidate physical mechanisms among vegetative drags, viscosity, inertia, pressure gradients, and light extinction coefficients (for the stratified case). For both models, viscosity is dominant in shallow water; while vegetative drags prevail in deep water. Distributions of vegetation can significantly alter the magnitude and patterns of circulation.

Second, coastal processes are studied through the use of several geophysical techniques. Acoustic and electromagnetic wave-based devices such as a subbottom profiler (SBP) and ground-penetration radar (GPR) were used in combination to measure bathymetry and sediment sublayers in shallow water with different sediment types. The advantage of this combined technique is a reduction of the limitations posed by the individual methods. In addition, utilizing signal responses from lake or river bottoms, an algorithm integrating SBP and GPR signals was established to estimate sediment porosity and the thickness of the top sediment layer. Through successive surveys, changes of bathymetry and sediment layer thickness were obtained and used to describe sediment erosion and deposition patterns. In the Great Lakes, downcutting (vertical lowering) on cohesive lake bottoms is an important factor for long-term bluff recession rates. The integrated geophysical techniques were applied at a site near Concordia University on Lake Michigan to investigate changes in the nearshore environment and downcutting rates after the coastal structures are built. The results provide information on bathymetry changes, downcutting rates and longshore currents hindcast from the meteorological data, which can possibly explain recent bluff slumping in the south shores of the coastal structures.

LIST OF TABLES

LIST OF FIGURES

Figure Page

Chapter 1 Introduction

Shallow water is connection between the land surface and the larger water body. In shallow water, physical processes involved with human activities are complex, dynamic and extremely important to the entire ecosystem (Komar 1998, Kamphuis 2000). For example, high bathymetrical variations and the presence of coastal structures in shallow water cause dramatic changes in hydrodynamic drivers such as waves (Sleath, 1984, and Nielsen, 1992) and currents (Graf, 1971, Vanoni, 1975, and van Rijn, 1984). As a result, coastal processes, including nearshore flows and sediment transport can negatively affect bluff stability in adjacent land areas, which can cause losses of property and human life (Trenhaile 1997).

In shallow water, the hydrodynamic response to thermal drivers (e.g. solar radiation) is also dynamic. For example, solar radiation over sloping bottoms can cause differences of density in the water column, thereby generating thermal-driven circulation, i.e. natural convective circulation (Adams and Wells, 1984, Patterson 1984, Monismith et al. 1990). Many studies (James and Barko, 1990, Farrow and Patterson 1993, MacIntyre and Melack, 1995) show that the thermal-driven circulation plays an important role in the exchange of chemical substances and nutrients between nearshore and deep water, especially without external momentums such as the wind or river flow. During the daytime, over a sloping bottom, the same amount of solar radiation entering into the water body leads to warmer water in the shallow regions and cooler water in the deep regions (Farrow and Patterson, 1993). As a result, circulation occurs from shallow water to deep water along the water surface and from deep to shallow water over the sloping bottom. The process is reverse during the nighttime. Furthermore, emergent vegetation in shallow aquatic systems can complicate nutrient cycles (James and Barko, 1990). Shading due

to emergent vegetation that blocks sunlight can also cause the horizontal temperature difference, generating the convective circulation over the vegetation zone (Coates and Ferris 1994, Lövstedt and Bengtsson, 2008, Zhang and Nepf, 2009). Meanwhile the inherent resistance from emergent vegetation slows down the generated circulation and increases residence time of nutrients and chemical substances (Horsh and Stefan 1988, Oldham and Sturman 2001).

To address these issues mentioned above, I employ an analytical approach and incorporate field measurements to better understand physical processes in shallow water. The thesis includes two themes: hydrodynamic response due to diurnal thermal drivers, and development of a method for the combination of the geophysical instruments to address coastal processes in the Great Lakes and inland lakes. Two chapters are devoted to the first theme. Specifically Chapter 2 is addressed with the role of emergent vegetation on thermal-driven circulation over weakly stratified sloping bottoms during diurnal cycles. In Chapter 3, an analytic solution developed in Chapter 2 is extended to a stratified sloping bottom to reveal the thermal-driven circulation within emergent vegetation. In these two chapters, two analytic models related to unstratified and stratified temperature structures over a vegetated sloping bottom are taken into consideration. For the unstratified model, the same amounts of solar radiation are assumed to be uniformly distributed over local water depths, and therefore temperature changes are inversely proportional with the local water depths. The other one is a more realistic physical model with solar radiation following Beer's law of exponential decay with water depths (Kirk, 1986). Physical mechanisms involving the balances between viscosity, inertia, vegetative drag, and buoyancy at different water depths and times are revealed and discussed. The roles of emergent vegetation on thermal-driven flows also are examined. An overall fundamental understanding of unsteady natural convections over a vegetated sloping bottom is achieved.

For the second theme, concerning coastal processes in the Great Lakes and inland lakes, two chapters are also presented. Specifically Chapter 4 presents combined and integrated acoustic and electromagnetic techniques to image bathymetry and sublayers in shallow water. To provide accurate surveys of bottom sediment stratigraphy in lakes, rivers, and oceans, I developed combined acoustic and electromagnetic geophysical techniques to continuously map bathymetry and subsurface information. The combined techniques build upon the advantages of two non-destructive geophysical devices. For example, acoustic signals are able to image clayey and silty substrates, but fail to map sublayers in coarse sediments (Morang et al. 1997). Electromagnetic signals attenuate rapidly in finer sediments, but provide useful information in coarse sediments (Annan, 2005). Therefore, combined geophysical techniques can reduce the individual techniques' limitations. Furthermore, an integrated algorithm of signal responses of acoustic and electromagnetic waves from sediment bottoms was developed to obtain sediment porosity and bottom sublayer thickness (Lin et al. 2009, 2010). Chapter 5 describes the applications of the combined and integrated methods developed in Chapter 4, which include monitoring changes of the nearshore environment and estimating downcutting rates around newly-built coastal structures in Lake Michigan. A five-year, long-term comprehensive field study was carried out to characterize coastal processes and changes of the nearshore environment due to the newly-built coastal structures in shallow water. Through successive surveys, changes in bathymetry, thickness of sublayers, and lakebed downcutting were quantified to help understand sediment erosion, deposition, and redistribution processes as well as effects of different physical drivers and man-made coastal structures in the nearshore environment.

Finally, Chapter 6 includes conclusions with some recommendations for future work. Theoretical derivations of thermal-driven flows over a vegetated sloping bottom were developed

to provide a simple estimation of circulation and exchange flowrates during diurnal cycles. The asymptotic solutions show that, in shallow water, viscosity is balanced by buoyancy; whereas vegetative drag is more important and balanced with buoyancy. The inertia effect is only important when the circulation is initiated. The circulation is larger in clear water, i.e., small light extinction coefficient, than in dirty water, i.e. large light extinction coefficient. In addition, the presence of emergent vegetation can interfere with topographic effects and significantly alter thermal-driven circulation under some specific vegetation distributions. In regard to the second theme, combined geophysical techniques were successful in providing accurate information of bathymetry and sublayers under different sediment types in shallow water. Furthermore, by integrating signal responses from acoustic and electromagnetic waves from sediment bottoms, sediment porosity and the thickness of the top sediment layer were accurately and efficiently estimated. Through successive surveys, zones of sediment erosion and deposition were identified, and downcutting rates were estimated. These changes were related to variations in local hydrodynamic factors associated with the coastal structures in the nearshore of Lake Michigan.

References

Adams, E.E. and Wells, S.A. (1984). “Field measurements on side arms of Lake Anna. Va.” *J. Hydraul.Engng*, 110, 773-793.

Annan, A.P., (2005). Ground penetrating radar. In Edited by K. Butler, *Near Surface Geophysics*, 357-438.

Coates, M., and J. Ferris. (1994). “The radiatively driven natural convection beneath a floating plant layer.” *Limnol. Oceanogr*., 39(5), 1186-1194.

Farrow, D.E. and Patterson, J.C. (1993). “On the response of a reservoir sidearm to diurnal heating and cooling.” *J. Fluid Mech*., 246, 143-161.

Graf, W.H. (1971). *Hydraulics of sediment transport*, McGraw-Hill, New York, pp513.

Horsh, G.M., and Stefan, H.G. (1988). “Convective circulation in littoral water due to surface cooling.” *Limnol. Oceanogr*., 33(5), 1068-1083.

James, W.F., and Barko, J.W. (1991). “Estimation of phosphorous exchange between littoral and pelagic zones during nighttime convection circulation.“ *Limnol. Oceanogr*., 36(1), 179-187.

Kamphuis, J.W. (2000). *Introduction to coastal engineering and management*. World Scientific, Singapore, 437 pp.

Kirk, J.T.O. (1986). Optical limnology - a manifesto. In *Limnology in Australia* (ed. P. de Dekker and W.D. Willams), pp. 33-62. CSIRO Publications Sales.

Komar, P.D. (1998). *Beach processes and sedimentation*. 2nd edn., Prentice-Hall, Englewood Cliffs, NJ, 544 pp.

Lövstedt and Bengtsson. (2008). “Density-driven current between reed belts and open water in a shallow lake.” *Water Resources Res*., 44(10), W10413.

MacIntyre S. and Melack, J.M. (1995). “Vertical and horizontal transport in lakes. Linking moral, benthic, and pelagic habits.” *J.N. Am. Benthol. Soc*. 14(4), 599-615.

Monismith, S.G., Imberger, J. and Morrison, M.L. (1990). “Convective motions in the sidearm of a small reservoir.” *Limnol. Oceanogr*. 35, 1676-1702.

Morang, A., Larson, R., and Gorman, L., 1997. “Monitoring the coastal environment; Part III:

Geophysical and research methods." *Journal of Coastal Research*, 13(4), 1064-1085.

Nielsen, P. (1992). *Coastal bottom boundary layers and sediment transport*, World Science, Singapore, 324pp.

Oldham, C.E., and Sturman, J.J. (2001). "The effect of emergent vegetation on convective flushing in shallow wetlands: scaling and experiment." *Limnol. Oceanogr*., 46(6), 1486-1493.

Pattersons, J.C. (1984). "Unsteady natural convection in a cavity with internal heating and cooling." *J. Fluid Mech.* 140, 135-151.

Sleath, J.F.A. (1984). *Sea bed mechanics*, Wiley, New York, 335pp.

Trenhaile, A.S. (1997). *Coastal Dynamics and Landforms*, Oxford, Clarendon Press, 366pp.

Van Rjin, L.C. (1984). "Sediment transport. Part II: Suspended load transport." *J. Hydraul. Eng.* 110(11), 1613-1641.

Vanoni, V.A. (1975). *Sedimentation engineering*, ASCE, New York, pp726.

Zhang, X, and Nepf, H.M. (2008). "Density driven exchange flow between open water and an aquatic canopy." *Water Resources Res*.,44(8), W08417.

Zhang, X. and Nepf, H.M. (2009). "Thermally driven exchange flow between open water and an aquatic canopy." *J. Fluid Mech*., 632, 227-243.

Chapter 2

The role of emergent vegetation on the response of a sloping bottom to diurnal heating and cooling

This chapter is to be submitted to *Journal of fluid mechanics*, as "The role of emergent vegetation on the response of a sloping bottom to diurnal heating and cooling." by Lin, Y. T., and Wu, C.H.

2.1 Abstract

Thermal-driven flow is generated due to topographic or vegetation shading effects. An asymptotic solution is found to discuss effects of emergent vegetation and interferences between emergent vegetation and a sloping bottom on thermal-driven flow. The results show that the zero-order horizontal velocity is significantly reduced by vegetative drag, and the time lag between the change of flow field and reversal of pressure gradient is also shortened. The solution clearly demonstrates that the viscous effect is dominant in very shallow water, and the drag force becomes important as the water depth increases. The inertial term is only important at the very beginning stage. Bottom shear stress due to the viscous effect is independent of vegetation density in very shallow water, and decreases as vegetation density increases when the water depth becomes deeper. Different vegetation distribution can significantly change the temperature fields, and affect the thermal-driven circulation, and exchange flowrates.

2.2 Introduction

Thermal-driven flow in the absence of wind or other momentum forcing, also called natural convection flow, arises from heterogeneous temperature distribution and subsequent density gradients in fluids (Monismith, Imberger, & Morrison 1990; James & Barko 1991). Specifically, horizontal transport of thermal-driven flows due to differential surface heating or cooling is commonly observed in effects of vegetation shading (Chinmey, Wenkert, & Pietro 2006) or a sloping bottom (Farrow & Patterson 1993) of lakes or geophysical fluid bodies. For example, floating or emergent vegetation can block parts of solar radiations into the water body, and therefore temperature in vegetation shading areas is cooler than that in open water or less vegetated areas during the daytime (Coates & Patterson 1993; Lightbody, Avener, & Nepf 2008; Lövstedt & Bengtsson 2008). The differential heating due to vegetation shading can lead to the variations of water density, driving thermal convective circulation from open water to vegetated areas along the surface and return to the open water along the bottom. The magnitude of such circulation, an important mechanism to renew littoral waters, can reach up to 1 cm/s, which is much faster than turbulence diffusion alone (Zhang & Nepf, 2009). Similarly on a sloping topographic bottom, during the daytime, the same amount of solar radiation entering into the water body leads to warmer water in the shallow regions and cooler water in the deeper regions. As a result, induced circulation flowing from shallow water to deep water along the water surface and underflow uphill over the sloping bottom toward the nearshore is generated. The process is reverse during the nighttime. For diurnal heating and cooling, generated circulation flushes back and forth, promoting the exchange of nutrients and chemical substances and reducing the flushing time between

the nearshore and the main water body (James & Barko, 1991). Because of abundant light and nutrients, vegetation is extensively present over a sloping bottom in shallow water. In this condition, during the daytime, horizontal temperature differences due to vegetation shading and sloping bottom perform different trends, and water temperature in shallow water may not be always warmer than that in deep water. In the past, studies of thermal-driven flow due to vegetation shading were limited over a flat bottom (Coates & Patterson 1993; Lövstedt & Bengtsson 2008; Zhang & Nepf 2009). Interferences or competitions between vegetation shading and topographic effects on thermal-driven flow are not yet well-understood.

Several previous studies have discussed horizontal thermal-driven flow over a sloping bottom. Observations conducted by Adam & Wells (1984) and Monismith et al. (1990) showed a significant lag (or spin-up time), up to one day, of the circulation in response to the changes of diurnal heating and cooling forcing in littoral regions of natural lakes. To examine the relationship between the time lag and dominant processes, Farrow & Patterson (1993) found a zero-order asymptotic solution of a simplified 2-D triangular cavity model with the assumptions of heat uniformly-distributed over the water column, a wedge-shaped domain with a small slope, and negligible nonlinear convective effects. In shallow water, the time taken for viscosity responses over the whole water depth is relatively short. The horizontal velocity immediately responds to changes in the horizontal pressure gradient due to diurnal forcing. In deep water, the inertia of fluids balanced with the horizontal pressure lags the pressure gradient by a quarter period of the forcing. The vertical velocity profile is characterized by this balance until viscosity diffuses into the water column. It is recognized that the failure of the zero-order

asymptotic solution near the tip of the wedge where nonlinearity becomes important. Farrow (2004) extended Farrow and Patterson's work to the second-order temperature solutions and presented numerical results including the effects of heat conduction and nonlinear advection. The horizontal advective heat transfer generated from the second-order temperature profiles also shows a viscous-dominated mechanism in shallow water and an inertia-dominated flow in deep water. A valid range of the zero-order asymptotic solution is also defined and verified with numerical simulations. In addition to the assumption of uniform heating distribution, a more realistic physical model is also adopted to discuss the thermal-driven circulation during daytime heating or nighttime cooling. Farrow and Patterson (1993), Lai and Patterson (2002), and Mao et al. (2009) assumed that solar radiation exponentially decays with water depths, and the flow regimes can be identified due to heat conduction, transient, and convection over a small bottom slope. Mao et al. (2010) considered heat dissipation through a water surface during the nighttime to discuss flow patterns and stability of the thermal boundary layer. However, in these studies, daytime heating and nighttime cooling are discussed separately, and diurnal effects are not taken into account.

Emergent and floating vegetation commonly found in aquatic systems produce shading effects, which can cause horizontal temperature differences, and generate the convective circulation (Coates & Pattersons, 1993; Lövstedt & Bengtsson 2008). The thermal-driven flow from shading of floating vegetation over a flat bottom can be classified as inertial and energy-limited regions, yielding corresponding magnitude of the circulation (Coates & Pattersons, 1993; Coates & Ferris, 1994). Zhang and Nepf (2009) considered the shading effects from emergent vegetation to generate thermal-driven flow

over a flat bottom. Unlike floating vegetation, emergent vegetation provides inherent resistance drag to slow down the generated circulation (Oldham & Sturman 2001; Zhang & Nepf 2008). Previous studies showed that horizontal velocity and volumetric flowrate of exchange flow both strongly decrease with increasing vegetation density in thermal-driven flow (Tanino, Nepf, & Kulis 2005; Zhang & Nepf 2008). Oldham and Sturm (2001) applied the porous media flow theory to study the impact of vegetative drag on exchange flow during surface cooling processes. Vegetative drag significantly reduces exchange flowrates and increases flushing time over vegetated regions. Recently Zhang and Nepf (2009) discussed the combined effects of vegetation shading and drag on the thermal-driven flow, and observed the exchange flow is inertia-dominated at the initial stage, and quickly transitions to be drag-dominated. The thickness of an intrusion layer corresponds to the length scale of light penetration. While their work has provided new insight to reveal the role of vegetation on the thermal driven flow, the effects of a sloping bottom is not well-understood. Specifically, the effects of vegetative drag on the time-lag and dominant mechanisms including viscosity, inertia, and horizontal pressure gradient of the thermal-driven flow have not yet been unveiled.

In this paper, an analytic approach was employed to discuss thermal-driven flow generated by vegetation shading and topographic effects during diurnal cycles. Asymptotic solutions including zero-order horizontal velocity and second-order temperature for thermal-driven flow within different vegetation distribution were found. Based upon the derived velocity and temperature profiles, the spatial and temporal dominant mechanisms for balances between viscosity, vegetative drag, inertia and buoyancy were revealed and compared with experimental findings from Zhang and Nepf

(2009). The asymptotic solutions were also used to discuss the interferences between vegetation shading and topographic effects, and perform the flow patterns in different vegetation distribution over a sloping bottom. In addition, the derived zero-order horizontal velocities were used to estimate exchange flowrates in various scales of water depth. The validity and feasibility of the asymptotic solutions were finally discussed and examined.

2.3 Mathematical formulation

2.3.1 Governing equations, initial and boundary conditions

The thermal-driven flow with emergent vegetation over a sloping boundary is schematized in figure 2.1. The wedge shape domain (x', z') is considered as a two-dimensional flow with the origin at the tip; x' and $z'(=-Sx')$ are the horizontal and vertical coordinates, respectively, where S is the bottom slope. The distribution of emergent vegetation can vary along the x' direction but is assumed to be vertically uniform. The drag due to vegetation is represented as: $\frac{C_D a u'|u'|}{2n_v}$ in the horizontal momentum equation, where u' is the horizontal velocity, C_D is the drag coefficient, a is the frontal area of vegetation per unit volume (Tanino, Nepf, & Kulis 2005). Under low stem Reynolds number $\mathrm{Re}_d\,(=u'd/\nu)$, where d is the stem diameter of the vegetation, C_D is inversely proportional to $|u'|$, i.e. $\frac{2C}{|u|n_v}$, where C is a linear drag coefficient (Zhang & Nepf 2008). The drag can therefore be simplified as Cau'. According to

experimental results in Zhang & Nepf (2009), the regression relationship between the linear drag coefficient C and the solid volume fraction ϕ is $C = -0.3788\phi^2 + 0.1134\phi$ the frontal area $a = \frac{4\phi}{\pi d}$.

The solar radiation is modeled as $I_0 \cos(2\pi t'/\tau)$, a periodic and uniform-distributed heat source over the depth, where I_0 is the solar radiation intensity at the water surface, τ is the forcing period of 24 hours, and $t' = 0$ corresponds to the time at noon. The internal heat source term is modeled as $Q_{heat}(x', z', t') = \frac{I_0 M(x'/L)\cos(2\pi t'/\tau)}{\rho_0 C_p A x'}$, where $M(x'/L_x')$, a reduction function to the solar radiation density, is related to vegetation distribution; L_x' is the length of the domain, ρ_0 is the reference density of fluid, and C_p is the specific heat of water. For example, if the vegetation is uniformly-distributed along the horizontal direction, $M(x'/L_x') = 1$. If the vegetation density linearly increases or decreases along the horizontal direction, $M(x'/L_x')$ can be expressed as: $M(x'/L_x') = a + b(x'/L_x')$ where *a, b* are related to vegetation features such as blockage percentage of solar radiation. For the one side of vegetation and the other side of water, $M(x'/L)$ is equal to $(1-B) + \frac{B}{1+\exp\left[-2k\left(\frac{x'}{L_x'} - 0.5\right)\right]}$, where B is the blockage percentage of solar radiation by vegetation, and k means the sharpness of the transition from vegetation to open water, which is related to the thermal diffusivity.

Assume the linear drag coefficient and the Boussinesq approximation due to relatively small temperature differences in the aquatic system here, the two-dimensional governing equations are:

$$\frac{\partial\left(n_v u'\right)}{\partial x'}+\frac{\partial\left(n_v w'\right)}{\partial z'}=0, \tag{2.1}$$

$$\frac{\partial u'}{\partial t'}+u'\frac{\partial u'}{\partial x'}+v'\frac{\partial u'}{\partial y'}=-\frac{1}{\rho}\frac{\partial P'}{\partial x'}-Cau'+\nu\left(\frac{\partial^2 u'}{\partial x'^2}+\frac{\partial^2 u'}{\partial z'^2}\right), \tag{2.2}$$

$$\frac{\partial w'}{\partial t'}+u'\frac{\partial w'}{\partial x'}+w'\frac{\partial w'}{\partial z'}=-\frac{1}{\rho_0}\frac{\partial P'}{\partial z'}+\nu\left(\frac{\partial^2 w'}{\partial x'^2}+\frac{\partial^2 w'}{\partial z'^2}\right)+g\alpha\left(T'-T_0\right), \tag{2.3}$$

$$\frac{\partial T'}{\partial t'}+u'\frac{\partial T'}{\partial x'}+w'\frac{\partial T'}{\partial z'}=\kappa\left(\frac{\partial^2 T'}{\partial x'^2}+\frac{\partial^2 T'}{\partial z'^2}\right)+Q_{heat}\left(x',z',t'\right), \tag{2.4}$$

where variables with a prime denote dimensional quantities, n_v is the porosity (the volume fraction occupied by water), u',w' are the horizontal and vertical velocity, P' is the pressure, ν is the kinematic viscosity, g is the gravity acceleration, α is the thermal expansion coefficient.

Initially fluids are at rest and isothermal. The thermal boundary conditions are insulated over the surface and bottom. At the surface, it is shear free due to the absence of wind or other momentum forcing, and no flow occurs across the surface. For the bottom, the flow is impermeable to the bottom, and abides by the no-slip condition. In summary, the initial and boundary conditions are

$$T' = T_0, u' = v' = 0 \text{ at } t = 0;$$

$$\frac{\partial T'}{\partial z'} = 0, \frac{\partial u'}{\partial z'} = 0 \left(\text{shear free}\right), v' = 0 \text{ on } z' = 0; \tag{2.5}$$

$$A\frac{\partial T'}{\partial x'} + \frac{\partial T'}{\partial z'} = 0, u' = v' = 0 \left(\text{no slip}\right) \text{ on } z' = -Ax'.$$

2.3.2 Scaling analysis

The resulting governing equations are non-dimensionalized as follows. The dominant time scale is characterized by the period of forcing τ (i.e. 24 hours). The vertical length scale H is defined as the growth of the boundary layer during one diurnal cycle, i.e., $H = \sqrt{\nu\tau}$ (Farrow & Patterson 1993) Due to the geometry of the wedge the horizontal length scale L is obtained by combining the slope S and vertical scale *H*, i.e., $x \sim L = H / S$. Balancing the unsteady and heat source terms in eq.(2.4) gives the temperature scale $T' - T_0 = \Delta T \sim \frac{I_0 \tau}{\rho_0 C_p \sqrt{\nu\tau}}$. The balance of the temperature difference and hydrostatic pressure yields a pressure scale $P' \sim \frac{g\alpha I_0 \tau}{c_p}$. By substituting the pressure scale into eq.(2.2) and assuming the pressure force is balanced by the unsteady horizontal velocity, the scale of horizontal velocity is $u' \sim SGr\sqrt{\nu / \tau}$, where the Grashof number is $Gr = \frac{g\alpha I_0 \tau^2}{\rho_0 C_p \nu}$. By using the continuity equation, the scale for the vertical velocity is $w' \sim S^2 Gr\sqrt{\nu / \tau}$.

By introducing the obtained scales, the non-dimensional energy equation becomes

$$\frac{\partial T}{\partial t}+S^2Gr\left(u\frac{\partial T}{\partial x}+w\frac{\partial T}{\partial z}\right)=\frac{1}{\sigma}\left(S^2\frac{\partial^2 T}{\partial x^2}+\frac{\partial^2 T}{\partial z^2}\right)+\frac{M(x)\cos(2\pi t)}{x}. \tag{2.6}$$

We use the stream function ψ ($u=-\frac{1}{n_v}\frac{\partial\psi}{\partial z}, w=\frac{1}{n_v}\frac{\partial\psi}{\partial x}$) and eliminate the pressure terms, yielding the non-dimensional stream function equation

$$\begin{aligned}\psi_{tzz}+S^2\psi_{txx}+S^2Gr\frac{1}{n_v}\left[\left(\psi_x\psi_{zzz}-\psi_z\psi_{xzz}\right)+S^2\left(\psi_x\psi_{xxz}-\psi_z\psi_{xxx}\right)\right] \\ =\psi_{zzzz}+2S^2\psi_{xxzz}+S^4\psi_{xxxx}-Ca\tau\psi_{zz}+n_vT_x\end{aligned}. \tag{2.7}$$

with the non-dimensionalized boundary conditions

$\psi=\psi_{zz}=0,\ \ T_z=0$ at $z=0$, and

$$\psi=\psi_z=0,\left(T_z+S^2T_x\right)/\sqrt{1+S^2}=0 \text{ at } z=-x. \tag{2.8}$$

Typical field values for Grashof number ranges from $Gr\approx10^7$ for an eddy viscosity of $\nu=10^{-4}$ to $Gr\approx10^9$ for a molecular viscosity of $\nu=10^{-6}$ by using input solar radiation I_0 of 1000 W/m^2 (Farrow, 2004). A typical value for the bottom slope S varies from 10^{-3} to 10^{-2} (Farrow, 2004). The coefficient S^2Gr for the convection terms in eq.(2.7) is not smaller than the viscous and temperature gradient on the right-hand side of eq.(2.7), i.e. the convective effects cannot be ignored in typical field conditions. Farrow (2004) was aware of this limitation, and finally defined a valid range for the asymptotic solution. In this study, by considering the vegetative drag, the horizontal velocity is reduced, and the convective effects in eq.(2.7) becomes less important. Following Farrow's method

(2004), a valid range for the linear asymptotic solutions, wider than Farrow suggested will be given later.

2.4 Asymptotic solutions

There is no analytic solution for eqs.(2.6) and (2.7). In order to obtain the analytic solution for T and ψ, parameter S is assumed to be small, i.e., $S \ll 1$, and the streamfunction ψ and temperature T can be expanded as a series of even powers for S (Cormack et al., 1974):

$$\psi = \psi^{(0)} + S^2\psi^{(2)} + S^4\psi^{(4)} + \ldots, \quad T = T^{(0)} + S^2T^{(2)} + S^4T^{(4)} + \ldots . \tag{2.9}$$

After substituting eq.(2.9) into eqs.(2.6) and (2.7), and equating the power of S, a system of equations are yielded, and can be solved recursively, in principle. The zero-order (S^0) temperature is firstly solved, and then the zero-order streamfunction equation can be solved according to the zero-order horizontal temperature gradient. The zero-order equations are:

$$T_t^{(0)} = \frac{1}{\sigma} T_{zz}^{(0)} + \frac{M(x)\cos(2\pi t)}{x} , \tag{2.10}$$

$$\psi_{tzz}^{(0)} = \psi_{zzzz}^{(0)} - c_d\psi_{zz}^{(0)} + n_v T_x^{(0)} , \tag{2.11}$$

where $c_d = Ca\tau$.

With boundary conditions:

$$\psi^{(0)} = \psi_{zz}^{(0)} = T_z^{(0)} = 0 \text{, on } z = 0,$$

$$\psi^{(0)} = \psi_z^{(0)} = 0, T_z^{(0)} = 0 \text{, on } z = -x. \tag{2.12}$$

And the initial condition is:

$$\psi^{(0)} = T^{(0)} = 0 \quad \text{at } t = 0. \tag{2.13}$$

2.4.1 Zero-order temperature and horizontal velocity

The zero-order temperature can be obtained by simply integrating eq.(2.10), which is:

$$T^{(0)} = \frac{M(x)\sin(2\pi t)}{2\pi x}. \tag{2.14}$$

Let $F(x) = M(x)/x$ represent the effects of vegetation distribution and topography. The zero-order streamfunction $\psi^{(0)}$ involves unsteady inertia, vertical shear, vegetative drag and buoyancy effects (temperature gradient: $T_x^{(0)} = \frac{dF(x)}{dx}\frac{\sin(2\pi t)}{2\pi}$). The streamline function $\psi^{(0)}$ can be written as:

$$\psi_{tzz}^{(0)} = \psi_{zzzz}^{(0)} - c_d \psi_{zz}^{(0)} + \frac{n_v \sin(2\pi t)}{2\pi}\frac{dF(x)}{dx}. \tag{2.15}$$

By using Laplace transform in *t*, eq.(2.15) can be solved, which is:

$$\psi^{(0)} = n_v \frac{dF(x)}{dx}\left\{\frac{\sinh\left(z\sqrt{c_d}\right)-z\sqrt{c_d}\cosh\left(x\sqrt{c_d}\right)}{\sinh\left(x\sqrt{c_d}\right)-x\sqrt{c_d}\cosh\left(x\sqrt{c_d}\right)}\left\{\frac{x^2}{2c_d}-\frac{1}{{c_d}^2}\left[\cosh\left(x\sqrt{c_d}\right)-1\right]\right\}\right.$$
$$-\frac{x\sinh\left(z\sqrt{c_d}\right)-z\sinh\left(x\sqrt{c_d}\right)}{\sinh\left(x\sqrt{c_d}\right)-x\sqrt{c}\cosh\left(x\sqrt{c_d}\right)}\left\{\frac{x}{c_d}-\frac{1}{{c_d}^2}\sqrt{c_d}\sinh\left(x\sqrt{c_d}\right)\right\}$$
$$\left.+\frac{1}{2}\frac{z^2}{c_d}-\frac{1}{{c_d}^2}\left[\cosh\left(z\sqrt{c_d}\right)-1\right]\right\}\times\frac{\sin(2\pi t)}{2\pi}$$
$$-2n_v x^3\frac{dF(x)}{dx}\sum_{n=1}^{\infty}\frac{1}{{\beta_n}^2\sin\beta_n}\left[\left(x\sin\left(\frac{\beta_n}{x}z\right)-\beta_n z\cos\beta_n\right)\left(\cos\beta_n+\frac{\cos\beta_n-1}{\beta_n^2}-\frac{1}{2}\right)\right]$$
$$\times\left\{\frac{\left(\left(\beta_n/x\right)^2+c_d\right)\cos(2\pi t)+2\pi\sin(2\pi t)-\left(\left(\beta_n/x\right)^2+c_d\right)\exp\left(-\left(\left(\beta_n/x\right)^2+c_d\right)t\right)}{\left[\left(\left(\beta_n/x\right)^2+c_d\right)^2+(2\pi)^2\right]\left({\beta_n}^2+c_d x^2\right)}\right\} \quad . \quad (2.16)$$

The horizontal velocity $u^{(0)}\left(=-\frac{1}{n_v}\frac{\partial\psi^{(0)}}{\partial z}\right)$ is then given by:

$$u^{(0)} = -\frac{dF(x)}{dx}\left\{\frac{\sqrt{c_d}\cosh\left(z\sqrt{c_d}\right)-\sqrt{c_d}\cosh\left(x\sqrt{c_d}\right)}{\sinh\left(x\sqrt{c_d}\right)-x\sqrt{c_d}\cosh\left(x\sqrt{c_d}\right)}\left\{\frac{x^2}{2c_d}-\frac{1}{{c_d}^2}\left[\cosh\left(x\sqrt{c_d}\right)-1\right]\right\}\right.$$
$$-\frac{\sqrt{c_d}x\cosh\left(z\sqrt{c_d}\right)-\sinh\left(x\sqrt{c_d}\right)}{\sinh\left(x\sqrt{c_d}\right)-x\sqrt{c_d}\cosh\left(x\sqrt{c_d}\right)}\left\{\frac{x}{c_d}-\frac{1}{{c_d}^2}\sqrt{c_d}\sinh\left(x\sqrt{c_d}\right)\right\}$$
$$\left.+\frac{z}{c_d}-\frac{\sqrt{c_d}\sinh\left(z\sqrt{c_d}\right)}{{c_d}^2}\right\}\times\frac{\sin(2\pi t)}{2\pi}$$
$$+2x^3\frac{dF(x)}{dx}\sum_{n=1}^{\infty}\frac{1}{\beta_n\sin\beta_n}\left[\left(\cos\left(\frac{\beta_n}{x}z\right)-\cos\beta_n\right)\left(\cos\beta_n+\frac{\cos\beta_n-1}{\beta_n^2}-\frac{1}{2}\right)\right]$$
$$\times\left\{\frac{\left(\left(\beta_n/x\right)^2+c_d\right)\cos(2\pi t)+2\pi\sin(2\pi t)-\left(\left(\beta_n/x\right)^2+c_d\right)\exp\left(-\left(\left(\beta_n/x\right)^2+c_d\right)t\right)}{\left[\left(\left(\beta_n/x\right)^2+c_d\right)^2+(2\pi)^2\right]\left({\beta_n}^2+c_d x^2\right)}\right\}, \quad (2.17)$$

where β_n are the positive roots for the equation $\sin\beta_n=\beta_n\cos\beta_n$. Without vegetation $\left(c_d=0,\ \text{and}\ F(x)=1/x\right)$, the horizontal velocity $u^{(0)}$ is reduced to

$$u^{(0)} = -\frac{1}{96\pi x^2}\sin(2\pi t)(z+x)\left(8z^2+zx-x^2\right) - 2x\sum_{n=1}^{\infty}\frac{1}{\beta_n{}^3\sin\beta_n}\left[\left(\cos\left(\frac{\beta_n}{x}z\right)-\cos\beta_n\right)\left(\cos\beta_n+\frac{\cos\beta_n-1}{\beta_n^2}-\frac{1}{2}\right)\right] \times\left\{\frac{(\beta_n/x)^2\cos(2\pi t)+2\pi\sin(2\pi t)-(\beta_n/x)^2\exp\left(-(\beta_n/x)^2 t\right)}{\left[(\beta_n/x)^4+(2\pi)^2\right]}\right\} \quad (2.18)$$

Eq.(2.18) is the same as Farrow and Patterson (1993) derived. The asymptotic solutions $T^{(0)}$ and $\psi^{(0)}$ are dependent on vegetation distribution and topographic effects, i.e. $F(x)$.

2.4.2 Exchange flowrate and bottom shear stress

The exchange flowrate Q_{ex}' and bottom shear stress $s_b^{'}$ are two indicators to perform the importance of thermal-driven flow on transport of nutrients and chemical substances. The first-order of dimensionless exchange flowrate Q_{ex} per unit width can be represented as (Horsch & Stefan 1988):

$$Q_{ex}{}^{(0)} = \frac{1}{2}\int_{-x}^{0}\left|u^{(0)}\right|dz\,. \quad (2.19)$$

Based upon the scaling analysis of u' and z', shear stress s' can be scaled by $\frac{\mu SGr}{\tau}$, and the dimensionless shear stress s_b is: $s_b = \frac{\partial u}{\partial z}$. The bottom shear stress s_b is then given by:

$$s_b = \left.\frac{\partial u^{(0)}}{\partial z}\right|_{z=-x} = -\frac{dF(x)}{dx}\left\{\frac{\left[\sqrt{c_d}x^2\sinh\left(x\sqrt{c_d}\right)+2x\left(1-\cosh\left(x\sqrt{c_d}\right)\right)\right]}{2\sqrt{c_d}\left[\sinh\left(x\sqrt{c_d}\right)-x\sqrt{c_d}\cosh\left(x\sqrt{c_d}\right)\right]}\right\}\times\frac{\sin(2\pi t)}{2\pi}$$
$$+4x^3\frac{dF(x)}{dx}\sum_{n=1}^{\infty}\left(\cos\beta_n+\frac{\cos\beta_n-1}{\beta_n^2}-\frac{1}{2}\right)$$
$$\times\left\{\frac{\left((\beta_n/x)^2+c_d\right)\cos(2\pi t)+2\pi\sin(2\pi t)-\left((\beta_n/x)^2+c_d\right)\exp\left(-\left((\beta_n/x)^2+c_d\right)t\right)}{\left[\left((\beta_n/x)^2+c_d\right)^2+(2\pi)^2\right]\left(\beta_n{}^2+c_dx^2\right)}\right\} \qquad (2.20)$$

Without vegetation, eq.(2.20) becomes:

$$s_b = \left.\frac{\partial u^{(0)}}{\partial z}\right|_{z=-x} = -\frac{1}{x^2}\frac{\sin(2\pi t)}{16\pi}$$
$$-\frac{1}{x^2}\sum_{n=1}^{\infty}\left(\cos\beta_n+\frac{\cos\beta_n-1}{\beta_n^2}-\frac{1}{2}\right)$$
$$\times\left\{\frac{(\beta_n/x)^2\cos(2\pi t)+2\pi\sin(2\pi t)-(\beta_n/x)^2\exp\left(-(\beta_n/x)^2t\right)}{\left[(\beta_n/x)^4+(2\pi)^2\right]\beta_n{}^2}\right\}. \qquad (2.21)$$

2.4.3 Second-order temperature

The energy equation for $O(S^2)$, including conduction from the bottom and advection of $T^{(0)}$ due to zero-order velocity $u^{(0)}$, is:

$$T_t^{(2)} = \frac{1}{\sigma}T_{zz}^{(2)} + \frac{1}{\sigma}T_{xx}^{(0)} - Gru^{(0)}T_x^{(0)}. \qquad (2.22)$$

The boundary conditions on $T^{(2)}$ are:

$T_z^{(2)} = 0$ on $z = 0$, (2.23)

$$T_z^{(2)} = -T_x^{(0)} \text{ on } z = -x. \tag{2.24}$$

The second boundary condition (eq 2.24) accounts for the sloping bottom effect. The solution of $T^{(2)}$ can be written as $T^{(2)} = T_{cond}^{(2)} + T_{adv}^{(2)}$, where $T_{cond}^{(2)}$ is to correct the horizontal conduction due to the sloping bottom and $T_{adv}^{(2)}$ is the correction to the advection (Farrow, 2004).

The solutions for $T_{cond}^{(0)}$ and $T_{adv}^{(0)}$ are provided below:

$$\therefore T_{cond}^{(2)} = \frac{1-\cos(2\pi t)}{4\pi^2\sigma}\left(\frac{d^2F(x)}{dx^2} + \frac{1}{x}\frac{dF(x)}{dx}\right) + \frac{1}{\pi x}\frac{dF(x)}{dx}\sum_{n=1}^{\infty}(-1)^n \cos\left(\frac{n\pi z}{x}\right) \times \frac{(n\pi/x)^2 \sin(2\pi t) + 2\pi\sigma\left[\exp\left(-(n\pi/x)^2 t/\sigma\right) - \cos(2\pi t)\right]}{(n\pi/x)^4 + (2\pi\sigma)^2} \tag{2.25}$$

$$T_{adv}^{(2)} = Gr\sigma x\sum_{m=1}^{\infty}\left\{\left[a_m(x,t) + \frac{4(-1)^m x^4}{\pi}\left(\frac{dF(x)}{dx}\right)^2 \sum_{n=1}^{\infty} b_{mn}(x,t)c_{mn}(x,t)\right]\cos\frac{m\pi z}{x}\right\} \tag{2.26}$$

The parameters in eq.(2.26) are given in Appendix 2.A. Only $T_{adv}^{(2)}$ is related to the vegetation distribution. For the case without vegetation, i.e., $c_d = 0$, and $F(x) = 1/x$, the solution for second-order temperature becomes the same as eqs.(A1) to (A4) shown in Farrow(2004). The dimensionless horizontal advective heat transfer per unit with q is: $q = S^2\int_{-x}^{0} u^{(0)}T^{(2)}dz$, and the zero-order temperature, constant along the water column, will not contribute to q (Farrow 2004).

2.5 Results and discussion

2.5.1 Zero-order asymptotic solutions

The results derived in the previous section allow estimation of the horizontal velocity under different vegetation distribution. The discussions here are firstly focused on uniform distribution of emergent vegetation, i.e. $F(x)=\frac{1}{x}$, $\frac{dF(x)}{dx}=-\frac{1}{x^2}$. The vegetation is assumed to be emergent and very close to the water surface. The emergent vegetation blocks part of solar radiation into the water, but meanwhile the volume occupied by water is also decreased. For example, 0.25% of vegetation (99.75% occupied by water) blocks 0.25% of solar radiation, i.e. allowing 99.75% solar radiation into 99.75% volume occupied by water. The induced temperature distribution is the same as the case without vegetation but additional vegetative drag would affect the flow field. The diameter of vegetation stem d is assumed to be 0.6 cm in this study.

The horizontal velocities with vegetative drags denoted by c_d are embedded almost in each term of eq. (2.17). On the contrary, without vegetation, the horizontal velocity (eq 2.18) can be separated as viscous (1st term), and inertia and transient responses (2nd term) as Farrow & Patterson (1994) indicated. Eq.(2.18) shows that in shallow water ($x \ll 1$), the first term is more important, i.e. viscosity is mainly balanced with buoyancy; whereas in deep water ($x \gg 1$), the second term is greater, i.e. inertia and transient effects are significant. The vegetative drag has impacts both on viscous and inertia responses (see eq 2.17).

The e-folding time (increasing or decreasing a quantity by a factor of *e*, i.e. Napier's constant) for the transient term in eq.(2.16) is:

$$t_e = \frac{1}{\left(\beta_1 / x\right)^2 + c_d} \approx \frac{1}{20.19 / x^2 + c_d}, \tag{2.27}$$

which is function of x and c_d. Because c_d is always positive, t_e with vegetation is smaller than that without vegetation, i.e. the transitional stage with vegetation is shorter than without vegetation. The ratios of e-folding time with 0.25% vegetation to no vegetation in shallow water ($x = 0.25$), intermediate depth ($x = 1$), and deep water ($x = 5$) are equal to 0.961, 0.03, and 0.06, respectively. This means that the e-folding time is reduced by the presence of vegetation, and decreased more in the deep water than in shallow water. At the same location of x, denser vegetation would have shorter e-folding time. Therefore, horizontal velocity experiences a shorter transient stage from the onset of the flow and becomes steady state faster due to the presence of emergent vegetation. Also, the vegetative drag c_d is include in the denominator of the 2nd term in eq.(2.17). As the vegetation becomes denser, i.e. larger c_d, the 2nd term becomes smaller, and therefore inertial and transient effects are less important within vegetation.

Figure 2.2 provides the time evolution ($t = 0 \sim 3$) of the viscous ($u_{zz}^{(0)}$), inertia ($u_t^{(0)}$), horizontal pressure gradient ($-p_x^{(0)}$) from buoyancy, vegetative drag ($-c_d u^{(0)}$), and horizontal velocity ($u^{(0)}$) at the water surface in zero-order horizontal momentum equation shown below:

$$u_t^{(0)} = -p_x^{(0)} - c_d u^{(0)} + u_{zz}^{(0)} \tag{2.28}$$

Each term in eq.(2.28) is obtained by integrating eqs.(2.17) or (2.18) with respect to *z* direction. The horizontal velocities can be correlated to the inertia term (acceleration *a*) by using $u = \int a dt$, and therefore the horizontal velocity *u* and inertia term u_t are always out of phase. With vegetation, in shallow water (*x*=0.25, see figure 2.2a), the viscous term is dominant and balanced with the buoyancy (i.e. pressure gradient). Effects of the vegetative drag are small with 0.25% vegetation. Without vegetation, viscosity is also dominant in shallow water (see figure 2.2d). Although the pressure gradient is larger in shallow water, the larger viscous effect counteracts the pressure gradient. Consequently, the resulting inertial term is too smaller to generate higher horizontal velocities. The pressure gradient and zero-order horizontal velocity $u^{(0)}$ are at the same phase, which means that flow will reverse immediately to the change of pressure gradient. For the limiting case of $x \to 0$, $u^{(0)}$ responses instantaneously to the reversal of pressure gradient. Because of small *x* values, e-folding time is small (see.eq 2.27). The transient behavior is too short to be observed in shallow water, and the flow shows a very regular pattern, i.e. large-time behavior is achieved in short time.

At the intermediate depth ($x = 1$, see figures 2.2b and e), vegetative drag becomes more important, but still smaller than the viscous effect. Because inertia is reduced by both viscosity and vegetative drag, the induced horizontal velocity is smaller than that without vegetation. As water becomes deeper, both viscous effects and pressure gradient decrease, but the viscous effect decreases faster than the pressure gradient. The resulting inertia term becomes more important as the water depth increases. Also, the phases of pressure gradient and horizontal velocity are not the same both in the cases with and without vegetation. The time lag in vegetation is smaller than without vegetation. If the

vegetation becomes denser, the vegetative drag would exceed the viscosity at this depth, and the time lag between horizontal velocity and pressure gradient becomes smaller as well.

In deep water ($x = 5$, see figures 2.2c and f), vegetative drag becomes more important than viscosity, and significantly reduce the magnitude of inertia as well as the horizontal velocity. Within vegetation, the time lag between the reversal of the horizontal velocity and pressure gradient is small. Without vegetation, larger inertia arises from smaller viscous effects, and leads to an apparent time-lag between the reversal of the horizontal velocity and pressure gradient. The inertia term is positive from $t = 0$ to $t \approx 0.5$, and in turn the maximum horizontal velocity occurs at $t \approx 0.5$, corresponding to the largest positive area under the inertia term with respect to time. The time lag between the reversal of the flow and pressure gradient is up to 0.25, i.e. a quarter of the forcing period as Farrow and Patterson (1993) mentioned. In deeper water and without vegetation, the inertia is approximately the same phase as pressure gradient, but is out of phase with the horizontal velocity. The positive horizontal velocity is larger than negative horizontal velocity at the beginning and then gradually become equal as time increases.

2.5.2 Transient velocity behavior in vegetation

Figure 2.3 shows streamlines at various times with 0.25% vegetation. At t=1, the residual inertia from cooling period results in counter-clockwise circulation over the entire flow field. At $t = 1.01$, short after the pressure gradient reverses, a zero streamline intersecting the water surface in the flow domain divides the flow into two opposite

circulation parts. In the areas close to the tip, the circulation is firstly reversed by the pressure gradient, and a propagating front flow from the tip to the deep water. In the remaining regions, an opposite propagating front flows from the deep water to the shallow water. The position of zero surface velocity keeps moving to the deep water as time increases until the entire flow field is completely reversed at $t = 1.07$. The flow field continues to accelerate and the recirculating region increases from the shallow water to the entire flow field. The flow patterns are very similar to the large-time behavior without presence of vegetation (see figure 4 in Farrow & Patterson, 1993). For the streamlines without vegetation, the larger inertia maintains the counter-clockwise circulation at t=1.12 in the intermediate water depth, and two propagating fronts, one in shallow water, and one in deep water toward to the deep water are evident (see figure 6 in Farrow and Patterson, 1993). The vegetative drag reduces the inertia of the circulation, and makes the counter-clockwise circulation survive shorter than the circulation without vegetation in the flow field.

The horizontal velocity profiles at various times for shallow, intermediate and deep water are provided and compared with limiting cases, i.e. viscous, inertia, and vegetative drag are separately included in eq.(2.28), and obtain the corresponding zero-order velocity profiles. The zero-order velocity for only considering viscosity $u_v^{(0)}$, inertia $u_i^{(0)}$, and vegetative drag $u_d^{(0)}$ is given by:

$$u_v^{(0)} = \frac{dF(x)}{dx}\frac{\sin(2\pi t)}{96\pi}(z+x)\left(8z^2 + zx - x^2\right) \tag{2.29}$$

$$u_i^{(0)} = \frac{1}{8\pi^2}\frac{dF(x)}{dx}(2z+x)\left[\cos(2\pi t) - 1\right] \tag{2.30}$$

$$u_d^{(0)} = -\frac{\sin(2\pi t)}{4\pi c_d}\frac{dF(x)}{dx}(2z+x) \ . \tag{2.31}$$

For the inertia- and drag-limiting cases, the bottom velocity is not equal to zero due to lack of viscosity. Only the velocity profiles derived from limiting cases close to the full solution are shown, and for the velocity profiles from limiting cases much larger than the full solution are excluded in figure 2.4. The horizontal velocity structures are initially balanced by the inertia and the horizontal pressure gradient, and then affected by viscosity and vegetative drag. At small time, the horizontal velocity profiles can be characterized as a straight line, corresponding to the inertia-limiting velocity profiles given by Farrow (2004) beside the regions near the boundary where viscosity prevails (see figure 2.4). The inertia-dominant region is based upon the time scale when viscosity diffuses to the entire water column, i.e. $t_v \sim x^2$, and for the vegetative drags to become dominant, it is $t_d \sim (Ca\tau)^{-1}$ suggested by Zhang and Nepf (2009). For 0.25% vegetation with diameter of 0.6cm, $t_d \sim 0.078$ in comparison with $t_v \sim 0.0625$ at $x = 0.25$, $t_v \sim 1$ at $x = 1$, and $t_v \sim 25$ at $x = 5$. According to experiments conducted in a constant depth and steady light source condition, Zhang and Nepf (2009) found that the flow becomes vegetative drag dominant as the time increases. With 0.25% vegetation, the inertia at $x = 0.25$, and 5 is dominated and balanced by buoyancy until $t = 0.002$ and 0.05 (see figure 2.4) respectively; whereas without vegetation, the time for inertia-dominance at $x = 0.25$, and 5 is longer, and can be up to $t = 0.25$ for $x = 5$ (Farrow, 2004). Figure 2.4a also shows as time increases, in shallow water ($x = 0.25$), the viscous effect is more important than the vegetative drag, and the horizontal velocity profiles can be simplified

as a viscous/buoyancy balance (eq.29) given by Farrow (2004). Within 0.25% vegetation, the small difference between the horizontal velocity profiles and viscous–dominated profiles shown in figure 2.4a are due to the effect of vegetative drag. As the vegetation becomes denser, the effect of vegetative drag becomes obvious in shallow water.

The straight-line velocity profiles (eq 2.31) are the feature of drag-dominant regime as Tamino, Nepf & Kulis (2005) indicated in the lock-exchange experiment. When the vegetation is denser, i.e. larger c_d, the slope of the velocity profiles becomes steeper. For deep water, the flow field is dominated by the inertia at the beginning as Farrow (2004) indicated, also show in figure 2.4b (t=0.25, $\phi = 0.25\%$). As time increases, the entire flow field will be eventually affected by viscosity. Within vegetation, the inertia is prevalent at very short time (see figure 2.4b, t=0.05, $\phi = 0.25\%$), and then vegetative drag becomes dominant. Therefore, the horizontal velocity profiles can be represented by a drag-limiting velocity profile (see figure 2.4b, t=0.25, $\phi = 0.25\%$). Near the boundary, the deviations between the full asymptotic and inertia and drag-dominant solutions are considerable, which are due to lack of boundary layer, i.e. viscous effects. In figure 2.4b, the distance from the bottom to the point where velocity profiles turn to the opposite direction can be regarded as the regions affected by viscosity. It is noted that with the presence of vegetation, the viscosity–dominated regions shrink and the vegetative drag suppresses the growth of boundary layer (see figure 2.4b, t =0.25, $\phi = 0\%$, and 0.25%). Based upon the scaling analysis (see section 2.2), the ratio of vegetative drag and inertia terms is $Ca\tau$. When $Ca\tau \ll 1$, the vegetative effect can be neglected, and with vegetation diameter assumed to be 0.006 m, the corresponding critical vegetative density $\phi_{critical}$ to

yield $Ca\tau = 1$ is ~0.069%. The vegetation density larger than $\phi_{critical}$ means the flow field will be affected by the presence of vegetation.

2.5.3 Large-time velocity behavior in vegetation

Due to the vegetation, the transient time becomes much shorter than that without vegetation. Streamlines shown in figure 2.3 are very similar to the streamlines in large-time scale. Figure 2.5 shows a series of velocity profiles in shallow, intermediate and deep water near the time when the pressure gradient is reversed. In shallow water, because viscous effects are more important than vegetative drag, the velocity profiles with and without vegetation are very similar. The time lag between the reversal of circulation and pressure gradient is very small, less than 0.005 (see figures 2.5a, d), i.e., the circulation is approximately in phase (lock phase) with the pressure gradient. As water becomes deeper, the viscous effects become less important, leading to larger inertia, and time lags between the reversal of circulation and pressure gradient become evident (see figures 2.5c~f). The vegetative drag reduces the inertia, and therefore shortens the time lag between the reversal of circulation and pressure gradient in comparisons with the circulation at the same depths but without vegetation. For the intermediate water depth, 0.25% vegetation can have a time lag of ~0.03; whereas the time lag becomes larger ~0.05 without the presence of vegetation. In deep water, for 0.25% vegetation, the flow is reversed between t=0.56 to 0.57 (figure 2.5d). The time lag t_{lag} is shortened by four times ($t_{lag} = 0.2 \sim 0.23$ without vegetation and $t_{lag} = 0.06 \sim 0.07$ with vegetation). As the vegetation becomes denser, the time lag will become smaller, for instance, for 0.5% and

1% vegetation, the time lags at x=1 are ~0.025 and ~0.005, respectively. Three-layer structure of the flow is observed both in shallow and deep water for vegetation and unvegetated cases.

2.5.4 Surface velocities, exchange flowrates, and bottom shear stresses

Figure 2.6 provides contours of surface velocity over (x-t) domain. Due to vegetative drag, the transient period of surface velocity becomes smaller, and the patterns of surface velocities are similar in the first four cycles, i.e. it reaches a large-time behavior. In addition, the time lag between reversal of velocity and pressure gradient in shallow water is close to zero, but at deep water ($x = 10$), the circulation is reversed at t~0.55, i.e. time-lag of ~0.05 (see figure 2.6a). Without vegetation, the time lag in shallow water is also close to zero, but in deep water ($x = 10$), the time lag significantly changes during the day and nighttime. At x=10, the circulation is revered at t=0.875, i.e. $t_{lag} = 0.375$, and the reversed flow due to the cooling period only lasts in a short time, i.e. the flow is reversed again at t=1.10, i.e. $t_{lag} = 0.10$. At the transient stage, the positive surface velocity (flow from the tip to offshore) lasts longer at the beginning, and the negative surface velocity (flow from deep water to shallow water) gradually becomes larger and finally equal to the positive surface velocity. However, after four cycles, the positive velocity is still larger than the negative velocity shown in figure 2.6b, i.e. the larger-time behavior has not reached yet. As time increases, the time-lag t_{lag} due to the heating and cooling period gradually turns into similar, and finally becomes the same, which is $t_{lag} = 0.25$ as Farrow and Patterson (1993) indicated.

It is also noted that because of vegetation, locations of maximum or minimum surface velocities move closer to the tip in comparison with no vegetation case. With 0.25% vegetation, the locations of maximum and minimum velocity occur at $x \sim 1.2$. On the other hand, for the no vegetation case, the locations for the maximum and minimum velocities are not equal at the transient stages. At the beginning, the locations of the maximum and minimum horizontal velocities during heating and cooling periods occur at $x \sim 2.5$ and 2, respectively. As time increases, the locations for extreme velocities gradually approach to $x \approx 2$ as Farrow and Patterson (1993) indicated.

According to the horizontal velocity profiles, the exchange flowrate Q can be estimated by using eq.(2.19). In figure 2.7, the exchange flowrate is proportional to the water depth both with and without vegetation, corresponding to findings from several previous studies (Sturman et al. 1999, Oldham & Sturman, 2001, and Chubarenko, 2010). In shallow water, the exchange flowrate in vegetation is smaller and approximately varies with $\sin(2\pi t)$, i.e. the maximum exchange flowrate occurring at $t = 0.25$ and $t = 0.75$ (see figure 2.7a). As the depth increases, the inertia effects lag the occurring of the maximum exchange flowrate to t=0.30 and 0.80. Without vegetation, at the transient stage, the positive surface velocity due to heating processes is larger than the negative surface velocity from the cooling processes, and as a result, the maximum exchange flowrates in the heating period are greater than in the cooling period at the initial stage. As time increases, the occurring time of the maximum exchange flowrates in heating and cooling periods gradually become equal, i.e. at $t = t_{\text{large}} + 0.5$ and 1, and the flow reaches large-time behavior. In comparisons with figure 2.7a and b, the presence of vegetation reduces the exchange flowrate, regulates the phase of exchange flowarte with the

pressure gradient, and also shortens the transient time for the exchange flowrate reaching large time behavior.

In terms of the dimensionless bottom shear stress with and without vegetation (see figure 2.8), the dominant viscous effects in shallow water can also be revealed. Firstly, in shallow water, the bottom shear stress (eqs. 2.20 and 2.21) shows a periodic pattern of $\sin(2\pi t)$ as velocity profiler, and at $t = 0.25$ and 0.75, the circulation will generate the maximum upward and downward bottom shear stress. When the water becomes deeper, due to inertial effects, the occurring time for the maximum and minimum bottom shears stress would be delayed. At $x = 10$, the time lag within 0.25% vegetation would be ~0.02, whereas without vegetation, it would be ~0.012. Because the bottom shear stress is generated due to the viscous effects, it reaches its maximum value when the water depth approaches zero as well as the case without vegetation. The vegetative drag has almost no effect on bottom shear stress as the water depth is close to zero. When the water depth becomes deeper, vegetative drag decreases the horizontal velocity, and then the bottom shear stress would be smaller with vegetation than that without vegetation. Additionally, within vegetation, the transient time is short, and bottom shear stress shows periodic patterns. Without vegetation, the clockwise circulation is larger than the counter-clockwise circulation at the beginning, and therefore the maximum bottom shear stress toward uphill is larger than that toward downhill. As time increases, the maximum uphill and downhill bottom shear stresses gradually become equal. The bottom shear stress is an important indicator to understand the nutrients or chemical substances entrained from bottom sediments to water column. Although the maximum bottom shear stress due to thermal-driven flow is very small $\sim 4.2\times10^{-3}\left(N/m^2\right)$ for $I_0 = 500W/m^2, A = 10^{-2}$

occurring at very near to the tip, back and forth flush along the bottom still can entrain lighter nutrients or chemical substances from the sediments, or loosen the bottom sediments, i.e. reducing the critical shear stress.

2.5.5 Vegetation distribution

In field conditions, spatial variations of nutrients and light climates commonly lead to non-uniform horizontal vegetation distribution, which change the heat source term in eq.(2.10) . The linearly increasing or decreasing vegetation distribution will not induce any additional temperature gradient in eq.(2.10). However, the extreme conditions such as vegetation occupied half of the entire domain, and open water in the other half domain commonly found in field (Lövstedt & Bengtsson, 2008; Zhang & Nepf, 2009) can result in additional heat drivers in eq.(2.10). A Heaviside function is adopted to describe the distribution of solar radiation for one-side vegetation (ϕ_0) and one-side open water ($\phi = 0\%$), which is:

$$I_0(x) = I \times \left[(1-B) + \frac{B}{1+\exp\left(-2k\left(\frac{x}{L_x} - 0.5\right)\right)} \right], \tag{2.32}$$

where I is the solar radiation in the open water, B is the blockage of solar radiation by vegetation shading, which is between 0 to 1, k is the coefficient meaning the sharpness

of the transition from vegetation to open water. L_x is the dimensionless length of the domain, and $M(x) = \left[(1-B) + \frac{B}{1+\exp\left(-2k\left(\frac{x}{L_x} - 0.5\right)\right)} \right]$.

The solid volume fraction of vegetation $\phi(=1-n)$ is:

$$\phi(x) = \phi_0 \cdot G(x), \tag{2.33}$$

where ϕ_0, the solid volume fraction of vegetation at the shoreline, and $G(x) = \left[\frac{1}{1+\exp\left(2k\left(\frac{x}{L_x} - 0.5\right)\right)} \right]$.

If the vegetation is emergent only several centimeters from the water surface, the solar radiation into the water is assumed to be inversely proportional to the vegetation densities, i.e. 0.5% of vegetation blocks 0.5% of solar radiation (99.5% penetrating into the water body). As a result, this kind of emergent vegetation causes identical temperature variations as the case without vegetation. Once the emergent vegetation is very high above the water surface, such as reed with 2~3m high from the water surface, small amount of high reeds can block ~85% incident solar radiation (Lövstedt & Bengtsson, 2008). The vegetation shading effect causes less solar radiation penetrating into the water body, and leads to lower temperature in dense vegetated areas than no or loose vegetated areas during the daytime. If the dense vegetation grows in shallow water, commonly found in the field, the shading effect would contradict with the topographic effect, and

may change the direction of the temperature gradient as well as the circulation patterns. By using eq.(2.32), temperature gradient $\frac{dF(x)}{dx}$ in eq.(2.15) can be rewritten as:

$$\frac{dF(x)}{dx} = -\frac{1}{x^2}\left[(1-B) + \frac{B}{1+\exp\left(-2k\left(\frac{x}{L_x}-0.5\right)\right)}\right] + \frac{2Bk\exp\left(-2k\left(\frac{x}{L_x}-0.5\right)\right)}{x\left[1+\exp\left(-2k\left(\frac{x}{L_x}-0.5\right)\right)\right]^2} . \quad (2.34)$$

In eq.(2.34), the first term represents the topographic effect, and the second and third terms indicate the effect of vegetation shading. The magnitude of these terms can be used to evaluate the dominance of topographic or vegetation shading effects. Figure 2.9 illustrates two extreme conditions, which are (i) for $k > 0$, vegetation in shallow water, and open in deep water; and (ii) for $k < 0$, open in shallow water, and vegetation in deep water. Assuming the domain length L_x is 10, vegetation density of 0.25%, and the interface between vegetation and open water is at the center line of $x = 5$, the exchange flowrates at the center with different blockages *B* and sharpness *k* are shown in figure 2.11. For the case of vegetation in shallow water, and open in deep water (see figure 2.10a), i.e. $k > 0$, as blockage factor *B* is larger, the first term in eq.(2.34) becomes smaller but the second and third term turns to be larger. Thereby, a critical blockage $B_{critical}$ resulting in zero exchange flowrate at the centerline of the domain can be found. Furthermore, as sharpness *k* increases, $B_{critical}$ will decrease. For example, *k*=1 yields $B_{critical} = 0.33$, and *k*=5 leads to $B_{critical} = 0.077$. The critical blockage $B_{critical}$ identifies the dominant regions of topographic and shading effects. For the ranges of $B < B_{critical}$, the driving force is generated from the sloping bottom but reduced by vegetation shading. As

a result, circulation patterns are the same, i.e. during the daytime, circulation flowing from deep water to shallow water along the surface, and downhill over the sloping bottom as those in no vegetation and uniform vegetation cases. On the contrary, when $B > B_{critical}$, the vegetation shading effect is dominant, and the flow patterns become opposite as the case of $B < B_{critical}$. When the blockage B is much larger than $B_{critical}$, the induced temperature gradient become greater, causing larger circulation and exchange flowrates.

For the other extreme case, i.e. open in shallow water, and vegetation in shallow water, the topographic and vegetation shading generate horizontal temperature gradients along the same direction, i.e. vegetation shading reinforces the topographic effects (see figure 2.10b). Also, this case would not lead to any zero exchange flowrate, and the exchange flowrate increases linearly as the blockage becomes larger. For a sharper temperature transition between open water and vegetation, i.e. larger absolute value of k, exchange flowrates increase faster than those with smaller k values. The comparisons of exchange flowrate of four cases, i.e.: (i) for no vegetation, (ii) 0.25% vegetation, (iii) vegetation in shallow water and open in deep water, and (iv) open in shallow water, and vegetation in deep water at centerline and with sharpness k of ±5 are shown in figure 2.11. The extreme vegetation distribution for cases (iii) and (iv) both can result in larger exchange flowrates than the case without any vegetation. Specifically, for case (iii), it also can lead to smaller exchange flowrates than the case of uniform-distributed vegetation. Therefore, the presence of emergent vegetation does not always decrease the exchange flowrates. The non-uniform vegetation distribution can dramatically change the magnitude of exchange flowrates.

The circulation patterns are mainly determined by the sharpness coefficient *k* and blockage *B*. Figures 2.12 to 2.14 show the large time behavior of streamline contours for the two extreme cases with different blockage *B*, and sharpness *k*. For figure 2.12 with *B*=0.05, circulation patterns are approximately the same as the case without any vegetation, and slight variations are shown at $x = 5$, the interface between the vegetation and open water. Because of residual inertia from the cooling period, the circulation is not yet reversed at $t = 0$. At $t = 0.1$, the circulation is reversed in shallow water but not in deep water. Since vegetation is in shallow water, the residual inertia is reduced, and the regions of the revered flow are larger than those without vegetation. At $x = 5$, the interface of the vegetation and the open water, the temperature gradient due to vegetation shading is toward the opposite direction to that from the sloping bottom, and therefore the magnitude of the streamlines are decreased (see circulation at $t = 0.3$ and 0.4 in figure 2.12). The circulation performs periodic patterns, and therefore the nighttime situations are neglected in figure 2.12. In figure 2.13, the circulation with the critical blockage $B_{critical} = \frac{1}{13}$ given $k = 5$ is shown. The zero vertical streamlines, i.e. zero exchange flowrate, are found at $x = 5$ and 5.66. Also, in this region, circulation affected by the vegetation shading always performs opposite patterns than those in shallow and deep water which are influenced by the sloping bottom effect (see figure 2.13). At *t*=0, the circulation follows the patterns from the cooling period. When the circulation starts to reverse from the cooling to heating periods, several regions with opposite circulation patterns are observed at *t* = 0.1~0.2. In short, only the center portions are influenced by the vegetation shading, and the other portions follow the same trends for uniform vegetation distribution in shallow water, and no vegetation in deep water. Once

$B_{critical} > \frac{1}{13}$, the circulation patterns at the center line are controlled by vegetation shading. Figure 2.14 shows the circulation patterns with $B = 0.85$, commonly found in shallow water with high reeds growth (Lövstedt & Bengtsson, 2008). The vegetation shading effect leads to larger temperature gradient, and then stronger circulation at the vegetation-water interface as well as larger exchange flowwrates. However, as very shallow and deep water, the circulation is not affected by vegetation shading. At $t = 0$, clockwise circulation exists in the most parts of the flow domain beside the very shallow and deep water. At $t = 0.1$, counter-clockwise circulation emerges from shallow water ($x > 1$), but the residue inertia keeps circulation direction unchanged in deep water. As time increases, the front of counter-clockwise circulation moves to the deep water. At $t = 0.3$, the circulation in the entire flow field is reversed. The peak of the circulation gradually moves to the deep water from $t = 0.4$ to 0.5.

For the case of open in shallow water, and vegetation in deep water with $B = 0.85$, and $k = -5$, the vegetation shading intensifies the topographic effect, and therefore stronger circulation occurs at the vegetation-water interface. In figure 2.15, at $t = 0$, counter-clockwise circulation is observed due to the residual inertia from the cooling period. When time increases, i.e. $t = 0.1$, due to the vegetation, the circulation in deep water is reversed earlier than that in shallow water. The circulation is completely reversed at $t = 0.2$, and then continuously increased until $t = 0.4$. At $t = 0.5$, the circulation magnitude is decreased by the temperature gradient arising from the cooling period. The circulation patterns can be significantly changed by the blockage of emergent vegetation, and the temperature differences between the vegetation and open water, which may be

related to vegetation species. As a result, the detailed investigations on these parameters are critical to provide accurately estimation of the exchange flowrates in the field.

2.5.6 Verifications of horizontal velocity and exchange flowrate

By using asymptotic solution, horizontal velocity with a given bottom slope and heat flux can be estimated. Oldman and Sturman (2001) estimated thermal-driven horizontal velocity through the nighttime cooling in a wetland mesocsom. The maximum of horizontal velocity measured at surface was 2 mm/s, agreement well of 2.2 mm/s from asymptotic solution by using eddy viscosity ($\nu = 10^{-4} m^2 / s$). Second, in this study, the stem Reynolds number Re_d is assumed to be small (<10, Zhang & Nepf 2009), and then the linear drag law can be applied. Without any assumption, the drag coefficient can be written as: (Koch & Ladd, 1997): $C_D \approx \frac{2}{\mathrm{Re}_d}\left(12 + 1.07\,\mathrm{Re}_d\right)$. In the horizontal momentum equation, the drag term can be represented as: $\frac{1}{n_v}\left(Cau + 1.07au|u|\right)$. By using the maximum velocity of 2.2 mm/s, and vegetation density of 17% and diameter of 0.16m in Oldman and Sturman (2001), the ratio of $Cau/\left(1.07au|u|\right) \approx 3.65 > 1$. Therefore, it is reasonable to neglect the second term in the drag coefficient. The exchange flowrate is an indicator to evaluate the importance of thermal-driven flow on transport of nutrients and chemical substances between the nearshore and deep water. In previous studies, exchange flowrates of thermal-driven flow were measured in the field and laboratory experiments (Sturman et al. 1999; Oldham & Sturman 2001; Chubarenko & Demchenko 2008).

Sturman et al. (1999) considered the nighttime cooling as a steady state process and linked the exchange flowrate to a bottom slope, buoyancy flux and local water depth. Oldham and Sturman (2001) extended Sturm et al.' scaling analysis and combined principles of porous media flow to include vegetation effects. They found the exchange flowrate is functions of buoyance flux, permeability of vegetated regions, and local depth, and verified with experimental and field measurements. By using the same parameters such as bottom slope, water depth, incident solar radiation and eddy viscosity ($\nu = 10^{-4} m^2 / s$), the derived asymptotic equation is adopted to estimate the exchange flowrates with and without vegetation, and verify with the measurements (see figure 2.16). Because some of these measurements were carried out under steady states, for comparing with the asymptotic solutions from diurnal cycles, the solar radiation from steady state measurements was converted to the equivalent solar radiations under diurnal cycles. According to the scaling analysis in sec.2.2, exchange flowrates are proportional to input solar radiations, bottom slope, water depth, and inversely related with vegetation density and stem diameters in asymptotic solutions. Thus, the smallest exchange flowrate was found at the smallest product of input solar radiation and bottom slope. The second and third datasets in Table 2.1 had similar input solar radiations and bottom slopes, but vegetation in the second dataset led to a smaller exchange flowrate than the third one. The asymptotic solutions show good agreements with those measurements. For the field measurements conducted by Adam &Wells (1984), and Monismith, Imberger & Morison (1990), exchange flowrates were obtained at the depths of 12m, and 8m, respectively, where stratified effects are important, and the assumption of uniform heat distribution over water column may not be suitable. In addition, the exchange flowrate with symbol

of ∇ obtained from Oldham and Sturman (2001) was carried out for vegetation in shallow water and open in deep water (see figure 3 in Oldham and Sturman, 2001). Their velocity profiles performed during the nighttime, surface flow from deep to shallow water, and bottom flows from shallow to deep water (see figure 4 in Oldham and Sturman, 2001). As a result, blockage due to vegetation shading did not alter the flow patterns but might decreases temperature gradients generated from topographic effects as well as reduced exchange flowrates. Based upon the results from figure 2.10a, the exchange flowrate might reduce to zero given the balance of vegetation shading and topographic effects. Due to lack of information of vegetation blockage and temperature gradients between vegetation and open water, a range of predicted exchange flowrate was provided for Oldham and Sturman's case (∇) in figure 2.16.

2.5.7 Limitations and valid ranges of zero-order horizontal velocities

The horizontal velocity approaches infinity in two situations, which are (1) at the tip of the wedge ($x \to 0$), and (2) c_d is very large. At the tip, the horizontal convective terms cannot be ignored (Farrow & Patterson, 1993). They also mentioned that the convection terms are only important for $x < S$, which is a very small part of domain of interest. For a large c_d, the dominant regions of viscous effects become smaller, and the horizontal velocity profiles experienced a sharper bend near the bottom in comparison with no vegetation case. Once c_d becomes larger, the sharp bed regime can lead to the instability, which need to be balanced by convective terms.

The asymptotic solution is valid when S^2 and S^2Gr are small, and stem Reynolds number Re_d is less than 1 to be in the linear drag law regime (Tanino, Nepf, & Kulis, 2005). In order to examine the above-mentioned assumptions, dimensional velocities are determined based upon reasonable field parameters. The eddy viscosity used in eq.(2.17) yields reasonable values for horizontal velocity, possibly because vortex shedding generated from vegetation stems and leaves make the flow field become turbulent. For the condition without vegetation, horizontal velocity estimated by using eddy viscosity shows good agreement with the field observation (Farrow and Patterson, 1993). By using $I = 500W/m^2$, $\nu = 10^{-4} m^2/s$, stem size $d = 0.6cm$, slope $S = 10^{-2}$, vegetation density ϕ is 0.25%, the maximum dimensional horizontal velocity is $u' \sim 1.2\times10^{-2} m/s$, and corresponding $\mathrm{Re} = 0.72 < 1$, consistent with the assumption of linear drag law. In scaling analysis, the $O\left(S^2Gr\right)$ terms are omitted which may not be suitable for field situation ($S \approx 10^{-2} \sim 10^{-3}, Gr \approx 1.8\times10^7$ for $\nu = 10^{-4} m^2/s$). The valid range of the linear results can be determined by the included terms larger than the omitted terms in governing equation. The maximum velocity U for $\phi = 0.25\%$ is $\sim 10^{-2}$. For $x \to 0$, the buoyance is mainly balanced by the vertical shears, i.e. $x < \dfrac{1}{S^2GrU} = \dfrac{100}{S^2Gr}$. For $x >> 0$, the main balance is between buoyancy and vegetative drag, which yields $x > \dfrac{S^2GrU}{c_d} = 7.7\times10^{-4} S^2Gr$. Combining these two results gives $S^2Gr < 360$ for the flow in the domain to be linear. The valid ranges for the linear results in vegetation are wider than those without vegetation ($S^2Gr < 200$ obtained in Farrow, 2004) because of the reduced horizontal velocity. As vegetation becomes denser, smaller horizontal

velocity leads to wider ranges of S^2Gr , i.e. the convective terms in eqs.(2.6) and (2.7) are less important. For the extreme case, i.e. vegetation in one side, and open water in the other side, the temperature gradient generated from the vegetation shading would change the valid range of the asymptotic solutions. By considering the case of open in shallow water, and vegetation in deep water, i.e. the vegetation shading improves the topographic effect, the range of S^2Gr can be obtained by comparing the unsteady and convective terms in eq.(2.6), which yield $S^2Gr < \dfrac{\left(\dfrac{\partial T}{\partial t}\right)}{\left(u\dfrac{\partial T}{\partial x}\right)}$. Using B=0.85, $k=-5$, x=5, and vegetation density in deep water of 0.25%, it gives the maximum horizontal velocity u of 2.5×10^{-2} and the valid range of $S^2Gr < 72$, smaller than the case without vegetation,

2.5.8 Second-order asymptotic solutions for temperature profiles

When the second-order temperature is taken into account, the tilted isotherm due to sloping bottom and advection effects can be observed (see figure 2.17). The second-order temperature is related to Gr. The larger Gr value exhibits higher nonlinearity. The Gr of 10^4 and S of 0.1 are chosen to confirm the suitability of the asymptotic solution, i.e. $S^2Gr < 200$. Without vegetation, the weak stratification can be observed due to the heat advection by $u^{(0)}$ (see figure 2.17a,c,e), whereas the vegetation retards the flow, and consequently keeps the temperature profiles less stratified (see figure 2.17f~j). For $t=0.5$, the residual heat due to velocity inertia results in higher temperature in the upper layer, and lower temperature near the bottom. The same situations can be observed at t=1.

However, at t=1, the zero-isotherm without vegetation is closer to the bottom, whereas with vegetation, the zero-isotherm is approximately at the middle of the water depth.

The horizontal heat transfer q is proportional to the product of zero-order horizontal velocity and second-order temperature profiles. Therefore, q with vegetation is smaller than q without vegetation (see figure 2.18). In shallow water ($x = 0.25$), viscosity is dominant and diffuses over the whole water column. The effect of vegetative drag is not apparent so that q with vegetation is slightly smaller than q without vegetation. q has extrema at $t = n \pm \frac{1}{4}$. For the intermediate water depth, the viscosity can diffuse to the entire water depth after the first period, and therefore the q values become periodic since the second cycle. For the deep water ($x = 5$), the heat transfer rate q keeps increasing as time marches until the boundary layer grows over the entire water column (Farrow, 2004). Within vegetation, it takes longer time for viscosity to diffuse over the entire water column. The larger inertia in deep water lags the extrema of q. The time lag in vegetation is smaller than that without vegetation due to smaller inertia within vegetation. The extreme of q in deep water are appeared at $t = n \pm \frac{1}{4}$, quarter period of forcing lag in comparison to the shallow water case, where 0.25% vegetation in deep water can shorten the time lag to one-eighth of forcing period.

2.6 Conclusions

The paper considers the vegetative drag into the horizontal momentum equation, and discusses the impact of emergent vegetation on the flow field. The horizontal velocity, exchange flowrate, and advective heat transfer rate are significantly reduced due to the presence of vegetation. In very shallow water, the viscous effects are still dominant, but in deep water, vegetative drag balances the pressure gradient, and results in smaller inertia, and i.e. smaller horizontal velocity. As a result, the phenomena of time-lag due to the inertia become indistinct. The flow patterns can be altered by vegetation distribution and height of emergent vegetation. Once the vegetation is tall, and grows in shallow water, and the deep water side is open, the effects of vegetation shading may interfere with the topographic effects, the subsequent induced circulation is complicated. As the variations of the vegetation blockage on solar radiation, the exchange flowrates may become zero. On the other hand, for the case of open in shallow water, and vegetation in deep water, the vegetation shading can strengthen the topographic effect to generate larger circulation as well as flow exchanges between the nearshore and offshore. Although the model ignores the light attenuation effect and vegetation distribution in vertical directions, the horizontal velocities and exchange flowrate estimated from the asymptotic solutions agree well with field and laboratory measurements.

In order to obtain the asymptotic solution, the linear drag coefficient is applied and the bottom slope is assumed to be small. The results of horizontal velocities indicate that the assumption of a linear drag coefficient is reasonable for the thermal-driven flow. Based upon the horizontal velocity estimated from asymptotic solution, the valid range of linear results can be up to $S^2Gr < 360$ for sparse vegetation ($\phi = 0.25\%$). For denser

vegetation, the horizontal velocity will be smaller and the range of S^2Gr fit to the linear assumption can be larger. The horizontal velocities approach infinity in: (1) at the tip ($x \to 0$), and (2) dense vegetation (large drag coefficient) due to the ignorance of convective terms in the governing equation.

Although the asymptotic solution can predict the magnitude of thermal-driven flow in emergent vegetation for weakly stratified environments, some limitations still need to be overcome in the future. Firstly, the assumption of weakly stratified environment is not usually met in practice. Development of an analytic solution including light attenuation effects is necessary. The drag coefficient is a critical input for the analytic solution; however, the drag coefficient is usually obtained from circular cylinder tests, and the morphology (stem flexibility and leafs) of the vegetation are not included. In the analytic solution, the drag coefficient is assumed to be uniform along the vertical direction, and the drag force applied along the vertical direction is also neglected. In addition, the absorption or release of heat from vegetation may play an important role on thermal-driven flow. Finally, submerged vegetation also grows extensively in the littoral zones, and its effect on thermal-driven flow is still unclear. More analytic analysis, numerical simulation, field and laboratory measurements are necessary to solve theses issues.

Appendix 2.A Coefficients of the solution of the second-order temperature profiles

$$
\begin{aligned}
a_m(t) &= \frac{A}{(m\pi)^2\left(m^4\pi^2+16\sigma^2x^4\right)} \\
&\quad\times\left[16\sigma^2x^4\left(1-\exp\left(-(m\pi/x)^2\,t/\sigma\right)\right)+m^4\pi^2\left(1-\cos(4\pi t)\right)-4\sigma m^2\pi x^2\sin(4\pi t)\right], \\
b_{mn}(x,t) &= \frac{\cos\beta_n+(\cos\beta_n-1)/\beta_n^2-\frac{1}{2}}{\left((m\pi)^2-\beta_n^2\right)\left[\left((\beta_n/x)^2+c_d\right)^2+(2\pi)^2\right]\left[\beta_n^2+c_dx^2\right]}, \\
c_{mn}(x,t) &= \left[\left(\frac{\beta_n}{x}\right)^2+c_d\right]\left\{\frac{x^2\sigma\left[e^{-(m\pi/x)^2t/\sigma}-\cos(4\pi t)\right]+\frac{1}{4}m^2\pi\sin(4\pi t)}{\pi\left(m^4\pi^2+16x^4\sigma^2\right)}\right. \\
&\quad\left.-\frac{\pi x^2\sigma\left[e^{-(m\pi/x)^2t/\sigma}-e^{-\left(\left(\frac{\beta_n}{x}\right)^2+c_d\right)t}\cos(2\pi t)\right]+\frac{1}{2}\left[m^2\pi^2-\left(\beta_n^2+c_dx^2\right)\sigma\right]e^{-\left[\left(\frac{\beta_n}{x}\right)^2+c_d\right]t}\sin(2\pi t)}{\left[(m\pi)^2-\left(\beta_n^2+c_dx^2\right)\sigma\right]^2+4\pi^2x^4\sigma^2}\right\} \\
&\quad-\pi\frac{\frac{1}{2}m^4\pi^2\left[\cos(4\pi t)-1\right]+2\pi x^2\sigma m^2\sin(4\pi t)+8x^4\sigma^2\left[e^{-(m\pi/x)^2t/\sigma}-1\right]}{(m\pi)^2\left(m^4\pi^2+16x^4\sigma^2\right)},
\end{aligned}
\tag{2A.1}
$$

where

$$
\begin{aligned}
A &= \frac{1}{4\pi^2}\left(\frac{dF(x)}{dx}\right)^2\left\{\frac{\left(2+c_dx^2-2\cosh\left(x\sqrt{c_d}\right)\right)(-1)^m x^2\sinh\left(x\sqrt{c_d}\right)}{2c_d\left(m^2\pi^2+c_dx^2\right)\left(\sqrt{c_d}\,x\cosh\left(x\sqrt{c_d}\right)-\sinh\left(x\sqrt{c_d}\right)\right)}-\frac{x^3\left(x(c_d)-\sqrt{c_d}\sinh\left(x\sqrt{c_d}\right)\right)(-1)^m\sinh\left(x\sqrt{c_d}\right)}{c_d\left(m^2\pi^2+c_dx^2\right)\left(\sqrt{c_d}\,x\cosh\left(x\sqrt{c_d}\right)-\sinh\left(x\sqrt{c_d}\right)\right)}\right. \\
&\quad\left.+\frac{x^2\left(-1+(-1)^m\right)}{c_dm^2\pi^2}+\frac{x^2\left(1-(-1)^m\cosh\left(x\sqrt{c_d}\right)\right)}{c_d\left[m^2\pi^2+c_dx^2\right]}\right\}.
\end{aligned}
\tag{2A.2}
$$

2.7 References

Adams, E.E. and Wells, S.A. (1984). "Field measurements on side arms of Lake Anna. Va." *J. Hydraul.Engng*, 110, 773-793.

Chimney, M.J., Wenkert, L., and Pietro, K.C. (2006). "Patterns of vertical stratification in a subtropical constructed wetland in south Florida (USA)." *Ecol. Engng*, 27, 322-330.

Chubarenko, I.P. and Demchenko, N.Y. (2008). "Laboratory modeling of the structure of a thermal bar and related circulation in a basin with a sloping bottom," *Oceanology*, 48(3), 356-370.

Chubarenko, I.P. (2010). "Horizontal convective water exchange above a sloping bottom: the mechanism of its formation and an analysis of its development." *Oceanology*, 50(2), 166-174.

Coates, M.J., and Patterson, J.C. (1993). "Unsteady natural convection in a cavity with non-uniform absorption of radiation." *J. Fluid Mech*., 256, 133-161.

Coates, M.J., and Ferris, J. (1994). "The radiatively driven natural convection beneath a floating plant layer.." *Limnol. Oceanogr*., 39(5), 1186-1194.

Cormack, D.E., Leal, L.G., and Imberger, J. (1974). "Natural convection in a shallow cavity with differentially heated end walls. Part 1. Asymptotic theory." *J. Fluid Mech*., 65, 209-229.

Farrow, D.E. and Patterson, J.C. (1993). "On the response of a reservoir sidearm to diurnal heating and cooling." *J. Fluid Mech*., 246, 143-161.

Farrow, D.E., and Patterson, J.C. (1994). "The daytime circulation and temperature pattern in a reservoir sidearm." *Intl J. Heat Mass Transfer*, 37, 1957-1968.

Farrow, D.E. (2004). "Periodically forced natural convection over slowly varying topography." *J. Fluid Mech*., 508, 1-21.

James, W.F., and Barko, J.W. (1991). "Estimation of phosphorous exchange between littoral and pelagic zones during nighttime convection circulation." Limnol. Oceanogr., 36(1), 179-187.

Koch, D.L., and Ladd, A.J.C. (1997). "Moderate Reynolds number flows through periodic and random arrays of aligned cylinders." *J. Fluid Mech*., 349, 31-66.

Lei, C. and Patterson, J.C. (2002). "Unsteady natural convection in a triangular enclosure induced by absorption of radiation." *J. Fluid Mech*., 460, 181-209.

Lightbody, A., Avener, M., and Nepf, H.M. (2008). "Observations of short-circuilting flow paths within a constructed treatment wetland in augusts, Georgia, USA." *Limnol. Oceanogr*., 53(3), 1040-1053.

Lövstedt and Bengtsson. (2008). "Density-driven current between reed belts and open water in a shallow lake." *Water Resources Res*.,44(10), W10413.

Mao, Y., Lei, C, and Patterson, J.C. (2009). "Unsteady natural convection in a triangular enclosure induced by absorption of radiation – a revisit by improved scaling analysis." *J. Fluid Mech*., 622, 75-102.

Mao, Y., Lei, C, and Patterson, J.C. (2010). "Unsteady near-shore natural convection induced by surface cooling." *J. Fluid Mech*., 642, 213-233.

Monismith, S.G., Imberger, J. and Morison, M.L. (1990). "Convective motion in the sidearm of a small reservoir." *Limnol. Oceanogr*., 35, 1676-1702.

Oldham, C.E., and Sturman, J.J. (2001). "The effect of emergent vegetation on convective flushing in shallow wetlands: scaling and experiment." *Limnol. Oceanogr*., 46(6), 1486-1493.

Sturman, J.J, Oldham, C.E., and Ivey, G.N. (1999). "Steady convection exchange flow down slopes." *Aquat. Sci*., 61, 260-278.

Tanino, Y., Nepf, H.M., and Kulis, P.S. (2005). "Gravity current in aquatic canopies." *Water Resources Res*.,41(12), W12402.

Zhang, X, and Nepf, H.M. (2008). "Density driven exchange flow between open water and an aquatic canopy." *Water Resources Res*.,44(8), W08417.

Zhang, X. and Nepf, H.M. (2009). "Thermally driven exchange flow between open water and an aquatic canopy." *J. Fluid Mech*., 632, 227-243.

Table 2.1 Field and laboratory measurements

Symbol	Category	$I_0\left(W/m^2\right)$	S	Depth(m)	$\phi(\%)$	d(m)	Data Source
★	Lab	3	0.1	0.2	–	–	1
△ 1	Lab	70	0.404	0.1	17	0.0124	2
◇	Lab	72	0.404	0.1	–	–	3
▽	Field	100	0.0874	0.8	16	0.15	2
△ 2	Lab	300	0.404	0.1	17	0.0124	2
△ 3	Lab	363	0.404	0.1	17	0.0124	2
○	Field	200	0.0175	1.8	–	–	3
+	Field	250	0.02	8	–	–	4
×	Field	400	0.007	12	–	–	5

Note: I_0 is the equivalent diurnal solar radiations.

Data source: 1: Chubarenko & Demchenko (2008); 2: Oldham & Sturman (2001); 3: Sturman (1999); 4: Monismith, Imberger, & Morison (1990); and 5: Adams & Wells (1984).

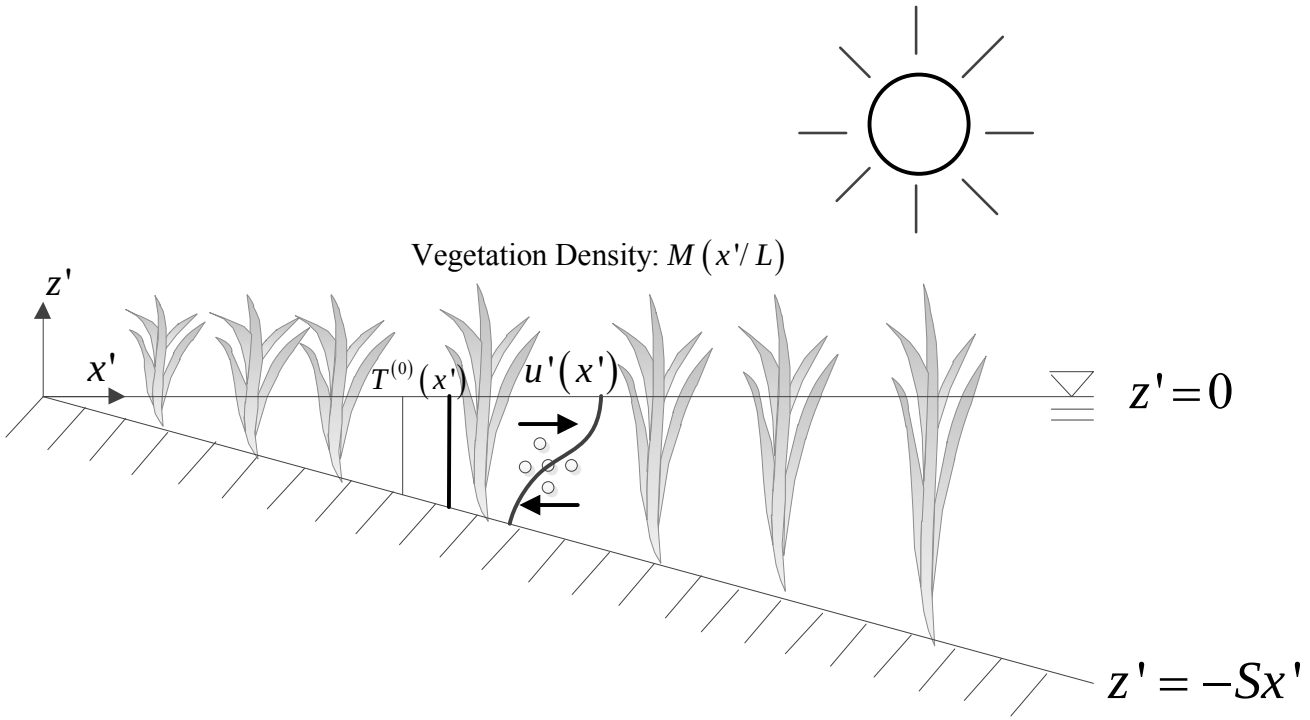

Figure 2.1 Geometry of the domain showing coordinate system and vegetation distributions.

Note: Distributions of emergent vegetation are function of the horizontal location x'.

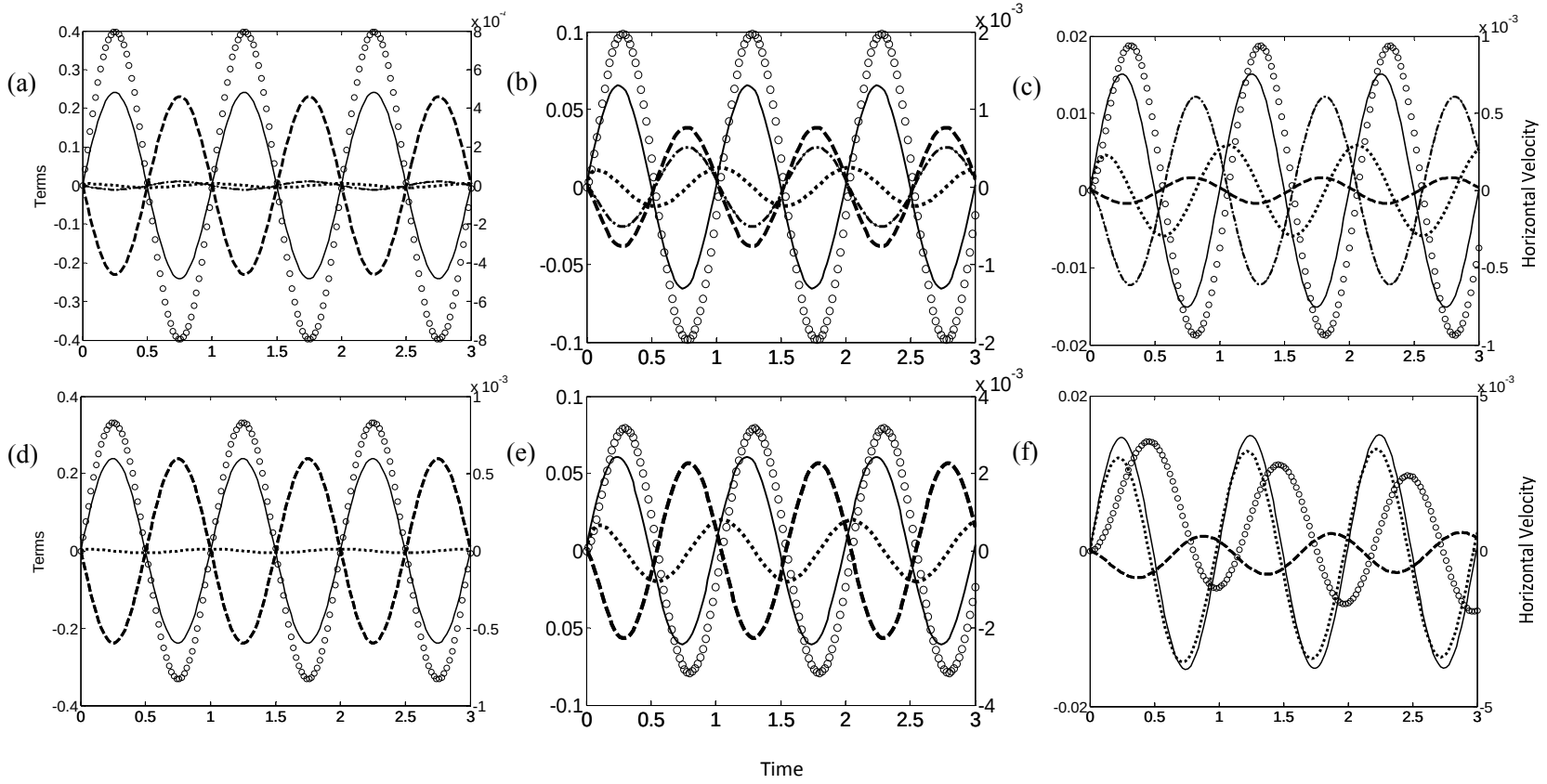

Figure 2.2 Different terms and horizontal velocity at the water surface (z=0) with vegetation density of 0% and 0.25% for three cycles. (a) x=0.25, $\phi = 0.25\%$; (b) x=1, $\phi = 0.25\%$; (c) x=5, $\phi = 0.25\%$; (d) x=0.25, $\phi = 0\%$; (e) x=1, $\phi = 0\%$; and (f). x=5, $\phi = 0\%$.

(—— : pressure gradient, ····· : inertia, – – – : viscosity, –·–·–: drag, ○:horizontal velocity)

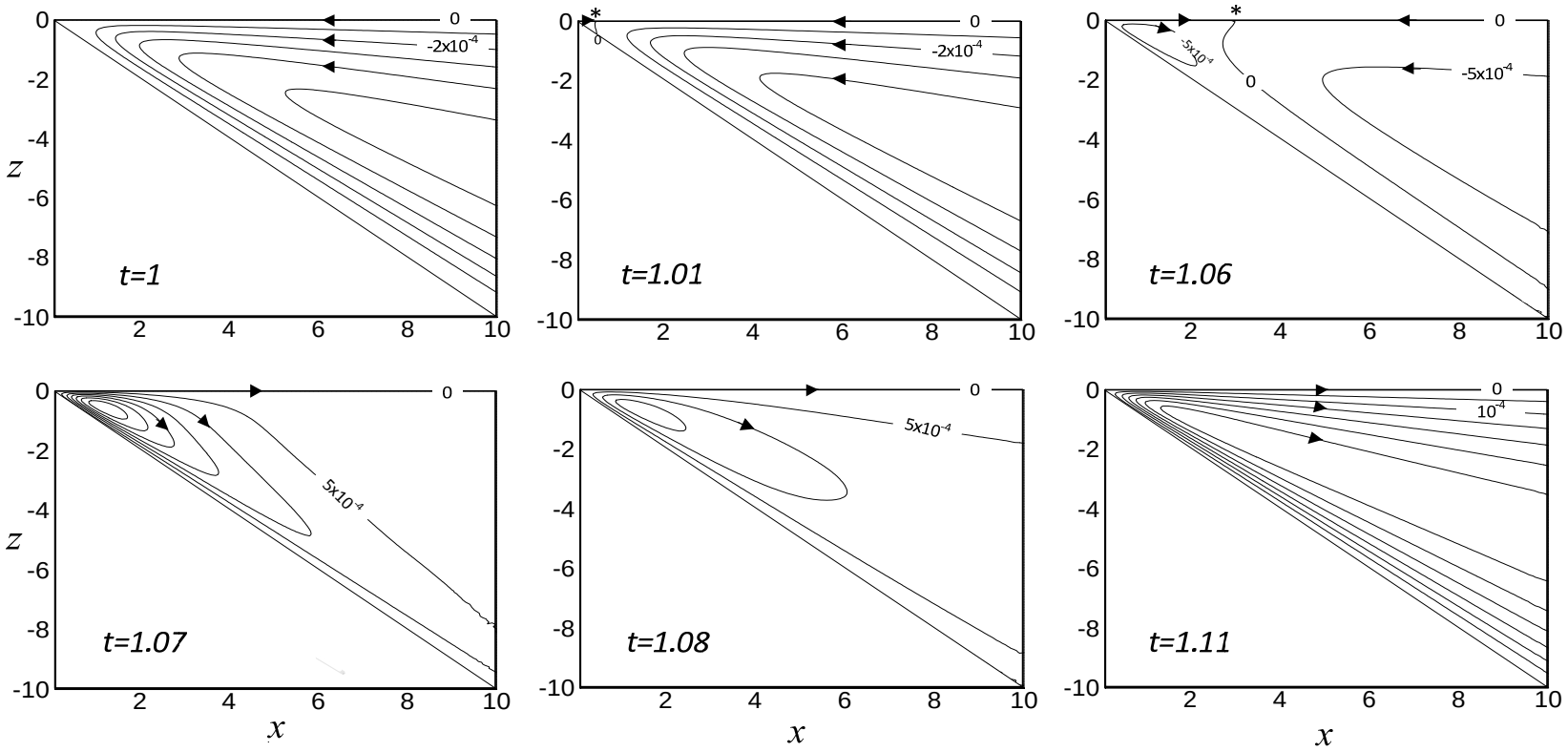

Figure 2.3 Streamlines for various times with 0.25% vegetation. The numbers denote the value for the streamlines, and the asterisk indicates the position of zero surface velocity.

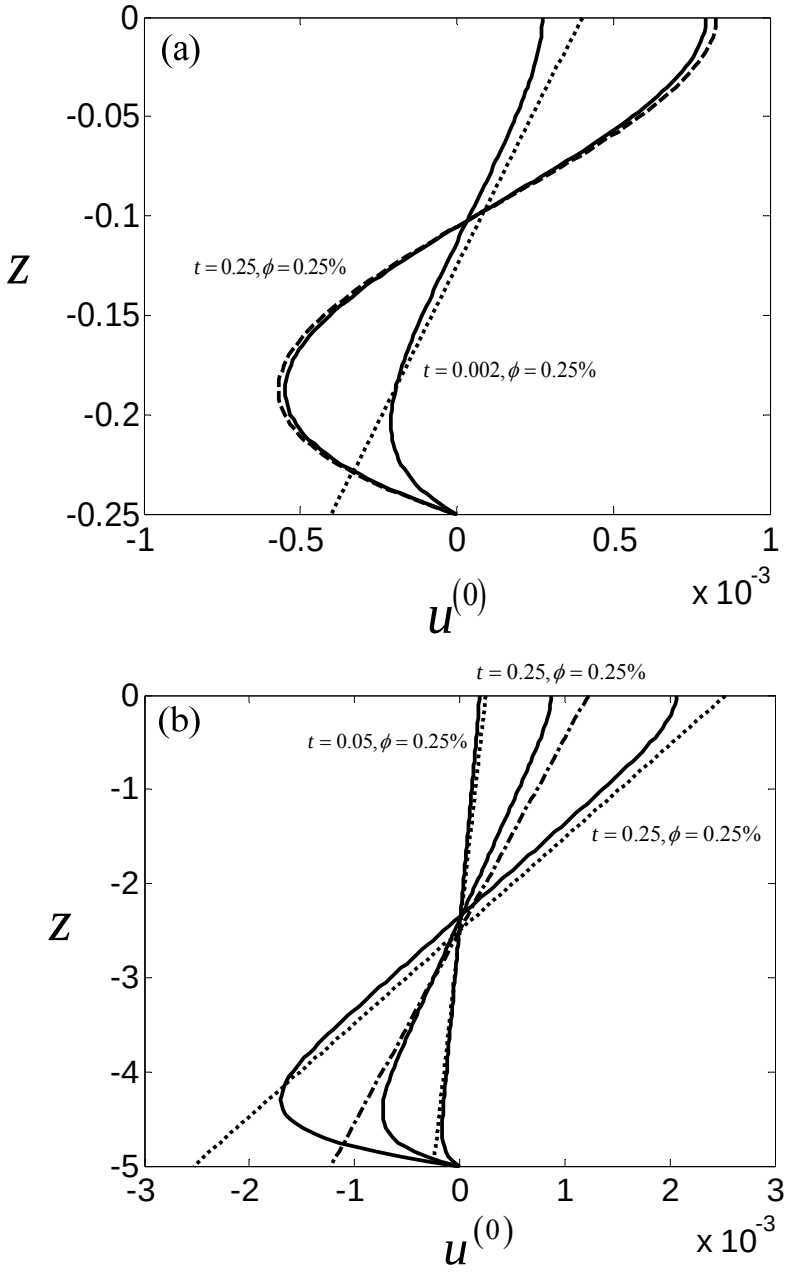

Figure 2.4 Horizontal velocity profiles within and without vegetation for various times in shallow and deep water. (—: full solution of horizontal velocity, ····· : viscous-limiting of horizontal velocity, ····· : inertia-limiting of horizontal velocity, and -·-·-: drag-limiting of horizontal velocity). In (a), the horizontal velocity profiles at t=0.002 are 100 times larger than its actual values. In (b), the horizontal velocity profiles at t=0.05 are 2 times larger than its actual values.

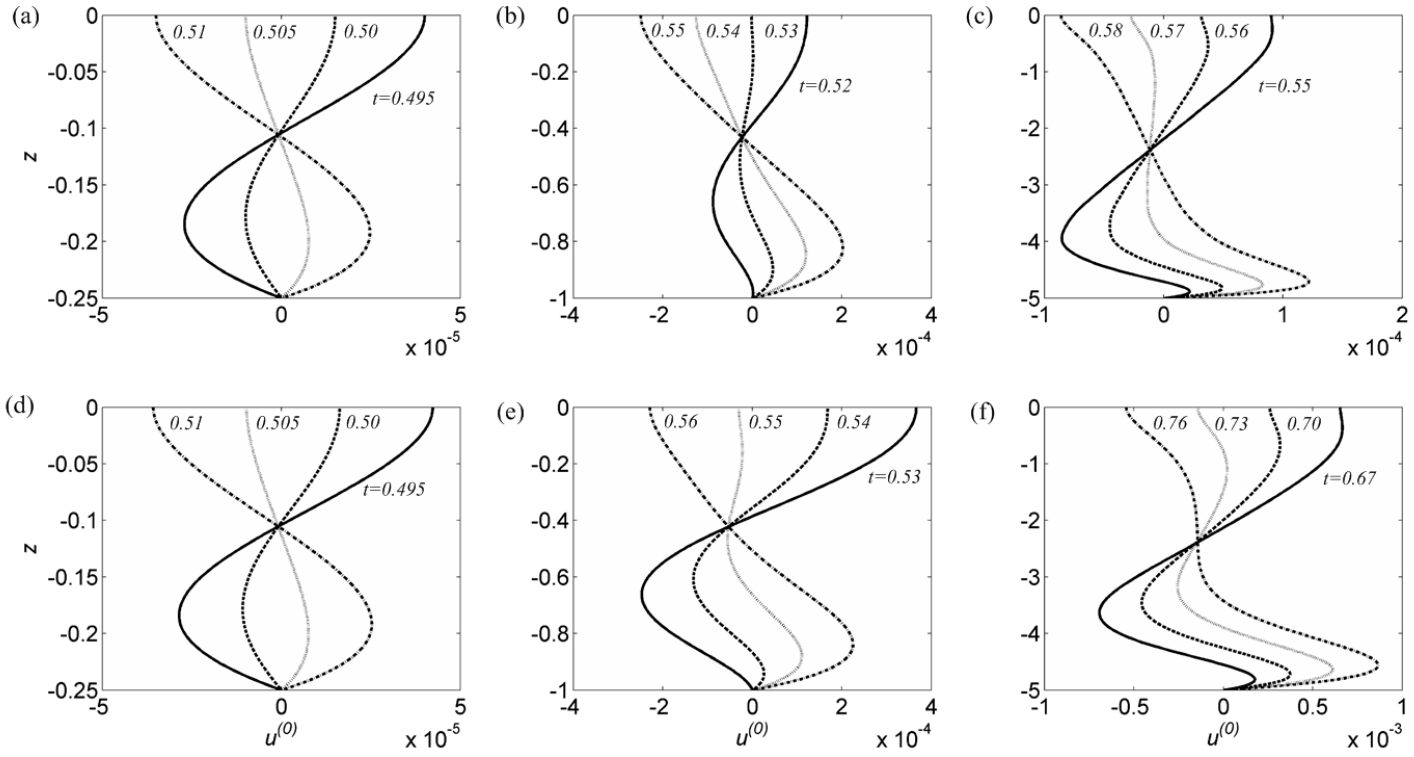

Figure 2.5 Velocity profiles near the time that the pressure gradient is reversed (the spin-time effect). (a) $x = 0.25, \phi = 0.25\%$, (b) $x = 1, \phi = 0.25\%$,(c) $x = 5, \phi = 0.25\%$, (d) $x = 0.25, \phi = 0\%$, (e) $x = 1, \phi = 0\%$ and (f) $x = 5, \phi = 0\%$.

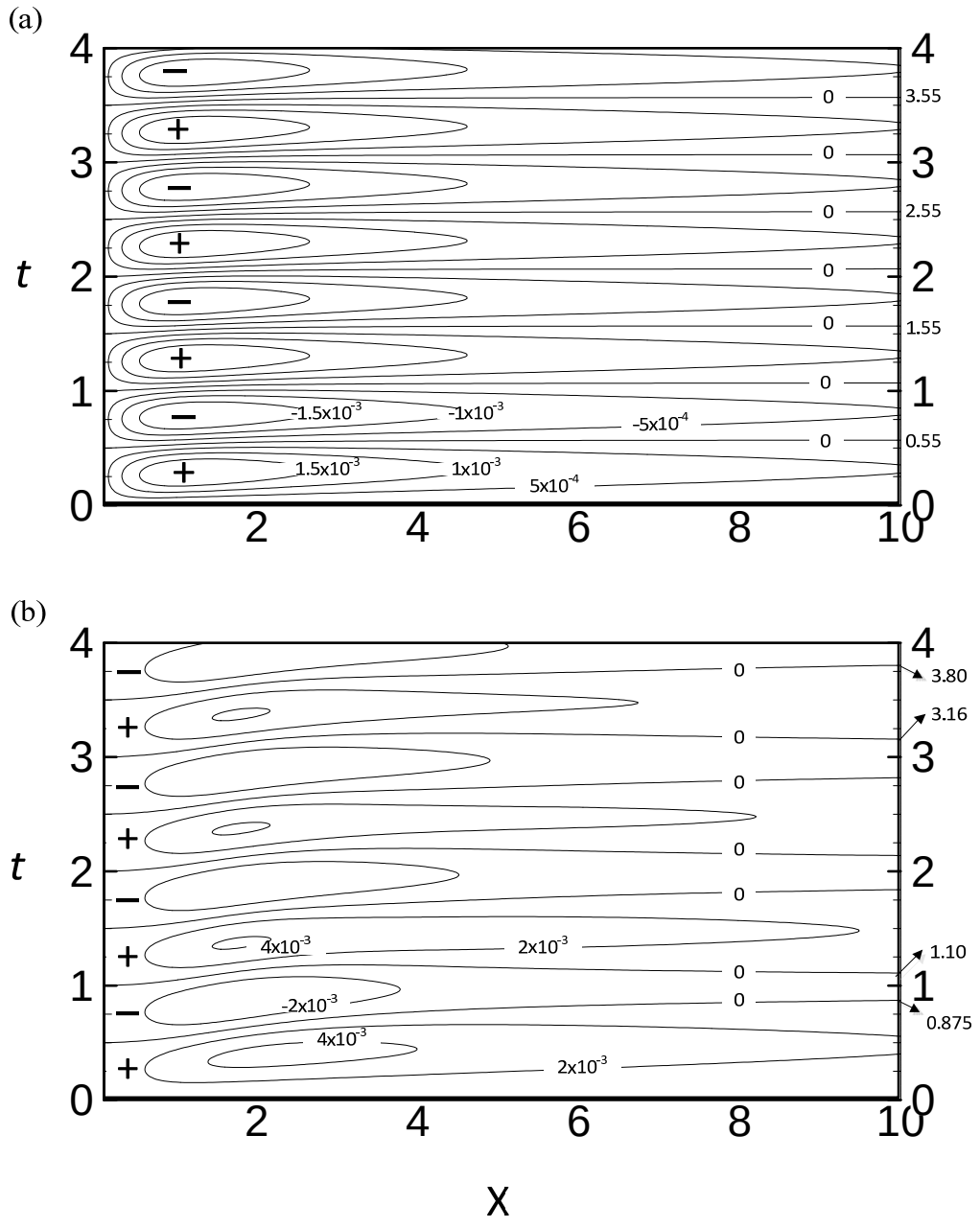

Figure 2.6 Contours of surface velocity in the *(x-t)* plane for (a) $\phi = 0.25\%$ and (b) $\phi = 0\%$ .The small numbers labeled on the right y-axis denote the time for the reversal of the circulation.

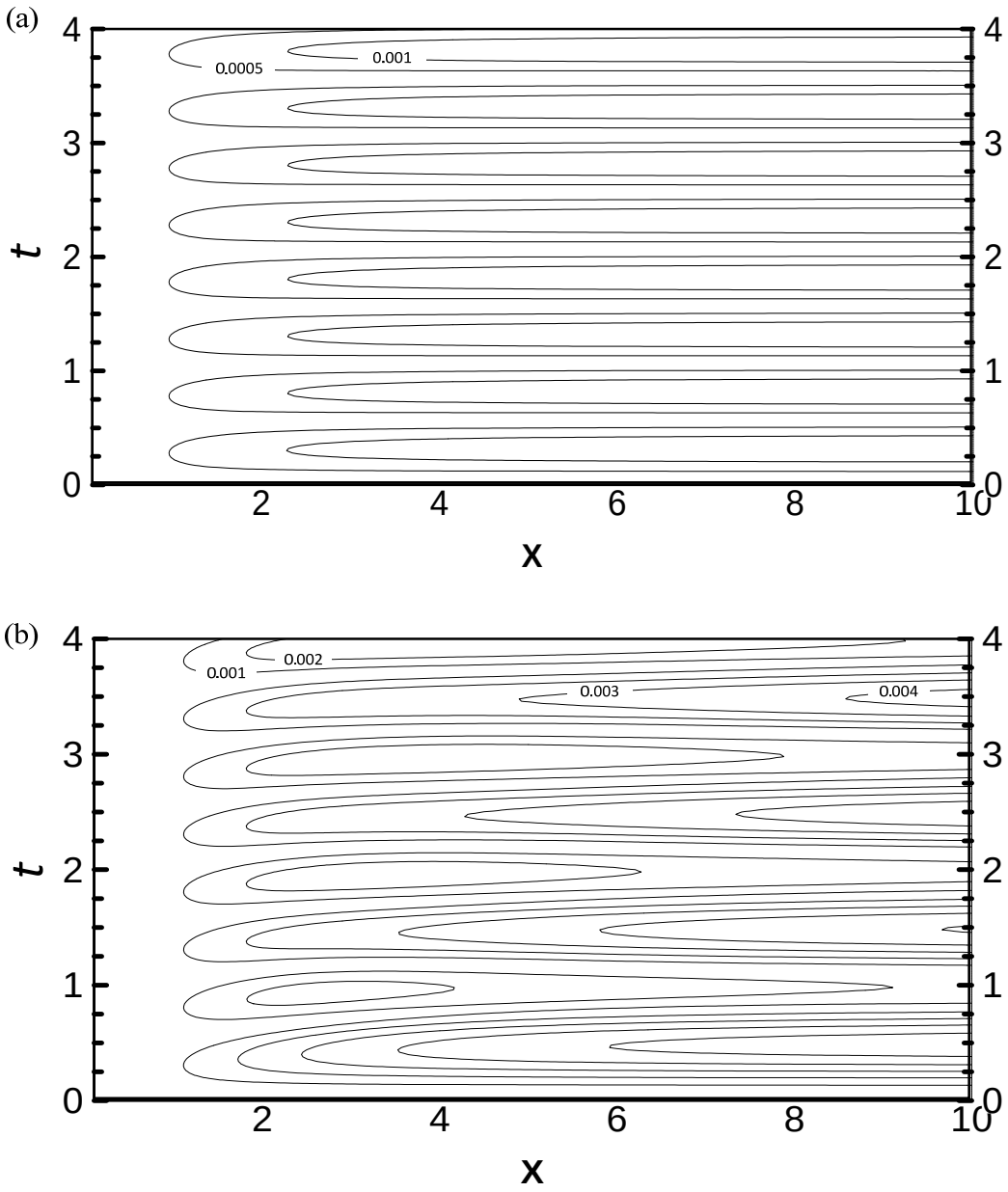

Figure 2.7 Contours of exchange flowrates in the *(x-t)* plane for (a) $\phi = 0.25\%$ and (b) $\phi = 0\%$.

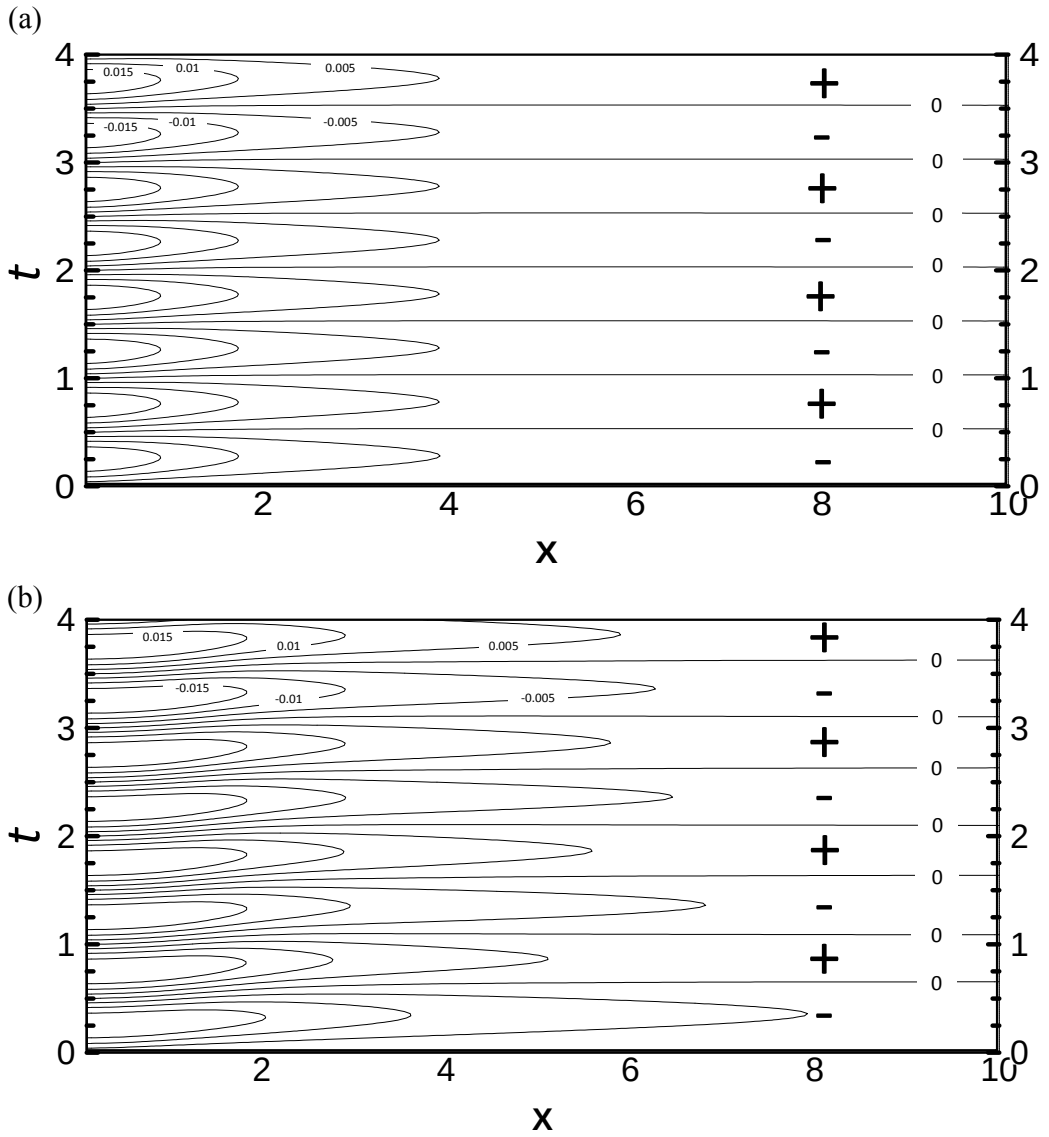

Figure 2.8 Contours of bottom shear stress in the *(x-t)* plane for (a) $\phi = 0.25\%$ and (b) $\phi = 0\%$. The contour interval is 5×10^{-3}.

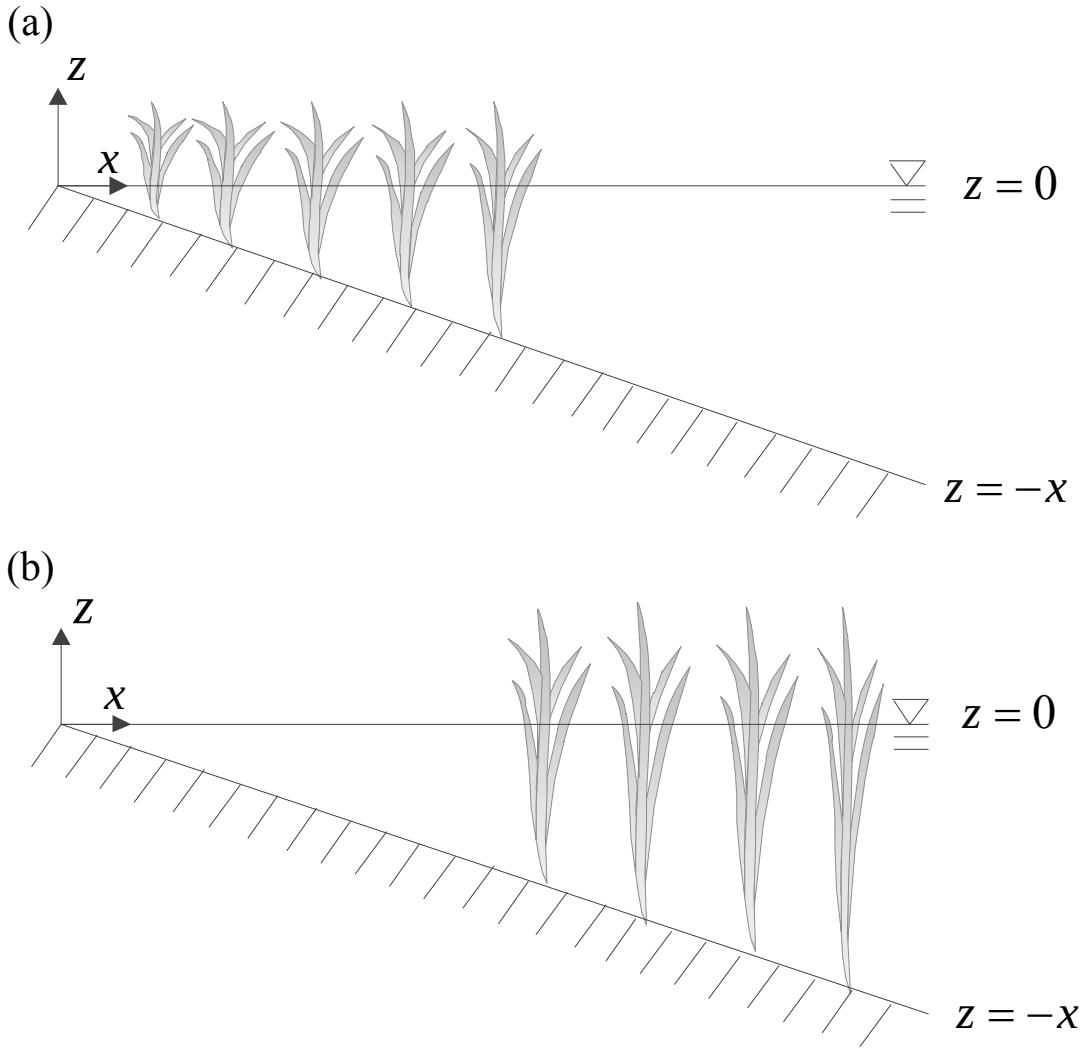

Figure 2.9 Schematics of one-side open water and the other-side vegetation over a sloping bottom: (a) vegetation in shallow water and open in deep water, and (b) open in shallow water and vegetation in deep water.

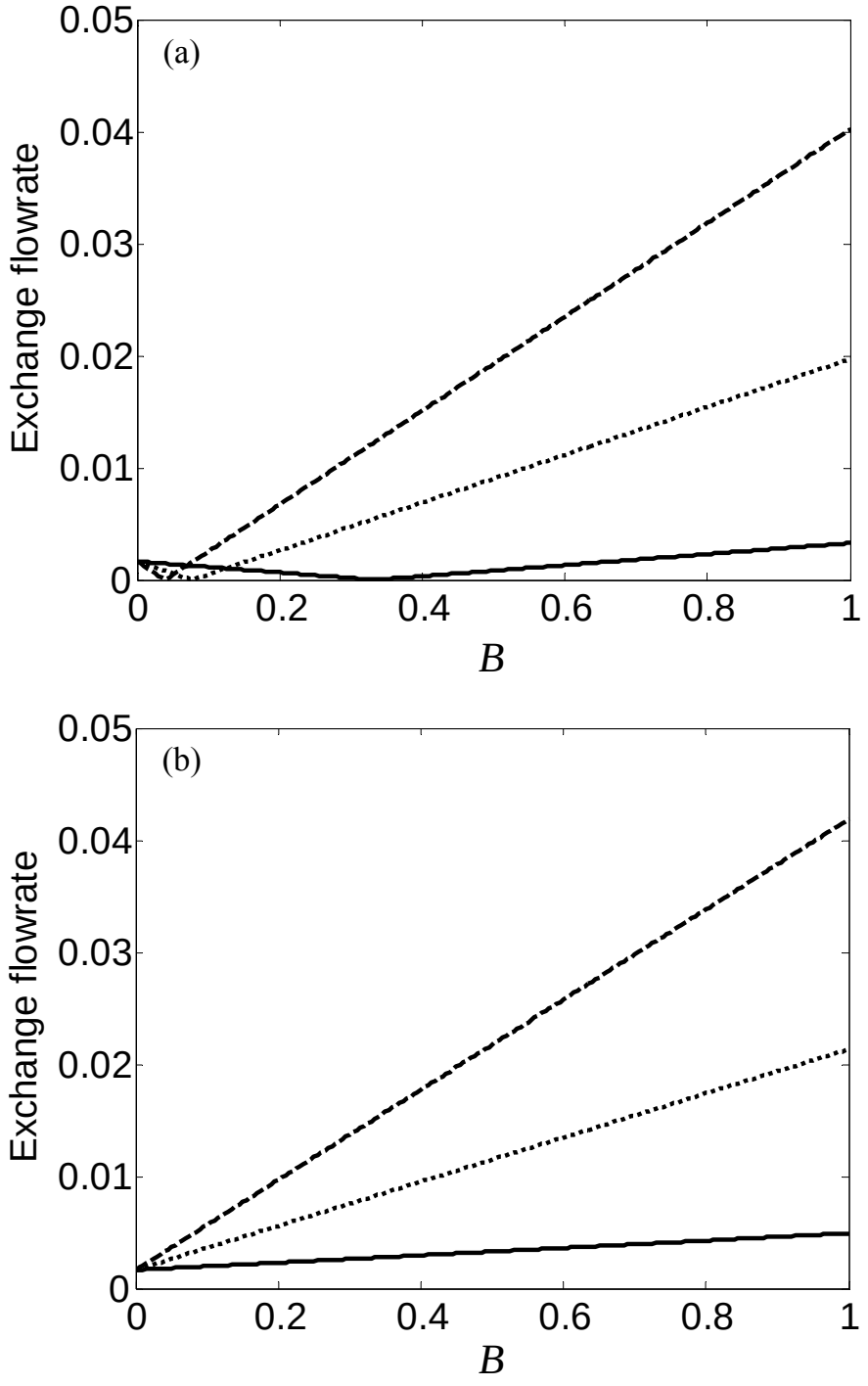

Figure 2.10 Exchange flowrates with different blockage *B* and sharpness *k*. (a) vegetation in shallow water, and open in deep water, and (b) open in shallow water, and vegetation in deep water. Note: —: $k = \pm 1$; ·····: $k = \pm 5$; and - - -: $k = \pm 10$.

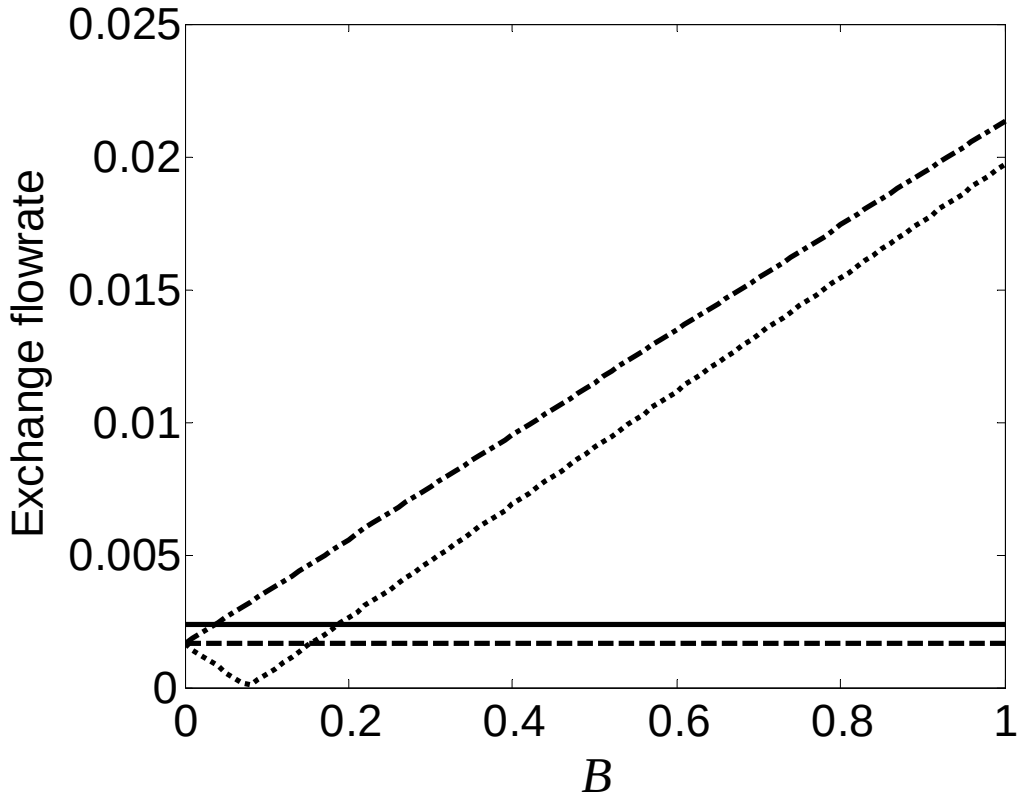

Figure 2.11 Exchange flowrates at center line of four cases with different blockage *B*. Note: '—' denotes case (i) for no vegetation; '- - -' represents case (ii) for 0.25% vegetation; '·····' means case (iii) for vegetation in shallow water and open in deep water; and '-·-·-' denotes case (iv) open in shallow water, and vegetation in deep water.

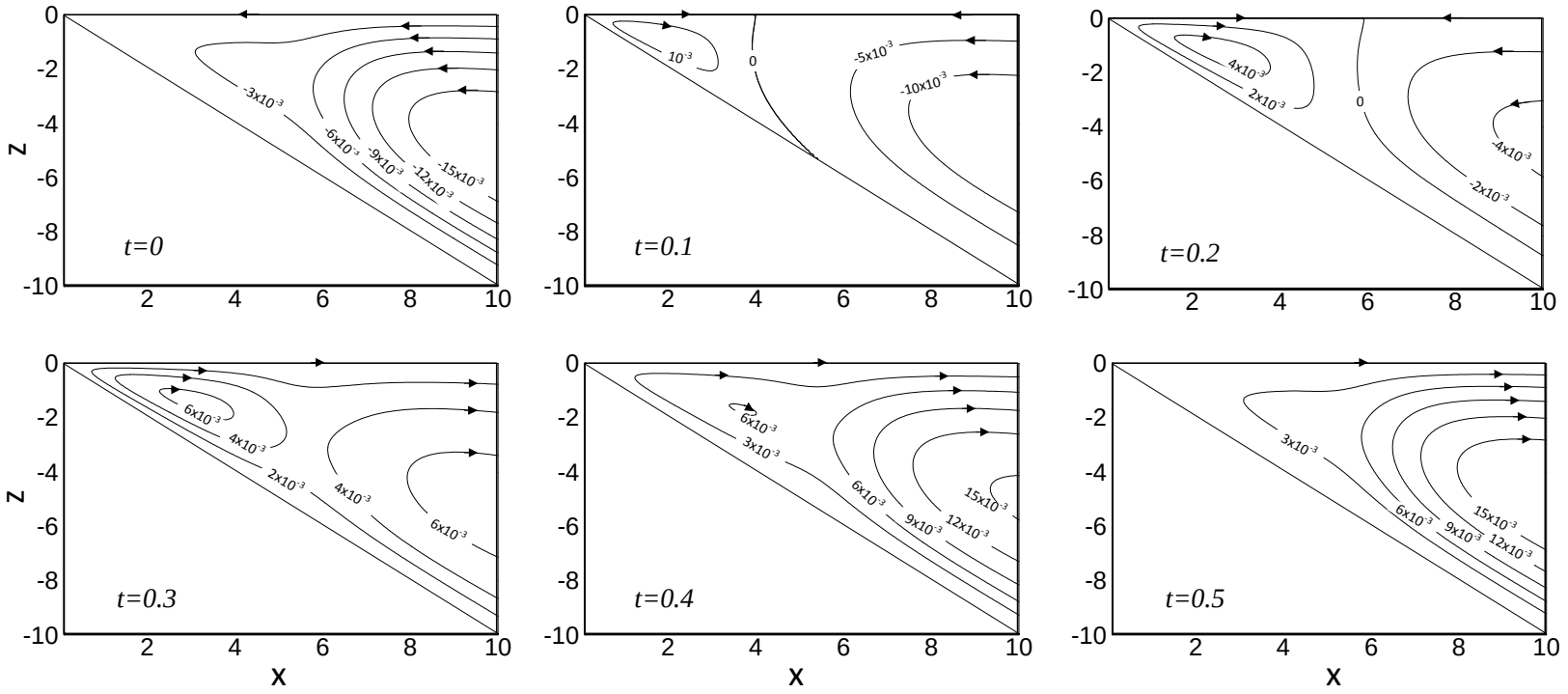

Figure 2.12 Streamlines for various time for vegetation in shallow water and open in deep water after the forcing is initiated for B=0.05, and k=5.

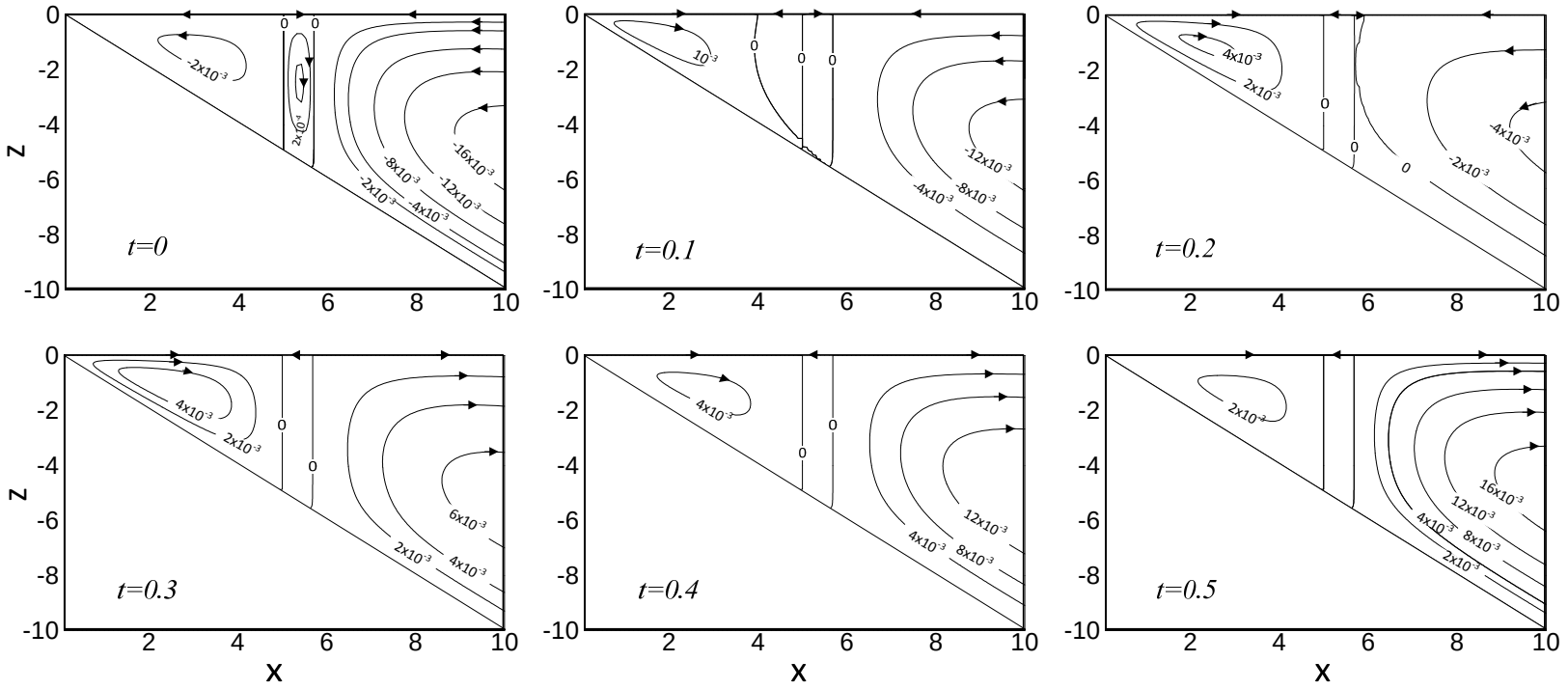

Figure 2.13 Streamlines for various time for vegetation in shallow water and open in deep water after the forcing is initiated for B=1/13, and k=5.

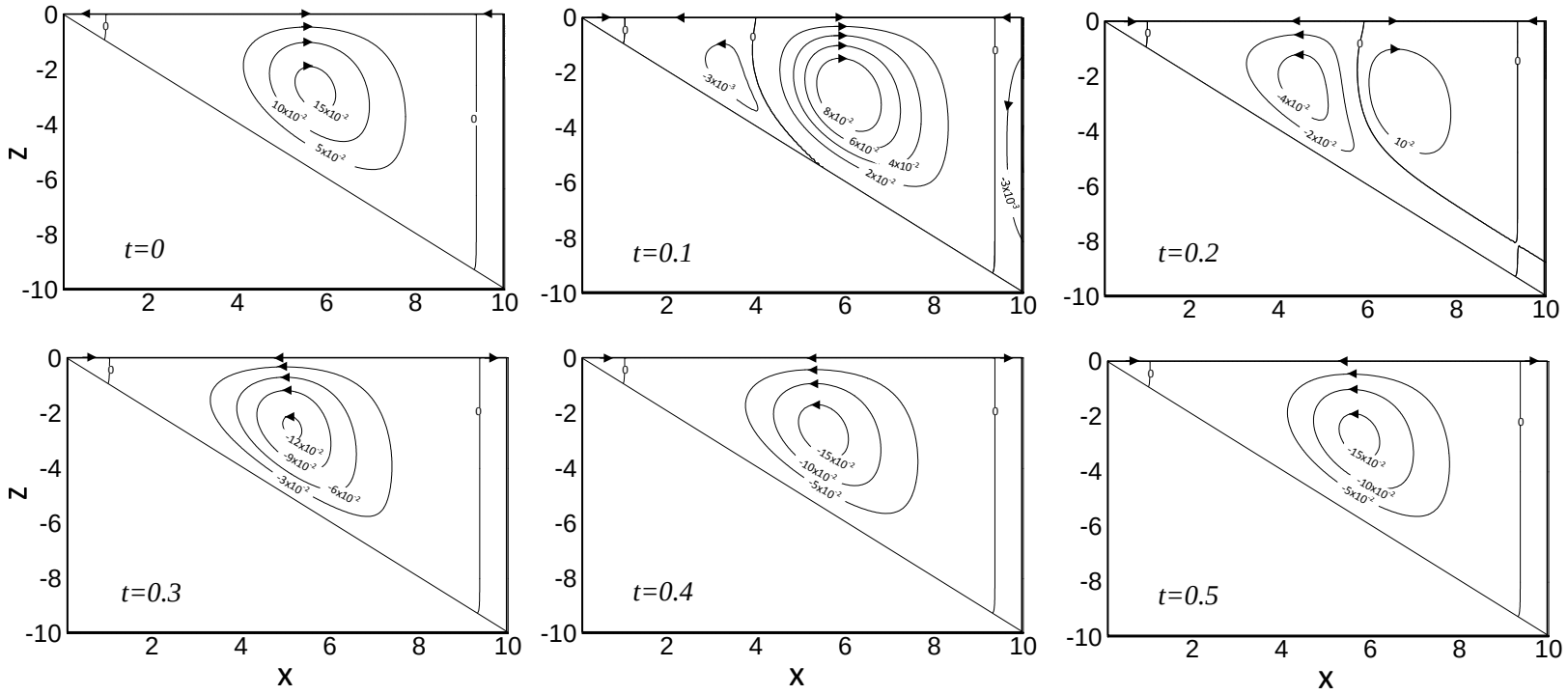

Figure 2.14 Streamlines for various time for vegetation in shallow water and open in deep water after the forcing is initiated for B=0.85, and k=5.

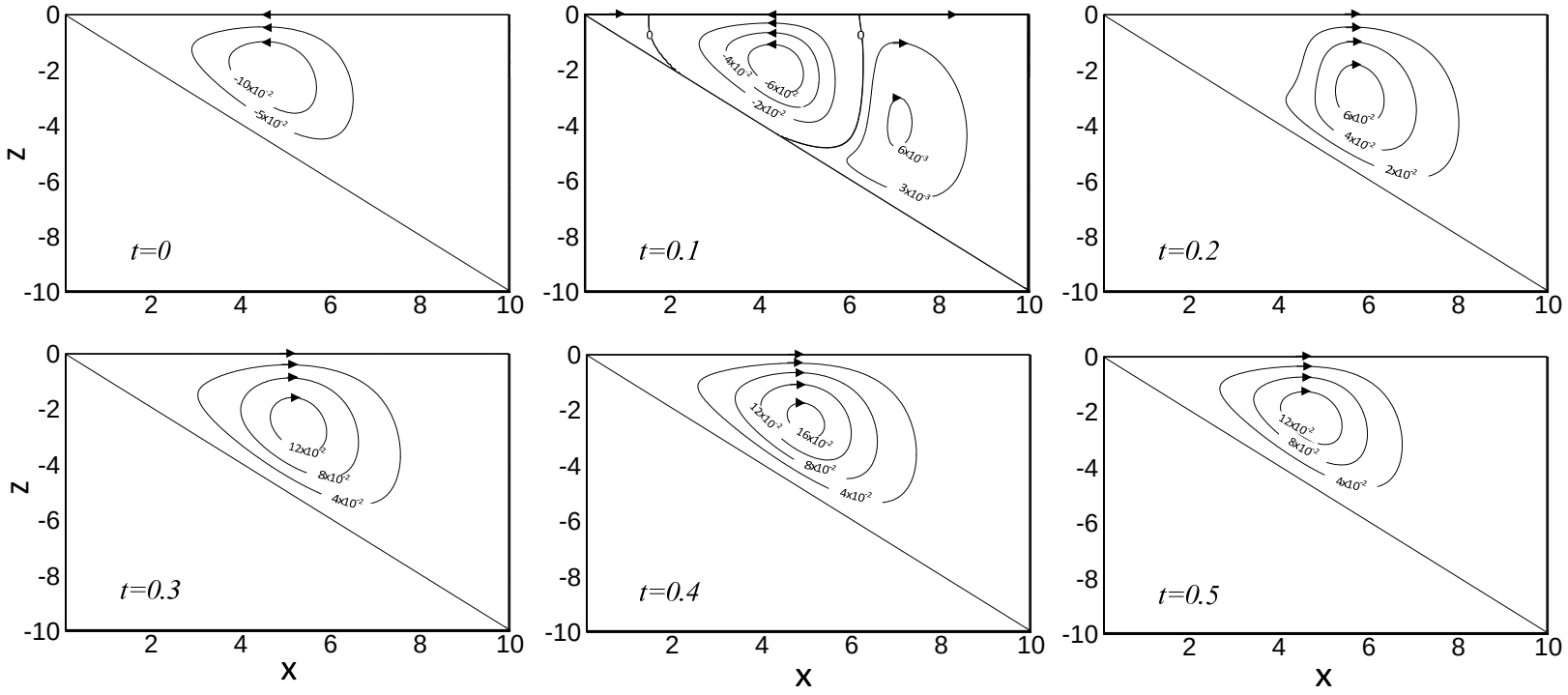

Figure 2.15 Streamlines for various time for open in shallow water and vegetation in deep water after the forcing is initiated for B=0.85, and k=-5.

.

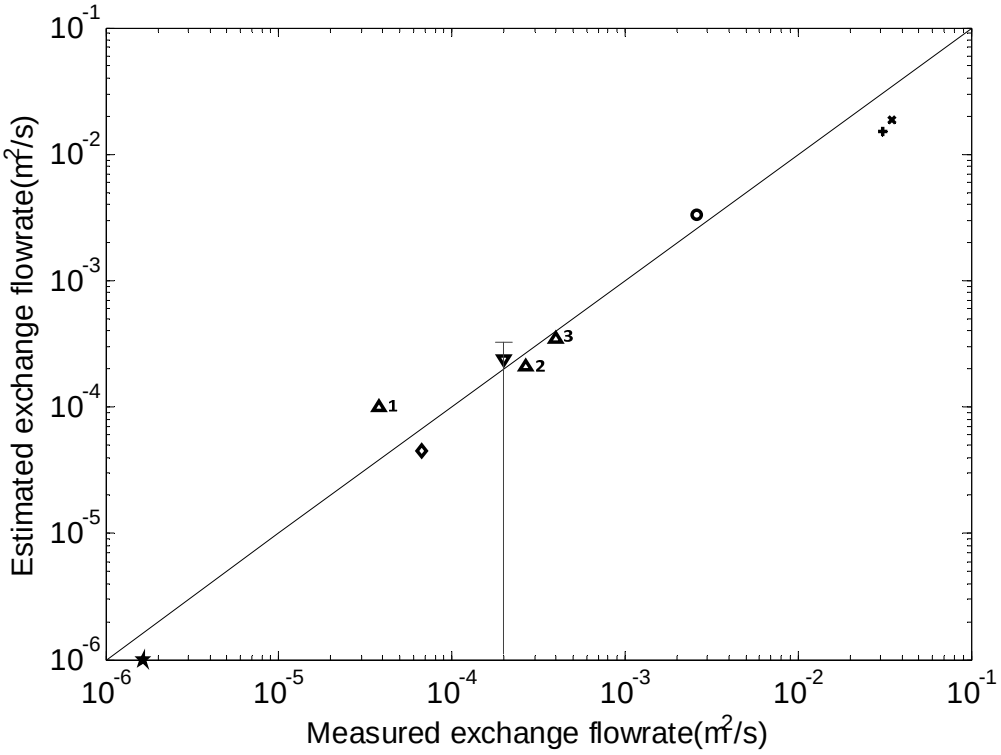

Figure 2.16 Comparisons of exchange flowrate between estimated from asymptotic solution and measurements. The upwarding (▵) and downwarding-triangles (▿) denote the laboratory and filed results within vegetation from Oldham and Sturman (2001). The others represent the results without vegetation, which are ' ○ ' and ' ◇ ' from field and laboratory measurements by Sturman et al. (1999), ★' from laboratory measurements by Chubarenko and Demchenko (2008). '✖' and '✚' are from field measurements carried out by Adam and Wells (1984), and Monismith et al. (1990).

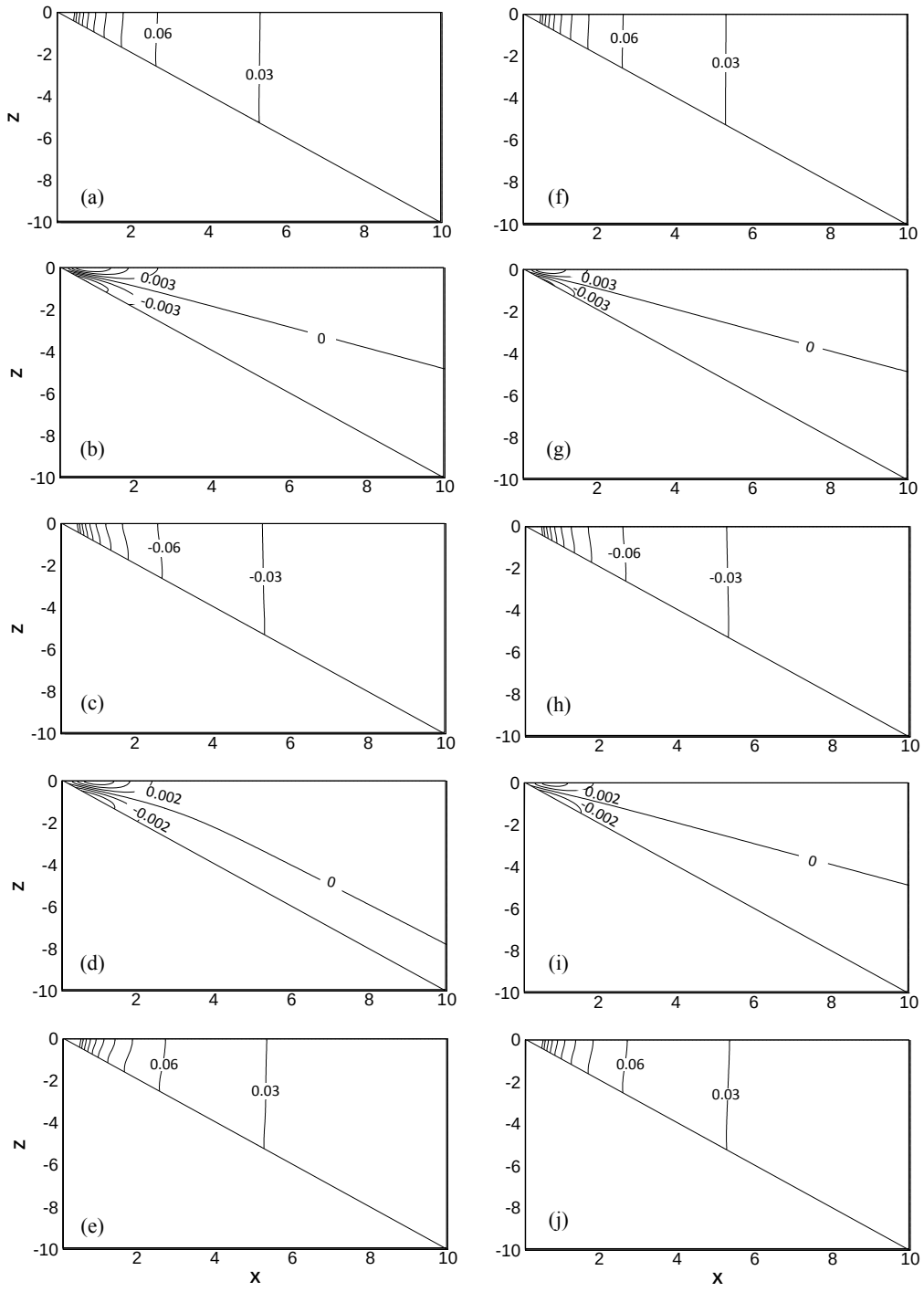

Figure 2.17 Temperature isotherms (first and second-order) for vegetation percentage of 0%, (a) to (e) and 0.25%, (f) to (j) at various times. The parameters of $S = 0.1$ and $Gr = 10^4$ are used. (a) and (f) $t = 0.25$, (b) and (g) $t = 0.50$, (c) and (h) $t = 0.75$, (d) and (i) $t = 1$, and (e) and (j) $t = 1.25$.

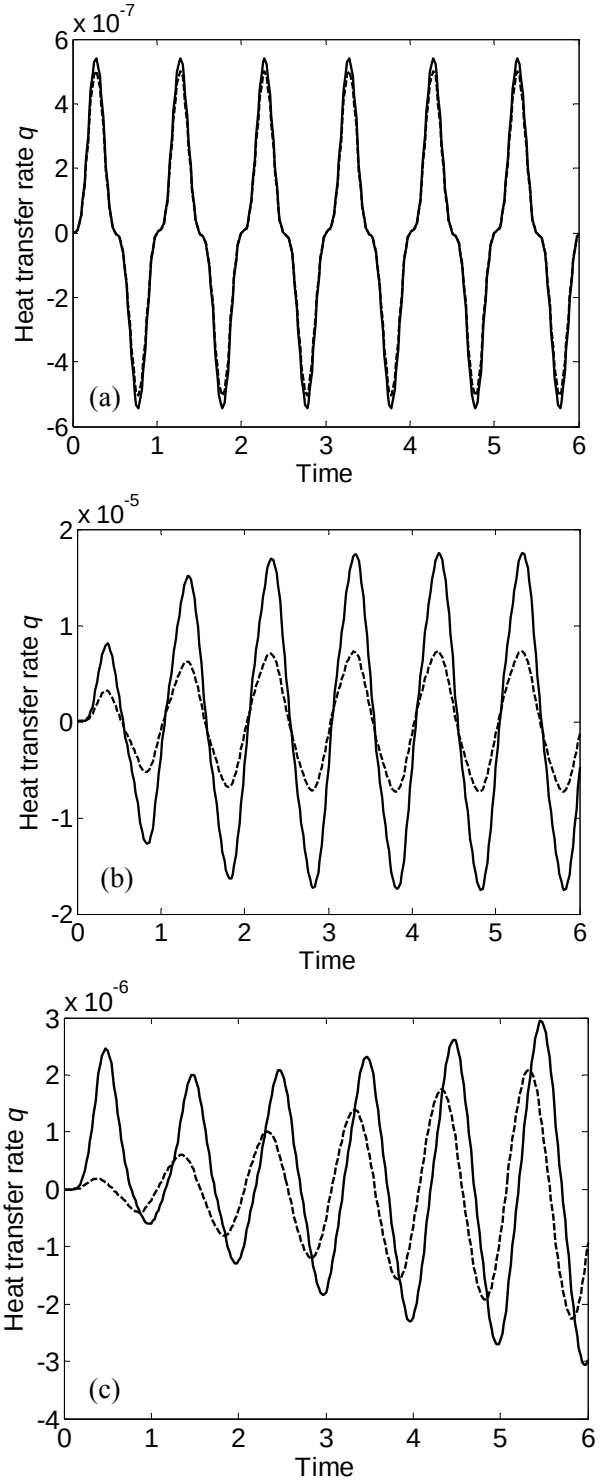

Figure 2.18 Time series of horizontal heat transfer rate at (a) $x = 0.25,$ (b) x=1, and (c) $x = 5$ (Note: Heat transfer rate q in the figure for $\phi = 0\%$ (——), and $\phi = 0.25\%$(-----).

Chapter 3

Thermal-driven flow over a stratified and vegetated sloping bottom during heating and cooling cycles

This chapter is to be submitted to *Journal of fluid mechanics*, as "Thermal-driven flow over a stratified and vegetated sloping bottom during heating and cooling cycles." by Lin, Y. T., and Wu, C.H.

3.1 Abstract

In this study, thermal-driven flow generated from topographic and vegetation shading effects is taken into consideration in a stratified environment. An asymptotic solution is developed to discuss the roles of emergent vegetation and light attenuation coefficients and the interferences and competitions between the shading and sloping bottom effects on thermal-drive flow. The results show for clear water, i.e. smaller light extinction coefficients, greater bottom heating can lead to greater circulation. In shallow water, viscosity is balanced with pressure gradient, whereas vegetative drag is dominant for both clear and turbid water. Also, in shallow water, due to heat mixtures over the water column, horizontal velocity is similar to the result from the assumptions of uniform heat distribution both with and without vegetation. Vegetative drag reduces the circulation and shortens the time lag between the circulation and reversal of pressure gradients. The different vegetation distribution and unequal heating and cooling processes can change the temperature fields, and therefore affect the thermal-driven circulation. For turbid water, its circulation is easily affected by the vegetation

distribution than clear water. The study also provides the valid ranges of the asymptotic solutions.

3.2 Introduction

In lakes and geophysical fluid bodies, during the daytime, the solar radiation penetrates into water, and is absorbed by water. The intensity of solar radiation decays exponentially with depth as Beer's law states (Kirk, 1986). The rate of decay is a function of the wavelength of the light and the turbidity of the water (Zhang & Nepf, 2009). The absorbed solar radiation is converted to heat, leading to warmer surface water than an underlying cold layer, and therefore the temperature varies vertically along the water column, i.e. stratification. Near the shore, sloping topography and profound vegetation have significant impacts on the structures of water temperature. For example, assuming the same amount of heat gains and losses over the water columns, on average, temperature in shallow water during daytime is warmer than that in deep water. The horizontal heterogeneous temperature differences lead to variations of water density, and cause circulation generated toward offshore at the surface, and onshore near the bottom (Farrow & Patterson, 1993). During the nighttime, the circulation pattern is reversed. On the other hand, floating and emergent vegetation can block certain portions of sunlight into the water body, lead to colder water areas than those without vegetation, and finally generate thermal-driven circulation. Unlike floating vegetation, emergent vegetation also provide inherent drag forces to slow down the circulation (Zhang & Nepf, 2008). Because of diurnal heating and cooling processes, the generated circulation flushes back

and forth over the littoral zones, promotes the exchange of nutrient and pollutants, and reduces the flushing time between the nearshore and main water body (Monismith, Imberger, & Morrison, 1990). In literatures, several studies investigated the mechanism of thermal-driven circulation over a sloping bottom (Farrow & Patterson, 1993; Farrow, 2004) or non-uniform distributed vegetation on a flat bottom (Coates & Patterson, 1993; Lövstedt & Bengtsson 2008; Zhang & Nepf, 2009), respectively. Studies discussing the effects of sloping bottom and emergent vegetation on thermal-driven flow especially in a stratified aquatic environment are still lack.

Thermal-driven circulation was firstly observed over a sloping nearshore environment (Adam & Wells, 1984 and Monismith et al. 1990). They observed that the circulation can be up to ~15cm/s, and time lag existing between the buoyancy and horizontal velocities is equal to the forcing period. In order to reveal the underlying physics of thermal-driven flow due to the topographic effects, two models considering distribution of solar radiation over water columns are commonly adopted. Farrow and Patterson (1993), and Farrow (2004) neglected the stratified effects and assumed the solar radiation is uniformly-distributed over the local water depth. They analytically found the time lag between buoyancy and horizontal velocities can be up to the forcing period, and the thermal-driven flow is viscous-dominated in shallow water, whereas inertia-dominated in deep water. In addition, a more physically realistic model is adopted, which assumes that during the daytime, the solar radiation exponentially decays with the water depth, and the residual heat reaching the bottom is re-emitted to the water column as a bottom heat flux. Farrow (1994) only included vertical heat conduction and derived an asymptotic solution to describe the thermal-driven circulation during the daytime heating.

The generated flow can be classified as three stages such as conductive, transient, and convective regimes according to the vertical temperature differences for both daytime heating and nighttime cooling. Once the vertical temperature gradient exceeds some specific criteria (Drazin & Reid 1981), thermal instability will occur and is an important mechanism in breaking the residual circulation and reversing the flow in deep waters (Lei and Patterson, 2002). Lei and Patterson (2006) found that bottom heating from the residual solar radiation is an important mechanism to drive the circulation, and smaller light extinction coefficients can lead to larger exchange flowrates. Lei and Patterson (2006) and Badnarz et al. (2009) both showed a time lag of flow responses to the switch of diurnal heating and cooling, consistent with the field measurements and analytical solutions. In the above-mentioned studies, physical mechanisms of thermal-driven flow between viscosity, inertia, and temperature gradients lack detailed discussions.

Emergent and floating vegetation also cause horizontal temperature gradients and generate circulation. Coates and Patterson (1993) revealed that the flow from shading of floating vegetation can be classified as inertial and energy-limited regimes, yielding corresponding magnitudes of the circulation. For floating vegetation with roots occupied a fraction of water depths, and rooted emergent vegetation, inherently resistant forces are imposed to significantly reduce the circulation, volumetric flowrate of exchange flow, and increase flushing time (Oldham & Sturman 2001; Tanino, Nepf, & Kulis 2005; Zhang & Nepf 2008; Zhang & Nepf 2009; Zhang & Nepf 2011). Oldham and Sturm (2001) applied the porous media flow theory to study the impact of vegetative drags on exchange flow during surface cooling processes. Zhang & Nepf (2008) added a drag force term in the momentum equation to obtain an empirical equation between density of

emergent vegetation and exchange flowrate. Zhang and Nepf (2009) discussed the combined effects of shading and drag from emergent vegetation on thermal-driven flow over a flat bottom. It was found that at the initial stage, the exchange flow is inertia-dominated, and quickly transitioned to drag-dominated. The transition time from inertia- to drag-dominant is a function of vegetative density. Recently, Zhang and Nepf (2011) considered the drag forces from roots of the floating vegetation on the exchange flowrates over a flat bottom. The generated flow showed different patterns in the root layer, and the open water portions underneath the root layer. As the flow moves more inside to the floating vegetation, the root layer acts as an obstruction to block the flow. Although these works provided new insight on the role of vegetation on the thermal driven flow, effects of diurnal heating and cooling such as time-lag and sloping bottom (topography) are not well-understood. In addition, temperature is warmer in shallow water over an unvegetated slope, whereas the presence of vegetation could reduce the input of solar radiation into the water column. The interferences between vegetation shading effects on thermal-driven flow, especially in stratified environments, at the best of the authors' knowledge, are not reported yet. Also, light extinction coefficients determine the level of stratified temperature structures, and its impact on thermal-driven flow within vegetation is not clear.

In this paper, a combined model regarding solar radiation decaying over the water column during the daytime and heat losses through the water surface during the nighttime is adopted to obtain an asymptotic solution for zero-order temperature and horizontal velocity profiles of thermal-driven flow for different distribution of emergent vegetation. Based upon the derived asymptotic solution, the spatial and temporal dominant

mechanisms for viscosity, vegetative drag and inertial terms, and effects of light attenuation coefficients are elucidated. The flow patterns and magnitude of thermal-driven circulation for different light attenuation coefficients and for different vegetation distribution are revealed. The asymptotic solution is then used to estimate exchange flowrates. Finally the validity and feasibility of the asymptotic solution are discussed and examined.

3.3 Mathematical Formulations

3.3.1 Governing equations, initial and boundary conditions

The flow domain is set up over a sloping bottom with emergent vegetation growth (see figure 3.1). The wedge shape domain (x', z') is considered as a two-dimensional flow, and the origin is at the tip, x' is the horizontal coordinate, and $z'(=-Sx')$ is the vertical coordinate, where S is the bottom slope. The vegetation distribution is assumed to change only in the *x* direction and vertically uniformed, i.e., the effects of leaves are neglected. The vegetative drag can be represented as: $\frac{C_D a u'|u'|}{2n_v}$ in the horizontal momentum equation, where u' is the horizontal velocity, C_D is the drag coefficient, a is the frontal area of vegetation per unit volume. Under low stem Reynolds number Re_d (= $u'd/\nu$, where d is the stem diameter of the vegetation), C_D is inversely proportional to $|u'|$ (Tanino, Nepf & Kulis 2005). The drag term can then be simplified as: Cau', where $C(m/s)$ is the linear drag coefficient. According to Zhang and Nepf's data (2009), the

relationship between the linear drag coefficient C and the solid volume fraction ϕ can be regressed as:

$$C = -0.3788\phi^2 + 0.1134\phi, \tag{3.1}$$

and the frontal area a is given by:

$$a = \frac{4\phi}{\pi d}. \tag{3.2}$$

The heating and cooling are described as different mechanisms. During the heating cycle, an internal heating source term $Q'_{heat}\left(^{\circ}C/s\right)$ is adopted to represent the solar radiation into the water column. The daytime solar radiation I_d is modeled by taking a periodic heat flux and its intensity attenuates exponentially with the depth following Beer's law, which is:

$$I_d = I_{d\_0}\cos\left(2\pi t'/\tau\right)e^{\eta z'}\left(W/m^2\right), \tag{3.3}$$

where I_{d_0} is the heat flux of solar radiation at the water surface during the daytime, τ is the period of the forcing (that is 24 hours), η is the extinction coefficient, and $t = 0$ is at noon. Eq.(3.3) is applied for the heating cycle, i.e. $\cos\left(2\pi t'/\tau\right) \geq 0$. For the cooling cycle, the heat dissipates through the water surface, i.e. $I_{d\_0} = 0$, for $\cos\left(2\pi t'/\tau\right) < 0$. The internal heat source term $Q'_{heat}\left(^{\circ}C/s\right)$ is then given by:

$$Q'_{heat}\left(x',z',t'\right)=\begin{cases}\dfrac{I_{d\_0}F\left(x'/L\right)\eta e^{\eta z'}\cos\left(2\pi t'/\tau\right)}{\rho_0 C_p}\ \left(^{\circ}C/s\right),\cos\left(2\pi t'/\tau\right)\geq 0\\ 0,\cos\left(2\pi t'/\tau\right)<0\end{cases}, \qquad (3.4)$$

where $F\left(x'/L\right)$ is a function related to the vegetation distribution, ρ_0 is the reference density of the fluid, and C_p is the specific heat of water. Due to the presence of emergent vegetation, input of solar radiation into the water body would be reduced. High stems of emergent vegetation grown above the water surface can block solar radiation from entering to the water column. For example, reeds usually grow 2~3m high from the water surface, and even small amount of high reeds ($\phi\approx 0.5\sim 1\%$) can block ~85% incident solar radiation (Lövstedt & Bengtsson, 2008). If emergent vegetation is uniformly distributed along the horizontal direction, the high and short stems of emergent vegetation lead to different reductions of solar radiation I_{d_0} into the water, but the reduction is constant along horizontal direction, i.e. a constant value of $F\left(x'/L\right)$. As a result for uniformly-distributed emergent vegetation over horizontal direction, height of vegetation stems only changes the magnitude of streamlines but not the patterns of streamlines. However, for non-uniformly distributed emergent vegetation, stem height of vegetation is an important factor to change horizontal temperature distribution, and subsequent circulation patterns. The effects of vegetation height on thermal-driven flow will be discussed later.

The extinction coefficient η is a function of the wavelength of the incident solar radiation and the turbidity of the water (Coates & Ferris 1994). In this paper, we consider

the bulk behavior of the radiation and the turbidity is uniform over the water column, and thus the extinction coefficient η is a single and constant value.

Temperature differences are usually small in the littoral zone, and the Boussinesq approximation on density variations can be adopted. With a 2-D flow, a linear drag force term, and the Boussinesq approximation, the governing equations are:

$$\frac{\partial\left(n_v u'\right)}{\partial x'}+\frac{\partial\left(n_v w'\right)}{\partial z'}=0, \tag{3.5}$$

$$\frac{\partial u'}{\partial t'}+u'\frac{\partial u'}{\partial x'}+v'\frac{\partial u'}{\partial y'}=-\frac{1}{\rho}\frac{\partial P'}{\partial x'}-Cau'+\nu\left(\frac{\partial^2 u'}{\partial x'^2}+\frac{\partial^2 u'}{\partial z'^2}\right), \tag{3.6}$$

$$\frac{\partial w'}{\partial t'}+u'\frac{\partial w'}{\partial x'}+w'\frac{\partial w'}{\partial z'}=-\frac{1}{\rho_0}\frac{\partial P'}{\partial z'}+\nu\left(\frac{\partial^2 w'}{\partial x'^2}+\frac{\partial^2 w'}{\partial z'^2}\right)+g\alpha\left(T'-T_0\right), \tag{3.7}$$

$$\frac{\partial T'}{\partial t'}+u'\frac{\partial T'}{\partial x'}+w'\frac{\partial T'}{\partial z'}=\kappa\left(\frac{\partial^2 T'}{\partial x'^2}+\frac{\partial^2 T'}{\partial z'^2}\right)+Q'_{heat}\left(x',z',t'\right), \tag{3.8}$$

where variables with a prime denote dimensional quantities, n_v is the porosity (the volume fraction occupied by water), u', w' are the horizontal and vertical velocities, P' is the pressure, ν is the kinematic viscosity, g is the gravity acceleration, α is the thermal expansion coefficient.

The fluids are at rest and isothermal at $t=0$, and the thermal boundary conditions are based upon the heating or cooling cycles. For the heating cycle (daytime), the water surface is insulated, and the residual heat is absorbed by the bottom which then immediately releases as a bottom boundary heat flux. This bottom boundary condition

confirms that the total heat into different water depths is identical. For the cooling cycle (nighttime), the heat releases through the water surface, and the bottom is assumed to be insulated. At the surface, it is shear free, and no flow can be across the surface. For the bottom, the flow is impermeable to the bottom, and abided by the no-slip condition. The initial and boundary conditions can be expressed as:

$$
\begin{aligned}
&T' = T_0, u' = v' = 0 \text{ at } t = 0;\\
&\frac{\partial u'}{\partial z'} = 0 \left(\text{shear free}\right), v' = 0 \text{ on } z' = 0;\\
&-k\frac{\partial T'}{\partial z'}\left(z' = 0\right) = \begin{cases} 0, & \text{if } \cos\left(2\pi t'/\tau\right) \ge 0 \\ -\dfrac{I_{n\_0} F\left(x'/L\right)}{\rho_0 C_p}\cos\left(2\pi t'/\tau\right), & \text{if } \cos\left(2\pi t'/\tau\right) < 0 \end{cases} \quad \text{on } z' = 0;\\
&u' = v' = 0 \left(\text{no slip}\right) \text{ on } z' = -Ax'.\\
&-\kappa\frac{\partial T'}{\partial \hat{n}}\left(z' = -Ax'\right) = \begin{cases} \dfrac{-\kappa}{\sqrt{1+A^2}}\left(A^2\dfrac{\partial T'}{\partial x'} + \dfrac{\partial T'}{\partial z'}\right) = \dfrac{I_{d\_0} F\left(x'/L\right)}{\rho_0 C_p} e^{-\eta z'}\cos\left(2\pi t'/\tau\right), & \text{if } \cos\left(2\pi t'/\tau\right) \ge 0 \\ 0, & \text{if } \cos\left(2\pi t'/\tau\right) < 0 \end{cases},
\end{aligned}
$$

(3.9)

where I_{n_0} is the flux of heat dissipation at water surface during nighttime.

3.3.2. Scaling analysis

The system of governing equations is firstly non-dimensionalized to identify the importance of each term. The timescale is characterized by the period of forcing, τ, i.e. 24 hrs. The vertical length scale H is defined as the inverse of extinction coefficient, i.e. $H \sim \eta^{-1}$ (Farrow and Patterson, 1994; Zhang and Nepf, 2009). Because of lack of a natural horizontal scale, the horizontal length scale L is obtained by combining the slope S and vertical scale H, which is $x \sim L = H / S$. By balancing the unsteady and heat

source terms in eq.(3.8), the temperature scale is obtained as: $T'-T_0=\Delta T\sim H_0\eta\tau$, where $H_0=I_{d\_0}/\left(\rho_0 C_p\right)$. The balance of temperature differences and hydrostatic pressures yields a pressure scale: $P'\sim\rho g\alpha H_0\tau$. By substituting the pressure scale into eq.(3.6) and assuming the pressure force is balanced by the unsteady horizontal velocity, the horizontal velocity can be scaled as: $u'\sim SGr\nu\eta$, where the Grashof number Gr is given by:

$$Gr=\frac{g\alpha H_0\tau^2}{\nu}. \tag{3.10}$$

Finally, the continuity equation gives a scale for the vertical velocity w':

$$w'\sim S^2Gr\nu\eta. \tag{3.11}$$

The non-dimensional energy equation is given by:

$$\frac{\partial T}{\partial t}+S^2Gr\eta^2\nu\tau\left(u\frac{\partial T}{\partial x}+w\frac{\partial T}{\partial z}\right)=S^2\eta^2\kappa\tau\frac{\partial^2 T}{\partial x^2}+\eta^2\kappa\tau\frac{\partial^2 T}{\partial z^2}+Q_{heat}\left(x,z,t\right), \tag{3.12}$$

Where $Q_{heat}\left(x,z,t\right)=\begin{cases}F\left(x\right)e^z\cos\left(2\pi t\right), \cos\left(2\pi t\right)\geq 0\\ 0, \cos\left(2\pi t\right)<0\end{cases}$, (3.13)

and by using stream function ψ ($u=-\frac{1}{n_v}\frac{\partial\psi}{\partial z}, w=\frac{1}{n_v}\frac{\partial\psi}{\partial x}$), and eliminating the pressure terms, the non-dimensional stream function equation is given by:

$$\psi_{tzz} + A^2\psi_{txx} + A^2 Gr\nu\eta^2\tau\frac{1}{n_v}\left[\left(\psi_x\psi_{zzz} - \psi_z\psi_{xzz}\right) + A^2\left(\psi_x\psi_{xxz} - \psi_z\psi_{xxx}\right)\right] = \nu\eta^2\tau\left(\psi_{zzzz} + 2A^2\psi_{xxzz} + A^4\psi_{xxxx}\right) - Ca\tau\psi_{zz} + n_v T_x \quad (3.14)$$

With the boundary conditions:

$$(1)\begin{cases} \psi = \psi_{zz} = 0, \\ \dfrac{\partial T}{\partial z} = 0 \text{ for } \cos(2\pi t) \geq 0, \qquad \text{on } z = 0;, \\ \dfrac{\partial T}{\partial z} = \dfrac{I_{n\_0}}{I_{d\_0}}\dfrac{\cos(2\pi t)}{\eta^2\kappa\tau} \text{ for } \cos(2\pi t) < 0, \end{cases} \quad (3.15)$$

$$(2)\begin{cases} \psi = \psi_z = 0, \\ \dfrac{\partial T}{\partial n} = \left(T_z + A^2 T_x\right)/\sqrt{1+A^2} = -\dfrac{e^{-x}\cos(2\pi t)}{\eta^2\kappa\tau} \text{ for } \cos(2\pi t) \geq 0, \text{ on } z = -x\,. \\ \dfrac{\partial T}{\partial n} = \left(T_z + A^2 T_x\right)/\sqrt{1+A^2} = 0 \text{ for } \cos(2\pi t) < 0, \end{cases} \quad (3.16)$$

In order to solve the governing equation, the discrete heat source term and boundary conditions for temperature gradients (eqs. 3.13, 3.15, and 3.16) need to become a continuous function. Therefore, the Fourier series are applied to expand the cosine function $\cos(2\pi t)$ from a half period cycle ($0 \leq t \leq 0.5$ or $0.5 \leq t \leq 1$) to the one whole period cycle ($0 \leq t \leq 1$). The half cycle heat source term and boundary conditions for temperature gradients then become:

$$Q_{heat}(x,z,t) = F(x)\left\{\frac{1}{\pi} + \frac{\cos(2\pi t)}{2} + \sum_{m=2}^{\infty}\frac{2}{\pi}\left[\frac{\cos(m\pi/2)}{1-m^2}\right]\cos(2m\pi t)\right\}e^z, \quad (3.17)$$

$$\begin{cases} \psi = \psi_{zz} = 0, \\ \dfrac{\partial T}{\partial z} = -\dfrac{1}{c_k}\left\{-\dfrac{1}{\pi} + \dfrac{\cos(2\pi t)}{2} - \sum_{m=2}^{\infty}\dfrac{2}{\pi}\left[\dfrac{\cos(m\pi/2)}{1-m^2}\right]\cos(2m\pi t)\right\}, \text{ on } z=0, \end{cases} \quad (3.18)$$

$$\begin{cases} \psi = \psi_{z} = 0, \\ \dfrac{\partial T}{\partial n} = -\dfrac{I_{n\_0}}{I_{d\_0}}\dfrac{e^{-x}}{c_k}\left\{\dfrac{1}{\pi} + \dfrac{\cos(2\pi t)}{2} + \sum_{m=2}^{\infty}\dfrac{2}{\pi}\left[\dfrac{\cos(m\pi/2)}{1-m^2}\right]\cos(2m\pi t)\right\}, \text{ on } z=-x.. \end{cases} \quad (3.19)$$

Where $c_k = \eta^2\kappa\tau$.

3.4 Asymptotic solutions

It is difficult to obtain the analytic solutions for eqs.(3.12) and (3.14). Instead, the parameter S is assumed to be small, i.e., $S \ll 1$, and the streamfunction ψ and temperature T can be expanded as a series of even power for S (Cormack et al.,1974)

$$\psi = \psi^{(0)} + S^2\psi^{(2)} + S^4\psi^{(4)} + \ldots, \quad T = T^{(0)} + S^2T^{(2)} + S^4T^{(4)} + \ldots. \quad (3.20)$$

After substituting eq.(3.20) into eqs (3.12), (3.14), and (3.17) to (3.19), and equating the power of S, a system of equations with corresponding boundary conditions are yielded, and can be solved recursively, in principle. The zero-order (S^0) temperature is firstly solved, and then the zero-order streamfunction equation can be solved according to the zero-order horizontal temperature gradient. The zero-order equations are:

$$T_t^{(0)} = c_k T_{zz}^{(0)} + F(x)\left\{\frac{1}{\pi} + \frac{\cos(2\pi t)}{2} + \sum_{m=2}^{\infty}\frac{2}{\pi}\left[\frac{\cos(m\pi/2)}{1-m^2}\right]\cos(2m\pi t)\right\}e^z, \quad (3.21)$$

$$\psi_{tzz}^{(0)} = c_v \psi_{zzzz}^{(0)} - c_d \psi_{zz}^{(0)} + n_v T_x^{(0)} \ , \tag{3.22}$$

where $c_k = \eta^2 \kappa \tau, c_v = \nu \eta^2 \tau, c_d = Ca\tau$.

With boundary conditions:

$$\begin{cases} \psi^{(0)} = \psi_{zz}^{(0)} = 0, \\ T_z^{(0)} = -\dfrac{1}{c_k}\left\{ -\dfrac{1}{\pi} + \dfrac{\cos(2\pi t)}{2} - \sum_{m=2}^{\infty} \dfrac{2}{\pi}\left[\dfrac{\cos(m\pi/2)}{1-m^2} \right] \cos(2m\pi t) \right\}, \text{ on } z = 0 \end{cases} \tag{3.23}$$

$$\begin{cases} \psi^{(0)} = \psi_{z}^{(0)} = 0, \\ T_z^{(0)} = -\dfrac{I_{n\_0}}{I_{d\_0}} \dfrac{e^{-x}}{c_k}\left\{ \dfrac{1}{\pi} + \dfrac{\cos(2\pi t)}{2} + \sum_{m=2}^{\infty} \dfrac{2}{\pi}\left[\dfrac{\cos(m\pi/2)}{1-m^2} \right] \cos(2m\pi t) \right\}, \text{ on } z = -x. \end{cases} \tag{3.24}$$

And the initial condition is:

$$\psi^{(0)} = T^{(0)} = 0 \quad \text{at } t = 0. \tag{3.25}$$

The convective terms in eqs.(3.12) and (3.14) are neglected, given that the $S^2 Gr$ term is smaller than conduction terms in eq.(3.12) and viscous term in eq.(3.14), which yields $S^2 Gr < \dfrac{\nu}{\kappa}$ (= $\dfrac{1}{7}$ for laminar flow). For typical field values, using $I_0 = 500 W/m^2$ and common values for the other parameters such as $g, \alpha, \rho,$ and C_p gives the Grashof number ranging from $Gr \approx 10^7$ for an eddy viscosity of $\nu = 10^{-4}$ to $Gr \approx 10^9$ for the molecular viscosity. The bottom slope *S* usually varies from 10^{-2} to 10^{-3}. Therefore, $S^2 Gr$ is usually larger than unity. Therefore, the asymptotic solution obtained in this study can be only applied to rare conditions such as very small bottom slopes or input solar

radiation *I*. In this study, the solar radiation I and bottom slope S are assumed to be 50 W/m^2 and 2.5×10^{-5}, and the laminar thermal diffusivity $\kappa\left(=1.4\times10^{-7}m^2/s\right)$ and viscosity $\nu\left(=10^{-6}m^2/s\right)$ used can yield $S^2Gr=0.11<\frac{1}{7}$. In addition, due to the neglect of the convective and horizontal conductive terms in eq.(3.12), the asymptotic solution can be only fit to the conductive flow regimes and lower transitional regions as Lei and Patterson (2002) mentioned. Following Farrow's method (2004), the valid regions of asymptotic solution will be defined later in this paper.

3.4.1 Zero-order temperature

The boundary value problem for zero-order temperature is linear and each term can be solved separately, and then the corresponding solutions are superimposed. The solution can be found by using Laplace transform in *t* and is given by:

$$
\begin{aligned}
T^{(0)} = F(x)\Bigg\{ & \frac{1}{\pi}\left(1-\frac{I_{n\_0}}{I_{d\_0}}\right)\left[\frac{t}{x}+\frac{1}{c_k}\left(\frac{z^2}{2x}+z+\frac{x}{3}\right)\right]+\frac{1}{c_k\pi}\left(\frac{1-e^{-x}}{x}-e^{z}\right) \\
& +\left(1+\frac{I_{n\_0}}{I_{d\_0}}\right)\frac{\sin(2\pi t)}{4\pi x}+\frac{\cos(2\pi t)}{2c_k}\left[\left(1+\frac{I_{n\_0}}{I_{d\_0}}\right)\left(\frac{z^2}{2x}+z+\frac{x}{3}\right)+\left(\frac{1-e^{-x}}{x}-e^{z}\right)\right] \\
& -\frac{2}{x\pi c_k}\sum_{n=1}^{\infty}\Bigg\{\left[\left(1-\frac{I_{n\_0}}{I_{d\_0}}\right)\frac{x^2}{n^2\pi^2}-\frac{1-(-1)^n e^{-x}}{1+(n\pi/x)^2}\right]\exp\left(-\frac{n^2\pi^2c_k}{x^2}t\right)+\frac{\pi}{2}\left[\left(1+\frac{I_{n\_0}}{I_{d\_0}}\right)\frac{x^2}{n^2\pi^2}-\frac{1-(-1)^n e^{-x}}{1+(n\pi/x)^2}\right] \\
& \times\left\{\exp\left(-\frac{n^2\pi^2c_k}{x^2}t\right)-2\pi\left[\frac{2\pi\exp\left(-n^2\pi^2c_kt/x^2\right)-2\pi\cos(2\pi t)+\left(n^2\pi^2c_k/x^2\right)\sin(2\pi t)}{n^4\pi^4{c_k}^2/x^4+4\pi^2}\right]\right\}\Bigg\}\times\cos\frac{n\pi z}{x} \\
& +\sum_{m=2}^{\infty}\frac{2}{\pi}\left[\frac{\cos(m\pi/2)}{1-m^2}\right]\left\{\left(1-\frac{I_{n\_0}}{I_{d\_0}}\right)\frac{\sin(2m\pi t)}{2m\pi x}+\frac{\cos(2m\pi t)}{c_k}\left[\left(1-\frac{I_{n\_0}}{I_{d\_0}}\right)\left(\frac{z^2}{2x}+z+\frac{x}{3}\right)+\left(\frac{1-e^{-x}}{x}-e^{z}\right)\right]\right\} \\
& -\frac{4}{x\pi c_k}\sum_{m=2}^{\infty}\sum_{n=1}^{\infty}\left[\frac{\cos(m\pi/2)}{1-m^2}\right]\left[\frac{x^2}{n^2\pi^2}\left(1-\frac{I_{n\_0}}{I_{d\_0}}\right)-\frac{1-(-1)^n e^{-x}}{1+(n\pi/x)^2}\right]\times\cos\frac{n\pi z}{x} \\
& \times\left\{\exp\left(-\frac{n^2\pi^2c_k}{x^2}t\right)-2m\pi\left[\frac{2m\pi\exp\left(-n^2\pi^2c_kt/x^2\right)-2m\pi\cos(2m\pi t)+\left(n^2\pi^2c_k/x^2\right)\sin(2m\pi t)}{n^4\pi^4{c_k}^2/x^4+4m^2\pi^2}\right]\right\}\Bigg\}
\end{aligned}
\tag{3.26}
$$

The terms with coefficient of $\left(1-\frac{I_{n\_0}}{I_{d\_0}}\right)$ present effects of unequal heating and cooling processes. If $I_n / I_d \neq 1$, temperature profiles could be increased or decreased with time *t*. For equal heating and cooling, i.e. $I_{d\_0} = I_{n\_0}$, these terms would disappear. The term $\left(1+\frac{I_{n\_0}}{I_{d\_0}}\right)\frac{\sin(2\pi t)}{4\pi x}$ is the solution for the uniform distribution of solar radiation over the water column for equal heating and cooling processes (see Farrow and Patterson, 1993). The terms with infinite sums show the transient features and ensure that the initial condition, i.e. $T = 0$, is satisfied. The remaining parts of the solution balance the internal heat source and satisfy the boundary conditions.

The temperature gradient $T_x^{(0)}$ (forcing term) in eq.(3.26) is given by:

$$
\begin{aligned}
T_x^{(0)} = {} & a_0(x) + b_0(x)t + c_0(x)z + d_0(x)z^2 + e_0(x)e^z + f_0(x)\sin(2\pi t) + g_0(x)\cos(2\pi t) \\
& + h_0(x)z\cos(2\pi t) + i_0(x)z^2\cos(2\pi t) + j_0(x)e^z\cos(2\pi t) \\
& + \sum_{n=1}^{\infty} a_n(x)\sin(2\pi t)\cos(n\pi z/x) + \sum_{n=1}^{\infty} b_n(x)\cos(2\pi t)\cos(n\pi z/x) + \sum_{n=1}^{\infty} c_n(x)z\sin(2\pi t)\sin(n\pi z/x) \\
& + \sum_{n=1}^{\infty} d_n(x)z\cos(2\pi t)\sin(n\pi z/x) + \sum_{n=1}^{\infty} e_n(x)\exp\left(-n^2\pi^2\sigma t/x^2\right)\cos(n\pi z/x) + \sum_{n=1}^{\infty} f_n(x)t\exp\left(-n^2\pi^2\sigma t/x^2\right)\cos(n\pi z/x) \\
& + \sum_{n=1}^{\infty} g_n(x)z\exp\left(-n^2\pi^2\sigma t/x^2\right)\sin(n\pi z/x) + \sum_{m=2}^{\infty} a_m\sin(2m\pi t) + \sum_{m=2}^{\infty} b_m\cos(2m\pi t) \\
& + \sum_{m=2}^{\infty} c_m(x)z\cos(2m\pi t) + \sum_{m=2}^{\infty} d_m(x)z^2\cos(2m\pi t) + \sum_{m=2}^{\infty} e_m(x)e^z\cos(2m\pi t) \\
& + \sum_{n=1}^{\infty}\sum_{m=2}^{\infty} a_{nm}(x)\sin(2m\pi t)\cos(n\pi z/x) + \sum_{n=1}^{\infty}\sum_{m=2}^{\infty} b_{nm}(x)\cos(2m\pi t)\cos(n\pi z/x) \\
& + \sum_{n=1}^{\infty}\sum_{m=2}^{\infty} c_{nm}(x)z\cos(2m\pi t)\sin(n\pi z/x) + \sum_{n=1}^{\infty}\sum_{m=2}^{\infty} d_{nm}(x)z\sin(2m\pi t)\sin(n\pi z/x)
\end{aligned}
\tag{3.27}
$$

The coefficients $a_0(x), b_0(x), \ldots d_{nm}(x)$ are given in the Appendix 3.A.

The effects of each term in eq.(3.27) can be described as follows. The *t* terms associated with sine or cosine functions represent the diurnal heating and cooling

phenomena. Terms with coefficient of $b_0(x), c_0(x), d_0(x), a_m(x), c_m(x),$ and $d_m(x)$ can be neglected in the equal magnitude of heating and cooling processes. For uniform distribution of emergent vegetation, zero-order temperature profiles are not affected by terms with coefficients of $c_0(x), e_0(x), h_0(x), j_0(x), a_m(x),$ and $e_m(x)$. For equal heating and cooling processes, and uniform-distributed vegetation, terms of $z^2\cos(2\pi t)$ representing changes of temperature gradient along with the depth result from the isotherms curling over to meet the boundary condition at $z=-x$. The infinite exponent terms associated with time denote the transient behavior of the temperature profiles. Under conditions of equal heating and cooling processes, and horizontally uniform-distributed emergent vegetation, it is interesting that the e^z terms will not lead to horizontal temperature gradients.

3.4.2 Zero-order horizontal velocity and exchange flowrate

The boundary value problems for $\psi^{(0)}$ are linear and the forcing term $T_x^{(0)}$ in eq.(3.27) can be solved separately, and then the full solution of $\psi^{(0)}$ can be obtained by superimposing. The solution of each forcing term in eq.(3.27) can be solved by using Laplace transform in t. The full solution for $\psi^{(0)}$ is given by:

$$\begin{aligned}\psi^{(0)} &= a_0(x)\psi_1^{(0)} + b_0(x)\psi_2^{(0)} + c_0(x)\psi_3^{(0)} + d_0(x)\psi_4^{(0)} + e_0(x)\psi_5^{(0)} + f_0(x)\psi_6^{(0)} + g_0(x)\psi_7^{(0)} \\ &+ h_0(x)\psi_8^{(0)} + i_0(x)\psi_9^{(0)} + j_0(x)\psi_{10}^{(0)} + \sum_{n=1}^{\infty} a_n(x)\psi_{11}^{(0)} + \sum_{n=1}^{\infty} b_n(x)\psi_{12}^{(0)} + \sum_{n=1}^{\infty} c_n(x)\psi_{13}^{(0)} \\ &+ \sum_{n=1}^{\infty} d_n(x)\psi_{14}^{(0)} + \sum_{n=1}^{\infty} e_n(x)\psi_{15}^{(0)} + \sum_{n=1}^{\infty} f_n(x)\psi_{16}^{(0)} + \sum_{n=1}^{\infty} g_n(x)\psi_{17}^{(0)} + \sum_{m=2}^{\infty} a_m\psi_{18}^{(0)} + \sum_{m=2}^{\infty} b_m\psi_{19}^{(0)} \\ &+ \sum_{m=2}^{\infty} c_m(x)\psi_{20}^{(0)} + \sum_{m=2}^{\infty} d_m(x)\psi_{21}^{(0)} + \sum_{m=2}^{\infty} e_m(x)\psi_{22}^{(0)} + \sum_{n=1}^{\infty}\sum_{m=2}^{\infty} a_{nm}(x)\psi_{23}^{(0)} + \sum_{n=1}^{\infty}\sum_{m=2}^{\infty} b_{nm}(x)\psi_{24}^{(0)} \\ &+ \sum_{n=1}^{\infty}\sum_{m=2}^{\infty} c_{nm}(x)\psi_{25}^{(0)} + \sum_{n=1}^{\infty}\sum_{m=2}^{\infty} d_{nm}(x)\psi_{26}^{(0)}\end{aligned} \tag{3.28}$$

where $\psi_1^{(0)},...,\psi_{26}^{(0)}$ are given in Appendix 3.B. The horizontal velocity can then be obtained as:

$u^{(0)} = -\frac{1}{n_v}\frac{\partial\psi^{(0)}}{\partial z}$. The Exchange flowrate is calculated as:

$$Q(t,x) = \frac{1}{2}\int_{-x}^{0}|u|\,dz\,. \tag{3.29}$$

3.5 Results and Discussions

3.5.1 Transient behavior

The e-folding times t_{e_T} and t_{e_ψ} of the transient terms of $T^{(0)}$ and $\psi^{(0)}$ are:

$$t_{e\_T} = \frac{1}{c_k}\left(\frac{x}{\pi}\right)^2, \tag{3.30}$$

$$t_{e\_\psi} = \frac{1}{c_v(\beta_1/x)^2 + c_d}, \tag{3.31}$$

where $\beta_1 \approx 4.49$. For $T^{(0)}$, the e-folding time is indicative of how long it takes for heat to diffuse across the local water depth, whereas for $\psi^{(0)}$, it is time taken for viscosity to diffuse momentum over the water local depth. The ratio of e-folding times t_{e_T} and t_{e_ψ} is:

$$\frac{t_{e\_T}}{t_{e\_\psi}} = \sigma\left(\frac{\beta_1}{\pi}\right)^2 + \frac{c_d}{c_k}\left(\frac{x}{\pi}\right)^2, \tag{3.32}$$

where σ is Prandtl number, and approximately equal to 7 for water in laminar flow. Since $\sigma\left(\frac{\beta_1}{\pi}\right)^2$ is larger than 1, t_{e_T} is always longer than t_{e_ψ} with and without the presence of vegetation. Also, the e-folding time vanish as *x* becomes smaller. Therefore, for any *t*>0, there will be a region near the tip that will exhibit the large-time behavior.

3.5.2 Temperature structure

The asymptotic solutions for $T^{(0)}$ shown in eq.(3.26) have different identifiable components. The *F* represents distribution of emergent vegetation, assumed only to be a function of horizontal location *x*, and therefore it will not affect the vertical structures of temperature profiles. Once vegetation is horizontally uniform-distributed, temperature structures would not be affected but only the magnitude is decreased. Figure 3.2 shows temperature contours with two light attenuation coefficients $\eta = 0.5$, and 50. The maximum physical depth H' in the wedge domain is set to 0.25m, and the corresponding dimensionless depths $H\left(=H'\eta\right)$ for $\eta = 0.5$ and 50 are 0.125 and 12.5. For $H \ll 1$,

shallow water, i.e. a maximum water depth less than the penetration depth of the solar radiation (i.e. $H' < \eta^{-1}$), it implies that a significant portion of the radiation will penetration all the way through water column and reach the bottom. The residual heat will be then reemitted from the bottom as a heat flux. For $H' \gg 1$, deep water, i.e. a maximum water depth greater than the penetration depth of the solar radiation (i.e. $H' > \eta^{-1}$), most of solar radiation will be absorbed in the top-layer of the water column, and little solar radiation can penetration through the water column and reach the bottom. The simulation is switched on at noon, i.e. $t = 0$ is 12 p.m. For $t = 0.25$, water temperature is increased, and in shallow water , i.e. $z / H < 0.2$, temperature profiles show approximate uniform distribution along the water column. For $z / H > 0.2$, and smaller η, i.e. clean water, less solar radiation is absorbed through the water column, and most of the solar radiation is reemitted as a bottom heat flux, i.e., water temperature is warmer near the bottom than near the water surface. The heating from the bottom boundary is more important than that from the internal heating as indicated by Farrow and Patterson (1994) and Lei and Patterson (2002). The warm, less dense fluid underlying cooler denser fluid is a potentially unstable source (Farrow and Patterson, 1993). Conversely, for $z / H > 0.2$ and a larger η, i.e. turbid water, temperature is warmer near the water surface, and colder near the bottom. The internal heating component dominates the bottom heating and in fact the bottom is effectively insulated (Farrow and Patterson, 1994), and stable stratified layers (horizontal isotherms) are formed. Heat begins to dissipate through the water surface at $t = 0.25$, and therefore, temperature at $t = 0.50$ are colder near the water surface and warmer near the bottom. Since the cooling mechanism is not associated with the light attenuation coefficients,

temperature profiles for $\eta = 0.5$ and 50 at $t = 0.75$ are similar, and for $z / H < 0.2$, the vertical isotherms can be observed. Once the heating is switched on again, temperature structures for $\eta = 0.5$ and 50 show distinct differences.

3.5.3 Dominant physical mechanisms and velocity structures

The zero-order dimensionless horizontal momentum equation can be written as:

$$u_t^{(0)} = -p_x^{(0)} - c_d u^{(0)} + c_v u_{zz}^{(0)} . \tag{3.33}$$

The convective terms and vertical velocity are second-order effects. Figures 3.3 and 3.4 provide time evolutions of the viscous ($c_v u_{zz}^{(0)}$), inertia ($u_t^{(0)}$), horizontal pressure gradient ($-p_x^{(0)}$) from buoyancy, vegetative drag ($-c_d u^{(0)}$), and horizontal velocity ($u^{(0)}$) at the water surface. Each term in eq.(3.33) is obtained by integrating eq.(3.22) with respect to the *z* direction. The horizontal velocity can be correlated to the inertia term (acceleration *a*) by using $V = \int a dt$. In shallow water (depth of 0.05m), viscous term is dominant and balanced by the pressure gradient. Effects of vegetative drag are small with 0.5% vegetation, i.e. horizontal velocities within and without vegetation are approximately the same. The horizontal velocity is at the same phase as the pressure gradient for $\eta = 0.5$ and 50. Since heat can diffuse through the water column at this depth, for $\eta = 0.5$ and 50, water is well mixed, and temperature is uniform-distributed over the water depth. Therefore, the magnitude of induced pressure gradients and horizontal velocity are similar for different light attenuation coefficients. As water depth becomes deeper,

pressure gradients generated in $\eta = 0.5$ are gradually larger than that in $\eta = 50$, and thus the induced circulation is larger in $\eta = 0.5$ than that in $\eta = 50$.

During the cooling period, pressure gradients generated are irrelevant with the light extinction coefficient for $\eta = 0.5$ and 50. For $\eta = 0.5$, pressure gradients generated during the heating period are greater than that during the cooling period. As a result, larger and longer surface circulation outflows from the tip to offshore can be found during the daytime but shorter and smaller reverse circulation during the nighttime. On the other hand, for $\eta = 50$, pressure gradients from the diurnal heating and cooling processes are approximately the same, and the magnitude and period of thermal-driven circulation during daytime and nighttime are similar. In deeper water (depth of 0.25m, see figure 3.4), no reversed flow can be found for $\eta = 0.5$; while for $\eta = 50$, flow reverses after $t = 2$. Also, for $\eta = 0.5$, larger pressure gradients can rapidly drive circulation; whereas for $\eta = 50$, the circulation is initiated until the input heat diffuses to the bottom to generate distinct pressure gradients. For example, for $\eta = 50$, the circulation at depth of 0.25 m is initiated at $t \approx 0.50$ slower than that at depth of 0.05 m.

With vegetative drag, horizontal velocities are reduced in both $\eta = 0.5$ and 50. In shallow water (depth of 0.05m), viscosity is more important than vegetative drag, and hence vegetative drag slightly decreases the horizontal velocities at the water surface. In deep water (depth of 0.25m), vegetative drag become the dominant resistance, and horizontal velocity is significantly reduced. For example, with $\eta = 0.5$ and 0.5% vegetation, horizontal velocities at the water surface is reduced by 93% and 34.5% at depth of 0.05 m and 0.25 m, respectively. Figures 3.3 and 3.4 also show the transient and

large-time velocity behavior. The transient time of horizontal velocity become longer as the water depth becomes deeper. In shallow water, the transient time $t_{transient}$ is ~0.25, whereas in deep water, the transient time $t_{transient}$ becomes ~3. Vegetative drag only reduces the magnitudes of horizontal velocity, but phases of horizontal velocity are similar as the cases without vegetation for shallow and deep water.

Dominant physical mechanisms mentioned above also affect contour patterns of surface velocities shown in figures 3.5 and 3.6. For $\eta = 0.5$, reversed flow is appeared in the regions of $z/H < 0.5$ from $t = 0.5$ to 1 when the reversal pressure gradients from surface cooling are large enough to overcome the residual inertia from the heating processes. For $z/H > 0.5$, reversed pressure gradient can reduce the circulation magnitude but is too weak to reverse the entire flow to the opposite direction. Also, in comparisons with the unvegetated case, vegetative drag decreases the circulation in the entire flow field but does not change the phases of circulations (viscosity is dominant). For $z/H < 0.5$, circulation is immediately changed with pressure gradients, i.e. time lag between circulation and reversal of pressure gradient is zero. On the other hand, for $z/H > 0.5$, the flow will not be reversed, i.e. time lag is infinite.

For $\eta = 50$, clockwise (surface flow from shallow to deep waters) and counter-clockwise (surface flow from deep to shallow waters) circulation appears alternatively. In very shallow water ($x \to 0$), changes of circulation directions are in phase with the reversal of pressure gradients, i.e. viscosity dominant and no time lag. The time lag increases as the water becomes deeper. For the first cycle, the time lag can be up to quarter cycle of forcing period. Vegetative drag reduces the circulation magnitude and

also moves locations of maximum and minimum horizontal velocities to the tip of the domain for both heating and cooling periods. Exchange flowrates obtained from integration of horizontal velocities over entire water columns show same patterns as surface horizontal velocity.

In figure 3.7, profiles of horizontal velocity for $\eta = 0.5$ and 50 as well as asymptotic solutions from assumption of uniform heat distribution (see Farrow and Patterson, 1993, and Chapter 2) are provided in shallow and deep waters. In shallow water, all of results at $t = 0.25$ and 0.75 are similar because heat diffuses and mixes over the whole water column. At $t = 0.50$, for the stratified case, heat losses from the water surface lead to weaker reversed pressure gradients compared with uniform heat losses over the entire water column. Therefore, clockwise circulation slowed down by weaker reversed pressure gradients in stratified cases is larger than that in unstratified cases. In deep water (depth of 0.25m), distinct differences of the positive horizontal velocity along water surface are revealed. Induced horizontal velocity for $\eta = 0.5$ is greater than uniform heat distribution. According to horizontal velocity, the magnitude of driving forces, i.e. horizontal pressure gradients P_x, can be listed as the following orders: $P_x(\eta = 0.5) > P_x$ (uniform-heat distribution) $> P_x(\eta = 50)$. At $t = 0.50$, due to the residual inertia, circulation for all three cases is not reversed yet. For $t = 0.75$, only horizontal velocity obtained from the uniform heat distribution is reversed. Pressure gradients for $\eta = 0.5$ from the heating period are larger than those from the cooling period especially as the water depth becomes deeper, and thus horizontal velocity is slowed down but not

reversed at $t = 0.75$. On the other hand, for $\eta = 50$, due to the residual inertia, flow is reversed at $t \sim 1.25$ (see figure 3.6b).

Reduced percentages of horizontal velocities within vegetation for different light extinction coefficients are of interest. Horizontal velocity during heating periods for $\eta = 0.5$ and 50 in shallow and deep water is provided in figure 3.8. In very shallow water (depth of 0.05m, see figures 3.8a and b), horizontal velocity for different light attenuation coefficients becomes similar at $t = 0.25$ as mentioned above. At the beginning ($t = 0.05$), the horizontal velocity is faster for $\eta = 0.5$ than that for $\eta = 50$, as a result of larger pressure gradients from the bottom heating for $\eta = 0.5$. As time increases, heat diffuses to the bottom and generates distinct horizontal pressure gradients for $\eta = 50$. From $t = 0.05$ to 0.25, horizontal acceleration for $\eta = 50$ is greater than that for $\eta = 0.5$. The reduction percentages of horizontal velocities due to vegetative drag are approximately the same for both light attenuation coefficients, i.e. 0.5% vegetation can reduce horizontal velocities by ~7%. In deeper water (depth of 0.25m, see figure 3.8c and d), horizontal pressure gradients have not be generated yet for $\eta = 50$ at $t = 0.05$. At $t = 0.25$, horizontal velocity in 0.5% vegetation becomes ~35% and 49% of velocity without vegetation for $\eta = 0.5$ and 50, respectively. Shapes of horizontal velocity profiles in deep water also perform different patterns during the heating period. For $\eta = 0.5$, i.e. bottom heating dominant, flow rapidly becomes viscosity prevalence, and shows cubic velocity profiles (Farrow 1994); while for $\eta = 50$, horizontal velocities are constant near the surface, and show a sharp turn near the bottom and acceleration along the slope. With

vegetation, thickness of the upslope flow decreases since viscous-dominant regions are suppressed by vegetative drag.

During the cooling period and in shallow water (see figure 3.9a and b), profiles of horizontal velocity with and without vegetation for $\eta = 0.5$ and 50 are similar. At deeper water, for $\eta = 0.5$, reversed pressure gradients are weaker compared with pressure gradients during the daytime, and therefore smaller reductions of horizontal velocities are found from $t = 0.55$ to 0.75. Contrarily, reversed pressure gradients significantly decrease horizontal velocity for $\eta = 50$. In addition, vegetation in presence can change the phases of horizontal velocity for $\eta = 50$. Therefore, reduction percentages of horizontal velocities for $\eta = 0.5$ and 50 due to vegetative drag show significant differences. Figure 3.10 show a time series of surface velocities for $\eta = 0.5$ and 50 at two depths of 0.05m and 0.25m. In shallow water (0.05m), horizontal velocity is similar, and reduction percentage of vegetative drags are constant at different times, i.e. ~93% for $\phi = 0.5\%$. In deep water, reversed flows are only found for $\eta = 50$, and time occurring for flow reversal is changed with and without vegetation. Vegetative drag decrease inertia, and therefore the time occurring for flow reversal is earlier. The reduction percentages of horizontal velocities due to vegetative drag are approximately 35% for $\eta = 0.5$, whereas for $\eta = 50$, reduction percentages vary with time, and at some specific time, it can show dramatic changes due to the changes of phases in velocity profiles.

3.5.4 Streamline structures

Figures 3.11 and 3.12 provide contours of streamlines at several specific times for $\eta = 0.5$ and 50, and shading zones represent the transition between clockwise and counter clockwise circulation. For $\eta = 0.5$, and $t = 0.25$ and $t = 0.75$ the circulation reaching its peak during the daytime and nighttime are shown. At $t = 0.25$, clockwise circulation are generated and reduced by vegetative drag. For $t = 0.75$, the flow is reversed until $z / H \sim 0.5$ (see the front of the zero streamline). For $z / H > 0.5$, reversed pressure gradients from the nighttime cooling is not large enough to reverse the circulation. With 0.5% vegetation, the front of zero streamline near the bottom can move further to the deep water (see shadows in figure 3.11c and d). For $\eta = 50$, three specific times, namely, $t = 0.25,\ 0.75,$ and 1.25 are examined. At $t = 0.25$, clockwise circulation can be seen with and without vegetation. The drag exerted by vegetation not only retards the circulation but also moves locations of the maximum circulation to the tip of the wedge. For $t = 0.75$, the reversal of circulation can be found in the region of $z / H \sim 0.5$, similar to the regions without any vegetation. The cooling processes are not related to the light extinction coefficients, and therefore the nighttime circulation would be identical for the cases with different light extinction coefficients. At $t = 1.25$, the flow field is heated again, and the flow patterns are different at the three regions, which are $z / H < 0.5$, $0.5 < z / H < 0.9$, and $z / H > 0.9$. The circulation are reversed at the regions of $z / H < 0.5$ and $z / H > 0.9$, because inertial are overcome by reversed pressure gradients. For $0.5 < z / H < 0.9$, residual inertia due to reversed pressure gradient leads to counter-clockwise circulation.

3.5.5 Uneqaul diurnal heating and cooling

In field conditions, the magnitude of heat gains and losses during diurnal cycles is not identical. Figure 3.13 shows contours of streamlines of different heating and cooling magnitude for $\eta = 0.5$ and 50 at specific times. For heating/cooling=1.1, i.e. heat absorption is more than heat losses in the water body, magnitude of clockwise streamlines as well as horizontal velocities for $\eta = 0.5$ and 50 are enhanced during the entire diurnal cycle. For $\eta = 0.5$, the front of zero streamline moves away from the tip in comparison with equal heating and cooling (see figure 3.11) as heating is more than cooling, and vice versa for the case of cooling more than heating. For $\eta = 50$, it is interesting that three distinct circulation regions can be found in unequal heating and cooling processes (see figure 3.14). For heating/cooling=1.1, clockwise circulation is intensified and regions occupied by clockwise circulation are expanded, whereas the zones of counter-clockwise circulation are narrowed. The situations become opposite for heating/cooling=0.9. For both cases, vegetative drag moves the front of zero streamline near the bottom further to the deep water as the case of equal heating and cooling magnitude.

3.5.6 Effects of vegetation distribution

In littoral zones, distribution of vegetation may vary as a result of local conditions such as light abundance, sediment types, wave climates, and nutrient supplies. Usually, vegetation can grow in shallow water due to abundant light and nutrients. However, wind-induced waves easily break in shallow water, and subsequently release energy to

inhibit vegetation growth (Koch 2001). Under this condition, vegetation can be found in deeper water rather than shallow water. In this section, two extreme cases, i.e. vegetation in one-side, and open water in the other side shown in figure 3.15 are discussed.

For simplicity, emergent vegetation occupies half of the entire domain, and the other half domain is open water. In conditions of one-side vegetation (ϕ_0) and one-side open water ($\phi = 0\%$), a Heaviside function is adopted to define the distribution of solar radiation for one-side vegetation (shallow) and one-side open water (deep), which is:

$$I_{d\_0}(x) = I_{d\_open} \times \left[(1-B) + \frac{B}{1+\exp\left(-2k\left(x/L_x - 0.5\right)\right)} \right], \tag{3.34}$$

where I_{d_open} is the of solar radiation in the open water, k is the coefficient meaning sharpness of transitions from vegetation to open water, B is the blockage of solar radiation by vegetation shading, which is between 0 to 1, and L_x is the dimensionless length of the domain.

The solid volume fraction of vegetation $\phi(=1-n)$ is:

$$\phi(x) = \phi_0 \cdot G(x), \tag{3.35}$$

where ϕ_0, the solid volume fraction of vegetation at the shoreline, and $G(x) = \left[\frac{1}{1+\exp\left(2k\left(x/L_x - 0.5\right)\right)} \right]$.

If the vegetation is emergent only several centimeters from the water surface, the solar radiation into the water is assumed to be inversely proportional to the vegetation density.

Meanwhile, areas occupied by vegetation in the water body are decreased proportional to vegetation density. Therefore, for short stems of emergent vegetation, temperature patterns as well as induced circulation are not changed. On the contrary, for high stems of emergent vegetation such as reed usually with 2~3m high from the water surface, small amount of high reeds can block ~85% incident solar radiation (Lövstedt & Bengtsson, 2008). Under this condition, the vegetation shading effect leads to significant changes of temperature structures, and so do the thermal-driven circulation.

Figure 3.16 illustrates contours of streamlines in two extreme cases for $\eta = 0.5$ at $t = 1.25$ (k is assumed to be 20). For no or uniform-distributed vegetation, only clockwise circulation can be found. For vegetation in shallow water, and open in deep water, less solar radiation into shallow water (assuming 15% solar radiation into the water body) leads to weaker circulation in shallow water during the heating period. Thermal-driven circulation arising from topographic effects is lessened by the vegetation distribution but still maintain clockwise circulation patterns. Furthermore, when open in shallow water and vegetation in deep water (15% solar radiation into the region, see figure 3.16b), vegetation distribution intensifies the topographic effect, and thus stronger circulation is found in shallow water. Also, larger temperature gradient at the water-vegetation interface results in a local peak of thermal-driven circulation (see figure 3.16b). In figure 3.17, small portions of solar radiation (0.1% and 0%) are assumedly into the shallow, and vegetated regions. With 0% penetration of solar radiation, counter-clockwise circulation is observed, and vegetation blocks all of solar radiations and completely alters flow patterns. However, as 0.1% solar radiation is into the water body, only small parts of vegetation regions show counter-clockwise circulation. With penetrating solar radiation

larger than 0.1%, few regions with counter-clockwise circulation can be observed. Therefore, for very clear water, i.e. smaller light attenuation coefficients, even small portions of solar radiation into the water body can still maintain the original flow patterns but with smaller magnitude. The *k* value determines the sharpness of the transition of temperature profiles between the vegetation and open water. Once the *k* value is smaller, i.e. a mild transition, the circulation directions may not be altered by the vegetation distribution.

Two extreme cases for $\eta = 50$ at $t = 1.25$ are shown in figure 3.18. Unlike the cases for $\eta = 0.5$, 15% solar radiation input, i.e., 85% blockage can change the regions of clockwise and counter-clockwise circulation. For vegetation in shallow water, and open in deep water, counter-clockwise circulation is observed in shallow regions, i.e. vegetation shading effects surpass topographic effects on driving circulation. On the contrary, vegetation in deep water can improve horizontal temperature gradients and thermal-driven circulation. Meanwhile, the regions with counter-clockwise circulation in deep water are narrowed. If more solar radiation into the water body in vegetated regions, regions affected by the vegetation distribution can still be seen. Figure 3.19 show 100% and 99.5% solar radiation penetrating into shallow water with vegetation. For 100% solar radiation input into the entire domain, circulation patterns are similar to those in figure 3.12c. On the other hand, for 99.5% of input solar radiation, a local peak of circulation can still be seen at the interface between vegetation and open water, i.e. the interface region is still affected by the vegetation distribution. Therefore, for turbid water, i.e. larger light extinction coefficient, thermal-driven circulation originated from weaker

induced pressure gradients are easily affected by input solar radiation which can be changed by the vegetation distribution.

Exchange flowrates at the center of the flow domain with different blockage of solar radiation are shown in figure 3.20. For the case of vegetation in shallow water, and open in deep water (see figure 3.20a), as the blockage increases, the vegetation shading (blockage of solar radiation) would interfere with the topographic effect in principle. For smaller light extinction coefficients, bottom heating by reemitting the residual solar radiation from the bottom is the main mechanism to drive the circulation. The blockage of solar radiation reduces the bottom heating, i.e. pressure gradient, which is more than the increase pressure gradient due to the blockage. Therefore, the exchange flowrates decrease as the blockage increases. For clear water, the interferences between the vegetation shading and topographic effects are not observed. As the water becomes dirty, i.e. larger light extinction coefficients, the pressure gradient increase by the blockage of the solar radiation is greater than the decreases of the pressure gradient from the blockage. In this conditions, exchange flowrates increase as the blockage percentage. For $\eta = 5$, the exchange flowrates decrease until the blockage is ~0.2, also called the critical blockage and then increase, which shows the interferences between the vegetation shading and topographic effects. It is dominant by the topographic effect for $B \leq 0.2$, whereas it becomes shading-controlled for $B > 0.2$. For $\eta = 50$, the exchange flowrate increases when the blockage is very small and is easily affected by the vegetation distribution. For the case of open in shallow water, and emergent vegetation in deep water (see figure 3.20b), the vegetation shading can theoretically promote the topographic effect and exchange flowrates. However, the exchange flowrates for $\eta = 0.5$ decreasing with the

increase of blockage contradict the theoretical statements mentioned above. This is because the blockage of the solar radiation reduces the bottom heating, and the pressure gradient increases from the vegetation shading is not large enough to compensate the reduction. As the light extinction coefficients become larger, the exchange flowrates also increase with the blockage of solar radiation. As a result, vegetation distribution has greater impact on circulation for water with larger light extinction coefficient, i.e. turbid water. Figure 3.21 shows the exchange flowrates at the center portion of the flow domain for four cases including: (i) no vegetation, (ii) uniform-distributed vegetation, (iii) vegetation in shallow water and open in deep water, and (iv) open in shallow water and vegetation in deep water. Due to the vegetation distribution, the exchange flowrates in cases (iii) and (iv) may be greater or smaller than cases (i) and (ii). Therefore, vegetation distribution is an important factor on estimating the exchange flowrates.

3.5.7 Data comparisons, limitation and valid range of zero-order horizontal velocities

In sec. 2.5.6, exchange flowrates of thermal-driven flow measured in the field and laboratory experiments were listed (see table 2.1). By using the same parameters such as slope, water depth, incident solar radiation, eddy viscosity ($\nu = 10^{-4} m^2 / s$) and turbulent thermal diffusivity ($\kappa = 1.18 \times 10^{-4} m^2 / s$), the derived asymptotic equation is adopted to estimate the exchange flowrates with and without vegetation, and verify with the measurements (see figure 3.22). The light extinction coefficients were usually not included in these previous studies, and the values commonly found in the filed were used,

which are $0.5 < \eta < 3$. Because some of these measurements were carried out under steady states, for comparing with the asymptotic solutions from diurnal cycles, the solar radiations from steady state measurements were converted to the equivalent solar radiations under diurnal cycles.

In shallow water, because of heat diffusion over the entire water column, the temperature is vertically uniformed, and thus no difference of predicted exchange flowrates for $\eta = 0.5$ to 3. The asymptotic solutions show good agreements with those measurements (see figure 3.22). For the field measurements conducted by Adam &Wells (1984), and Monismith, Imberger & Morison (1990), exchange flowrates were obtained at the depths of 12m, and 8m, respectively, where stratified effects are important, and a range of exchange flowrates derived from $\eta = 0.5$ to 3 is provided. In addition, the exchange flowrate with symbol of ∇ obtained from Oldham and Sturman (2001) was carried out at vegetation in shallow water and open in deep water (see figure 3 in Oldham and Sturman, 2001). As sec. 2.5.6 points out, the vegetation shading did not change the flow patterns. Due to lack of information of vegetation blockage and temperature gradients between vegetation and open water, a range of predicted exchange flowrate was provided for Oldham and Sturman's case (∇) in figure 3.22.

The asymptotic solution is valid when S^2 and $S^2 Gr$ are small, and stem Reynolds number Re_d is less than 1 to be in the linear drag law regime (Tanino, Nepf, & Kulis, 2005). The valid range of the linear results can be determined by the included terms larger than the omitted terms (convective terms) in governing equation (Farrow, 2004). Without vegetation, for $x \to 0$, the buoyance is mainly balanced by the vertical shears,

i.e. $x < \frac{1}{S^2 GrU}$. For $x >> 0$, the main balance is between buoyancy and viscosity, which yields $x > S^2 GrU$. Within emergent vegetation, for deep water, vegetative drag is balanced with the buoyance, which yields $x > \frac{S^2 GrU \cdot \nu\eta^2\tau}{c_d}$. Combining these two results gives the range of $S^2 Gr$ for the flow in the domain to be linear. However, limitation ranges also need to satisfy with the constraints of energy equation, i.e. convective terms are smaller than conduction terms in eq.(3.12). Because larger temperature gradients are generated along the vertical direction, constraints are given by:

$$S^2 Gr\eta^2\nu\tau w\frac{T}{z} < \eta^2\kappa\tau\frac{T}{z^2} \Rightarrow S^2 Gr < \frac{1}{zw}\frac{\kappa}{\nu} \approx \frac{1}{zU_{\max}}\frac{\kappa}{\nu} \tag{3.36}$$

Valid ranges derived from energy equations are much smaller than from horizontal momentum equations. Vegetative drags reduce the velocities, lead to a wider range of $S^2 Gr$, and expand the linear regions of asymptotic solutions. Table 3.1 provided valid ranges of $S^2 Gr$.

By using $I = 50W/m^2$, $\nu = 10^{-6} m^2/s$, stem size $d = 0.6cm$, slope $A = 2.5\times10^{-5}$, vegetation density ϕ is 0.5%, the maximum dimensional horizontal velocity u' for $\eta = 0.5$ and 50 is 7.5×10^{-5}, and $2\times10^{-5}\ m/s$, and corresponding $\mathrm{Re}_d = 0.45$, and 0.12<1, consistent with the assumption of linear drag law.

3.6 Conclusions

The paper includes the vegetative drag into the horizontal momentum equation, and discussed the flow patterns under the presence of emergent vegetation in a stratified environment. The asymptotic solutions show that in shallow water, horizontal velocity derived is similar to that with assumptions of uniform heat distribution. In deeper water, for smaller light extinction coefficients, larger pressure gradients from bottom heating lead to higher horizontal velocity, and also reversed flow is not observed. For larger light extinct coefficients, time-lag between reversal of circulation and pressure gradients is found, and can be up to a quarter period. In very shallow water, viscous effects are still dominant, while in deep water, vegetative drag balances the pressure gradient, and result in smaller inertia forces, i.e. smaller horizontal velocity. The flow patterns can be altered by vegetation distribution and height of emergent vegetation. Once vegetation is tall and grows in shallow water, and the deep water side is open, effects of vegetation shading may interfere with the topographic effects, and subsequently induced circulation is complicated. Circulation in dirty water environment, i.e. larger light attenuation coefficients are easily influenced by different vegetation distribution.

In order to obtain the asymptotic solution, the linear drag coefficient is applied and the bottom slope is assumed to be small. The results of horizontal velocity indicate that the assumption of linear drag coefficient is reasonable for the thermal-driven flow. Based upon the horizontal velocity estimated from asymptotic solution, the valid range of linear results can be up to $S^2Gr < 29$ and 286 for $\eta = 0.5$ and 50 with sparse vegetation

($\phi = 0.5\%$). For denser vegetation, horizontal velocity is smaller and the range of S^2Gr fit to the linear assumption can be larger.

Although the asymptotic solution can predict the magnitude of the thermal-driven flow in emergent vegetation, some limitations still need to be overcome in the future. First, the asymptotic solutions derived can only applied to a very small range of flow conditions. In order to expand suitable ranges, numerical modeling is worth and necessary. The drag coefficient is a critical input for the analytic solution. However, the drag coefficient is usually obtained from circular cylinder tests, and the morphology (stem flexibility and leafs) of the vegetation are not included. Also, the drag coefficient is assumed to be uniform along the vertical direction, and variations of vegetative drag applied along the vertical direction are also neglected. In addition, the absorption or release of heat from vegetation may play an important role on thermal-driven flow. Finally, submerged vegetation also grows extensively in the littoral zones, and its effect on thermal-driven flow still need to be further understood. More analytic analysis, numerical simulation, field and laboratory measurements are necessary to solve these issues.

Appendix 3.A Coefficients of temperature solutions

$$a_0(x)=\frac{1}{c_k\pi}\left\{\frac{1}{3}\left(1-\frac{I_{n\_0}}{I_{d\_0}}\right)\left(F+xF'\right)+F\left(-\frac{1-e^{-x}}{x^2}+\frac{e^{-x}}{x}\right)+F'\left(\frac{1-e^{-x}}{x}\right)\right\}$$

$$b_0(t)=\frac{1}{\pi x}\left(1-\frac{I_{n\_0}}{I_{d\_0}}\right)\left(F'-\frac{F}{x}\right)$$

$$c_0(x)=\frac{1}{c_k\pi}\left(1-\frac{I_{n\_0}}{I_{d\_0}}\right)F'$$

$$d_0(t)=\frac{1}{2c_k\pi x}\left(1-\frac{I_{n\_0}}{I_{d\_0}}\right)\left(F'-\frac{F}{x}\right)$$

$$e_0(z)=-\frac{F'}{c_k\pi}$$

$$f_0(x)=\frac{1}{4\pi x}\left(1+\frac{I_{n\_0}}{I_{d\_0}}\right)\left(F'-\frac{F}{x}\right)$$

$$g_0(x)=\frac{1}{2c_k}\left[\frac{1}{3}\left(1+\frac{I_{n\_0}}{I_{d\_0}}\right)\left(xF'+F\right)+\left(\frac{1-e^{-x}}{x}\right)\left(F'-\frac{F}{x}\right)+F\left(\frac{e^{-x}}{x}\right)\right]$$

$$h_0(x)=\frac{F'}{2c_k}\left(1+\frac{I_{n\_0}}{I_{d\_0}}\right)$$

$$i_0(x)=\frac{1}{4c_k x}\left(1+\frac{I_{n\_0}}{I_{d\_0}}\right)\left(F'-\frac{F}{x}\right)$$

$$j_0(x)=\frac{-F'}{2c_k}$$

$$a_n(x)=\frac{2n^2\pi^2}{x^3\left(4\pi^2+c_k{}^2n^4\pi^4/x^4\right)}\left\{F\pi\left[-\frac{(-1)^n e^{-x}}{1+n^2\pi^2/x^2}-\frac{2\left(1-(-1)^n e^{-x}\right)n^2\pi^2}{\left(1+n^2\pi^2/x^2\right)^2x^3}+\frac{2\left(1+I_{n\_0}/I_{d\_0}\right)x}{n^2\pi^2}\right.\right.$$
$$\left.\left.-\frac{1}{x}\left(-\frac{1-(-1)^n e^{-x}}{1+n^2\pi^2/x^2}+\frac{\left(1+I_{n\_0}/I_{d\_0}\right)x^2}{n^2\pi^2}\right)\left(3-\frac{4c_k{}^2n^4\pi^4}{\left(4\pi^2+c_k{}^2n^4\pi^4/x^4\right)x^4}\right)\right]+\pi F'\left[-\frac{1-(-1)^n e^{-x}}{1+n^2\pi^2/x^2}+\frac{\left(1+I_{n\_0}/I_{d\_0}\right)x^2}{n^2\pi^2}\right]\right\}$$

$$b_n(x)=-\frac{4\pi^2}{c_kx\left(4\pi^2+c_k{}^2n^4\pi^4/x^4\right)}\left\{F\left[-\frac{(-1)^n e^{-x}}{1+n^2\pi^2/x^2}-\frac{2\left(1-(-1)^n e^{-x}\right)n^2\pi^2}{\left(1+n^2\pi^2/x^2\right)^2x^3}+\frac{2\left(1+I_{n\_0}/I_{d\_0}\right)x}{n^2\pi^2}\right.\right.$$
$$\left.\left.+\frac{1}{x}\left(-\frac{1-(-1)^n e^{-x}}{1+n^2\pi^2/x^2}+\frac{\left(1+I_{n\_0}/I_{d\_0}\right)x^2}{n^2\pi^2}\right)\left(\frac{4c_k{}^2n^4\pi^4}{\left(4\pi^2+c_k{}^2n^4\pi^4/x^4\right)x^4}-1\right)+F'\left(-\frac{1-(-1)^n e^{-x}}{1+n^2\pi^2/x^2}+\frac{\left(1+I_{n\_0}/I_{d\_0}\right)x^2}{n^2\pi^2}\right)\right\}$$

$$c_n(x)=\frac{2n^3\pi^4F}{x^5\left(4\pi^2+c_k{}^2n^4\pi^4/x^4\right)}\left(-\frac{1-(-1)^n e^{-x}}{1+n^2\pi^2/x^2}+\frac{\left(1+I_{n\_0}/I_{d\_0}\right)x^2}{n^2\pi^2}\right)$$

$$d_n(x)=-\frac{4n\pi^3F}{c_kx^3\left(4\pi^2+c_k{}^2n^4\pi^4/x^4\right)}\left(-\frac{1-(-1)^n e^{-x}}{1+n^2\pi^2/x^2}+\frac{\left(1+I_{n\_0}/I_{d\_0}\right)x^2}{n^2\pi^2}\right)$$

$$e_n(x)=-\frac{F}{c_kx}\left\{\frac{2}{\pi}\left[-\frac{(-1)^n e^{-x}}{1+n^2\pi^2/x^2}-\frac{2\left(1-(-1)^n e^{-x}\right)n^2\pi^2}{\left(1+n^2\pi^2/x^2\right)^2x^3}+\frac{\left(1-I_{n\_0}/I_{d\_0}\right)x}{n^2\pi^2}+\frac{1}{x}\frac{1-(-1)^n e^{-x}}{1+n^2\pi^2/x^2}\right]\right.$$
$$+\left[-\frac{(-1)^n e^{-x}}{1+n^2\pi^2/x^2}-\frac{2\left(1-(-1)^n e^{-x}\right)n^2\pi^2}{\left(1+n^2\pi^2/x^2\right)^2x^3}+\frac{\left(1+I_{n\_0}/I_{d\_0}\right)x}{n^2\pi^2}+\frac{1}{x}\frac{1-(-1)^n e^{-x}}{1+n^2\pi^2/x^2}\right]\left(1-\frac{4\pi^2}{\left(4\pi^2+c_k{}^2n^4\pi^4/x^4\right)}\right)$$
$$\left.-\frac{16c_k{}^2n^4\pi^6}{x^5\left(4\pi^2+c_k{}^2n^4\pi^4/x^4\right)^2}\left(-\frac{1-(-1)^n e^{-x}}{1+n^2\pi^2/x^2}+\frac{\left(1+I_{n\_0}/I_{d\_0}\right)x^2}{n^2\pi^2}\right)\right\}$$
$$-\frac{F'}{c_kx}\left\{\frac{2}{\pi}\left[-\frac{1-(-1)^n e^{-x}}{1+n^2\pi^2/x^2}+\frac{\left(1-I_{n\_0}/I_{d\_0}\right)x^2}{n^2\pi^2}\right]+\left[-\frac{1-(-1)^n e^{-x}}{1+n^2\pi^2/x^2}+\frac{\left(1+I_{n\_0}/I_{d\_0}\right)x^2}{n^2\pi^2}\right]\left[1-\frac{4\pi^2}{\left(4m^2\pi^2+c_k{}^2n^4\pi^4/x^4\right)}\right]\right\}$$
$$-\frac{4}{c_k\pi x}\sum_{m=2}^{\infty}\left\{\frac{\cos(m\pi/2)}{1-m^2}\left\{F\left(-\frac{(-1)^n e^{-x}}{1+n^2\pi^2/x^2}-\frac{2\left(1-(-1)^n e^{-x}\right)n^2\pi^2}{\left(1+n^2\pi^2/x^2\right)^2x^3}+\frac{\left(1-I_{n\_0}/I_{d\_0}\right)x}{n^2\pi^2}+\frac{1}{x}\frac{1-(-1)^n e^{-x}}{1+n^2\pi^2/x^2}\right)\left(1-\frac{4m^2\pi^2}{\left(4\pi^2+c_k{}^2n^4\pi^4/x^4\right)}\right)\right.\right.$$
$$\left.\left.-\frac{16c_k{}^2m^2n^4\pi^6F}{x^5\left(4\pi^2+c_k{}^2n^4\pi^4/x^4\right)^2}\left(-\frac{1-(-1)^n e^{-x}}{1+n^2\pi^2/x^2}+\frac{\left(1-I_{n\_0}/I_{d\_0}\right)x^2}{n^2\pi^2}\right)+F'\left(1-\frac{4m^2\pi^2}{\left(4m^2\pi^2+c_k{}^2n^4\pi^4/x^4\right)}\right)\left(-\frac{1-(-1)^n e^{-x}}{1+n^2\pi^2/x^2}+\frac{\left(1-I_{n\_0}/I_{d\_0}\right)x^2}{n^2\pi^2}\right)\right\}\right\}$$

$$f_n(x)=-\frac{2n^2\pi F}{x^4}\left[2\left(-\frac{1-(-1)^n e^{-x}}{1+n^2\pi^2/x^2}+\frac{\left(1-I_{n\_0}/I_{d\_0}\right)x^2}{n^2\pi^2}\right)+\pi\left(-\frac{1-(-1)^n e^{-x}}{1+n^2\pi^2/x^2}+\frac{\left(1+I_{n\_0}/I_{d\_0}\right)x^2}{n^2\pi^2}\right)\left(1-\frac{4\pi^2}{\left(4\pi^2+c_k{}^2n^4\pi^4/x^4\right)}\right)\right]$$
$$-\frac{8n^2\pi F}{x^4}\sum_{m=2}^{\infty}\frac{\cos(m\pi/2)}{1-m^2}\left(1-\frac{4m^2\pi^2}{\left(4m^2\pi^2+c_k{}^2n^4\pi^4/x^4\right)}\right)\left(-\frac{1-(-1)^n e^{-x}}{1+n^2\pi^2/x^2}+\frac{\left(1-I_{n\_0}/I_{d\_0}\right)x^2}{n^2\pi^2}\right)$$

$$g_n(x) = -\frac{nF}{c_k x^3}\left[\pi\left(-\frac{1-(-1)^n e^{-x}}{1+n^2\pi^2/x^2}+\frac{(1+I_n/I_d)x^2}{n^2\pi^2}\right)\left(1-\frac{4\pi^2}{\left(4\pi^2+D^2n^4\pi^4/x^4\right)}\right)+2\left(-\frac{1-(-1)^n e^{-x}}{1+n^2\pi^2/x^2}+\frac{(1-I_n/I_d)x^2}{n^2\pi^2}\right)\right]$$
$$-\frac{4nF}{c_k x^3}\sum_{m=2}^{\infty}\frac{\cos(m\pi/2)}{1-m^2}\left(-\frac{1-(-1)^n e^{-x}}{1+n^2\pi^2/x^2}+\frac{(1-I_n/I_d)x^2}{n^2\pi^2}\right)\left(1-\frac{4m^2\pi^2}{\left(4m^2\pi^2+D^2n^4\pi^4/x^4\right)}\right)$$

$$a_m(x) = \frac{1}{2m\pi x}\frac{2}{\pi}\sum_{m=2}^{\infty}\left[\frac{\cos(m\pi/2)}{1-m^2}\right]\left(1-\frac{I_{n\_0}}{I_{d\_0}}\right)\left(F'-\frac{F}{x}\right)$$

$$b_m(x) = \frac{1}{c_k}\frac{2}{\pi}\sum_{m=2}^{\infty}\left[\frac{\cos(m\pi/2)}{1-m^2}\right]\left[\frac{1}{3}\left(1-\frac{I_{n\_0}}{I_{d\_0}}\right)(xF'+F)+\left(\frac{1-e^{-x}}{x}\right)\left(F'-\frac{F}{x}\right)+F\left(\frac{e^{-x}}{x}\right)\right]$$

$$c_m(x) = \frac{1}{c_k}\frac{2}{\pi}\sum_{m=2}^{\infty}\left[\frac{\cos(m\pi/2)}{1-m^2}\right]\left(1-\frac{I_{n\_0}}{I_{d\_0}}\right)F'$$

$$d_m(x) = \frac{1}{x\pi c_k}\sum_{m=2}^{\infty}\left[\frac{\cos(m\pi/2)}{1-m^2}\right]\left(1-\frac{I_n}{I_d}\right)\left(F'-\frac{F}{x}\right)$$

$$e_m(x) = \frac{-1}{c_k}\frac{2}{\pi}\sum_{m=2}^{\infty}\left[\frac{\cos(m\pi/2)}{1-m^2}\right]F'$$

$$a_{mn}(x) = -\frac{8mn^2\pi^2}{\left(4m^2\pi^2+c_k^2n^4\pi^4/x^4\right)x^3}\sum_{m=2}^{\infty}\frac{\cos(m\pi/2)}{1-m^2}\left\{F(x)\left[-\left(-\frac{(-1)^n e^{-x}}{1+n^2\pi^2/x^2}-\frac{2\left(1-(-1)^n e^{-x}\right)n^2\pi^2}{\left(1+n^2\pi^2/x^2\right)^2x^3}+\frac{2\left(1-I_{n\_0}/I_{d\_0}\right)x}{n^2\pi^2}\right)\right.\right.$$
$$\left.\left.+\frac{1}{x}\left(-\frac{1-(-1)^n e^{-x}}{1+n^2\pi^2/x^2}+\frac{(1-I_n/I_d)x^2}{n^2\pi^2}\right)\left(3-\frac{4D^2n^4\pi^4}{x^4\left(4\pi^2+D^2n^4\pi^4/x^4\right)}\right)\right]-\frac{dF}{dx}\left(-\frac{1-(-1)^n e^{-x}}{1+n^2\pi^2/x^2}+\frac{(1-I_n/I_d)x^2}{n^2\pi^2}\right)\right\}$$

$$b_{mn}(x) = -\frac{4}{c_k x}\left[\frac{4m^2\pi}{\left(4m^2\pi^2+c_k^2n^4\pi^4/x^4\right)}\right]\sum_{m=2}^{\infty}\frac{\cos(m\pi/2)}{1-m^2}\left\{F\left[\left(-\frac{(-1)^n e^{-x}}{1+n^2\pi^2/x^2}-\frac{2\left(1-(-1)^n e^{-x}\right)n^2\pi^2}{\left(1+n^2\pi^2/x^2\right)^2x^3}+\frac{2\left(1-I_{n\_0}/I_{d\_0}\right)x}{n^2\pi^2}\right)\right.\right.$$
$$\left.\left.+\frac{1}{x}\left(-\frac{1-(-1)^n e^{-x}}{1+n^2\pi^2/x^2}+\frac{\left(1-I_{n\_0}/I_{d\_0}\right)x^2}{n^2\pi^2}\right)\left(\frac{4c_k^2n^4\pi^4}{\left(4m^2\pi^2+c_k^2n^4\pi^4/x^4\right)x^4}-1\right)\right]+F'\left(-\frac{1-(-1)^n e^{-x}}{1+n^2\pi^2/x^2}+\frac{\left(1-I_{n\_0}/I_{d\_0}\right)x^2}{n^2\pi^2}\right)\right\}$$

$$c_{mn}(x) = \frac{8mn^3\pi^3F(x)}{\left(4m^2\pi^2+c_k^2n^4\pi^4/x^4\right)x^5}\sum_{m=2}^{\infty}\frac{\cos(m\pi/2)}{1-m^2}\left(-\frac{1-(-1)^n e^{-x}}{1+n^2\pi^2/x^2}+\frac{\left(1-I_{n\_0}/I_{d\_0}\right)x^2}{n^2\pi^2}\right)$$

$$d_{mn}(x) = -\frac{16nm^2\pi^2F}{c_k\left(4m^2\pi^2+c_k^2n^4\pi^4/x^4\right)x^3}\sum_{m=2}^{\infty}\frac{\cos(m\pi/2)}{1-m^2}\left(-\frac{1-(-1)^n e^{-x}}{1+n^2\pi^2/x^2}+\frac{\left(1-I_{n\_0}/I_{d\_0}\right)x^2}{n^2\pi^2}\right)$$

Appendix 3.B Coefficients of streamfuctions

(1) $\psi_1^{(0)}$:

$$\psi_1^{(0)} = n_v \left\{ \frac{\sinh\left(z\sqrt{c_d/c_v}\right) - z\sqrt{c_d/c_v}\cosh\left(x\sqrt{c_d/c_v}\right)}{\sinh\left(x\sqrt{c_d/c_v}\right) - x\sqrt{c_d/c_v}\cosh\left(x\sqrt{c_d/c_v}\right)} \left\{ \frac{x^2}{2c_v\left(c_d/c_v\right)} - \frac{1}{c_v\left(c_d/c_v\right)^2}\left[\cosh\left(x\sqrt{c_d/c_v}\right) - 1\right] \right\} \right.$$
$$- \frac{x\sinh\left(z\sqrt{c_d/c_v}\right) - z\sinh\left(x\sqrt{c_d/c_v}\right)}{\sinh\left(x\sqrt{c_d/c_v}\right) - x\sqrt{c_d/c_v}\cosh\left(x\sqrt{c_d/c_v}\right)} \left\{ \frac{x}{c_v\left(c_d/c_v\right)} - \frac{1}{c_v\left(c_d/c_v\right)^2}\sqrt{c_d/c_v}\sinh\left(x\sqrt{c_d/c_v}\right) \right\}$$
$$\left. + \frac{1}{2}\frac{z^2}{c_v\left(c_d/c_v\right)} - \frac{\left[\cosh\left(z\sqrt{c_d/c_v}\right) - 1\right]}{c_v\left(c_d/c_v\right)^2} \right\}$$
$$- \frac{2n_v x^3}{c_v}\sum_{n=1}^{\infty}\left\{ \frac{1}{\beta_n{}^2\sin\beta_n}\left[\left(x\sin\left(\beta_n z/x\right) - z\sin\beta_n\right)\left(\cos\beta_n + \left(\cos\beta_n - 1\right)/\beta_n{}^2 - \frac{1}{2}\right) \right] \right.$$
$$\left. \times \left\{ \frac{\exp\left[-\left(c_v\left(\beta_n/x\right)^2 + c_d\right)t\right]}{\left(\beta_n{}^2 + \left(c_d/c_v\right)x^2\right)} \right\} \right.$$

If $c_d = 0$:

$$\psi_1^{(0)} = -\frac{n_v}{48c_v} z\left(z+x\right)^2\left(2z-x\right)$$
$$- \frac{2n_v x^3}{c_v}\sum_{n=1}^{\infty}\frac{1}{\beta_n{}^4\sin\beta_n}\left(x\sin\left(\beta_n z/x\right) - z\sin\beta_n\right)\left(\left(\frac{\cos\beta_n - 1}{\beta_n{}^2}\right) + \cos\beta_n - \frac{1}{2}\right) \times \exp\left(-c_v\left(\frac{\beta_n}{x}\right)^2 t\right)$$

(2) $\psi_2^{(0)}$:

$$\psi_2^{(0)} = n_v \frac{\sinh\left(z\sqrt{c_d/c_v}\right) - z\sqrt{c_d/c_v}\cosh\left(x\sqrt{c_d/c_v}\right)}{\sinh\left(x\sqrt{c_d/c_v}\right) - x\sqrt{c_d/c_v}\cosh\left(x\sqrt{c_d/c_v}\right)} \left\{ \frac{x^2}{2c_v\left(c_d/c_v\right)} - \frac{1}{c_v\left(c_d/c_v\right)^2}\left[\cosh\left(x\sqrt{c_d/c_v}\right) - 1\right] \right\} t$$
$$- n_v \frac{x\sinh\left(z\sqrt{c_d/c_v}\right) - z\sinh\left(x\sqrt{c_d/c_v}\right)}{\sinh\left(x\sqrt{c_d/c_v}\right) - x\sqrt{c_d/c_v}\cosh\left(x\sqrt{c_d/c_v}\right)} \left\{ \frac{x}{sc_v\left(c_d/c_v\right)} - \frac{1}{sc_v\left(c_d/c_v\right)^2}\sqrt{c_d/c_v}\sinh\left(x\sqrt{c_d/c_v}\right) \right\} t$$
$$+ \frac{n_v}{2}\frac{z^2 t}{c_v\left(c_d/c_v\right)} - \frac{n_v t}{c_v\left(c_d/c_v\right)^2}\left[\cosh\left(z\sqrt{c_d/c_v}\right) - 1\right]$$
$$- \frac{2n_v x^5}{c_v{}^2}\sum_{n=1}^{\infty}\left\{ \frac{1}{\beta^2\sin\beta}\left[\left(x\sin\left(\beta z/x\right) - z\sin\beta\right)\left(\cos\beta + \left(\cos\beta - 1\right)/\beta^2 - \frac{1}{2}\right) \right] \right.$$
$$\left. \times \left\{ \frac{1 - \exp\left[-\left(c_v\left(\beta/x\right)^2 + c_d\right)t\right]}{\left(\beta^2 + \left(c_d/c_v\right)x^2\right)^2} \right\} \right.$$

If $c_d = 0$:

$$\psi_2^{(0)} = -\frac{n_v}{48c_v} z\left(z+x\right)^2\left(2z-x\right)t$$
$$-\frac{2n_v x^5}{{c_v}^2}\sum_{n=1}^{\infty}\frac{1}{\beta^6\sin\beta}\left(x\sin\left(\beta z/x\right)-z\sin\beta\right)\left(\left(\frac{\cos\beta-1}{\beta^2}\right)+\cos\beta-\frac{1}{2}\right)\times\left[1-\exp\left(-c_v\left(\frac{\beta_n}{x}\right)^2 t\right)\right]$$

(3) $\psi_3^{(0)}$:

$$\psi_3^{(0)} = \frac{n_v\left[x\sinh\left(z\sqrt{c_d/c_v}\right)-z\sinh\left(x\sqrt{c_d/c_v}\right)\right]}{\left[\sinh\left(x\sqrt{c_d/c_v}\right)-x\sqrt{c_d/c_v}\cosh\left(x\sqrt{c_d/c_v}\right)\right]}\times\left\{\frac{x^2}{3\left(c_d/c_v\right)c_v}\right\}+\frac{n_v z^3}{6\left(c_d/c_v\right)c_v}-\frac{n_v x^2 z}{6\left(c_d/c_v\right)c_v}$$
$$-\frac{2n_v x^3}{3}\sum_{n=1}^{\infty}\frac{\left[\sin\left(\beta_n z/x\right)-\left(\beta_n z/x\right)\cos\beta_n\right]\exp\left[-\left(c_v\left(\beta_n/x\right)^2+c_d\right)t\right]}{{\beta_n}^2\left[c_v\left(\beta_n/x\right)^2+c_d\right]\sin\beta_n}$$

If $c_d = 0$:

$$\psi_3^{(0)} = -\frac{n_v z\left(x^2-z^2\right)^2}{120c_v}-\frac{2n_v x^3}{3}\sum_{n=1}^{\infty}\frac{\left[\sin\left(\beta_n z/x\right)-\left(\beta_n z/x\right)\cos\beta_n\right]\exp\left[-\left(c_v\left(\beta_n/x\right)^2+c_d\right)t\right]}{{\beta_n}^2\left[c_v\left(\beta_n/x\right)^2+c_d\right]\sin\beta_n}$$

(4) $\psi_4^{(0)}$:

$$\psi_4^{(0)} = n_v\left\{\frac{12z^2\left(c_d/c_v\right)-24\left[\cosh\left(z\sqrt{c_d/c_v}\right)-1\right]+z^4\left(c_d/c_v\right)^2}{12c_v\left(c_d/c_v\right)^3}\right.$$
$$+\frac{\left[\sinh\left(z\sqrt{c_d/c_v}\right)-z\sqrt{c_d/c_v}\cosh\left(x\sqrt{c_d/c_v}\right)\right]}{\left[\sinh\left(x\sqrt{c_d/c_v}\right)-x\sqrt{c_d/c_v}\cosh\left(x\sqrt{c_d/c_v}\right)\right]}\times\left\{\frac{12x^2\left(c_d/c_v\right)-24\left[\cosh\left(x\sqrt{c_d/c_v}\right)-1\right]+x^4\left(c_d/c_v\right)^2}{12c_v\left(c_d/c_v\right)^3}\right\}$$
$$\left.+\frac{\left[x\sinh\left(z\sqrt{c_d/c_v}\right)-z\sinh\left(x\sqrt{c_d/c_v}\right)\right]}{\left[\sinh\left(x\sqrt{c_d/c_v}\right)-x\sqrt{c_d/c_v}\cosh\left(x\sqrt{c_d/c_v}\right)\right]}\times\left\{\frac{6\sqrt{c_d/c_v}\left[\sinh\left(x\sqrt{c_d/c_v}\right)-x\sqrt{c_d/c_v}\right]-x^3\left(c_d/c_v\right)^2}{3c_v\left(c_d/c_v\right)^3}\right\}\right\}$$
$$-\frac{2n_v x^5}{c_v}\sum_{n=1}^{\infty}\frac{1}{\beta_n^6\sin\beta_n\left(1+\frac{c_d}{c_v}\frac{x^2}{{\beta_n}^2}\right)}\left[x\sin\left(\beta_n z/x\right)-z\sin\beta_n\right]\left(1-\beta_n^2/4-2\cos\beta_n-2\left(\cos\beta_n-1\right)/\beta_n^2\right)$$
$$\times\exp\left[-\left(c_v\left(\beta_n/x\right)^2+c_d\right)t\right]$$

If $c_d = 0$:

$$\psi_4^{(0)} = \frac{n_v}{720c_v} z\left(x+z\right)^2\left(3x^3-6x^2z+4xz^2-2z^3\right)$$
$$-\frac{2n_v x^5}{c_v}\sum_{n=1}^{\infty}\frac{1}{\beta_n^6\sin\beta_n}\left[x\sin\left(\beta_n z/x\right)-z\sin\beta_n\right]\left(1-\beta_n^2/4-2\cos\beta_n-2\left(\cos\beta_n-1\right)/\beta_n^2\right)\exp\left[-c_v\left(\beta_n/x\right)^2 t\right]$$

(5) $\psi_5^{(0)}$:

$$\psi_5^{(0)} = n_v\left\{\frac{1-\cosh\left(z\sqrt{c_d/c_v}\right)}{\left[-1+c_d/c_v\right]\left[c_d/c_v\right]c_v}+\frac{e^z-1}{\left[-1+c_d/c_v\right]c_v}\right\}$$
$$+n_v\frac{\left[\sinh\left(z\sqrt{c_d/c_v}\right)-z\sqrt{c_d/c_v}\cosh\left(x\sqrt{c_d/c_v}\right)\right]}{\left[\sinh\left(x\sqrt{c_d/c_v}\right)-x\sqrt{c_d/c_v}\cosh\left(x\sqrt{c_d/c_v}\right)\right]}\times\left\{\frac{1-\cosh\left(x\sqrt{c_d/c_v}\right)}{\left(-1+c_d/c_v\right)\left(c_d/c_v\right)c_v}+\frac{e^{-x}-1}{\left(-1+c_d/c_v\right)c_v}\right\}$$
$$+n_v\frac{\left[x\sinh\left(z\sqrt{c_d/c_v}\right)-z\sinh\left(x\sqrt{c_d/c_v}\right)\right]}{\left[\sinh\left(x\sqrt{c_d/c_v}\right)-x\sqrt{c_d/c_v}\cosh\left(x\sqrt{c_d/c_v}\right)\right]}\times\left\{\frac{\sinh\left(x\sqrt{c_d/c_v}\right)}{\left(-1+c_d/c_v\right)\sqrt{c_d/c_v}c_v}+\frac{e^{-x}}{\left(-1+c_d/c_v\right)c_v}\right\}$$
$$-2n_v\sum_{n=1}^{\infty}\frac{\left[\sin\left(\beta_n z/x\right)-\left(\beta_n z/x\right)\cos\beta_n\right]\exp\left[-\left(c_v\left(\beta_n/x\right)^2+c_d\right)t\right]}{x^2\sin\beta_n\left[c_v\left(\beta_n/x\right)^2+c_d\right]}\times\left\{\frac{-1+\cos\beta_n+\beta_n^2\cos\beta_n}{\left[1+\left(\beta_n/x\right)^2\right]\left(\beta_n/x\right)^2}+\frac{\left(1+x\right)e^{-x}-1}{\left[1+\left(\beta_n/x\right)^2\right]}\right\}$$

If $c_d = 0$:

$$\psi_5^{(0)} = n_v\left\{\frac{4x^3\left(1-e^z\right)+2z\left(1-e^{-x}\right)\left(3x^2-z^2\right)+\left(x+z\right)\left[x^2z\left(x+z\right)-2xz\left(x-z\right)e^{-x}\right]}{4c_v x^3}\right\}$$
$$-2n_v\sum_{n=1}^{\infty}\frac{\left[\sin\left(\beta_n z/x\right)-\left(\beta_n z/x\right)\cos\beta_n\right]\exp\left[-\left(c_v\left(\beta_n/x\right)^2+c_d\right)t\right]}{x^2\sin\beta_n\left[c_v\left(\beta_n/x\right)^2+c_d\right]}\times\left\{\frac{-1+\cos\beta_n+\beta_n^2\cos\beta_n}{\left[1+\left(\beta_n/x\right)^2\right]\left(\beta_n/x\right)^2}+\frac{\left(1+x\right)e^{-x}-1}{\left[1+\left(\beta_n/x\right)^2\right]}\right\}$$

(6) $\psi_6^{(0)}$:

$$\psi_6^{(0)} = n_v \sin(2\pi t)\left\{\frac{\sinh\left(z\sqrt{c_d/c_v}\right) - z\sqrt{c_d/c_v}\cosh\left(x\sqrt{c_d/c_v}\right)}{\sinh\left(x\sqrt{c_d/c_v}\right) - x\sqrt{c_d/c_v}\cosh\left(x\sqrt{c_d/c_v}\right)}\left\{\frac{x^2}{2c_v(c_d/c_v)} - \frac{1}{c_v(c_d/c_v)^2}\left[\cosh\left(x\sqrt{c_d/c_v}\right)-1\right]\right\}\right.$$
$$- \frac{x\sinh\left(z\sqrt{c_d/c_v}\right) - z\sinh\left(x\sqrt{c_d/c_v}\right)}{\sinh\left(x\sqrt{c_d/c_v}\right) - x\sqrt{c_d/c_v}\cosh\left(x\sqrt{c_d/c_v}\right)}\left\{\frac{x}{c_v(c_d/c_v)} - \frac{1}{c_v(c_d/c_v)^2}\sqrt{c_d/c_v}\sinh\left(x\sqrt{c_d/c_v}\right)\right\}$$
$$\left. + \frac{1}{2}\frac{z^2}{c_v(c_d/c_v)} - \frac{1}{c_v(c_d/c_v)^2}\left[\cosh\left(z\sqrt{c_d/c_v}\right)-1\right]\right\}$$
$$+ \frac{2n_v x^3}{c_v}(2\pi)\sum_{n=1}^{\infty}\left\{\frac{1}{\beta_n^{\,2}\left(\beta_n^{\,2} + (c_d/c_v)x^2\right)\sin\beta_n}\left[\left(x\sin(\beta_n z/x) - z\sin\beta_n\right)\left(\cos\beta_n + (\cos\beta_n - 1)/\beta_n^{\,2} - \frac{1}{2}\right)\right]\right.$$
$$\left.\times\left\{\frac{\left[c_v(\beta_n/x)^2 + c_d\right]\exp\left[-\left(c_v(\beta_n/x)^2 + c_d\right)t\right] - \left[c_v(\beta_n/x)^2 + c_d\right]\cos(2\pi t) - 2\pi\sin(2\pi t)}{\left[c_v(\beta_n/x)^2 + c_d\right]^2 + 4\pi^2}\right\}\right.$$

If $c_d = 0$,

$$\psi_6^{(0)} = n_v \frac{z(x+z)^2(x-2z)\sin(2\pi t)}{48c_v}$$
$$+ \frac{2n_v x^3}{c_v}(2\pi)\sum_{n=1}^{\infty}\left\{\frac{1}{\beta_n^{\,2}\left(\beta_n^{\,2} + (c_d/c_v)x^2\right)\sin\beta_n}\left[\left(x\sin(\beta_n z/x) - z\sin\beta_n\right)\left(\cos\beta_n + (\cos\beta_n - 1)/\beta_n^{\,2} - \frac{1}{2}\right)\right]\right.$$
$$\left.\times\left\{\frac{\left[c_v(\beta_n/x)^2 + c_d\right]\exp\left[-\left(c_v(\beta_n/x)^2 + c_d\right)t\right] - \left[c_v(\beta_n/x)^2 + c_d\right]\cos(2\pi t) - 2\pi\sin(2\pi t)}{\left[c_v(\beta_n/x)^2 + c_d\right]^2 + 4\pi^2}\right\}\right.$$

(7) $\psi_7^{(0)}$:

$$\psi_7^{(0)} = n_v \cos(2\pi t)\left\{\frac{\sinh\left(z\sqrt{c_d/c_v}\right) - z\sqrt{c_d/c_v}\cosh\left(x\sqrt{c_d/c_v}\right)}{\sinh\left(x\sqrt{c_d/c_v}\right) - x\sqrt{c_d/c_v}\cosh\left(x\sqrt{c_d/c_v}\right)}\left\{\frac{x^2}{2c_v(c_d/c_v)} - \frac{1}{c_v(c_d/c_v)^2}\left[\cosh\left(x\sqrt{c_d/c_v}\right)-1\right]\right\}\right.$$
$$- \frac{x\sinh\left(z\sqrt{c_d/c_v}\right) - z\sinh\left(x\sqrt{c_d/c_v}\right)}{\sinh\left(x\sqrt{c_d/c_v}\right) - x\sqrt{c_d/c_v}\cosh\left(x\sqrt{c_d/c_v}\right)}\left\{\frac{x}{c_v(c_d/c_v)} - \frac{1}{c_v(c_d/c_v)^2}\sqrt{c_d/c_v}\sinh\left(x\sqrt{c_d/c_v}\right)\right\}$$
$$\left. + \frac{1}{2}\frac{z^2}{c_v(c_d/c_v)} - \frac{1}{c_v(c_d/c_v)^2}\left[\cosh\left(z\sqrt{c_d/c_v}\right)-1\right]\right\}$$
$$- \frac{2n_v x^3}{c_v}\sum_{n=1}^{\infty}\left\{\frac{1}{\beta_n^2\left(\beta_n^2 + (c_d/c_v)x^2\right)\sin\beta_n}\left[\left(x\sin(\beta_n z/x) - z\sin\beta_n\right)\left(\cos\beta_n + (\cos\beta_n - 1)/\beta_n^2 - \frac{1}{2}\right)\right]\right.$$
$$\times\left\{\exp\left[-\left(c_v(\beta_n/x)^2 + c_d\right)t\right]\right.$$
$$\left.\left. + 2\pi\frac{-2\pi\exp\left[-\left(c_v(\beta_n/x)^2 + c_d\right)t\right] - \left[c_v(\beta_n/x)^2 + c_d\right]\sin(2\pi t) + 2\pi\cos(2\pi t)}{\left[c_v(\beta_n/x)^2 + c_d\right]^2 + 4\pi^2}\right\}\right\}$$

If $c_d = 0$:

$$\psi_7^{(0)} = n_v\frac{z(x+z)^2(x-2z)\cos(2\pi t)}{48c_v}$$
$$- \frac{2n_v x^3}{c_v}\sum_{n=1}^{\infty}\left\{\frac{1}{\beta_n^2\left(\beta_n^2 + (c_d/c_v)x^2\right)\sin\beta_n}\left[\left(x\sin(\beta_n z/x) - z\sin\beta_n\right)\left(\cos\beta_n + (\cos\beta_n - 1)/\beta_n^2 - \frac{1}{2}\right)\right]\right.$$
$$\times\left\{\exp\left[-\left(c_v(\beta_n/x)^2 + c_d\right)t\right]\right.$$
$$\left.\left. + 2\pi\frac{-2\pi\exp\left[-\left(c_v(\beta_n/x)^2 + c_d\right)t\right] - \left[c_v(\beta_n/x)^2 + c_d\right]\sin(2\pi t) + 2\pi\cos(2\pi t)}{\left[c_v(\beta_n/x)^2 + c_d\right]^2 + 4\pi^2}\right\}\right\}$$

(8) $\psi_8^{(0)}$:

$$\psi_8^{(0)} = n_v\cos(2\pi t)\left\{\frac{\left[x\sinh\left(z\sqrt{c_d/c_v}\right) - z\sinh\left(x\sqrt{c_d/c_v}\right)\right]}{\left[\sinh\left(x\sqrt{c_d/c_v}\right) - x\sqrt{c_d/c_v}\cosh\left(x\sqrt{c_d/c_v}\right)\right]}\times\left\{\frac{x^2}{3(c_d/c_v)c_v}\right\} + \frac{z^3}{6(c_d/c_v)c_v} - \frac{x^2 z}{6(c_d/c_v)c_v}\right\}$$
$$- \frac{2n_v x^3}{3}\sum_{n=1}^{\infty}\frac{\left[\sin(\beta_n z/x) - (\beta_n z/x)\cos\beta_n\right]}{\beta_n^2\left[c_v(\beta_n/x)^2 + c_d\right]\sin\beta_n}$$
$$\times\left\{\exp\left[-\left(c_v(\beta_n/x)^2 + c_d\right)t\right] - 2\pi\frac{2\pi\exp\left[-\left(c_v(\beta_n/x)^2 + c_d\right)t\right] + \left[c_v(\beta_n/x)^2 + c_d\right]\sin(2\pi t) - 2\pi\cos(2\pi t)}{\left[c_v(\beta_n/x)^2 + c_d\right]^2 + 4\pi^2}\right\}$$

If $c_d = 0$;

$$\psi_8^{(0)} = -n_v \cos(2\pi t) z\left(x^2 - z^2\right)^2 - \frac{2n_v x^3}{3}\sum_{n=1}^{\infty}\frac{\left[\sin(\beta_n z/x) - (\beta_n z/x)\cos\beta_n\right]}{\beta_n{}^2\left[c_v(\beta_n/x)^2 + c_d\right]\sin\beta_n} \times\left\{\exp\left[-\left(c_v(\beta_n/x)^2 + c_d\right)t\right] - 2\pi\frac{2\pi\exp\left[-\left(c_v(\beta_n/x)^2 + c_d\right)t\right] + \left[c_v(\beta_n/x)^2 + c_d\right]\sin(2\pi t) - 2\pi\cos(2\pi t)}{\left[c_v(\beta_n/x)^2 + c_d\right]^2 + 4\pi^2}\right\}$$

(9) $\psi_9^{(0)}$:

$$\psi_9^{(0)} = n_v \cos(2\pi t)\left\{\frac{12z^2(c_d/c_v) - 24\left[\cosh\left(z\sqrt{c_d/c_v}\right) - 1\right] + z^4(c_d/c_v)^2}{12c_v(c_d/c_v)^3} + \frac{\left[\sinh\left(z\sqrt{c_d/c_v}\right) - z\sqrt{c_d/c_v}\cosh\left(x\sqrt{c_d/c_v}\right)\right]}{\left[\sinh\left(x\sqrt{c_d/c_v}\right) - x\sqrt{c_d/c_v}\cosh\left(x\sqrt{c_d/c_v}\right)\right]} \times\left\{\frac{12x^2(c_d/c_v) - 24\left[\cosh\left(x\sqrt{c_d/c_v}\right) - 1\right] + x^4(c_d/c_v)^2}{12c_v(c_d/c_v)^3}\right\} + \frac{\left[x\sinh\left(z\sqrt{c_d/c_v}\right) - z\sinh\left(x\sqrt{c_d/c_v}\right)\right]}{\left[\sinh\left(x\sqrt{c_d/c_v}\right) - x\sqrt{c_d/c_v}\cosh\left(x\sqrt{c_d/c_v}\right)\right]} \times\left\{\frac{6\sqrt{c_d/c_v}\left[\sinh\left(x\sqrt{c_d/c_v}\right) - x\sqrt{c_d/c_v}\right] - x^3(c_d/c_v)^2}{3c_v(c_d/c_v)^3}\right\}\right\} - \frac{2n_v x^5}{c_v}\sum_{n=1}^{\infty}\frac{1}{\beta_n^6\sin\beta_n\left[1 + c_d x^2/\left(c_v\beta_n^2\right)\right]}\left[x\sin(\beta_n z/x) - z\sin\beta_n\right]\left(1 - \beta_n^2/4 - 2\cos\beta_n - 2(\cos\beta_n - 1)/\beta_n^2\right) \times\left\{\exp\left[-\left(c_v\beta_n^2/x^2 + c_d\right)t\right] - 2\pi\frac{2\pi\exp\left[-\left(c_v\beta_n^2/x^2 + c_d\right)t\right] - 2\pi\cos(2\pi t) + \left(c_v\beta_n^2/x^2 + c_d\right)\sin(2\pi t)}{\left(c_v\beta_n^2/x^2 + c_d\right)^2 + 4\pi^2}\right\}$$

If $c_d = 0$;

$$\psi_9^{(0)} = n_v\frac{\cos(2\pi t)}{720c_v}z(x+z)^2\left(3x^3 - 6x^2z + 4xz^2 - 2z^3\right) - \frac{2n_v x^5}{c_v}\sum_{n=1}^{\infty}\frac{1}{\beta_n^6\sin\beta_n\left[1 + c_d x^2/\left(c_v\beta_n^2\right)\right]}\left[x\sin(\beta_n z/x) - z\sin\beta_n\right]\left(1 - \beta_n^2/4 - 2\cos\beta_n - 2(\cos\beta_n - 1)/\beta_n^2\right) \times\left\{\exp\left[-\left(c_v\beta_n^2/x^2 + c_d\right)t\right] - 2\pi\frac{2\pi\exp\left[-\left(c_v\beta_n^2/x^2 + c_d\right)t\right] - 2\pi\cos(2\pi t) + \left(c_v\beta_n^2/x^2 + c_d\right)\sin(2\pi t)}{\left(c_v\beta_n^2/x^2 + c_d\right)^2 + 4\pi^2}\right\}$$

(10) $\psi_{10}^{(0)}$:

$$\psi_{10}^{(0)} = n_v \cos(2\pi t)\left\{\left\{\frac{1-\cosh\left(z\sqrt{c_d/c_v}\right)}{\left[-1+c_d/c_v\right]\left[c_d/c_v\right]c_v}+\frac{e^z-1}{\left[-1+c_d/c_v\right]c_v}\right\}\right.$$
$$+\frac{\left[\sinh\left(z\sqrt{c_d/c_v}\right)-z\sqrt{c_d/c_v}\cosh\left(x\sqrt{c_d/c_v}\right)\right]}{\left[\sinh\left(x\sqrt{c_d/c_v}\right)-x\sqrt{c_d/c_v}\cosh\left(x\sqrt{c_d/c_v}\right)\right]}\times\left\{\frac{1-\cosh\left(x\sqrt{c_d/c_v}\right)}{\left(-1+c_d/c_v\right)\left(c_d/c_v\right)c_v}+\frac{e^{-x}-1}{\left(-1+c_d/c_v\right)c_v}\right\}$$
$$\left.+\frac{\left[x\sinh\left(z\sqrt{c_d/c_v}\right)-z\sinh\left(x\sqrt{c_d/c_v}\right)\right]}{\left[\sinh\left(x\sqrt{c_d/c_v}\right)-x\sqrt{c_d/c_v}\cosh\left(x\sqrt{c_d/c_v}\right)\right]}\times\left\{\frac{\sinh\left(x\sqrt{c_d/c_v}\right)}{\left(-1+c_d/c_v\right)\sqrt{c_d/c_v}c_v}+\frac{e^{-x}}{\left(-1+c_d/c_v\right)c_v}\right\}\right\}$$
$$-2n_v\sum_{n=1}^{\infty}\frac{\left[\sin\left(\beta_n z/x\right)-\left(\beta_n z/x\right)\cos\beta_n\right]}{x^2\sin\beta_n\left[c_v\left(\beta_n/x\right)^2+c_d\right]}\times\left\{-\frac{1-\cos\beta_n}{\left[1+\left(\beta_n/x\right)^2\right]\left(\beta_n/x\right)^2}+\frac{x\sin\beta_n}{\left[1+\left(\beta_n/x\right)^2\right]\left(\beta_n/x\right)}+\frac{(1+x)e^{-x}-1}{\left[1+\left(\beta_n/x\right)^2\right]}\right\}$$
$$\times\left\{\exp\left[-\left(c_v\left(\beta_n/x\right)^2+c_d\right)t\right]-2\pi\frac{2\pi\exp\left[-\left(c_v\left(\beta_n/x\right)^2+c_d\right)t\right]+\left[c_v\left(\beta_n/x\right)^2+c_d\right]\sin(2\pi t)-2\pi\cos(2\pi t)}{\left[c_v\left(\beta_n/x\right)^2+c_d\right]^2+4\pi^2}\right\}$$

If $c_d = 0$:

$$\psi_{10}^{(0)} = n_v \cos(2\pi t)\left\{\frac{4x^3\left(1-e^z\right)+2z\left(1-e^{-x}\right)\left(3x^2-z^2\right)+(x+z)\left[x^2z(x+z)-2xz(x-z)e^{-x}\right]}{4c_v x^3}\right\}$$
$$-2n_v\sum_{n=1}^{\infty}\frac{\left[\sin\left(\beta_n z/x\right)-\left(\beta_n z/x\right)\cos\beta_n\right]}{x^2\sin\beta_n\left[c_v\left(\beta_n/x\right)^2+c_d\right]}\times\left\{-\frac{1-\cos\beta_n}{\left[1+\left(\beta_n/x\right)^2\right]\left(\beta_n/x\right)^2}+\frac{x\sin\beta_n}{\left[1+\left(\beta_n/x\right)^2\right]\left(\beta_n/x\right)}+\frac{(1+x)e^{-x}-1}{\left[1+\left(\beta_n/x\right)^2\right]}\right\}$$
$$\times\left\{\exp\left[-\left(c_v\left(\beta_n/x\right)^2+c_d\right)t\right]-2\pi\frac{2\pi\exp\left[-\left(c_v\left(\beta_n/x\right)^2+c_d\right)t\right]+\left[c_v\left(\beta_n/x\right)^2+c_d\right]\sin(2\pi t)-2\pi\cos(2\pi t)}{\left[c_v\left(\beta_n/x\right)^2+c_d\right]^2+4\pi^2}\right\}$$

(11) $\psi_{11}^{(0)}$:

$$\psi_{11}^{(0)} = n_v \left\{ \frac{\left[1-\cosh\left(x\sqrt{c_d/c_v}\right)\right]\left[\sinh\left(z\sqrt{c_d/c_v}\right)-z\sqrt{c_d/c_v}\cosh\left(x\sqrt{c_d/c_v}\right)\right]}{c_v\left(c_d/c_v\right)\left(c_d/c_v+\frac{n^2\pi^2}{x^2}\right)\left[\sinh\left(x\sqrt{c_d/c_v}\right)-x\sqrt{c_d/c_v}\cosh\left(x\sqrt{c_d/c_v}\right)\right]} \right.$$

$$+\frac{\left[1-\cosh\left(z\sqrt{c_d/c_v}\right)\right]}{c_v\left(c_d/c_v\right)\left(c_d/c_v+\frac{n^2\pi^2}{x^2}\right)}+\frac{\sinh\left(x\sqrt{c_d/c_v}\right)\left[x\sinh\left(z\sqrt{c_d/c_v}\right)-z\sinh\left(x\sqrt{c_d/c_v}\right)\right]}{c_v\sqrt{c_d/c_v}\left(c_d/c_v+\frac{n^2\pi^2}{x^2}\right)\left[\sinh\left(x\sqrt{c_d/c_v}\right)-x\sqrt{c_d/c_v}\cosh\left(x\sqrt{c_d/c_v}\right)\right]}$$

$$\left.+\frac{x^2}{n^2\pi^2}\frac{\left[1-\cos\left(n\pi z/x\right)\right]}{c_v\left(c_d/c_v+\frac{n^2\pi^2}{x^2}\right)}+\frac{x^2}{n^2\pi^2}\frac{\left[1-(-1)^n\right]\left[\sinh\left(z\sqrt{c_d/c_v}\right)-z\sqrt{c_d/c_v}\cosh\left(x\sqrt{c_d/c_v}\right)\right]}{c_v\left(c_d/c_v+\frac{n^2\pi^2}{x^2}\right)\left[\sinh\left(x\sqrt{c_d/c_v}\right)-x\sqrt{c_d/c_v}\cosh\left(x\sqrt{c_d/c_v}\right)\right]}\right\}\sin\left(2\pi t\right)$$

$$+(2\pi)\frac{2x^3n_v}{n^2\pi^2}\sum_{m=1}^{\infty}\frac{\left[x\sin\left(\beta_m z/x\right)-z\sin\beta_m\right]}{\left(c_v{\beta_m}^2+c_d x^2\right)\left(n^2\pi^2-{\beta_m}^2\right)\sin\beta_m}\left\{\left[1-(-1)^n\right]-\frac{n^2\pi^2}{{\beta_m}^2}\left(1-\cos\beta_m\right)+\frac{n^2\pi^2}{\beta_m}\sin\beta_m\right\}$$

$$\times\frac{-\left(c_v\left(\beta_m/x\right)^2+c_d\right)\exp\left[-\left(c_v\left(\beta_m/x\right)^2+c_d\right)t\right]+\left(c_v\left(\beta_m/x\right)^2+c_d\right)\cos\left(2\pi t\right)+2\pi\sin\left(2\pi t\right)}{\left[c_v\left(\beta_m/x\right)^2+c_d\right]^2+4\pi^2}$$

If $c_d = 0$:

$$\psi_{11}^{(0)} = n_v\frac{x\sin\left(2\pi t\right)\left\{4x^3\left[1-\cos\left(n\pi z/x\right)\right]+2z\left(3x^2-z^2\right)\left[1-(-1)^n\right]-n^2\pi^2z\left(x+z\right)^2\right\}}{4c_v n^4\pi^4}$$

$$+(2\pi)\frac{2x^3n_v}{n^2\pi^2}\sum_{m=1}^{\infty}\frac{\left[x\sin\left(\beta_m z/x\right)-z\sin\beta_m\right]}{\left(c_v{\beta_m}^2+c_d x^2\right)\left(n^2\pi^2-{\beta_m}^2\right)\sin\beta_m}\left\{\left[1-(-1)^n\right]-\frac{n^2\pi^2}{{\beta_m}^2}\left(1-\cos\beta_m\right)+\frac{n^2\pi^2}{\beta_m}\sin\beta_m\right\}$$

$$\times\frac{-\left(c_v\left(\beta_m/x\right)^2+c_d\right)\exp\left[-\left(c_v\left(\beta_m/x\right)^2+c_d\right)t\right]+\left(c_v\left(\beta_m/x\right)^2+c_d\right)\cos\left(2\pi t\right)+2\pi\sin\left(2\pi t\right)}{\left[c_v\left(\beta_m/x\right)^2+c_d\right]^2+4\pi^2}$$

(12) $\psi_{12}^{(0)}$:

$$\psi_{12}^{(0)} = n_v \cos(2\pi t)\left\{ \frac{\left[1-\cosh\left(x\sqrt{c_d/c_v}\right)\right]\left[\sinh\left(z\sqrt{c_d/c_v}\right)-z\sqrt{c_d/c_v}\cosh\left(x\sqrt{c_d/c_v}\right)\right]}{c_v\left(c_d/c_v\right)\left(c_d/c_v+\frac{n^2\pi^2}{x^2}\right)\left[\sinh\left(x\sqrt{c_d/c_v}\right)-x\sqrt{c_d/c_v}\cosh\left(x\sqrt{c_d/c_v}\right)\right]} \right.$$
$$+\frac{\left[1-\cosh\left(z\sqrt{c_d/c_v}\right)\right]}{c_v\left(c_d/c_v\right)\left(c_d/c_v+\frac{n^2\pi^2}{x^2}\right)}+\frac{\sinh\left(x\sqrt{c_d/c_v}\right)\left[x\sinh\left(z\sqrt{c_d/c_v}\right)-z\sinh\left(x\sqrt{c_d/c_v}\right)\right]}{c_v\sqrt{c_d/c_v}\left(c_d/c_v+\frac{n^2\pi^2}{x^2}\right)\left[\sinh\left(x\sqrt{c_d/c_v}\right)-x\sqrt{c_d/c_v}\cosh\left(x\sqrt{c_d/c_v}\right)\right]}$$
$$\left.+\frac{x^2}{n^2\pi^2}\frac{\left[1-\cos\left(n\pi z/x\right)\right]}{c_v\left(c_d/c_v+\frac{n^2\pi^2}{x^2}\right)}+\frac{x^2}{n^2\pi^2}\frac{\left[1-(-1)^n\right]\left[\sinh\left(z\sqrt{c_d/c_v}\right)-z\sqrt{c_d/c_v}\cosh\left(x\sqrt{c_d/c_v}\right)\right]}{c_v\left(c_d/c_v+\frac{n^2\pi^2}{x^2}\right)\left[\sinh\left(x\sqrt{c_d/c_v}\right)-x\sqrt{c_d/c_v}\cosh\left(x\sqrt{c_d/c_v}\right)\right]}\right\}$$
$$+\frac{2x^3 n_v}{n^2\pi^2}\sum_{m=1}^{\infty}\frac{\left[x\sin\left(\beta_m z/x\right)-z\sin\beta_m\right]}{\left(c_v\beta_m{}^2+c_d x^2\right)\left(n^2\pi^2-\beta_m{}^2\right)\sin\beta_m}\left\{\left[1-(-1)^n\right]-\frac{n^2\pi^2}{\beta_m{}^2}\left(1-\cos\beta_m\right)+\frac{n^2\pi^2}{\beta_m}\sin\beta_m\right\}$$
$$\times\left\{\exp\left[-\left(c_v\left(\beta_m/x\right)^2+c_d\right)t\right]-(2\pi)\frac{2\pi\exp\left[-\left(c_v\left(\beta_m/x\right)^2+c_d\right)t\right]-2\pi\cos(2\pi t)+\left[c_v\left(\beta_m/x\right)^2+c_d\right]\sin(2\pi t)}{\left[c_v\left(\beta_m/x\right)^2+c_d\right]^2+4\pi^2}\right\}$$

If $c_d = 0$;

$$\psi_{12}^{(0)} = n_v \frac{x\cos(2\pi t)\left\{4x^3\left[1-\cos\left(n\pi z/x\right)\right]+2z\left(3x^2-z^2\right)\left[1-(-1)^n\right]-n^2\pi^2 z\left(x+z\right)^2\right\}}{4c_v n^4\pi^4}$$
$$+\frac{2x^3 n_v}{n^2\pi^2}\sum_{m=1}^{\infty}\frac{\left[x\sin\left(\beta_m z/x\right)-z\sin\beta_m\right]}{\left(c_v\beta_m{}^2+c_d x^2\right)\left(n^2\pi^2-\beta_m{}^2\right)\sin\beta_m}\left\{\left[1-(-1)^n\right]-\frac{n^2\pi^2}{\beta_m{}^2}\left(1-\cos\beta_m\right)+\frac{n^2\pi^2}{\beta_m}\sin\beta_m\right\}$$
$$\times\left\{\exp\left[-\left(c_v\left(\beta_m/x\right)^2+c_d\right)t\right]-(2\pi)\frac{2\pi\exp\left[-\left(c_v\left(\beta_m/x\right)^2+c_d\right)t\right]-2\pi\cos(2\pi t)+\left[c_v\left(\beta_m/x\right)^2+c_d\right]\sin(2\pi t)}{\left[c_v\left(\beta_m/x\right)^2+c_d\right]^2+4\pi^2}\right\}$$

(13) $\psi_{13}^{(0)}$:

$$\psi_{13}^{(0)}=\frac{n_v\sin(2\pi t)}{\left(c_d+\frac{c_v n^2\pi^2}{x^2}\right)^2}\left\{\left\{\frac{2x}{n\pi}\left(2c_v+c_d x^2/n^2\pi^2\right)\left[1-(-1)^n\right]+\frac{2{c_v}^2 n\pi}{c_d x}\left[1-\cosh\left(x\sqrt{c_d/c_v}\right)\right]\right\}\right.$$
$$\times\left[\frac{\sinh\left(z\sqrt{c_d/c_v}\right)-z\sqrt{c_d/c_v}\cosh\left(x\sqrt{c_d/c_v}\right)}{\sinh\left(x\sqrt{c_d/c_v}\right)-x\sqrt{c_d/c_v}\cosh\left(x\sqrt{c_d/c_v}\right)}\right]$$
$$+\frac{\sin(2\pi t)}{\left(c_d+\frac{c_v n^2\pi^2}{x^2}\right)}\frac{x^2}{n^2\pi^2}\left\{n\pi(-1)^n+\frac{2{c_v}^{3/2}\sinh\left(x\sqrt{c_d/c_v}\right)}{\sqrt{c_d}\left(c_d+c_v\frac{n^2\pi^2}{x^2}\right)}\frac{n^3\pi^3}{x^3}\right\}\times\left[\frac{x\sinh\left(z\sqrt{c_d/c_v}\right)-z\sinh\left(x\sqrt{c_d/c_v}\right)}{\sinh\left(x\sqrt{c_d/c_v}\right)-x\sqrt{c_d/c_v}\cosh\left(x\sqrt{c_d/c_v}\right)}\right]$$
$$\left.+\frac{c_v\sin(2\pi t)}{\left(c_d+\frac{c_v n^2\pi^2}{x^2}\right)^2}\left\{\frac{2x}{n\pi}\left[1-\cos(n\pi z/x)\right]\left(2+\frac{c_d}{c_v}\frac{x^2}{n^2\pi^2}\right)-z\sin(n\pi z/x)\left(1+\frac{c_d}{c_v}\frac{x^2}{n^2\pi^2}\right)+\frac{2c_v n\pi\left[1-\cosh\left(z\sqrt{c_d/c_v}\right)\right]}{c_d x}\right\}\right\}$$
$$-\frac{2c_v n_v(2\pi)}{x^3}\sum_{m=1}^{\infty}\frac{1}{\sin\beta_m}\left[x\sin(\beta_m z/x)-z\sin\beta_m\right]\left[F_{13nm}\big|_{z=-x}+x\frac{\partial F_{13nm}}{\partial z}\Big|_{z=-x}\right]$$

Where

$$F_{13nm}\big|_{z=-x}+x\frac{\partial F_{13nm}}{\partial z}\Big|_{z=-x}$$
$$=\left(-\frac{x^4}{c_v}\right)\left(\frac{x^2}{n^2\pi^2}\right)\frac{1}{\left(n^2\pi^2-{\beta_m}^2\right)\left(-c_v{\beta_m}^2-c_d x^2\right)}\frac{-\left(c_v(\beta_m/x)^2+c_d\right)\exp\left(-\left(c_v(\beta_m/x)^2+c_d\right)t\right)+\left(c_v(\beta_m/x)^2+c_d\right)\cos(2\pi t)+2\pi\sin(2\pi t)}{\left[c_v(\beta_m/x)^2+c_d\right]^2+4\pi^2}\times$$
$$\left\{\frac{2x^2\left(2n^2\pi^2-{\beta_m}^2\right)}{n\pi\left(n^2\pi^2-{\beta_m}^2\right)}\left[(-1)^n-1\right]-n\pi x(-1)^n-\frac{2x^4}{{\beta_m}^2}\left(\frac{n\pi}{x}\right)^3\frac{\sin\beta_m}{\left(n^2\pi^2-{\beta_m}^2\right)}-\frac{2x^5}{{\beta_m}^2}\left(\frac{n\pi}{x}\right)^3\frac{1}{\left(n^2\pi^2-\beta_m^2\right)}(\cos\beta_m-1)\right\}$$

If $c_d=0$:

$$\psi_{13}^{(0)}=\frac{n_v}{2c_v n^5\pi^5}\left\{\left[1-(-1)^n\right]\left(12x^4z-n^2\pi^2x^4z-4x^2z^3\right)-n^2\pi^2x^2z^3\left[1+(-1)^n\right]\right.$$
$$\left.+8x^5\left[1-\cos(n\pi z/x)\right]-2n\pi x^3z\left[x\sin(n\pi z/x)+n\pi z\right]\right\}$$
$$-\frac{2c_v(2\pi)}{x^3}\sum_{m=1}^{\infty}\frac{1}{\sin\beta_m}\left[x\sin(\beta_m z/x)-z\sin\beta_m\right]\left[F_{13nm}\big|_{z=-x}+x\frac{\partial F_{13nm}}{\partial z}\Big|_{z=-x}\right]$$

(14) $\psi_{14}^{(0)}$:

$$\psi_{14}^{(0)}=\frac{n_v\cos(2\pi t)}{\left(c_d+c_v\frac{n^2\pi^2}{x^2}\right)^2}\left\{\left\{\frac{2x}{n\pi}\left(2c_v+c_dx^2/n^2\pi^2\right)\left[1-(-1)^n\right]+\frac{2{c_v}^2n\pi}{c_dx}\left[1-\cosh\left(x\sqrt{c_d/c_v}\right)\right]\right\}\right.$$
$$\times\left[\frac{\sinh\left(z\sqrt{c_d/c_v}\right)-z\sqrt{c_d/c_v}\cosh\left(x\sqrt{c_d/c_v}\right)}{\sinh\left(x\sqrt{c_d/c_v}\right)-x\sqrt{c_d/c_v}\cosh\left(x\sqrt{c_d/c_v}\right)}\right]$$
$$+\frac{\cos(2\pi t)}{\left(c_d+c_v\frac{n^2\pi^2}{x^2}\right)}\frac{x^2}{n^2\pi^2}\left\{n\pi(-1)^n+\frac{2{c_v}^{3/2}\sinh\left(x\sqrt{c_d/c_v}\right)}{\sqrt{c_d}\left(c_d+c_v\frac{n^2\pi^2}{x^2}\right)}\frac{n^3\pi^3}{x^3}\right\}\times\left[\frac{x\sinh\left(z\sqrt{c_d/c_v}\right)-z\sinh\left(x\sqrt{c_d/c_v}\right)}{\sinh\left(x\sqrt{c_d/c_v}\right)-x\sqrt{c_d/c_v}\cosh\left(x\sqrt{c_d/c_v}\right)}\right]$$
$$\left.+\frac{c_v}{\left(c_d+\frac{c_vn^2\pi^2}{x^2}\right)^2}\left\{\frac{2x}{n\pi}\left[1-\cos(n\pi z/x)\right]\left(2+\frac{c_d}{c_v}\frac{x^2}{n^2\pi^2}\right)-z\sin(n\pi z/x)\left(1+\frac{c_d}{c_v}\frac{x^2}{n^2\pi^2}\right)+\frac{2c_vn\pi\left[1-\cosh\left(z\sqrt{c_d/c_v}\right)\right]}{c_dx}\right\}\right\}$$
$$-\frac{2n_vc_v}{x^3}\sum_{m=1}^{\infty}\frac{1}{\sin\beta_m}\left[x\sin(\beta_mz/x)-z\sin\beta_m\right]\left[F_{14nm}\big|_{z=-x}+x\frac{\partial F_{14nm}}{\partial z}\Big|_{z=-x}\right]$$

Where

$$F_{14nm}\big|_{z=-x}+x\frac{\partial F_{14nm}}{\partial z}\Big|_{z=-x}$$
$$=\left(-\frac{x^4}{\sigma}\right)\left(\frac{x^2}{n^2\pi^2}\right)\frac{1}{\left(n^2\pi^2-{\beta_m}^2\right)\left(-c_v{\beta_m}^2-c_dx^2\right)}\left[\exp\left(-\left(c_v(\beta_m/x)^2+c_d\right)t\right)-(2\pi)\frac{2\pi\exp\left(-\left(c_v(\beta_m/x)^2+c_d\right)t\right)-2\pi\cos(2\pi t)+\left[c_v(\beta_m/x)^2+c_d\right]\sin(2\pi t)}{\left[c_v(\beta_m/x)^2+c_d\right]^2+4\pi^2}\right]\times$$
$$\left\{\frac{2x^2\left(2n^2\pi^2-{\beta_m}^2\right)}{n\pi\left(n^2\pi^2-{\beta_m}^2\right)}\left[(-1)^n-1\right]-n\pi x(-1)^n-\frac{2x^4}{\beta_m}\left(\frac{n\pi}{x}\right)^3\frac{\sin\beta_m}{\left(n^2\pi^2-{\beta_m}^2\right)}-\frac{2x^5}{{\beta_m}^2}\left(\frac{n\pi}{x}\right)^3\frac{1}{\left(n^2\pi^2-\beta_m^2\right)}(\cos\beta_m-1)\right\}$$

If $c_d=0$:

$$\psi_{14}^{(0)}=\frac{n_v}{2c_vn^5\pi^5}\left\{\left[1-(-1)^n\right]\left(12x^4z-n^2\pi^2x^4z-4x^2z^3\right)-n^2\pi^2x^2z^3\left[1+(-1)^n\right]\right.$$
$$\left.+8x^5\left[1-\cos(n\pi z/x)\right]-2n\pi x^3z\left[x\sin(n\pi z/x)+n\pi z\right]\right\}$$
$$-\frac{2n_vc_v}{x^3}\sum_{m=1}^{\infty}\frac{1}{\sin\beta_m}\left[x\sin(\beta_mz/x)-z\sin\beta_m\right]\left[F_{14nm}\big|_{z=-x}+x\frac{\partial F_{14nm}}{\partial z}\Big|_{z=-x}\right]$$

(15) $\psi_{15}^{(0)}$:

$$\psi_{15}^{(0)}=\frac{n_v\left[\sinh\left(z\sqrt{\left(-c_k n^2\pi^2/x^2+c_d\right)/c_v}\right)-z\sqrt{\left(-c_k n^2\pi^2/x^2+c_d\right)/c_v}\cosh\left(x\sqrt{\left(-c_k n^2\pi^2/x^2+c_d\right)/c_v}\right)\right]}{\left[\sinh\left(x\sqrt{\left(-c_k n^2\pi^2/x^2+c_d\right)/c_v}\right)-x\sqrt{\left(-c_k n^2\pi^2/x^2+c_d\right)/c_v}\cosh\left(x\sqrt{\left(-c_k n^2\pi^2/x^2+c_d\right)/c_v}\right)\right]}F_{15n0}\Big|_{z=-x}$$
$$+\frac{n_v\left[x\sinh\left(z\sqrt{\left(-c_k n^2\pi^2/x^2+c_d\right)/c_v}\right)-z\sinh\left(x\sqrt{\left(-c_k n^2\pi^2/x^2+c_d\right)/c_v}\right)\right]}{\left[\sinh\left(x\sqrt{\left(-c_k n^2\pi^2/x^2+c_d\right)/c_v}\right)-x\sqrt{\left(-c_k n^2\pi^2/x^2+c_d\right)/c_v}\cosh\left(x\sqrt{\left(-c_k n^2\pi^2/x^2+c_d\right)/c_v}\right)\right]}\frac{\partial F_{15n0}}{\partial z}\Big|_{z=-x}$$
$$+n_v F_{15n0}+\frac{2n_v c_v}{x^3}\sum_{m=1}^{\infty}\frac{1}{\sin\beta_m}\left[x\sin\left(\beta_m z/x\right)-z\sin\beta_m\right]\left[F_{15nm}\Big|_{z=-x}+x\frac{\partial F_{15nm}}{\partial z}\Big|_{z=-x}\right]$$

Where

$$F_{15n0}=-\frac{1}{c_v-c_k+c_d x^2/(n\pi)^2}\left(\frac{x}{n\pi}\right)^4\left\{\left[\cos(n\pi z/x)-1\right]-\frac{c_v}{\left(c_k-c_d x^2/(n\pi)^2\right)}\left[\cosh\left(z\sqrt{\left(-n^2\pi^2c_k/x^2+c_d\right)/c_v}\right)-1\right]\right\}\times\exp\left[-(n\pi/x)^2c_k t\right]$$

$$F_{15nm}\Big|_{z=-x}+x\frac{\partial F_{15nm}}{\partial z}\Big|_{z=-x}=\frac{x^4}{c_v}\left(\frac{x}{n\pi}\right)^2\frac{\exp\left[-\left(c_v(\beta/x)^2+c_d\right)t\right]}{\left(n^2\pi^2-\beta^2\right)\left(c_k n^2\pi^2-c_v\beta^2-c_d x^2\right)}\times\left\{\left[(-1)^n-1\right]-\frac{n^2\pi^2}{\beta^2}(\cos\beta-1)-n^2\pi^2\cos\beta\right\}$$

If $c_d=0$:

$$\psi_{15}^{(0)}=\frac{n_v}{4c_v n^4\pi^4}\left\{4x^4\left[1-\cos(n\pi z/x)\right]+2xz\left(3x^2-z^2\right)\left(1-(-1)^n\right)-xzn^2\pi^2(x+z)^2\right\}\exp\left[-(n\pi/x)^2c_k t\right]$$
$$+\frac{2n_v c_v}{x^3}\sum_{m=1}^{\infty}\frac{1}{\sin\beta_m}\left[x\sin\left(\beta_m z/x\right)-z\sin\beta_m\right]\left[F_{15nm}\Big|_{z=-x}+x\frac{\partial F_{15nm}}{\partial z}\Big|_{z=-x}\right]$$

(16) $\psi_{16}^{(0)}$:

$$\psi_{16}^{(0)}=\frac{n_v\left[\sinh\left(z\sqrt{\left(-c_k n^2\pi^2/x^2+c_d\right)/c_v}\right)-z\sqrt{\left(-c_k n^2\pi^2/x^2+c_d\right)/c_v}\cosh\left(x\sqrt{\left(-c_k n^2\pi^2/x^2+c_d\right)/c_v}\right)\right]}{\left[\sinh\left(x\sqrt{\left(-c_k n^2\pi^2/x^2+c_d\right)/c_v}\right)-x\sqrt{\left(-c_k n^2\pi^2/x^2+c_d\right)/c_v}\cosh\left(x\sqrt{\left(-c_k n^2\pi^2/x^2+c_d\right)/c_v}\right)\right]}F_{16n0}\Big|_{z=-x}$$
$$+\frac{n_v\left[x\sinh\left(z\sqrt{\left(-c_k n^2\pi^2/x^2+c_d\right)/c_v}\right)-z\sinh\left(x\sqrt{\left(-c_k n^2\pi^2/x^2+c_d\right)/c_v}\right)\right]}{\left[\sinh\left(x\sqrt{\left(-c_k n^2\pi^2/x^2+c_d\right)/c_v}\right)-x\sqrt{\left(-c_k n^2\pi^2/x^2+c_d\right)/c_v}\cosh\left(x\sqrt{\left(-c_k n^2\pi^2/x^2+c_d\right)/c_v}\right)\right]}\frac{\partial F_{16n0}}{\partial z}\Big|_{z=-x}$$
$$+n_v F_{16n0}+\frac{2n_v c_v}{x^3}\sum_{m=1}^{\infty}\frac{1}{\sin\beta_m}\left[x\sin\left(\beta_m z/x\right)-z\sin\beta_m\right]\left[F_{16nm}\Big|_{z=-x}+x\frac{\partial F_{16nm}}{\partial z}\Big|_{z=-x}\right]$$

Where

$$F_{16n0}=-\frac{1}{c_v-c_k+c_d x^2/(n\pi)^2}\left(\frac{x}{n\pi}\right)^4\left\{\left[\cos(n\pi z/x)-1\right]-\frac{c_v}{\left(c_k-c_d x^2/(n\pi)^2\right)}\left[\cosh\left(z\sqrt{\frac{-n^2\pi^2c_k/x^2+c_d}{c_v}}\right)-1\right]\right\}\times t\exp\left[-(n\pi/x)^2c_k t\right]$$

$$F_{16nm}|_{z=-x}+x\left.\frac{\partial F_{16nm}}{\partial z}\right|_{z=-x}=\frac{x^6}{c_v}\left(\frac{x}{n\pi}\right)^2\frac{\exp\left[-\left(c_v(\beta/x)^2+c_d\right)t\right]-\exp\left[-c_k(n\pi/x)^2t\right]}{\left(n^2\pi^2-\beta^2\right)\left(c_k n^2\pi^2-c_v\beta^2-c_d x^2\right)}\times\left\{\left[(-1)^n-1\right]-\frac{n^2\pi^2}{\beta^2}(\cos\beta-1)-n^2\pi^2\cos\beta\right\}$$

If $c_d=0$:

$$\psi_{16}^{(0)}=\frac{1}{4c_v n^4\pi^4}\left\{4x^4\left[1-\cos(n\pi z/x)\right]+2xz\left(3x^2-z^2\right)\left(1-(-1)^n\right)-xzn^2\pi^2(x+z)^2\right\}t\exp\left[-(n\pi/x)^2c_k t\right]$$
$$+n_v G_{16n0}+\frac{2n_v c_v}{x^3}\sum_{m=1}^{\infty}\frac{1}{\sin\beta_m}\left[x\sin(\beta_m z/x)-z\sin\beta_m\right]\left[F_{16nm}|_{z=-x}+x\left.\frac{\partial F_{16nm}}{\partial z}\right|_{z=-x}\right]$$

(17) $\psi_{17}^{(0)}$:

$$\psi_{17}^{(0)}=n_v\frac{\sinh\left(z\sqrt{\left(-c_k n^2\pi^2/x^2+c_d\right)/c_v}\right)-z\sqrt{\left(-c_k n^2\pi^2/x^2+c_d\right)/c_v}\cosh\left(x\sqrt{\left(-c_k n^2\pi^2/x^2+c_d\right)/c_v}\right)}{\sinh\left(x\sqrt{\left(-c_k n^2\pi^2/x^2+c_d\right)/c_v}\right)-x\sqrt{\left(-c_k n^2\pi^2/x^2+c_d\right)/c_v}\cosh\left(x\sqrt{\left(-c_k n^2\pi^2/x^2+c_d\right)/c_v}\right)}F_{17n0}|_{z=-x}$$
$$+\frac{n_v x\sinh\left(z\sqrt{\left(-c_k n^2\pi^2/x^2+c_d\right)/c_v}\right)-z\sinh\left(x\sqrt{\left(-c_k n^2\pi^2/x^2+c_d\right)/c_v}\right)}{\sinh\left(x\sqrt{\left(-c_k n^2\pi^2/x^2+c_d\right)/c_v}\right)-x\sqrt{\left(-c_k n^2\pi^2/x^2+c_d\right)/c_v}\cosh\left(x\sqrt{\left(-c_k n^2\pi^2/x^2+c_d\right)/c_v}\right)}\left.\frac{\partial F_{17n0}}{\partial z}\right|_{z=-x}$$
$$-\frac{n_v}{\left(c_v+c_d\frac{x^2}{n^2\pi^2}-c_k\right)}\left(\frac{x^4}{n^4\pi^4}\right)\times\exp\left[-c_k(n\pi/x)^2t\right]$$
$$\times\left\{\frac{2x}{n\pi}\frac{2c_v-\left(c_k-c_d x^2/n^2\pi^2\right)}{\left(c_v+c_d\frac{x^2}{n^2\pi^2}-c_k\right)}\left[\cos(n\pi z/x)-1\right]+z\sin(n\pi z/x)-\frac{2c_v^2}{\left(c_v+c_d\frac{x^2}{n^2\pi^2}-c_k\right)\left(c_k-c_d x^2/n^2\pi^2\right)}\left(\frac{x}{n\pi}\right)\left[\cosh\left(z\sqrt{\frac{-c_k n^2\pi^2/x^2+c_d}{c_v}}\right)-1\right]\right\}$$
$$+\frac{2n_v c_v}{x^3}\sum_{m=1}^{\infty}\frac{1}{\sin\beta_m}\left[x\sin(\beta_m z/x)-z\sin\beta_m\right]\left[F_{6nm}|_{z=-x}+x\left.\frac{\partial F_{6nm}}{\partial z}\right|_{z=-x}\right]$$

Where

$$F_{17n0} = -\frac{1}{\left(c_v + c_d\frac{x^2}{n^2\pi^2} - c_k\right)}\left(\frac{x^4}{n^4\pi^4}\right)\times\exp\left[-c_k\left(n\pi/x\right)^2 t\right]$$
$$\times\left\{\frac{2x}{n\pi}\frac{2c_v - \left(c_k - c_d x^2/n^2\pi^2\right)}{\left(c_v + c_d\frac{x^2}{n^2\pi^2} - c_k\right)}\left[\cos\left(n\pi z/x\right)-1\right] + z\sin\left(n\pi z/x\right) - \frac{2{c_v}^2}{\left(c_v + c_d\frac{x^2}{n^2\pi^2} - c_k\right)\left(c_k - c_d x^2/n^2\pi^2\right)}\left(\frac{x}{n\pi}\right)\left[\cosh\left(z\sqrt{\frac{-c_k n^2\pi^2/x^2 + c_d}{c_v}}\right)-1\right]\right\}$$

$$F_{17nm}\big|_{z=-x} + x\frac{\partial F_{17nm}}{\partial z}\bigg|_{z=-x}$$
$$= \left(-\frac{x^4}{c_v}\right)\left(\frac{x^2}{n^2\pi^2}\right)\frac{\exp\left(-\left(c_v\left(\beta/x\right)^2 + c_d\right)t\right)}{\left(n^2\pi^2 - \beta^2\right)\left(c_k n^2\pi^2 - c_v\beta^2 - c_d x^2\right)}\times$$
$$\left\{\frac{2x^2\left(2n^2\pi^2 - \beta^2\right)}{n\pi\left(n^2\pi^2 - \beta^2\right)}\left[\left(-1\right)^n - 1\right] - n\pi x\left(-1\right)^n - \frac{2x^4}{\beta}\left(\frac{n\pi}{x}\right)^3\frac{\sin\beta}{\left(n^2\pi^2 - \beta^2\right)} - \frac{2x^5}{\beta^2}\left(\frac{n\pi}{x}\right)^3\frac{1}{\left(n^2\pi^2 - \beta^2\right)}\left(\cos\beta - 1\right)\right\}$$

If $c_d = 0$:

$$\psi_{17}^{(0)} = \frac{n_v}{2c_v n^5\pi^5}\left\{\left[1-\left(-1\right)^n\right]\left(12x^4 z - n^2\pi^2 x^4 z - 4x^2 z^3\right) - n^2\pi^2 x^2 z^3\left[1+\left(-1\right)^n\right]\right.$$
$$\left. + 8x^5\left[1-\cos\left(n\pi z/x\right)\right] - 2n\pi x^3 z\left[x\sin\left(n\pi z/x\right) + n\pi z\right]\right\}\exp\left(-n^2\pi^2 Dt/x^2\right)$$
$$+\frac{2n_v c_v}{x^3}\sum_{m=1}^{\infty}\frac{1}{\sin\beta_m}\left[x\sin\left(\beta_m z/x\right) - z\sin\beta_m\right]\left[F_{17nm}\big|_{z=-x} + x\frac{\partial F_{17nm}}{\partial z}\bigg|_{z=-x}\right]$$

(18) $\psi_{18}^{(0)}$:

$$\psi_{18}^{(0)}(x,z,t)=n_v\sin(2m\pi t)\left\{\frac{\sinh\left(z\sqrt{c_d/c_v}\right)-z\sqrt{c_d/c_v}\cosh\left(x\sqrt{c_d/c_v}\right)}{\sinh\left(x\sqrt{c_d/c_v}\right)-x\sqrt{c_d/c_v}\cosh\left(x\sqrt{c_d/c_v}\right)}\left\{\frac{x^2}{2c_v(c_d/c_v)}-\frac{1}{c_v(c_d/c_v)^2}\left[\cosh\left(x\sqrt{c_d/c_v}\right)-1\right]\right\}\right.$$
$$-\frac{x\sinh\left(z\sqrt{c_d/c_v}\right)-z\sinh\left(x\sqrt{c_d/c_v}\right)}{\sinh\left(x\sqrt{c_d/c_v}\right)-x\sqrt{c_d/c_v}\cosh\left(x\sqrt{c_d/c_v}\right)}\left\{\frac{x}{c_v(c_d/c_v)}-\frac{1}{c_v(c_d/c_v)^2}\sqrt{c_d/c_v}\sinh\left(x\sqrt{c_d/c_v}\right)\right\}$$
$$\left.+\frac{1}{2}\frac{z^2}{c_v(c_d/c_v)}-\frac{1}{c_v(c_d/c_v)^2}\left[\cosh\left(z\sqrt{c_d/c_v}\right)-1\right]\right\}$$
$$+\frac{2n_vx^3}{c_v}(2m\pi)\sum_{n=1}^{\infty}\left\{\frac{1}{\beta_n^2\left(\beta_n^2+(c_d/c_v)x^2\right)\sin\beta_n}\left[\left(x\sin(\beta_nz/x)-z\sin\beta_n\right)\left(\cos\beta_n+(\cos\beta_n-1)/\beta_n^2-\frac{1}{2}\right)\right]\right.$$
$$\left.\times\left\{\frac{\left[c_v(\beta_n/x)^2+c_d\right]\exp\left[-\left(c_v(\beta_n/x)^2+c_d\right)t\right]-\left[c_v(\beta_n/x)^2+c_d\right]\cos(2m\pi t)-2m\pi\sin(2m\pi t)}{\left[c_v(\beta_n/x)^2+c_d\right]^2+4m^2\pi^2}\right\}\right.$$

If $c_d=0$:

$$\psi_{18}^{(0)}=n_v\frac{z(x+z)^2(x-2z)\sin(2m\pi t)}{48c_v}$$
$$+\frac{2n_vx^3}{c_v}(2m\pi)\sum_{n=1}^{\infty}\left\{\frac{1}{\beta_n^2\left(\beta_n^2+(c_d/c_v)x^2\right)\sin\beta_n}\left[\left(x\sin(\beta_nz/x)-z\sin\beta_n\right)\left(\cos\beta_n+(\cos\beta_n-1)/\beta_n^2-\frac{1}{2}\right)\right]\right.$$
$$\left.\times\left\{\frac{\left[c_v(\beta_n/x)^2+c_d\right]\exp\left[-\left(c_v(\beta_n/x)^2+c_d\right)t\right]-\left[c_v(\beta_n/x)^2+c_d\right]\cos(2m\pi t)-2m\pi\sin(2m\pi t)}{\left[c_v(\beta_n/x)^2+c_d\right]^2+4m^2\pi^2}\right\}\right.$$

(19) $\psi_{19}^{(0)}$:

$$\psi_{19}^{(0)}(x,z,t)=n_v\cos(2m\pi t)\left\{\frac{\sinh\left(z\sqrt{c_d/c_v}\right)-z\sqrt{c_d/c_v}\cosh\left(x\sqrt{c_d/c_v}\right)}{\sinh\left(x\sqrt{c_d/c_v}\right)-x\sqrt{c_d/c_v}\cosh\left(x\sqrt{c_d/c_v}\right)}\left\{\frac{x^2}{2c_v(c_d/c_v)}-\frac{1}{c_v(c_d/c_v)^2}\left[\cosh\left(x\sqrt{c_d/c_v}\right)-1\right]\right\}\right.$$
$$-\frac{x\sinh\left(z\sqrt{c_d/c_v}\right)-z\sinh\left(x\sqrt{c_d/c_v}\right)}{\sinh\left(x\sqrt{c_d/c_v}\right)-x\sqrt{c_d/c_v}\cosh\left(x\sqrt{c_d/c_v}\right)}\left\{\frac{x}{c_v(c_d/c_v)}-\frac{1}{c_v(c_d/c_v)^2}\sqrt{c_d/c_v}\sinh\left(x\sqrt{c_d/c_v}\right)\right\}$$
$$\left.+\frac{1}{2}\frac{z^2}{c_v(c_d/c_v)}-\frac{1}{c_v(c_d/c_v)^2}\left[\cosh\left(z\sqrt{c_d/c_v}\right)-1\right]\right\}$$
$$-\frac{2n_vx^3}{c_v}\sum_{n=1}^{\infty}\left\{\frac{1}{\beta_n^2\left(\beta_n^2+(c_d/c_v)x^2\right)\sin\beta_n}\left[\left(x\sin(\beta_nz/x)-z\sin\beta_n\right)\left(\cos\beta_n+(\cos\beta_n-1)/\beta_n^2-\frac{1}{2}\right)\right]\right.$$
$$\times\left\{\exp\left[-\left(c_v(\beta_n/x)^2+c_d\right)t\right]\right.$$
$$\left.\left.+2m\pi\frac{-2m\pi\exp\left[-\left(c_v(\beta_n/x)^2+c_d\right)t\right]-\left[c_v(\beta_n/x)^2+c_d\right]\sin(2m\pi t)+2m\pi\cos(2m\pi t)}{\left[c_v(\beta_n/x)^2+c_d\right]^2+4m^2\pi^2}\right\}\right\}$$

If $c_d=0$:

$$\psi_{19}^{(0)}=n_v\frac{z(x+z)^2(x-2z)\cos(2m\pi t)}{48c_v}$$
$$-\frac{2n_vx^3}{c_v}\sum_{n=1}^{\infty}\left\{\frac{1}{\beta_n^2\left(\beta_n^2+(c_d/c_v)x^2\right)\sin\beta_n}\left[\left(x\sin(\beta_nz/x)-z\sin\beta_n\right)\left(\cos\beta_n+(\cos\beta_n-1)/\beta_n^2-\frac{1}{2}\right)\right]\right.$$
$$\left.\times\left\{\exp\left[-\left(c_v(\beta_n/x)^2+c_d\right)t\right]+2m\pi\frac{-2m\pi\exp\left[-\left(c_v(\beta_n/x)^2+c_d\right)t\right]-\left[c_v(\beta_n/x)^2+c_d\right]\sin(2m\pi t)+2m\pi\cos(2m\pi t)}{\left[c_v(\beta_n/x)^2+c_d\right]^2+4m^2\pi^2}\right\}\right\}$$

(20) $\psi_{20}^{(0)}$:

$$\psi_{20}^{(0)}=n_v\cos(2m\pi t)\left\{\frac{\left[x\sinh\left(z\sqrt{c_d/c_v}\right)-z\sinh\left(x\sqrt{c_d/c_v}\right)\right]}{\left[\sinh\left(x\sqrt{c_d/c_v}\right)-x\sqrt{c_d/c_v}\cosh\left(x\sqrt{c_d/c_v}\right)\right]}\times\left\{\frac{x^2}{3(c_d/c_v)c_v}\right\}+\frac{z^3}{6(c_d/c_v)c_v}-\frac{x^2z}{6(c_d/c_v)c_v}\right\}$$
$$-\frac{2n_vx^3}{3}\sum_{n=1}^{\infty}\frac{\left[\sin(\beta_nz/x)-(\beta_nz/x)\cos\beta_n\right]}{\beta_n^2\left[c_v(\beta_n/x)^2+c_d\right]\sin\beta_n}$$
$$\times\left\{\exp\left[-\left(c_v(\beta_n/x)^2+c_d\right)t\right]-2m\pi\frac{2m\pi\exp\left[-\left(c_v(\beta_n/x)^2+c_d\right)t\right]+\left[c_v(\beta_n/x)^2+c_d\right]\sin(2m\pi t)-2m\pi\cos(2m\pi t)}{\left[c_v(\beta_n/x)^2+c_d\right]^2+4m^2\pi^2}\right\}$$

If $c_d = 0$:

$$\psi_{20}^{(0)} = -n_v \cos(2\pi t) z\left(x^2 - z^2\right)^2 - \frac{2n_v x^3}{3} \sum_{n=1}^{\infty} \frac{\left[\sin(\beta_n z/x) - (\beta_n z/x)\cos\beta_n\right]}{\beta_n{}^2\left[c_v(\beta_n/x)^2 + c_d\right]\sin\beta_n} \times \left\{ \exp\left[-\left(c_v(\beta_n/x)^2 + c_d\right)t\right] - 2m\pi \frac{2m\pi \exp\left[-\left(c_v(\beta_n/x)^2 + c_d\right)t\right] + \left[c_v(\beta_n/x)^2 + c_d\right]\sin(2m\pi t) - 2m\pi\cos(2m\pi t)}{\left[c_v(\beta_n/x)^2 + c_d\right]^2 + 4m^2\pi^2} \right\}$$

(21) $\psi_{21}^{(0)}$:

$$\psi_{21}^{(0)} = n_v \cos(2m\pi t) \left\{ \frac{12z^2(c_d/c_v) - 24\left[\cosh\left(z\sqrt{c_d/c_v}\right) - 1\right] + z^4(c_d/c_v)^2}{12c_v(c_d/c_v)^3} + \frac{\left[\sinh\left(z\sqrt{c_d/c_v}\right) - z\sqrt{c_d/c_v}\cosh\left(x\sqrt{c_d/c_v}\right)\right]}{\left[\sinh\left(x\sqrt{c_d/c_v}\right) - x\sqrt{c_d/c_v}\cosh\left(x\sqrt{c_d/c_v}\right)\right]} \times \left\{ \frac{12x^2(c_d/c_v) - 24\left[\cosh\left(x\sqrt{c_d/c_v}\right) - 1\right] + x^4(c_d/c_v)^2}{12c_v(c_d/c_v)^3} \right\} + \frac{\left[x\sinh\left(z\sqrt{c_d/c_v}\right) - z\sinh\left(x\sqrt{c_d/c_v}\right)\right]}{\left[\sinh\left(x\sqrt{c_d/c_v}\right) - x\sqrt{c_d/c_v}\cosh\left(x\sqrt{c_d/c_v}\right)\right]} \times \left\{ \frac{6\sqrt{c_d/c_v}\left[\sinh\left(x\sqrt{c_d/c_v}\right) - x\sqrt{c_d/c_v}\right] - x^3(c_d/c_v)^2}{3c_v(c_d/c_v)^3} \right\} \right\} - \frac{2n_v x^5}{c_v} \sum_{n=1}^{\infty} \frac{1}{\beta_n^6 \sin\beta_n \left[1 + c_d x^2/\left(c_v\beta_n^2\right)\right]} \left[x\sin(\beta_n z/x) - z\sin\beta_n\right]\left(1 - \beta_n^2/4 - 2\cos\beta_n - 2(\cos\beta_n - 1)/\beta_n^2\right) \times \left\{ \exp\left[-\left(c_v\beta_n^2/x^2 + c_d\right)t\right] - 2m\pi \frac{2m\pi\exp\left[-\left(c_v\beta_n^2/x^2 + c_d\right)t\right] - 2m\pi\cos(2m\pi t) + \left(c_v\beta_n^2/x^2 + c_d\right)\sin(2m\pi t)}{\left(c_v\beta_n^2/x^2 + c_d\right)^2 + 4m^2\pi^2} \right\}$$

If $c_d = 0$:

$$\psi_{21}^{(0)} = \frac{n_v \cos(2m\pi t)}{720c_v} z(x+z)^2\left(3x^3 - 6x^2 z + 4xz^2 - 2z^3\right) - \frac{2n_v x^5}{c_v} \sum_{n=1}^{\infty} \frac{1}{\beta_n^6 \sin\beta_n \left[1 + c_d x^2/\left(c_v\beta_n^2\right)\right]} \left[x\sin(\beta_n z/x) - z\sin\beta_n\right]\left(1 - \beta_n^2/4 - 2\cos\beta_n - 2(\cos\beta_n - 1)/\beta_n^2\right) \times \left\{ \exp\left[-\left(c_v\beta_n^2/x^2 + c_d\right)t\right] - 2m\pi \frac{2m\pi\exp\left[-\left(c_v\beta_n^2/x^2 + c_d\right)t\right] - 2m\pi\cos(2m\pi t) + \left(c_v\beta_n^2/x^2 + c_d\right)\sin(2m\pi t)}{\left(c_v\beta_n^2/x^2 + c_d\right)^2 + 4m^2\pi^2} \right\}$$

(22) $\psi_{22}^{(0)}$:

$$\psi_{22}^{(0)} = n_v \cos(2m\pi t)\left\{\left\{\frac{1-\cosh\left(z\sqrt{c_d/c_v}\right)}{\left[-1+c_d/c_v\right]\left[c_d/c_v\right]c_v}+\frac{e^z-1}{\left[-1+c_d/c_v\right]c_v}\right\}\right.$$
$$+\frac{\left[\sinh\left(z\sqrt{c_d/c_v}\right)-z\sqrt{c_d/c_v}\cosh\left(x\sqrt{c_d/c_v}\right)\right]}{\left[\sinh\left(x\sqrt{c_d/c_v}\right)-x\sqrt{c_d/c_v}\cosh\left(x\sqrt{c_d/c_v}\right)\right]}\times\left\{\frac{1-\cosh\left(x\sqrt{c_d/c_v}\right)}{\left(-1+c_d/c_v\right)\left(c_d/c_v\right)c_v}+\frac{e^{-x}-1}{\left(-1+c_d/c_v\right)c_v}\right\}$$
$$\left.+\frac{\left[x\sinh\left(z\sqrt{c_d/c_v}\right)-z\sinh\left(x\sqrt{c_d/c_v}\right)\right]}{\left[\sinh\left(x\sqrt{c_d/c_v}\right)-x\sqrt{c_d/c_v}\cosh\left(x\sqrt{c_d/c_v}\right)\right]}\times\left\{\frac{\sinh\left(x\sqrt{c_d/c_v}\right)}{\left(-1+c_d/c_v\right)\sqrt{c_d/c_v}c_v}+\frac{e^{-x}}{\left(-1+c_d/c_v\right)c_v}\right\}\right\}$$
$$-\frac{2n_v}{x^2}\sum_{n=1}^{\infty}\frac{\left[\sin\left(\beta_n z/x\right)-\left(\beta_n z/x\right)\cos\beta_n\right]}{\sin\beta_n\left[c_v\left(\beta_n/x\right)^2+c_d\right]}\times\left\{-\frac{1-\cos\beta_n}{\left[1+\left(\beta_n/x\right)^2\right]\left(\beta_n/x\right)^2}+\frac{x\sin\beta_n}{\left[1+\left(\beta_n/x\right)^2\right]\left(\beta_n/x\right)}+\frac{(1+x)e^{-x}-1}{\left[1+\left(\beta_n/x\right)^2\right]}\right\}$$
$$\times\left\{\exp\left[-\left(c_v\left(\beta_n/x\right)^2+c_d\right)t\right]-2m\pi\frac{2m\pi\exp\left[-\left(c_v\left(\beta_n/x\right)^2+c_d\right)t\right]+\left[c_v\left(\beta_n/x\right)^2+c_d\right]\sin\left(2m\pi t\right)-2m\pi\cos\left(2m\pi t\right)}{\left[c_v\left(\beta_n/x\right)^2+c_d\right]^2+4m^2\pi^2}\right\}$$

If $c_d = 0$:

$$\psi_{22}^{(0)} = n_v \cos(2m\pi t)\left\{\frac{4x^3\left(1-e^z\right)+2z\left(1-e^{-x}\right)\left(3x^2-z^2\right)+(x+z)\left[x^2z(x+z)-2xz(x-z)e^{-x}\right]}{4c_v x^3}\right\}$$
$$-\frac{2n_v}{x^2}\sum_{n=1}^{\infty}\frac{\left[\sin\left(\beta_n z/x\right)-\left(\beta_n z/x\right)\cos\beta_n\right]}{\sin\beta_n\left[c_v\left(\beta_n/x\right)^2+c_d\right]}\times\left\{-\frac{1-\cos\beta_n}{\left[1+\left(\beta_n/x\right)^2\right]\left(\beta_n/x\right)^2}+\frac{x\sin\beta_n}{\left[1+\left(\beta_n/x\right)^2\right]\left(\beta_n/x\right)}+\frac{(1+x)e^{-x}-1}{\left[1+\left(\beta_n/x\right)^2\right]}\right\}$$
$$\times\left\{\exp\left[-\left(c_v\left(\beta_n/x\right)^2+c_d\right)t\right]-2\pi\frac{2\pi\exp\left[-\left(c_v\left(\beta_n/x\right)^2+c_d\right)t\right]+\left[c_v\left(\beta_n/x\right)^2+c_d\right]\sin\left(2\pi t\right)-2\pi\cos\left(2\pi t\right)}{\left[c_v\left(\beta_n/x\right)^2+c_d\right]^2+4\pi^2}\right\}$$

(23) $\psi_{23}^{(0)}$:

$$\psi_{23}^{(0)} = n_v \left\{ \frac{\left[1-\cosh\left(x\sqrt{c_d/c_v}\right)\right]\left[\sinh\left(z\sqrt{c_d/c_v}\right)-z\sqrt{c_d/c_v}\cosh\left(x\sqrt{c_d/c_v}\right)\right]}{c_v\left(c_d/c_v\right)\left(\frac{c_d}{c_v}+\frac{n^2\pi^2}{x^2}\right)\left[\sinh\left(x\sqrt{c_d/c_v}\right)-x\sqrt{c_d/c_v}\cosh\left(x\sqrt{c_d/c_v}\right)\right]} \right.$$
$$+\frac{\left[1-\cosh\left(z\sqrt{c_d/c_v}\right)\right]}{c_v\left(c_d/c_v\right)\left(\frac{c_d}{c_v}+\frac{n^2\pi^2}{x^2}\right)}+\frac{\sinh\left(x\sqrt{c_d/c_v}\right)\left[x\sinh\left(z\sqrt{c_d/c_v}\right)-z\sinh\left(x\sqrt{c_d/c_v}\right)\right]}{c_v\sqrt{\left(c_d/c_v\right)}\left(\frac{c_d}{c_v}+\frac{n^2\pi^2}{x^2}\right)\left[\sinh\left(x\sqrt{c_d/c_v}\right)-x\sqrt{c_d/c_v}\cosh\left(x\sqrt{c_d/c_v}\right)\right]}$$
$$\left.+\frac{x^2}{n^2\pi^2}\frac{\left[1-\cos\left(n\pi z/x\right)\right]}{c_v\left(\frac{c_d}{c_v}+\frac{n^2\pi^2}{x^2}\right)}+\frac{x^2}{n^2\pi^2}\frac{\left[1-(-1)^n\right]\left[\sinh\left(z\sqrt{c_d/c_v}\right)-z\sqrt{c_d/c_v}\cosh\left(x\sqrt{c_d/c_v}\right)\right]}{c_v\left(\frac{c_d}{c_v}+\frac{n^2\pi^2}{x^2}\right)\left[\sinh\left(x\sqrt{c_d/c_v}\right)-x\sqrt{c_d/c_v}\cosh\left(x\sqrt{c_d/c_v}\right)\right]}\right\}\sin\left(2m\pi t\right)$$
$$+\left(2m\pi\right)\frac{2x^3n_v}{n^2\pi^2}\sum_{m=1}^{\infty}\frac{\left[x\sin\left(\beta_m z/x\right)-z\sin\beta_m\right]}{\left(c_v{\beta_m}^2+c_d x^2\right)\left(n^2\pi^2-{\beta_m}^2\right)\sin\beta_m}\left\{\left[1-(-1)^n\right]-\frac{n^2\pi^2}{{\beta_m}^2}\left(1-\cos\beta_m\right)+\frac{n^2\pi^2}{\beta_m}\sin\beta_m\right\}$$
$$\times\frac{-\left(c_v\left(\beta_m/x\right)^2+c_d\right)\exp\left[-\left(c_v\left(\beta_m/x\right)^2+c_d\right)t\right]+\left(c_v\left(\beta_m/x\right)^2+c_d\right)\cos\left(2m\pi t\right)+2m\pi\sin\left(2m\pi t\right)}{\left[c_v\left(\beta_m/x\right)^2+c_d\right]^2+4m^2\pi^2}$$

If $c_d = 0$:

$$\psi_{23}^{(0)} = \frac{n_v x\sin\left(2m\pi t\right)\left\{4x^3\left[1-\cos\left(n\pi z/x\right)\right]+2z\left(3x^2-z^2\right)\left[1-(-1)^n\right]-n^2\pi^2 z\left(x+z\right)^2\right\}}{4c_v n^4\pi^4}$$
$$+\left(2m\pi\right)\frac{2x^3n_v}{n^2\pi^2}\sum_{m=1}^{\infty}\frac{\left[x\sin\left(\beta_m z/x\right)-z\sin\beta_m\right]}{\left(c_v{\beta_m}^2+c_d x^2\right)\left(n^2\pi^2-{\beta_m}^2\right)\sin\beta_m}\left\{\left[1-(-1)^n\right]-\frac{n^2\pi^2}{{\beta_m}^2}\left(1-\cos\beta_m\right)+\frac{n^2\pi^2}{\beta_m}\sin\beta_m\right\}$$
$$\times\left\{\frac{-\left(c_v\left(\beta_m/x\right)^2+c_d\right)\exp\left[-\left(c_v\left(\beta_m/x\right)^2+c_d\right)t\right]+\left(c_v\left(\beta_m/x\right)^2+c_d\right)\cos\left(2m\pi t\right)+2m\pi\sin\left(2m\pi t\right)}{\left[c_v\left(\beta_m/x\right)^2+c_d\right]^2+4m^2\pi^2}\right\}$$

(24) $\psi_{24}^{(0)}$:

$$\psi_{24}^{(0)}=\cos(2m\pi t)\left\{\frac{n_v\left[1-\cosh\left(x\sqrt{c_d/c_v}\right)\right]\left[\sinh\left(z\sqrt{c_d/c_v}\right)-z\sqrt{c_d/c_v}\cosh\left(x\sqrt{c_d/c_v}\right)\right]}{c_v\left(\frac{c_d}{c_v}\right)\left(\frac{c_d}{c_v}+\frac{n^2\pi^2}{x^2}\right)\left[\sinh\left(x\sqrt{c_d/c_v}\right)-x\sqrt{c_d/c_v}\cosh\left(x\sqrt{c_d/c_v}\right)\right]}\right.$$
$$+\frac{n_v\left[1-\cosh\left(z\sqrt{c_d/c_v}\right)\right]}{c_v\left(c_d/c_v\right)\left(\frac{c_d}{c_v}+\frac{n^2\pi^2}{x^2}\right)}+\frac{n_v\sinh\left(x\sqrt{c_d/c_v}\right)\left[x\sinh\left(z\sqrt{c_d/c_v}\right)-z\sinh\left(x\sqrt{c_d/c_v}\right)\right]}{c_v\sqrt{\left(c_d/c_v\right)}\left(\frac{c_d}{c_v}+\frac{n^2\pi^2}{x^2}\right)\left[\sinh\left(x\sqrt{c_d/c_v}\right)-x\sqrt{c_d/c_v}\cosh\left(x\sqrt{c_d/c_v}\right)\right]}$$
$$\left.+\frac{x^2}{n^2\pi^2}\frac{n_v\left[1-\cos\left(n\pi z/x\right)\right]}{c_v\left(\frac{c_d}{c_v}+\frac{n^2\pi^2}{x^2}\right)}+\frac{x^2}{n^2\pi^2}\frac{n_v\left[1-(-1)^n\right]\left[\sinh\left(z\sqrt{c_d/c_v}\right)-z\sqrt{c_d/c_v}\cosh\left(x\sqrt{c_d/c_v}\right)\right]}{c_v\left(\frac{c_d}{c_v}+\frac{n^2\pi^2}{x^2}\right)\left[\sinh\left(x\sqrt{c_d/c_v}\right)-x\sqrt{c_d/c_v}\cosh\left(x\sqrt{c_d/c_v}\right)\right]}\right\}$$
$$+\frac{2x^3n_v}{n^2\pi^2}\sum_{m=1}^{\infty}\frac{\left[x\sin\left(\beta_m z/x\right)-z\sin\beta_m\right]}{\left(c_v{\beta_m}^2+c_dx^2\right)\left(n^2\pi^2-{\beta_m}^2\right)\sin\beta_m}\left\{\left[1-(-1)^n\right]-\frac{n^2\pi^2}{{\beta_m}^2}\left(1-\cos\beta_m\right)+\frac{n^2\pi^2}{\beta_m}\sin\beta_m\right\}$$
$$\times\left\{\exp\left[-\left(c_v\left(\beta_m/x\right)^2+c_d\right)t\right]-(2m\pi)\frac{2m\pi\exp\left[-\left(c_v\left(\beta_m/x\right)^2+c_d\right)t\right]-2m\pi\cos(2m\pi t)+\left[c_v\left(\beta_m/x\right)^2+c_d\right]\sin(2m\pi t)}{\left[c_v\left(\beta_m/x\right)^2+c_d\right]^2+4m^2\pi^2}\right\}$$

If $c_d=0$:

$$\psi_{24}^{(0)}=\frac{n_vx\cos(2\pi t)\left\{4x^3\left[1-\cos\left(n\pi z/x\right)\right]+2z\left(3x^2-z^2\right)\left[1-(-1)^n\right]-n^2\pi^2z\left(x+z\right)^2\right\}}{4c_vn^4\pi^4}$$
$$+\frac{2x^3n_v}{n^2\pi^2}\sum_{m=1}^{\infty}\frac{\left[x\sin\left(\beta_m z/x\right)-z\sin\beta_m\right]}{\left(c_v{\beta_m}^2+c_dx^2\right)\left(n^2\pi^2-{\beta_m}^2\right)\sin\beta_m}\left\{\left[1-(-1)^n\right]-\frac{n^2\pi^2}{{\beta_m}^2}\left(1-\cos\beta_m\right)+\frac{n^2\pi^2}{\beta_m}\sin\beta_m\right\}$$
$$\times\left\{\exp\left[-\left(c_v\left(\beta_m/x\right)^2+c_d\right)t\right]-(2m\pi)\frac{2m\pi\exp\left[-\left(c_v\left(\beta_m/x\right)^2+c_d\right)t\right]-2m\pi\cos(2m\pi t)+\left[c_v\left(\beta_m/x\right)^2+c_d\right]\sin(2m\pi t)}{\left[c_v\left(\beta_m/x\right)^2+c_d\right]^2+4m^2\pi^2}\right\}$$

(25) $\psi_{25}^{(0)}$:

$$\psi_{25}^{(0)}=\frac{n_v\sin(2m\pi t)}{\left(c_d+c_v\frac{n^2\pi^2}{x^2}\right)^2}\left\{\left\{\frac{2x}{n\pi}\left(2c_v+c_dx^2/n^2\pi^2\right)\left[1-(-1)^n\right]+\frac{2c_v{}^2n\pi}{c_dx}\left[1-\cosh\left(x\sqrt{c_d/c_v}\right)\right]\right\}\right.$$
$$\times\left[\frac{\sinh\left(z\sqrt{c_d/c_v}\right)-z\sqrt{c_d/c_v}\cosh\left(x\sqrt{c_d/c_v}\right)}{\sinh\left(x\sqrt{c_d/c_v}\right)-x\sqrt{c_d/c_v}\cosh\left(x\sqrt{c_d/c_v}\right)}\right]$$
$$+\frac{\sin(2m\pi t)}{\left(c_d+c_v\frac{n^2\pi^2}{x^2}\right)}\frac{x^2}{n^2\pi^2}\left\{n\pi(-1)^n+\frac{2c_v{}^{3/2}\sinh\left(x\sqrt{c_d/c_v}\right)}{\sqrt{c_d}\left(c_d+c_v\frac{n^2\pi^2}{x^2}\right)}\frac{n^3\pi^3}{x^3}\right\}\times\left[\frac{x\sinh\left(z\sqrt{c_d/c_v}\right)-z\sinh\left(x\sqrt{c_d/c_v}\right)}{\sinh\left(x\sqrt{c_d/c_v}\right)-x\sqrt{c_d/c_v}\cosh\left(x\sqrt{c_d/c_v}\right)}\right]$$
$$\left.+\frac{c_v\sin(2m\pi t)}{\left(c_d+\frac{c_vn^2\pi^2}{x^2}\right)^2}\left\{\frac{2x}{n\pi}\left[1-\cos(n\pi z/x)\right]\left(2+\frac{c_d}{c_v}\frac{x^2}{n^2\pi^2}\right)-z\sin(n\pi z/x)\left(1+\frac{c_d}{c_v}\frac{x^2}{n^2\pi^2}\right)+\frac{2c_vn\pi\left[1-\cosh\left(z\sqrt{c_d/c_v}\right)\right]}{c_dx}\right\}\right\}$$
$$-\frac{2c_vn_v(2m\pi)}{x^3}\sum_{m=1}^{\infty}\frac{1}{\sin\beta_m}\left[x\sin(\beta_mz/x)-z\sin\beta_m\right]\left[F_{25nm}\big|_{z=-x}+x\frac{\partial F_{25nm}}{\partial z}\Big|_{z=-x}\right]$$

Where

$$F_{25nm}\big|_{z=-x}+x\frac{\partial F_{25nm}}{\partial z}\Big|_{z=-x}$$
$$=\left(-\frac{x^4}{c_v}\right)\left(\frac{x^2}{n^2\pi^2}\right)\frac{1}{\left(n^2\pi^2-\beta_m{}^2\right)\left(-c_v\beta_m{}^2-c_dx^2\right)}\frac{-\left(c_v(\beta_m/x)^2+c_d\right)\exp\left(-\left(c_v(\beta_m/x)^2+c_d\right)t\right)+\left(c_v(\beta_m/x)^2+c_d\right)\cos(2m\pi t)+2m\pi\sin(2m\pi t)}{\left[c_v(\beta_m/x)^2+c_d\right]^2+4m^2\pi^2}\times$$
$$\left\{\frac{2x^2\left(2n^2\pi^2-\beta_m{}^2\right)}{n\pi\left(n^2\pi^2-\beta_m{}^2\right)}\left[(-1)^n-1\right]-n\pi x(-1)^n-\frac{2x^4}{\beta_m}\left(\frac{n\pi}{x}\right)^3\frac{\sin\beta_m}{\left(n^2\pi^2-\beta_m{}^2\right)}-\frac{2x^5}{\beta_m{}^2}\left(\frac{n\pi}{x}\right)^3\frac{1}{\left(n^2\pi^2-\beta_m^2\right)}(\cos\beta_m-1)\right\}$$

If $c_d=0$:

$$\psi_{25}{}^{(0)}=\frac{n_v}{2c_vn^5\pi^5}\left\{\left[1-(-1)^n\right]\left(12x^4z-n^2\pi^2x^4z-4x^2z^3\right)-n^2\pi^2x^2z^3\left[1+(-1)^n\right]\right.$$
$$\left.+8x^5\left[1-\cos(n\pi z/x)\right]-2n\pi x^3z\left[x\sin(n\pi z/x)+n\pi z\right]\right\}\sin(2m\pi t)$$
$$-\frac{2c_vn_v(2\pi)}{x^3}\sum_{m=1}^{\infty}\frac{1}{\sin\beta_m}\left[x\sin(\beta_mz/x)-z\sin\beta_m\right]\left[F_{25nm}\big|_{z=-x}+x\frac{\partial F_{25nm}}{\partial z}\Big|_{z=-x}\right]$$

(26) $\psi_{26}^{(0)}$:

$$\psi_{26}^{(0)}=\frac{n_v\cos(2m\pi t)}{\left(c_d+c_v\dfrac{n^2\pi^2}{x^2}\right)^2}\left\{\frac{2x}{n\pi}\left(2c_v+c_dx^2/n^2\pi^2\right)\left[1-(-1)^n\right]+\frac{2c_v{}^2n\pi}{c_dx}\left[1-\cosh\left(x\sqrt{c_d/c_v}\right)\right]\right\}$$
$$\times\left[\frac{\sinh\left(z\sqrt{c_d/c_v}\right)-z\sqrt{c_d/c_v}\cosh\left(x\sqrt{c_d/c_v}\right)}{\sinh\left(x\sqrt{c_d/c_v}\right)-x\sqrt{c_d/c_v}\cosh\left(x\sqrt{c_d/c_v}\right)}\right]$$
$$+\frac{n_v\cos(2m\pi t)}{\left(c_d+c_v\dfrac{n^2\pi^2}{x^2}\right)}\frac{x^2}{n^2\pi^2}\left\{n\pi(-1)^n+\frac{2c_v{}^{3/2}\sinh\left(x\sqrt{c_d/c_v}\right)}{\sqrt{c_d}\left(c_d+c_v\dfrac{n^2\pi^2}{x^2}\right)}\frac{n^3\pi^3}{x^3}\right\}\times\left[\frac{x\sinh\left(z\sqrt{c_d/c_v}\right)-z\sinh\left(x\sqrt{c_d/c_v}\right)}{\sinh\left(x\sqrt{c_d/c_v}\right)-x\sqrt{c_d/c_v}\cosh\left(x\sqrt{c_d/c_v}\right)}\right]$$
$$+\frac{c_vn_v\cos(2m\pi t)}{\left(c_d+\dfrac{c_vn^2\pi^2}{x^2}\right)^2}\left\{\frac{2x}{n\pi}\left[1-\cos(n\pi z/x)\right]\left(2+\frac{c_d}{c_v}\frac{x^2}{n^2\pi^2}\right)-z\sin(n\pi z/x)\left(1+\frac{c_d}{c_v}\frac{x^2}{n^2\pi^2}\right)+\frac{2c_vn\pi\left[1-\cosh\left(z\sqrt{c_d/c_v}\right)\right]}{c_dx}\right\}$$
$$-\frac{2n_vc_v}{x^3}\sum_{m=1}^{\infty}\frac{1}{\sin\beta_m}\left[x\sin(\beta_mz/x)-z\sin\beta_m\right]\left[F_{26nm}\big|_{z=-x}+x\frac{\partial F_{26nm}}{\partial z}\bigg|_{z=-x}\right]$$

Where

$$F_{26nm}\big|_{z=-x}+x\frac{\partial F_{26nm}}{\partial z}\bigg|_{z=-x}$$
$$=\left(-\frac{x^4}{\sigma}\right)\left(\frac{x^2}{n^2\pi^2}\right)\frac{1}{\left(n^2\pi^2-\beta_m{}^2\right)\left(-c_v\beta_m{}^2-c_dx^2\right)}\left[\exp\left(-\left(c_v(\beta_m/x)^2+c_d\right)t\right)-(2m\pi)\frac{2m\pi\exp\left(-\left(c_v(\beta_m/x)^2+c_d\right)t\right)-2m\pi\cos(2m\pi t)+\left[c_v(\beta_m/x)^2+c_d\right]\sin(2m\pi t)}{\left[c_v(\beta_m/x)^2+c_d\right]^2+4m^2\pi^2}\right]$$
$$\times\left\{\frac{2x^2\left(2n^2\pi^2-\beta_m{}^2\right)}{n\pi\left(n^2\pi^2-\beta_m{}^2\right)}\left[(-1)^n-1\right]-n\pi x(-1)^n-\frac{2x^4}{\beta_m}\left(\frac{n\pi}{x}\right)^3\frac{\sin\beta_m}{\left(n^2\pi^2-\beta_m{}^2\right)}-\frac{2x^5}{\beta_m{}^2}\left(\frac{n\pi}{x}\right)^3\frac{1}{\left(n^2\pi^2-\beta_m^2\right)}(\cos\beta_m-1)\right\}$$

If $c_d=0$:

$$\psi_{26}{}^{(0)}=\frac{n_v}{2c_vn^5\pi^5}\left\{\left[1-(-1)^n\right]\left(12x^4z-n^2\pi^2x^4z-4x^2z^3\right)-n^2\pi^2x^2z^3\left[1+(-1)^n\right]\right.$$
$$\left.+8x^5\left[1-\cos(n\pi z/x)\right]-2n\pi x^3z\left[x\sin(n\pi z/x)+n\pi z\right]\right\}\cos(2m\pi t)$$
$$-\frac{2n_vc_v}{x^3}\sum_{m=1}^{\infty}\frac{1}{\sin\beta_m}\left[x\sin(\beta_mz/x)-z\sin\beta_m\right]\left[F_{26nm}\big|_{z=-x}+x\frac{\partial F_{26nm}}{\partial z}\bigg|_{z=-x}\right]$$

3.7 References

Adams, E.E. and Wells, S.A. (1984). “Field measurements on side arms of Lake Anna. Va.” *J. Hydraul.Engng*, 110, 773-793.

Bednarz, T.P., Lei, C, and Patterson, J.C. (2009). “Unsteady natural convection induced by diurnal temperature changes in a reservoir with slowly varying bottom topography.” *Intl J. Ther. Science*, 48, 1932-1942.

Chubarenko, I.P. and Demchenko, N.Y. (2008). “Laboratory modeling of the structure of a thermal bar and related circulation in a basin with a sloping bottom,” *Oceanology*, 48(3), 356-370.

Chubarenko, I.P. (2010). “Horizontal convective water exchange above a sloping bottom: the mechanism of its formation and an analysis of its development.” *Oceanology*, 50(2), 166-174.

Coates, M.J., and Patterson, J.C. (1993). “Unsteady natural convection in a cavity with non-uniform absorption of radiation.” *J. Fluid Mech*., 256, 133-161.

Coates, M., and Ferris, J. (1994). “The radiatively driven natural convection beneath a floating plant layer. ” *Limnol. Oceanogr*., 39(5), 1186-1194.

Cormack, D.E., Leal, L.G., and Imberger, J. (1974). “Natural convection in a shallow cavity with differentially heated end walls. Part 1. Asymptotic theory.” *J. Fluid Mech*., 65, 209-229.

Drazin, P.G. and Reid, W.H. (1981). *Hydrodynamic Stability*. Combridge University Press.

Farrow, D.E. and Patterson, J.C. (1993). “On the response of a reservoir sidearm to diurnal heating and cooling.” *J. Fluid Mech*., 246, 143-161.

Farrow, D.E., and Patterson, J.C. (1994). “The daytime circulation and temperature pattern in a reservoir sidearm.” *Intl J. Heat Mass Transfer*, 37, 1957-1968.

Farrow, D.E. (2004). “Periodically forced natural convection over slowly varying topography.” *J. Fluid Mech*., 508, 1-21.

Kirk, J.T.O. (1986). *Light and Photosynthesis in Aquatic Ecosystem*. London: Cambridge University Press, 239pp.

Koch, E.W. (2001). “Beyond light: physical, geological, and geochemical parameters as possible submersed aquatic vegetation habitat requirements.” *Estuaries*, 24(1), 1-17.

Lei, C. and Patterson, J.C. (2002). “Unsteady natural convection in a triangular enclosure induced by absorption of radiation.” *J. Fluid Mech*., 460, 181-209.

Lei, C. and Patterson, J.C. (2006). “Natural convection induced by diurnal heating and cooling in a reservoir with slowly varying topography.” *JSME International Journal, Series B*: *Fluids and Thermal Engineering*, 49(3), 605-615.

Lövstedt and Bengtsson. (2008). “Density-driven current between reed belts and open water in a shallow lake.” *Water Resources Res*., 44(10), W10413.

Monismith, S.G., Imberger, J. and Morison, M.L. (1990). “Convective motion in the sidearm of a small reservoir.” *Limnol. Oceanogr*., 35, 1676-1702.

Oldham, C.E., and Sturman, J.J. (2001). “The effect of emergent vegetation on convective flushing in shallow wetlands: scaling and experiment.” *Limnol. Oceanogr*., 46(6), 1486-1493.

Sturman, J.J, Oldham, C.E., and Ivey, G.N. (1999). “Steady convection exchange flow down slopes.” *Aquat. Sci*., 61, 260-278.

Tanino, Y., Neph, H.M., and Kulis, P.S. (2005). “Gravity current in aquatic canopies.” *Water Resources Res*., 41(12), W12402.

Zhang, X, and Nepf, H.M. (2008). “Density driven exchange flow between open water and an aquatic canopy.” *Water Resources Res*.,44(8), W08417.

Zhang, X. and Nepf, H.M. (2009). “Thermally driven exchange flow between open water and an aquatic canopy.” *J. Fluid Mech*., 632, 227-243.

Zhang, X. and Nepf, H.M. (2011). “Exchange flow between open water and floating vegetation.” *Environ. Fluid Mech*., 11(5), 531-546.

Table 3.1 Valid ranges of S^2Gr (Note: the flow domain is up to depth of 0.25m)

$\eta = 0.5, z = 0.125$			$\eta = 50, z = 12.5$		
Vegetation density	$U_{\max}$	S^2Gr	Vegetation density	$U_{\max}$	S^2Gr
0%	0.06	19	0%	7×10^{-5}	163
0.5%	0.04	29	0.5%	4×10^{-5}	286

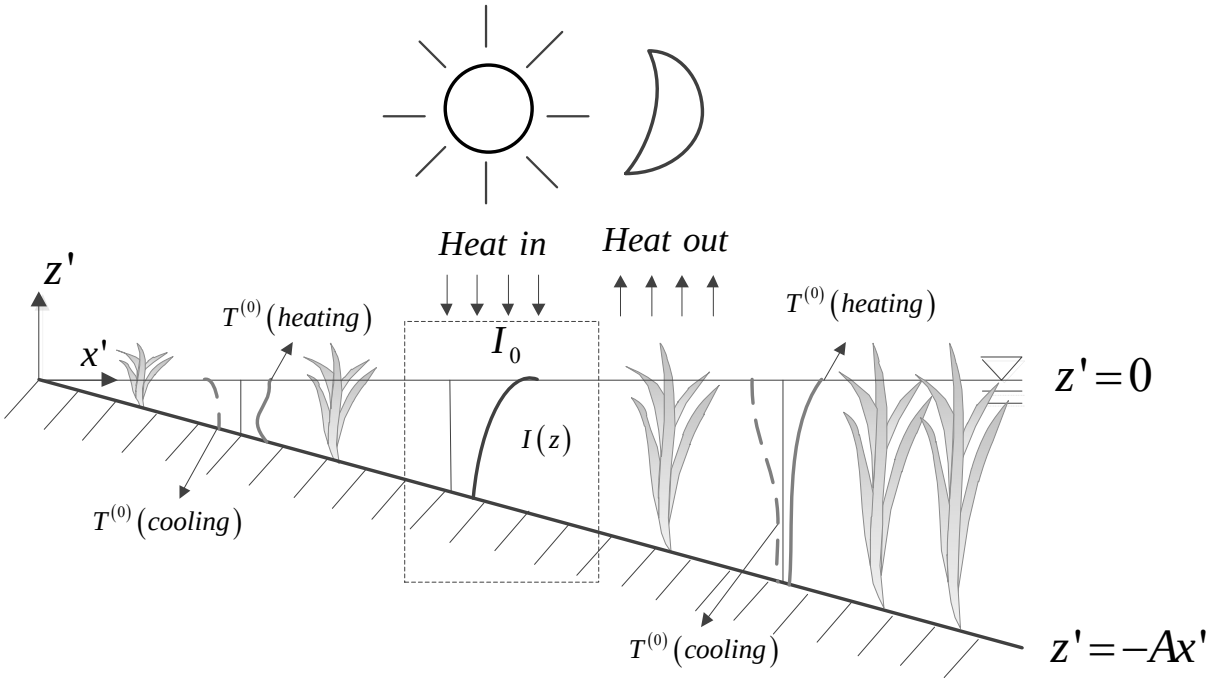

Figure 3.1 Geometry of the domain showing coordinate system. For the heating period, the solar radiation is exponentially distributed over the water column. In shallow water, some heating is absorbed over the water column, and the residual heat reaches the bottom and re-emits to the water column immediately. In deep water, solar radiation is almost absorbed in the top layer of water column. During the cooling period, heat dissipates through the water surface, and therefore the temperature in the top-layer is cooler than that in the bottom layer.

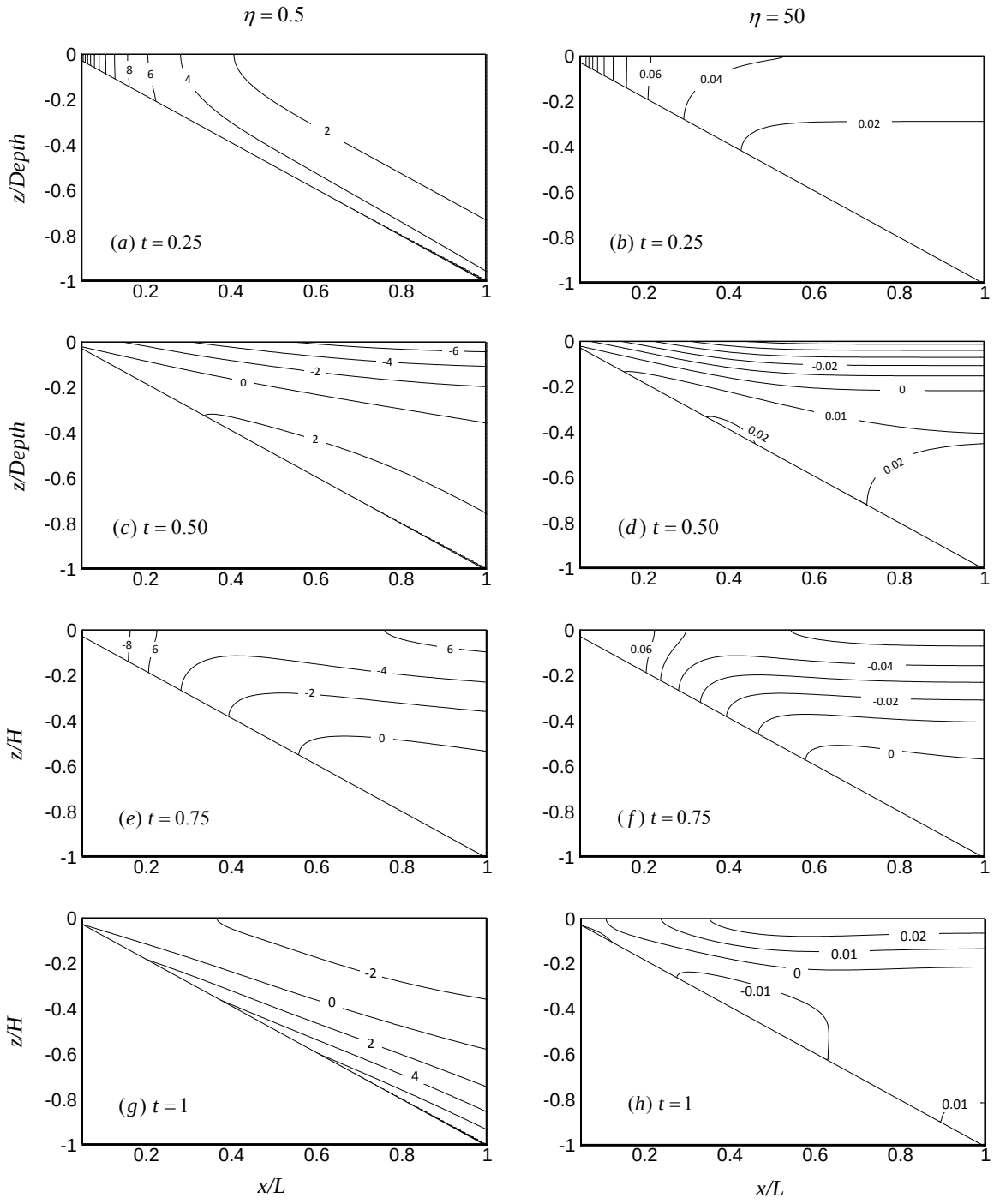

Figure 3.2 Temperature contours for $\eta = 0.5$ and 50 at various times

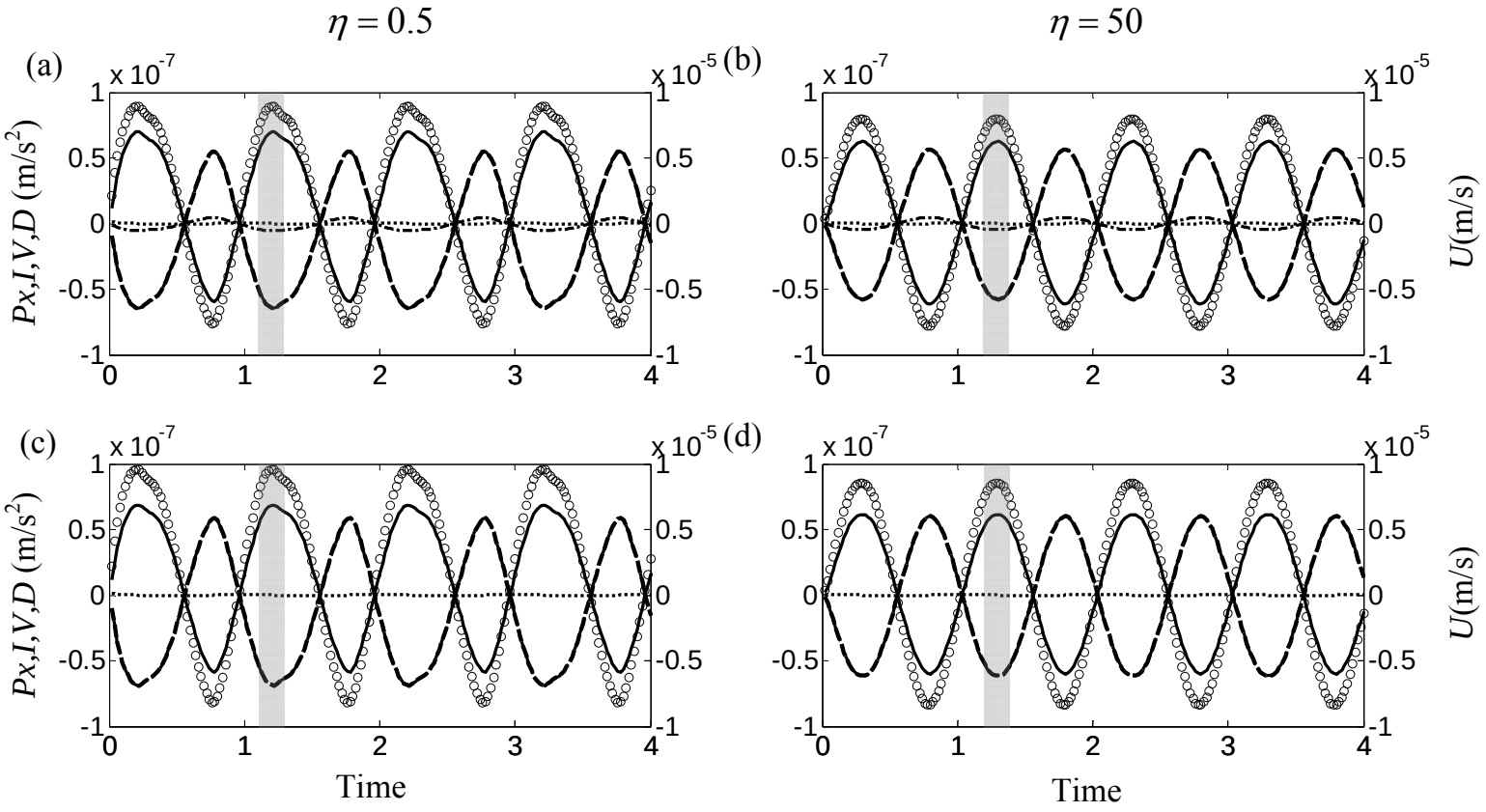

Figure 3.3 Different terms and horizontal velocity at the water surface (z=0) at depth of 0.05m for four cycles. (a) $\eta = 0.5, \phi = 0.5\%$; (b) $\eta = 50, \phi = 0.5\%$ (c) $\eta = 0.5, \phi = 0\%$; (d) $\eta = 50, \phi = 0\%$.

(—— : P_x, ····· : I, – – – : V, –·–·–: D, ○:U, where P_x, I, V, D, and U represent pressure gradient, inertia, viscosity, vegetative drag, and horizontal velocity)

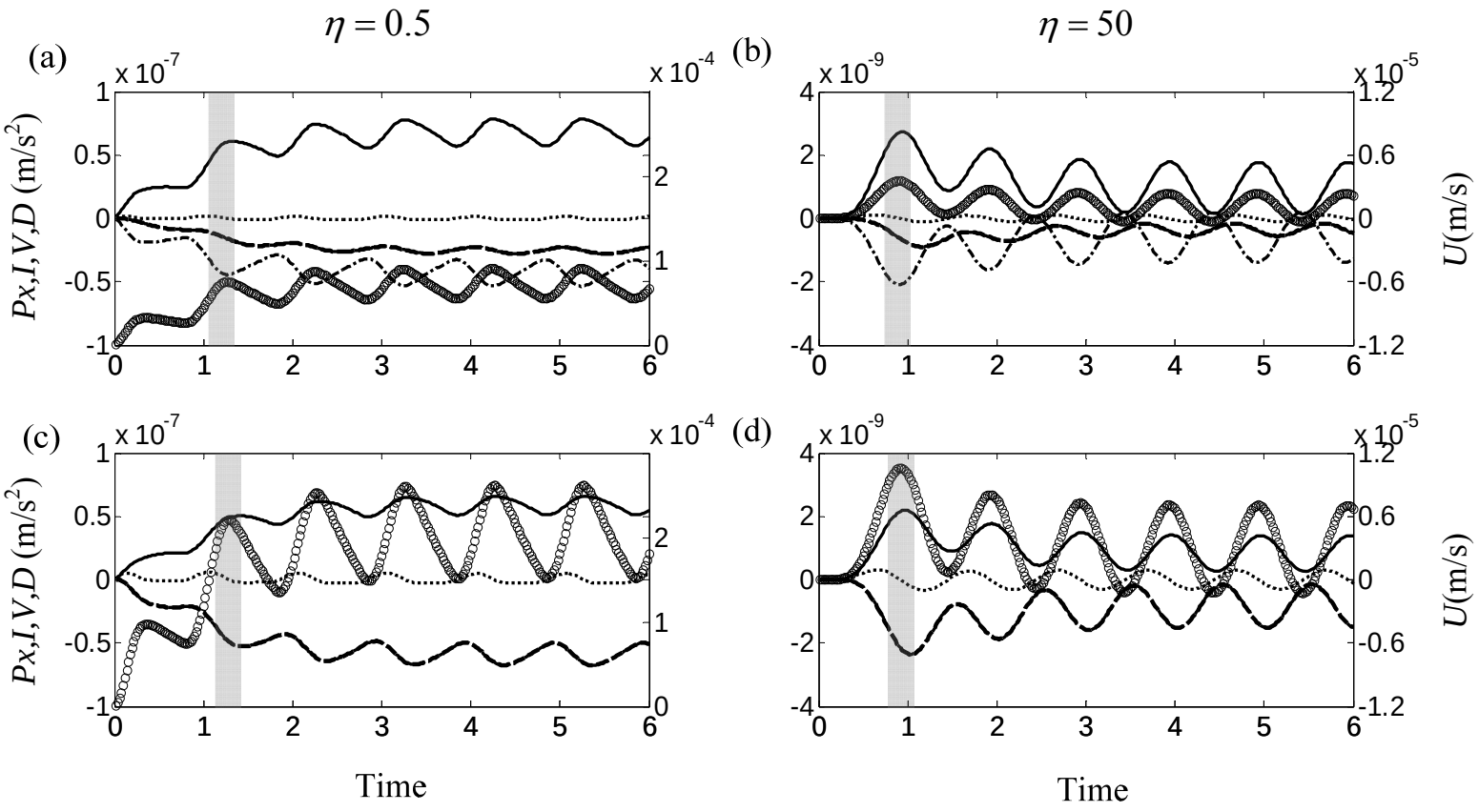

Figure 3.4 Different terms and horizontal velocity at the water surface (z=0) at depth of 0.25m for six cycles. (a) $\eta = 0.5, \phi = 0.5\%$; (b) $\eta = 50, \phi = 0.5\%$ (c) $\eta = 0.5, \phi = 0\%$; (d) $\eta = 50, \phi = 0\%$.

(—— : P_x, ····· : I, – – – : V, –·–·–: D, ○:

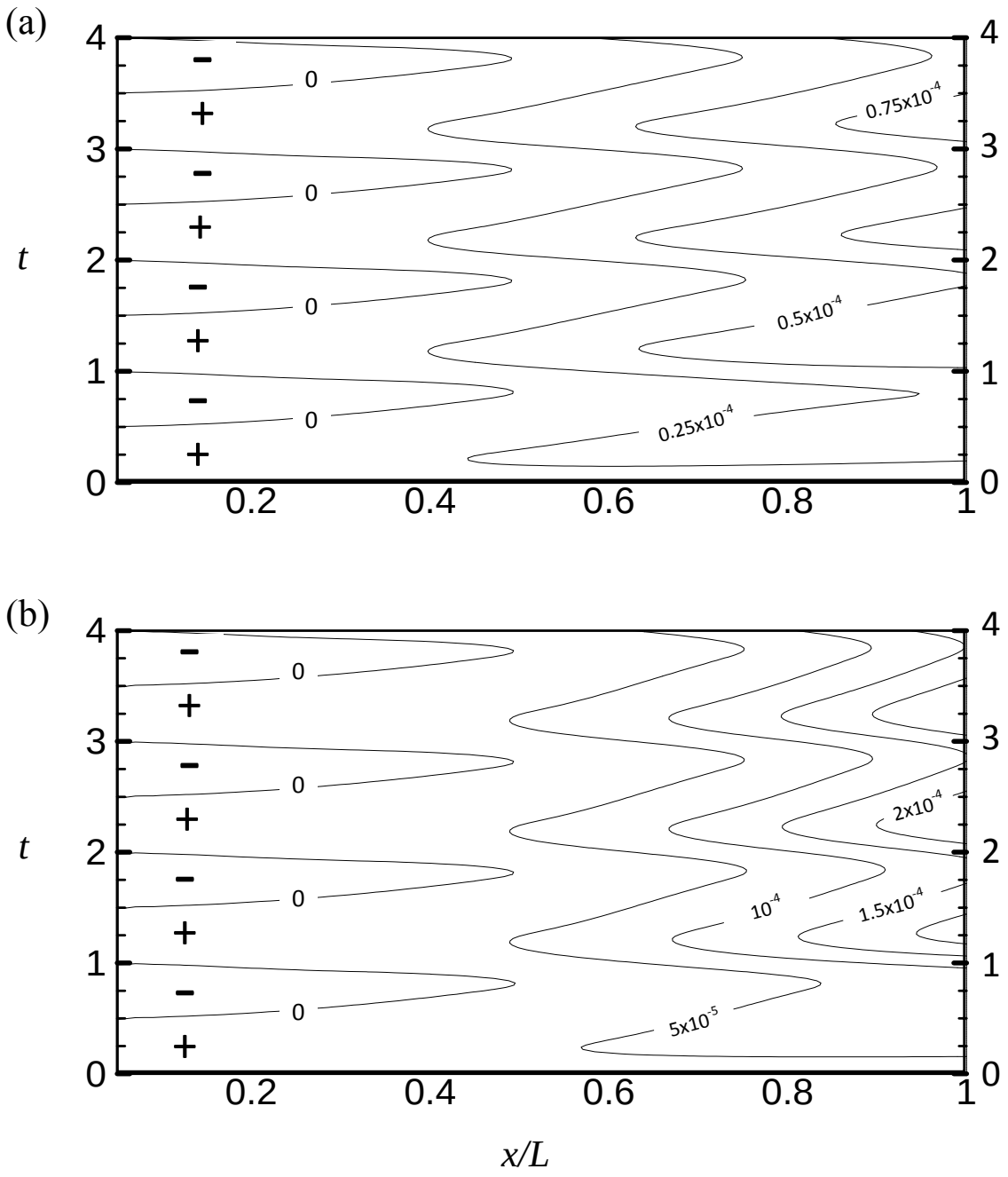

Figure 3.5 Surface velocity for $\eta = 0.5$:(a) $\phi = 0.5\%$ and (b) $\phi = 0\%$. Note: unit (m/s).

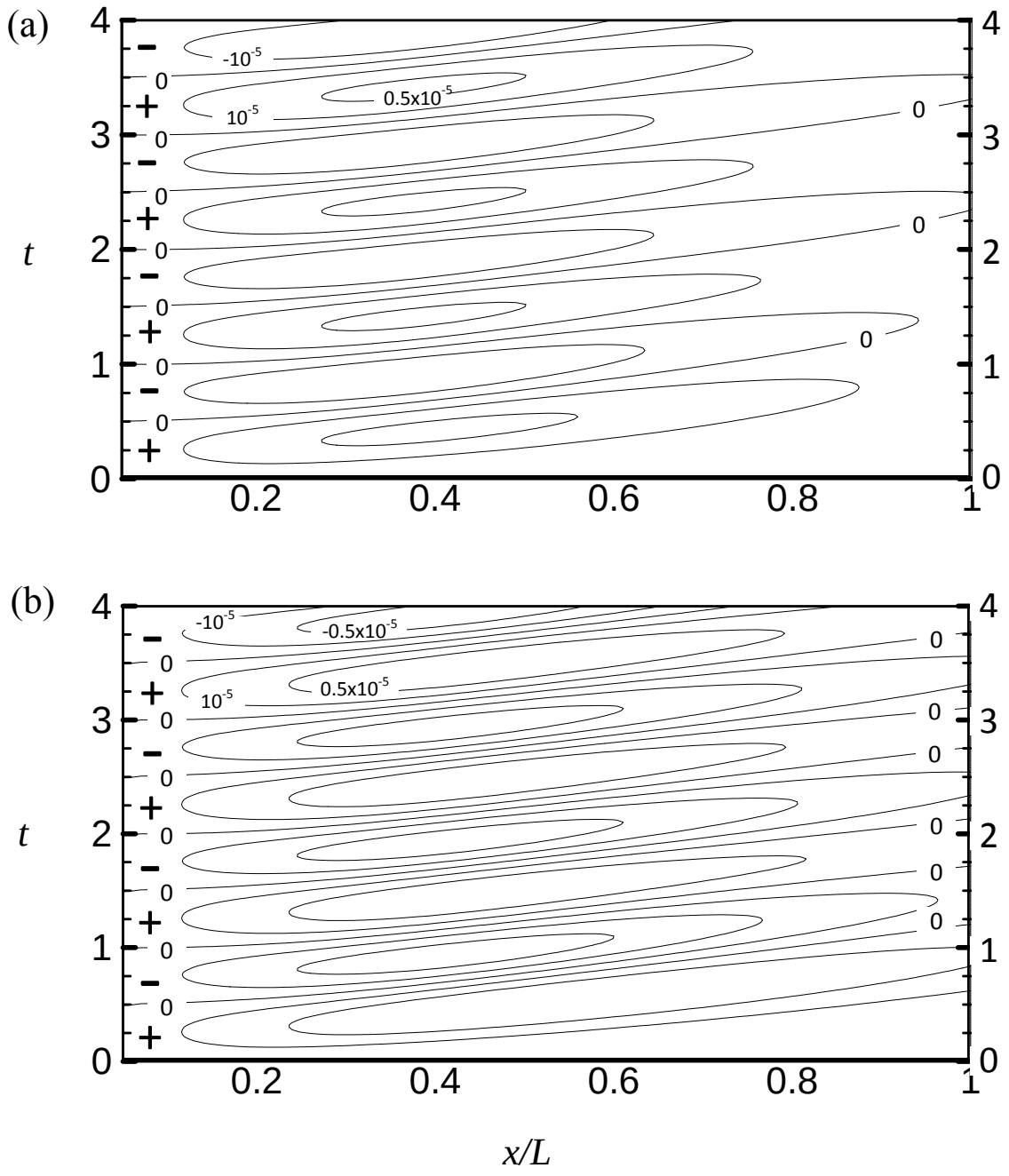

Figure 3.6 Surface velocity for $\eta = 50$:(a) $\phi = 0.5\%$, and (b) $\phi = 0\%$. Note: unit (m/s).

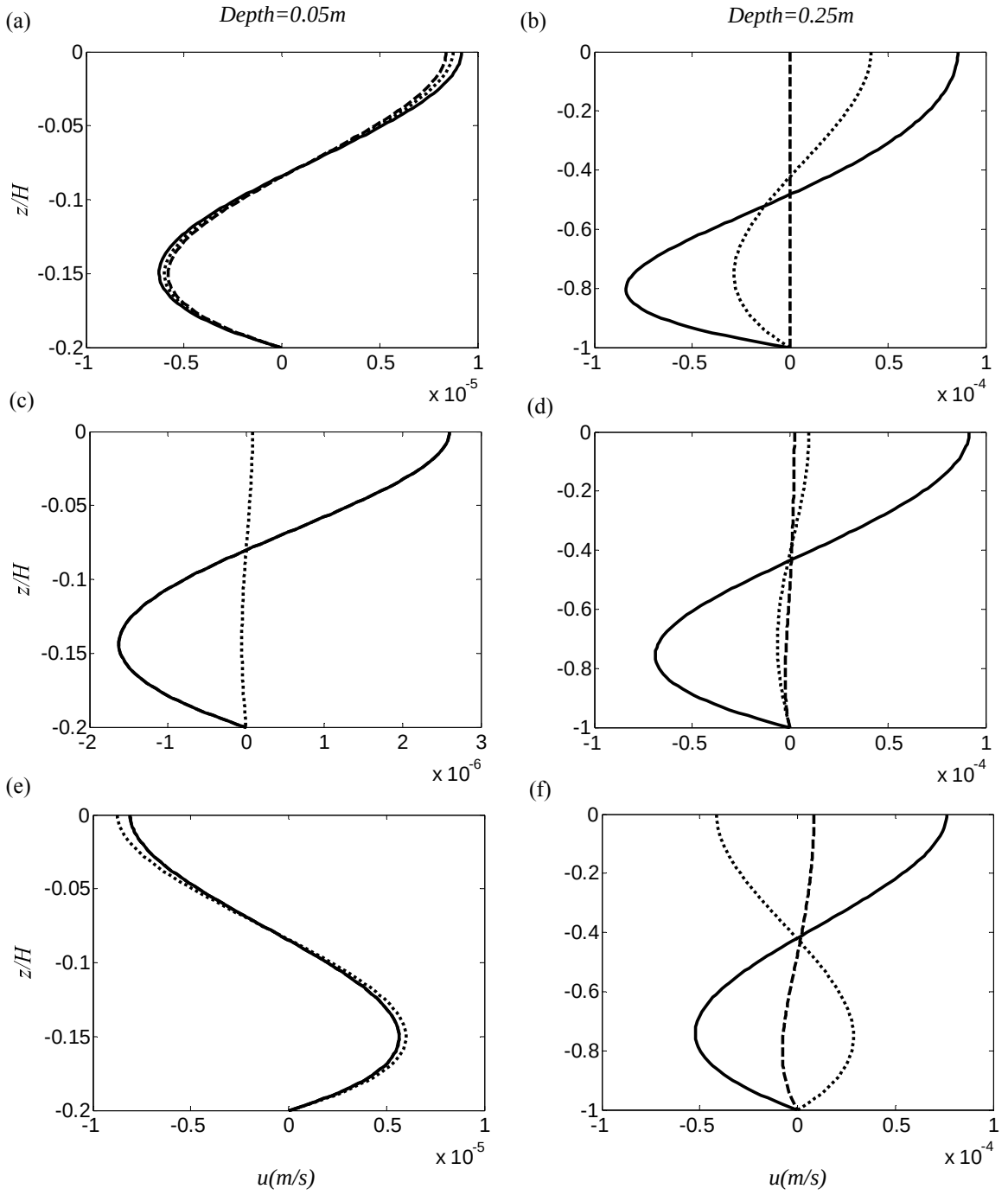

Figure 3.7 Velocity profiles without vegetation at shallow (*z/H=0.20*) and deep waters (*z/H=1*) with and without vegetation, where *H* is equal to 0.25m. (a) and (b) denote *t*=0.25, (c) and (d) denote *t*=0.50, and (e) and (d) denote *t*=0.75. (——: $\eta = 0.5$, – – –: $\eta = 50$, • • • : uniform temperature profile). The important parameters used are described as follows:

$I_0 = 50W / m^2, A = 5 \times 10^{-5},$ Eddy Viscosity $\nu = 10^{-6} m^2 / s,$ Prandtl number $\Pr = 7$

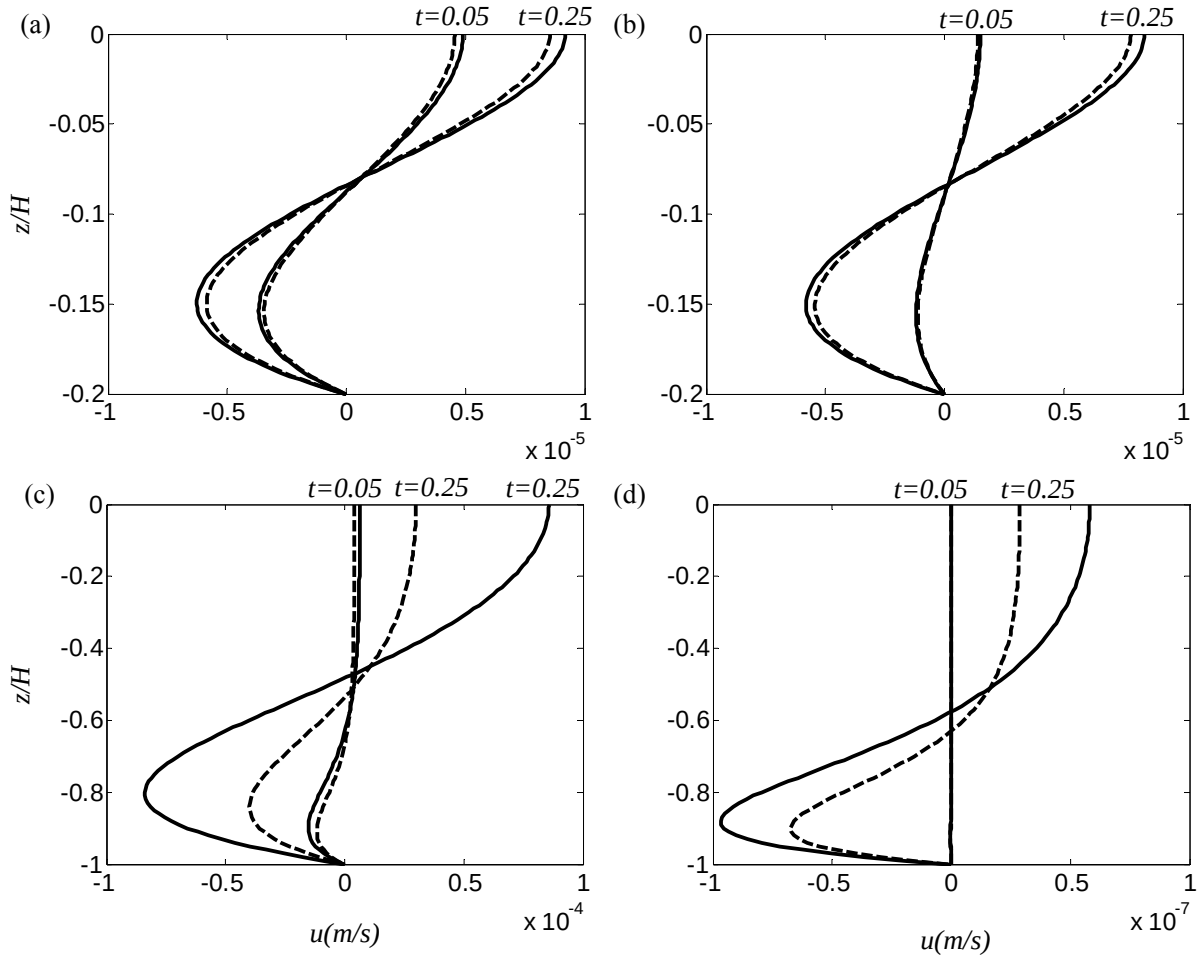

Figure 3.8 Comparisons of velocity profiles with and without vegetation during heating period, where H is equal to 0.25m. (a) and (c) for $\eta = 0.5$, (b) and (d) for $\eta = 50$. (——: $\phi = 0\%$, – – –:).

The important parameters used are described as follows:

$I_0 = 50W/m^2, A = 5\times10^{-5},$ Eddy Viscosity $\nu = 10^{-6}m^2/s,$ Prandtl number $\mathrm{Pr} = 7$

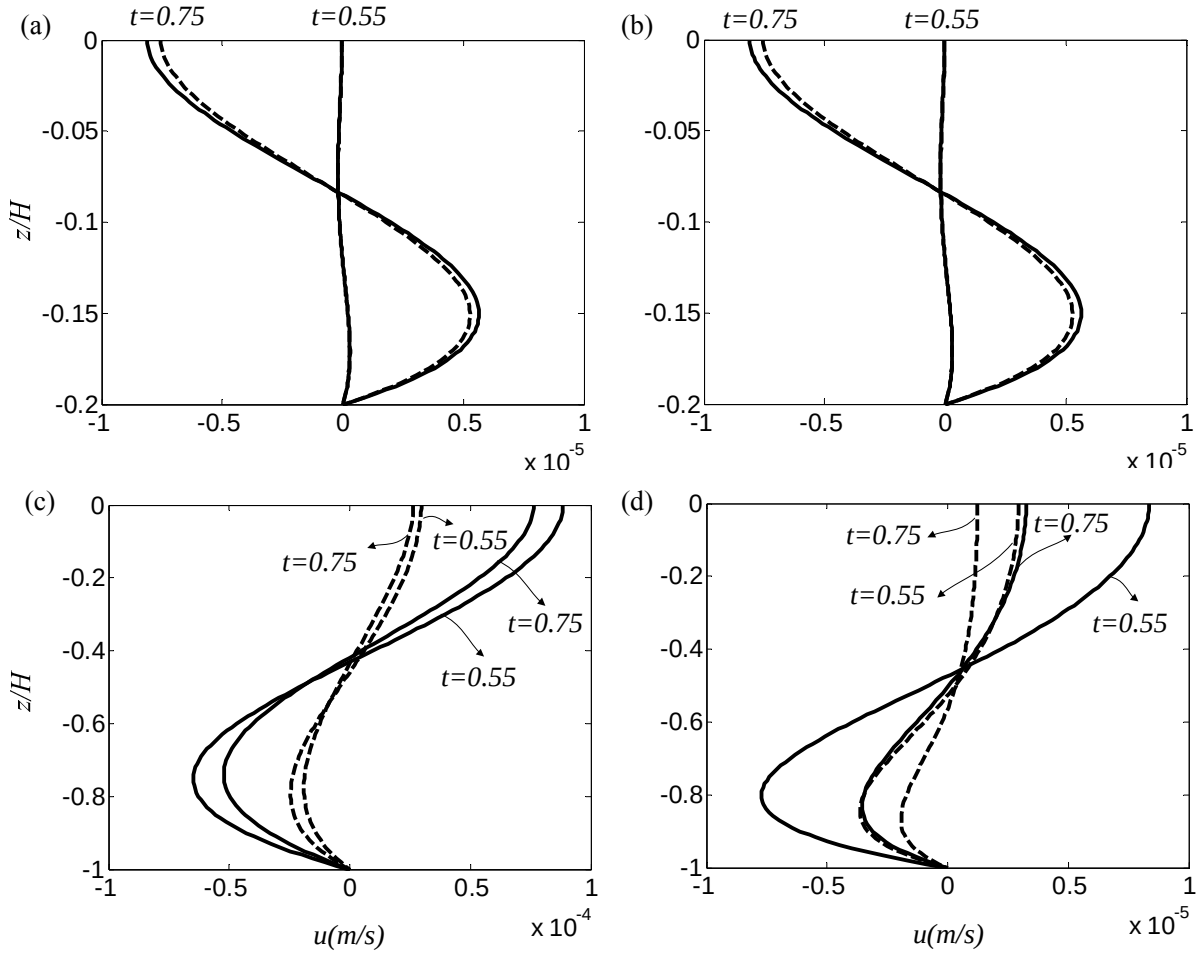

Figure 3.9 Comparisons of velocity profiles with and without vegetation during cooling period, where H is equal to 0.25m. (a) and (c) for $\eta = 0.5$, (b) and (d) for $\eta = 50$. (——: $\phi = 0\%$, – – –:).

The important parameters used are described as follows:

$I_0 = 50W / m^2, A = 5 \times 10^{-5},$ Eddy Viscosity $\nu = 10^{-6} m^2 / s,$ Prandtl number $\mathrm{Pr} = 7$

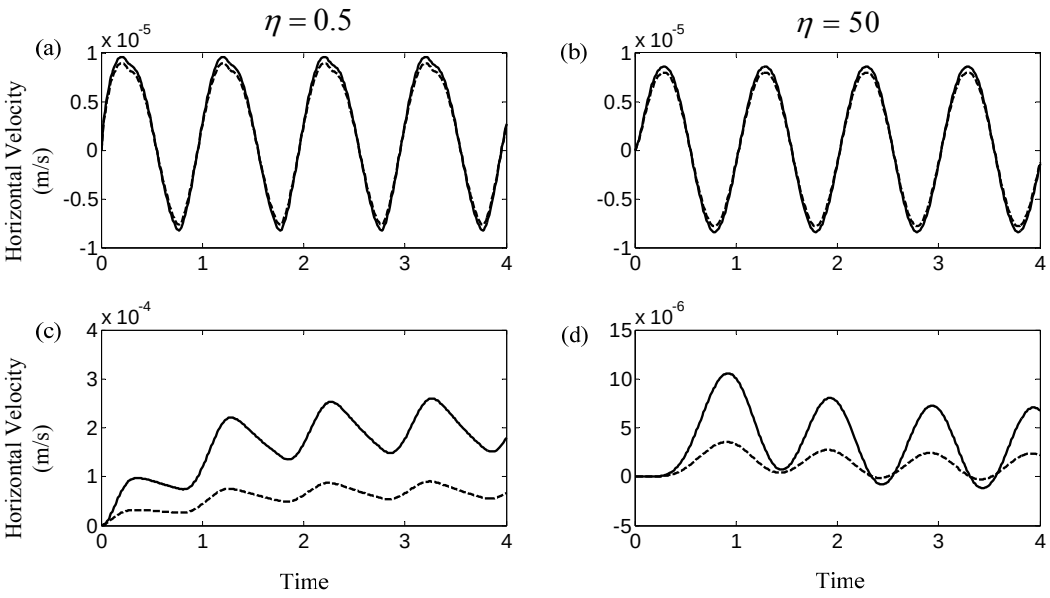

Figure 3.10 Comparisons of surface velocity with and without vegetation. (a) and (b) for depth of 0.05m, and (c) and (d) for depth of 0.25m. (——: $\phi = 0\%$, – – : $\phi = 0.5\%$)

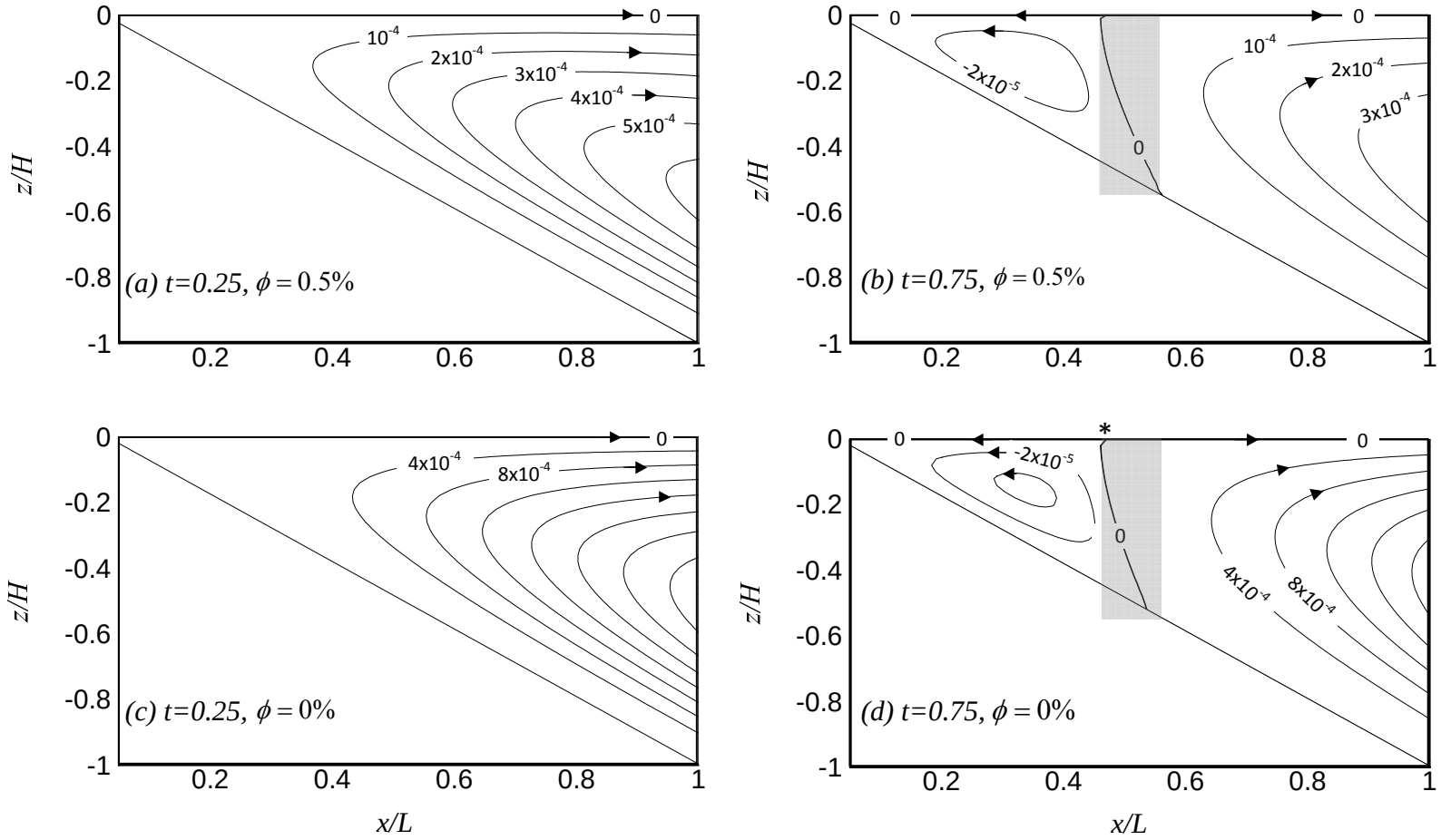

Figure 3.11 Streamline contours for $\eta = 0.5$ with 0.5% vegetation and without vegetation at various times

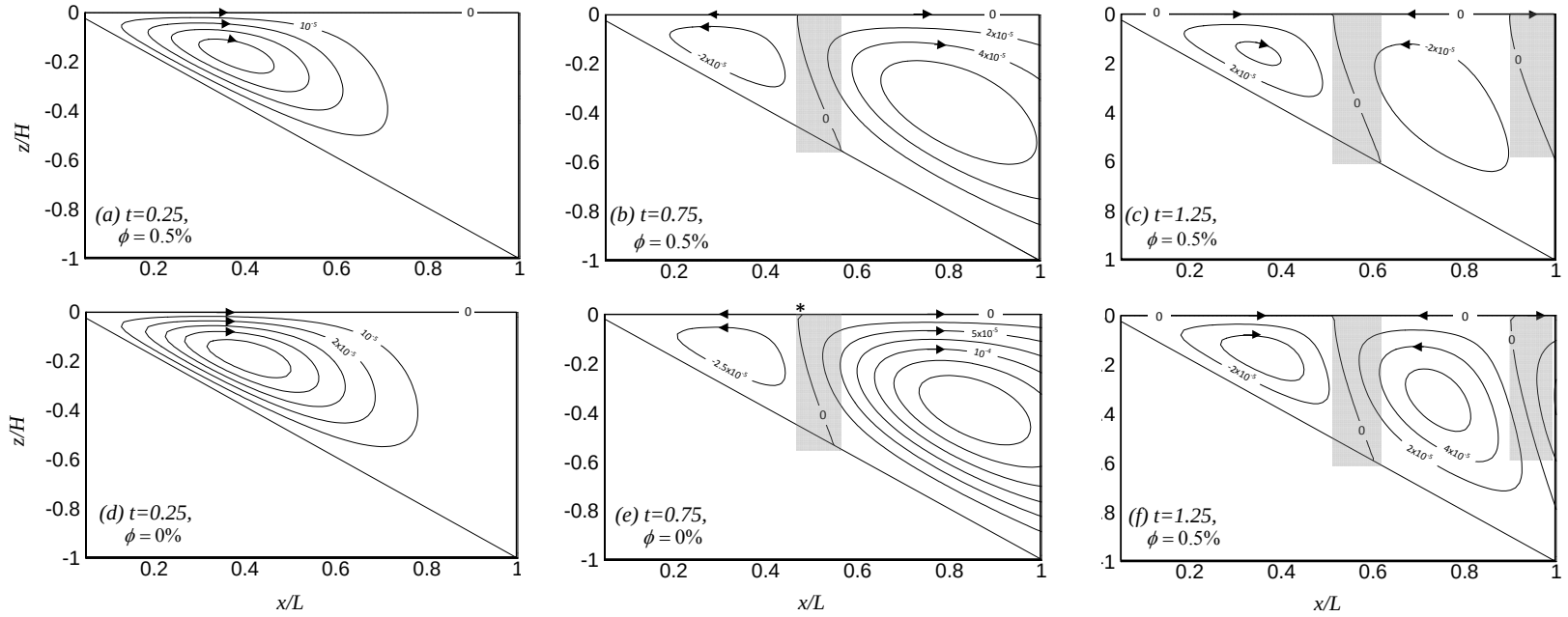

Figure 3.12 Streamline contours for $\eta = 50$ with 0.5% vegetation and without vegetation at various times

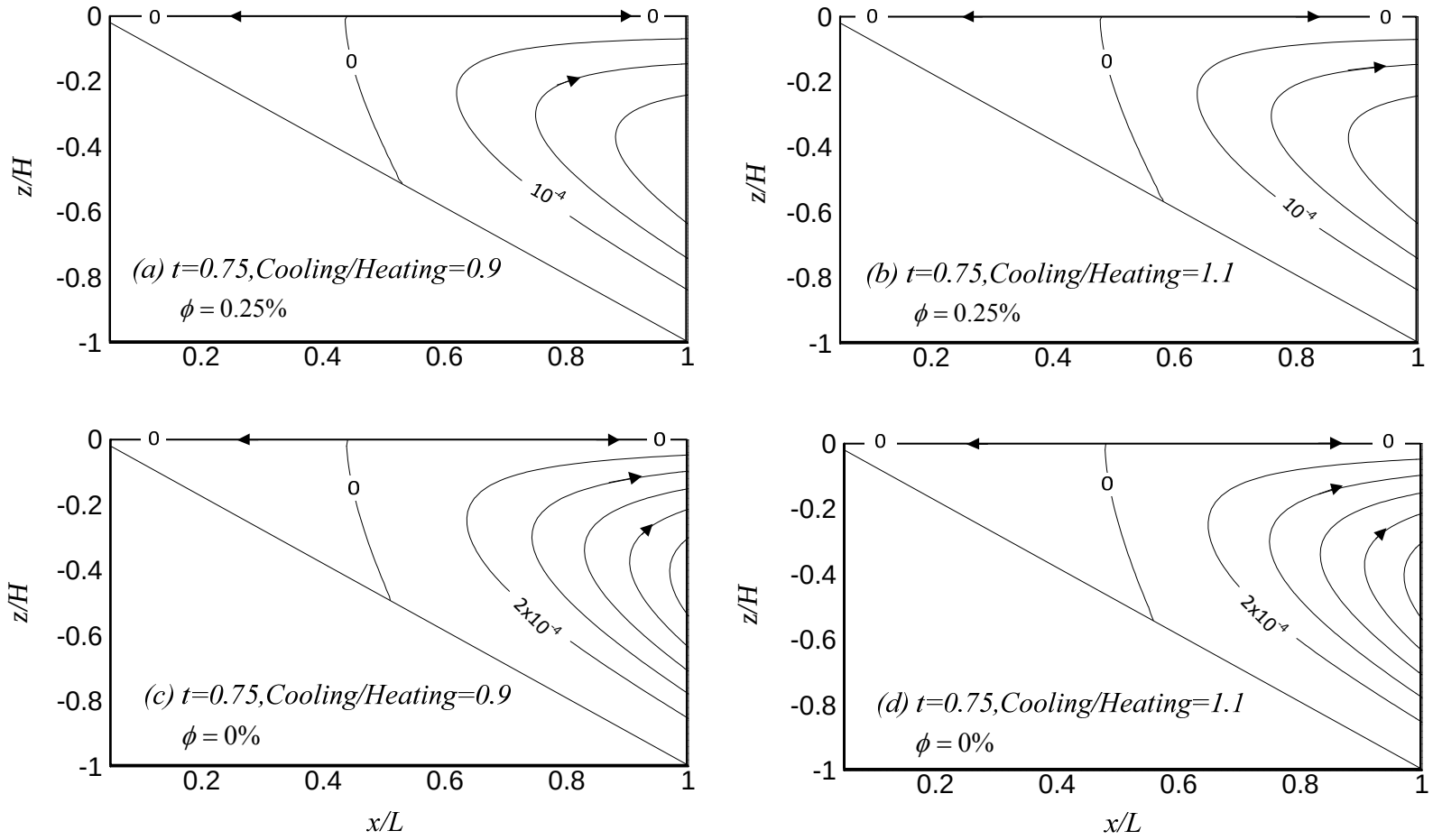

Figure 3.13 Streamline contours for $\eta = 0.5$ with 0.5% vegetation and without vegetation at various times for cooling/heating=0.9 and 1.1.

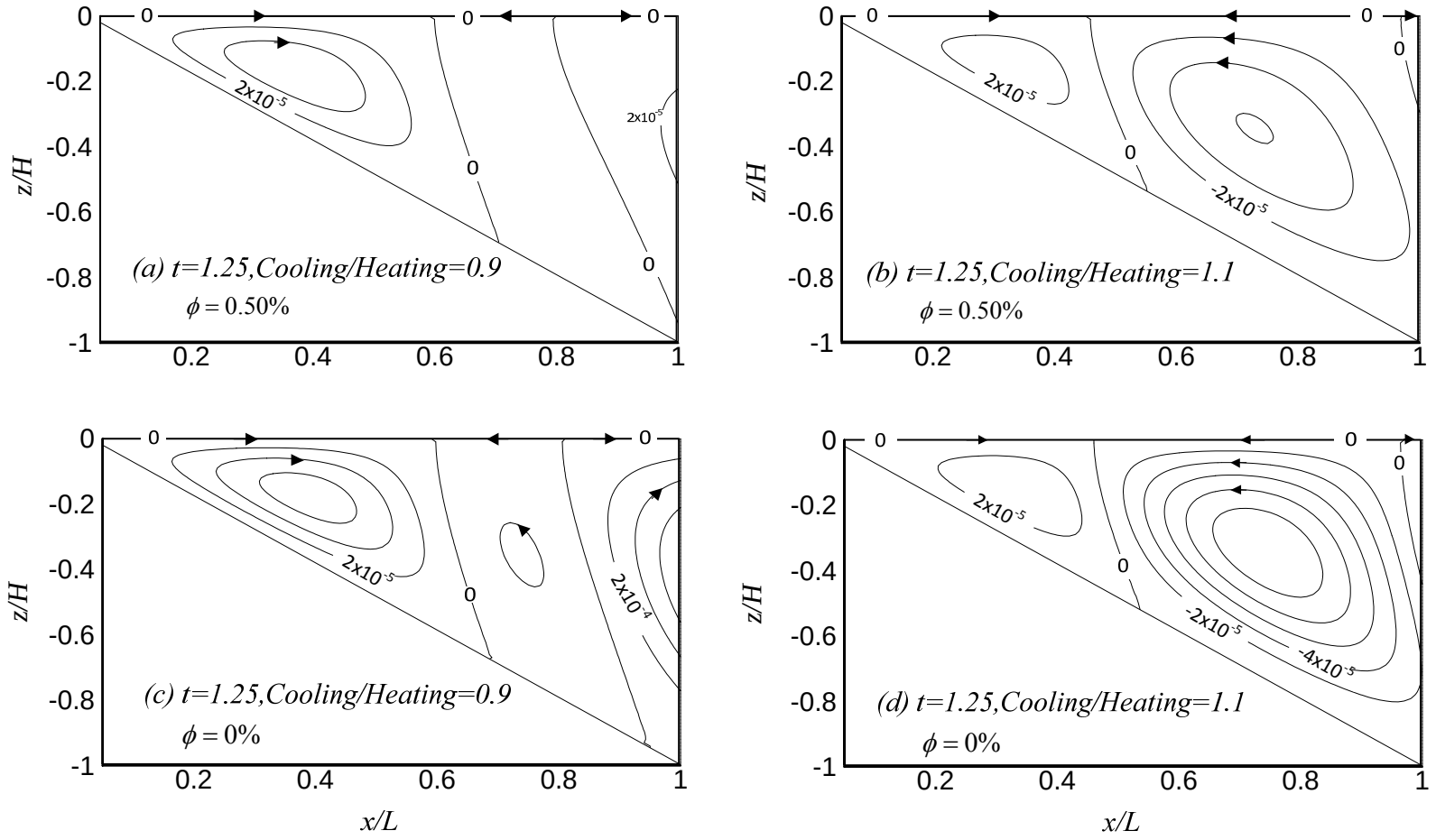

Figure 3.14 Streamline contours for $\eta = 50$ with 0.5% vegetation and without vegetation at various times for cooling/heating=0.9 and 1.1.

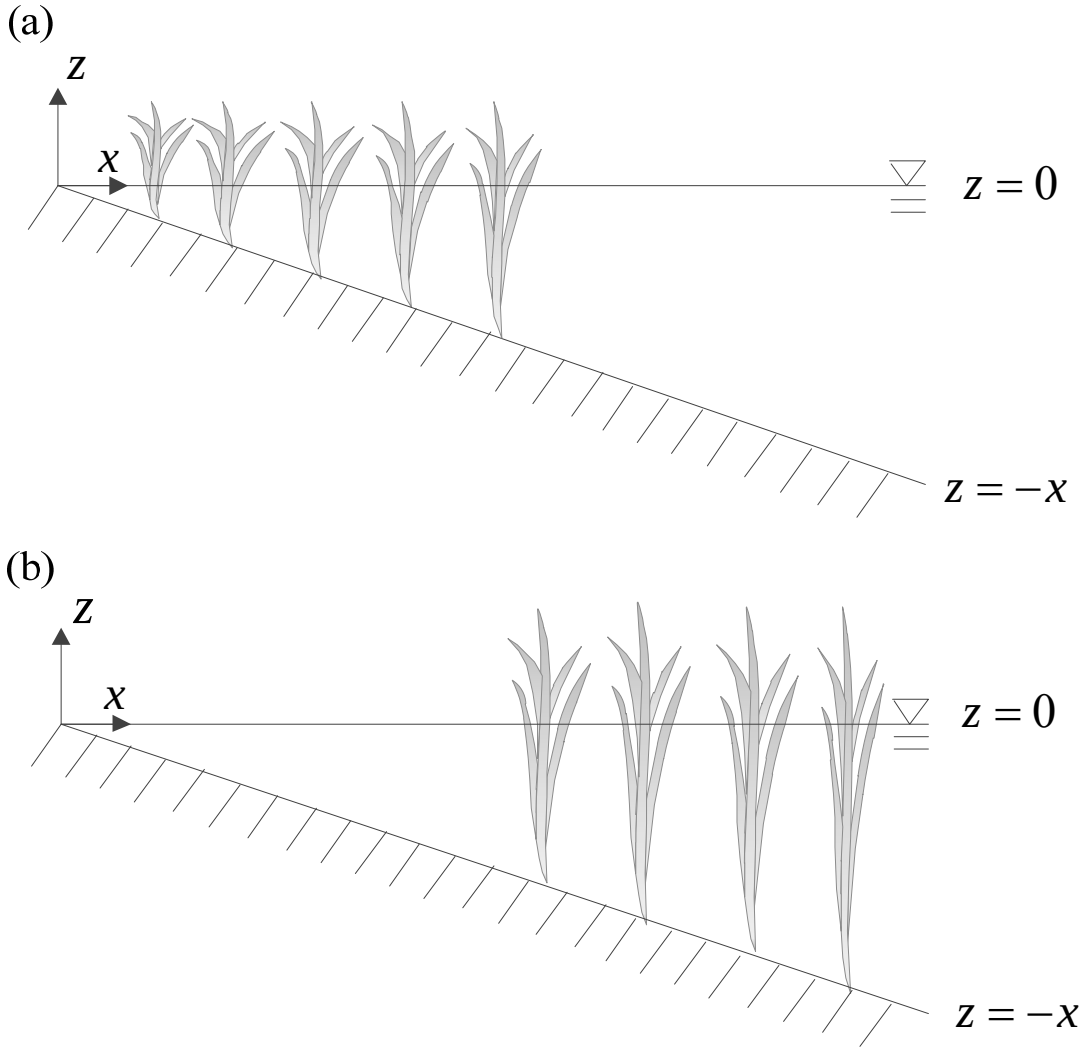

Figure 3.15 Schematics of one-side open water and the other-side vegetation over a sloping bottom: (a) vegetation in shallow water and open in deep water, and (b) open in shallow water and vegetation in deep water.

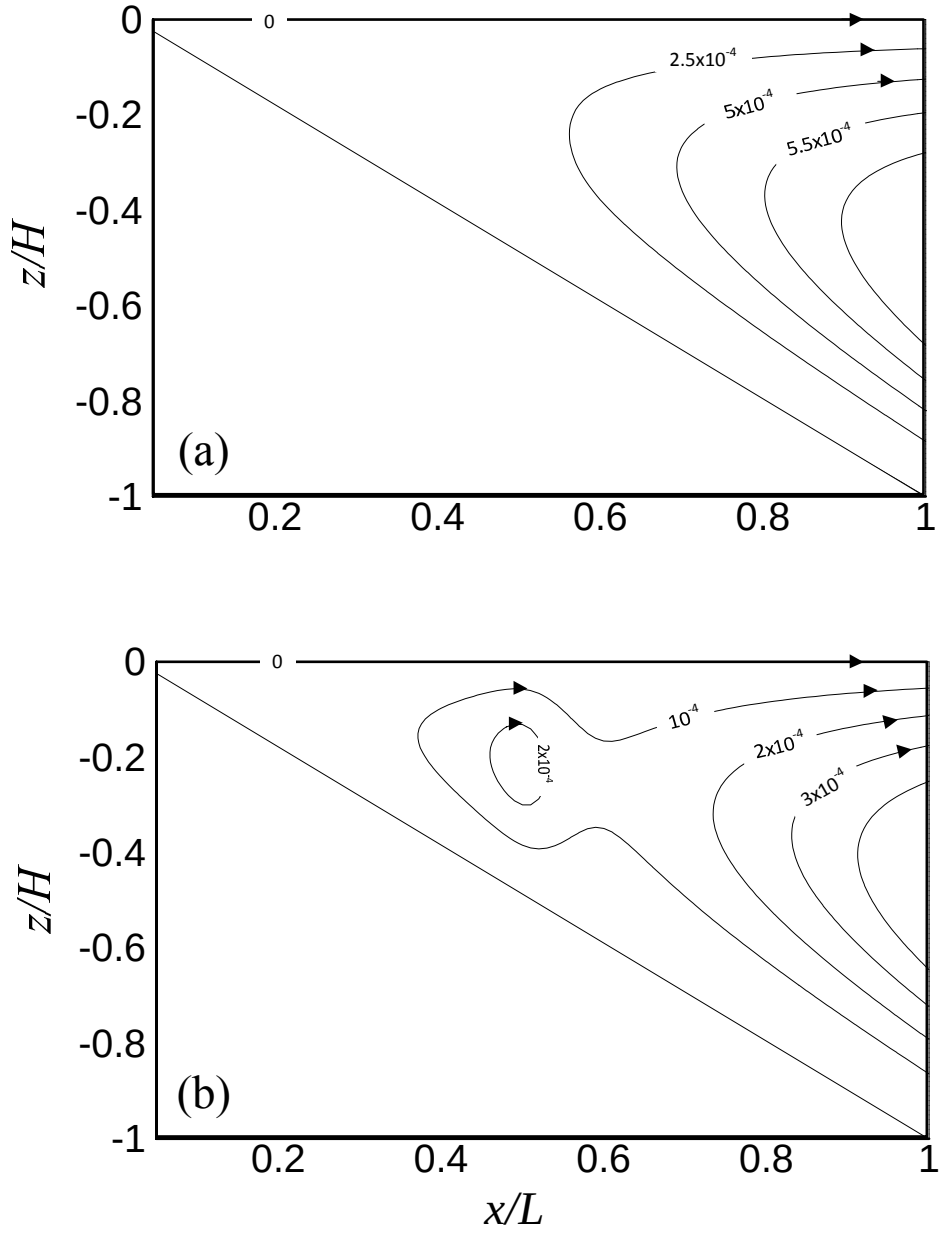

Figure 3.16 Streamline contours for $\eta = 0.5, t = 1.25$ for equal heating and cooling: (a) high vegetation in shallow water, and open in deep water; and (b) open in shallow water, and high vegetation in deep water. Note: $k = 20$, and blockage of solar radiation *B* is 85%, i.e. 15% penetration.

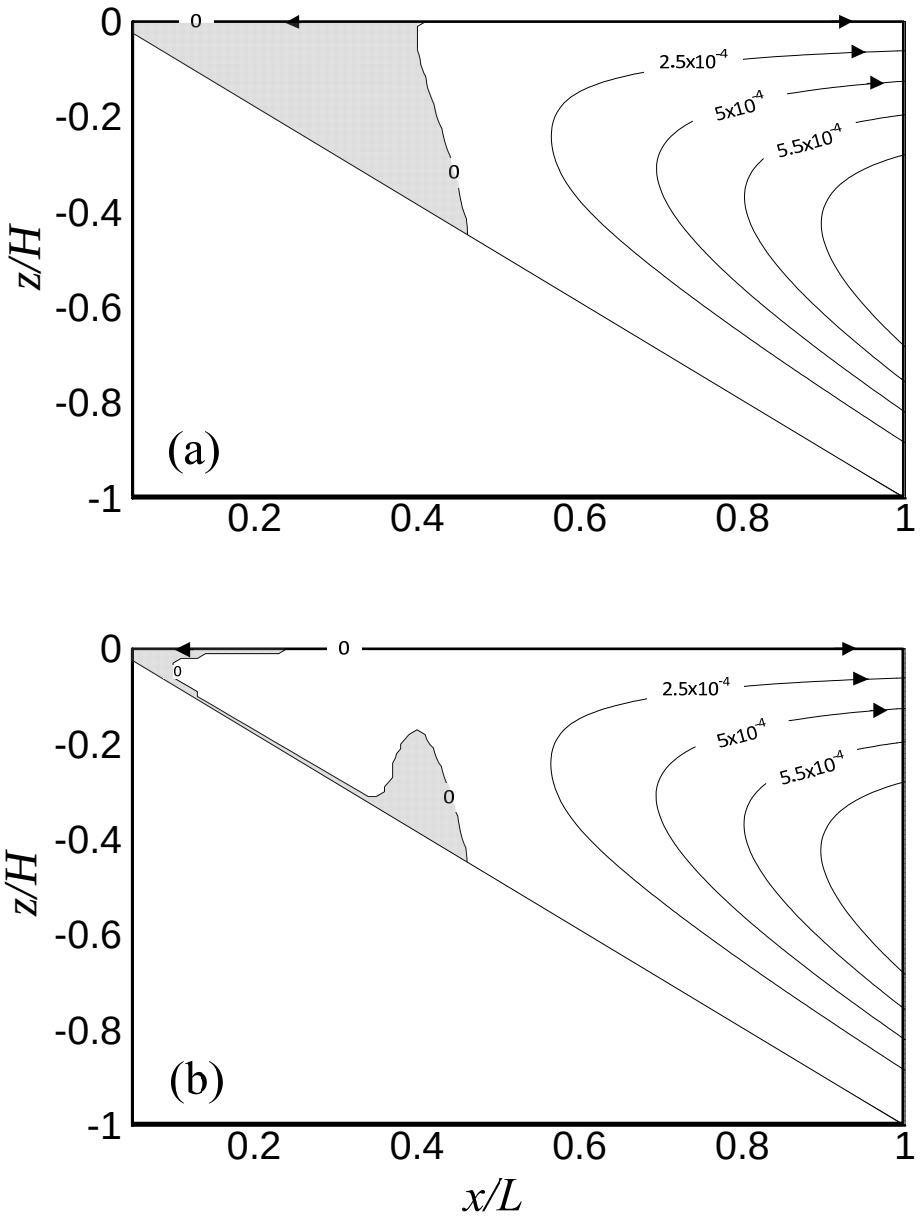

Figure 3.17 Streamline contours for $\eta = 0.5, t = 1.25$ of equal heating and cooling for high vegetation in shallow water, and open in deep water: (a) 0% solar radiation penetration; and (b) 0.1% solar radiation penetration. Note: $k = 20$, and shadow areas denote counter-clockwise circulations.

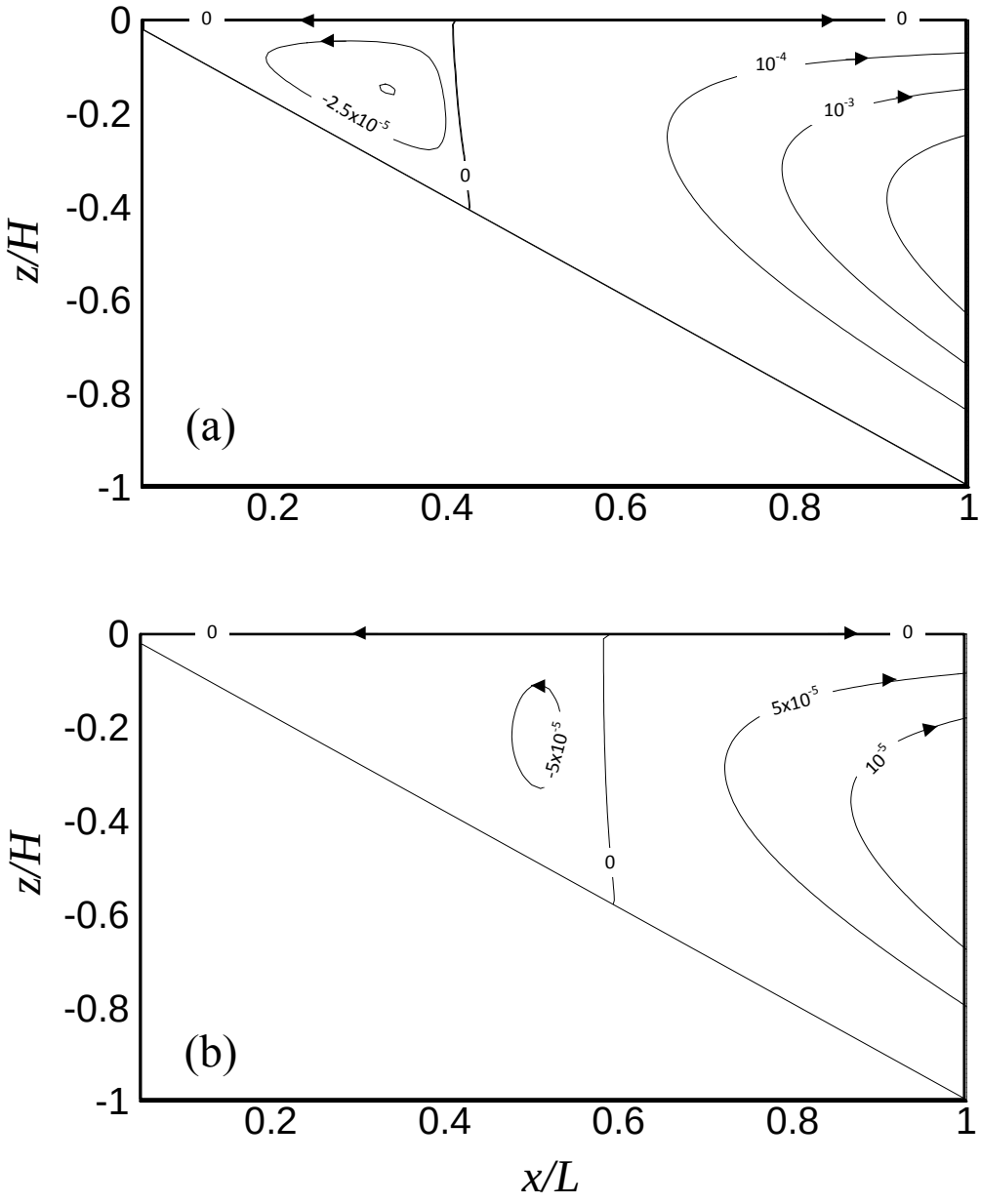

Figure 3.18 Streamline contours for $\eta = 0.5, t = 0.75$ for equal heating and cooling: (a) high vegetation in shallow water, and open in deep water; and (b) open in shallow water, and high vegetation in deep water. Note: $k = 20$, and blockage of solar radiation *B* is 85%, i.e. 15% penetration.

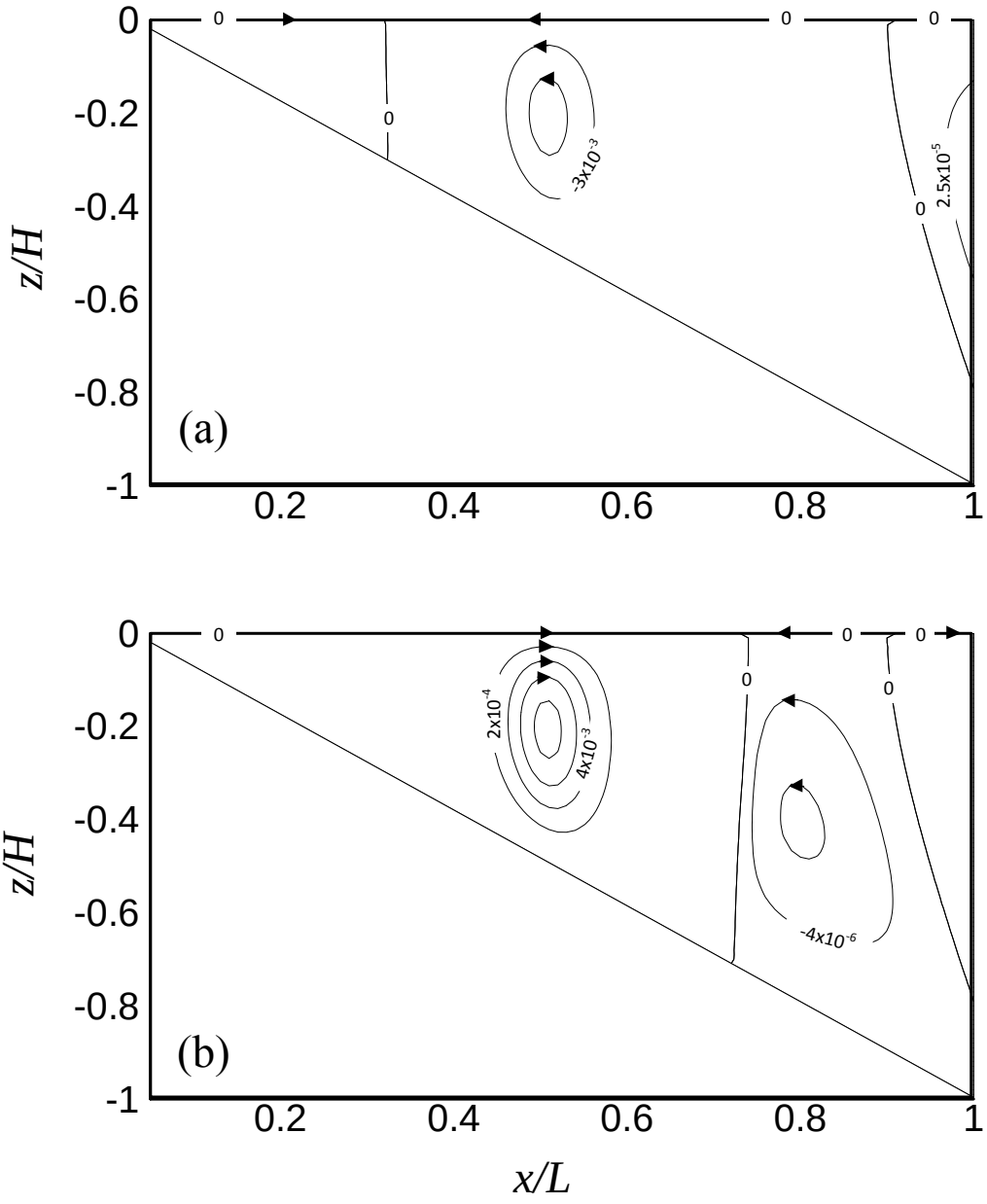

Figure 3.19 Streamline contours for $\eta = 50, t = 1.25$ for equal heating: (a) high vegetation in shallow water, and open in deep water; and (b) open in shallow water, and high vegetation in deep water. Note: $k = 20$.

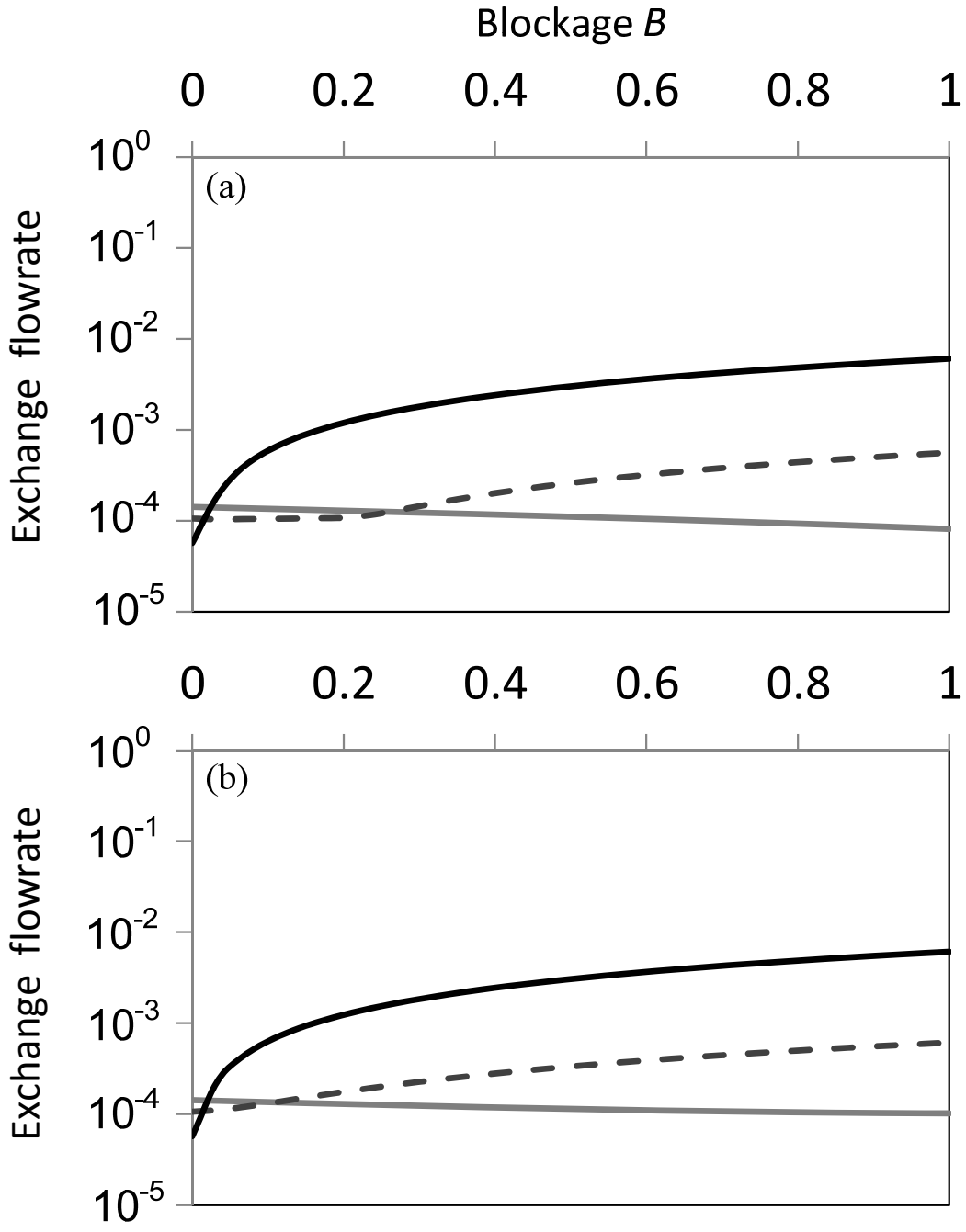

Figure 3.20 Exchange flowrate with different blockage of solar radiation: (a) emergent vegetation in shallow water, and open in deep water, and (b) open in shallow water, and emergent vegetation in deep water. (—: $\eta = 0.5$, —: $\eta = 50$, – –: $\eta = 5$).

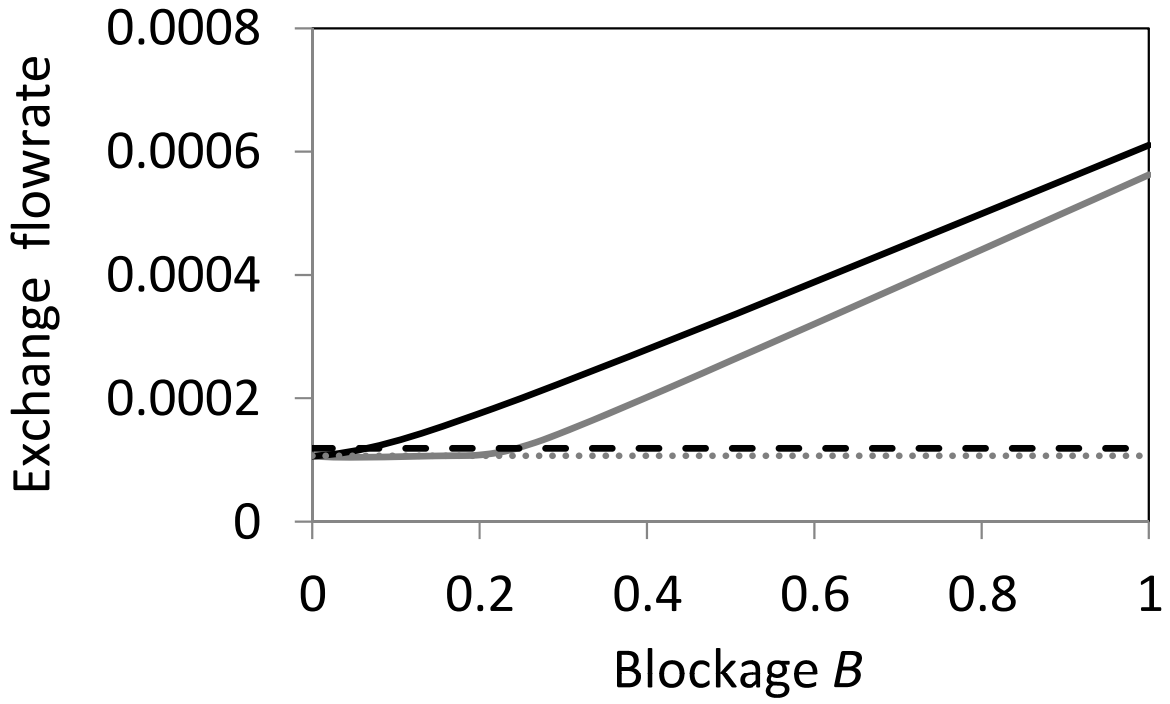

Figure 3.21 Exchange flowrate of $\eta = 5$ for four cases: (i) no vegetation (– –), (ii) uniform-distributed vegetation (‘‘‘‘‘‘), (iii) vegetation in shallow water and open in deep water (——), and (iv) open in shallow water and vegetation in deep water (——).

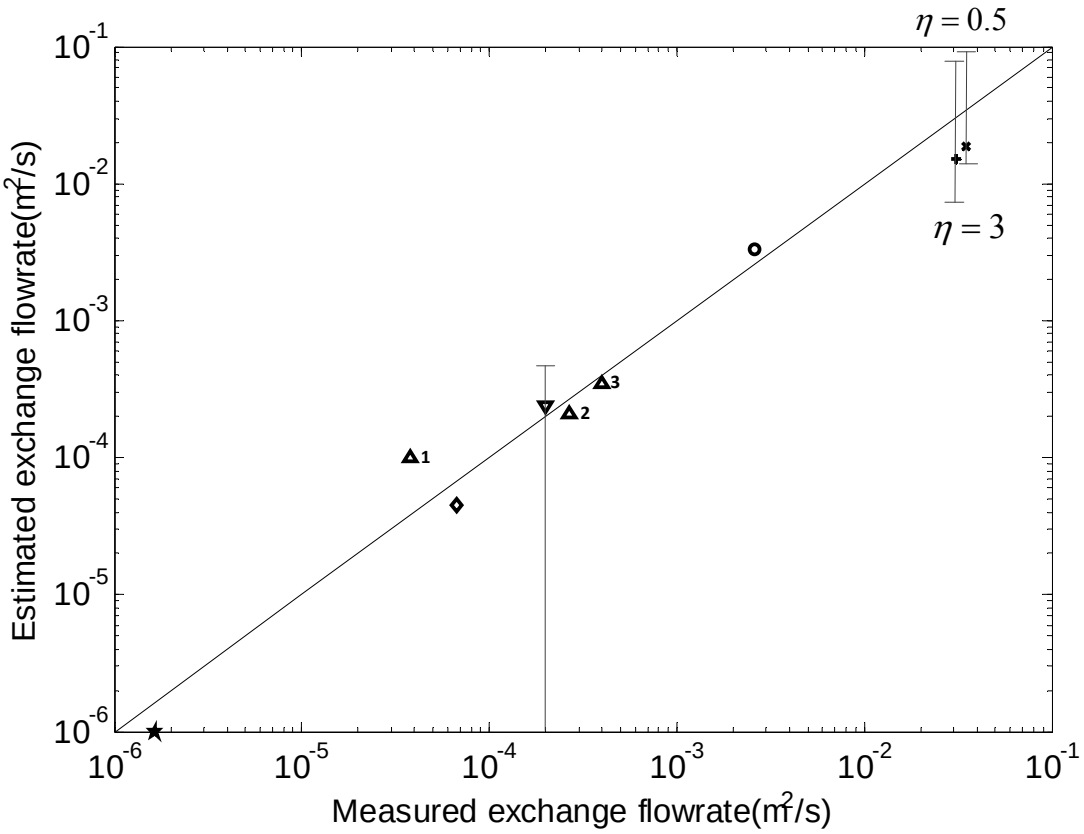

Figure 3.22 Comparisons of exchange flowrate between estimated from asymptotic solution and measurements. The upwarding (▵) and downwarding-triangles (▽) denote the laboratory and filed results within vegetation from Oldham and Sturman (2001). The others represent the results without vegetation, which are ‘ ○ ’ and ‘ ◇ ’ from field and laboratory measurements by Sturman et al. (1999), ★’ from laboratory measurements by Chubarenko and Demchenko (2008). ‘ ✖ ’ and ‘ ✚ ’ are from field measurements carried by Adam and Wells (1984), and Monismith et al. (1990).

Chapter 4

An integrated acoustic and electromagnetic wave-based technique to estimate subbottom sediment properties in freshwater environment

This chapter was published in Near Surface Geophysics, 8(3), 213-221, as "Integrated acoustic and electromagnetic wave-based technique to estimate subbottom sediment properties in aquatic environment" by Lin, Y. T., Wu, C.H., Fratta, D., and Kung, K.-J.S.

4.1 Abstract

An integrated acoustic and electromagnetic (EM) wave-based technique was developed to estimate sediment porosity and top-layer thickness in shallow waters. The combined methodology reduces the limitation of each of the individual techniques and combines the data for a more robust inversion solution. The acoustic and EM-wave reflection coefficients are determined based on the ratios of reflected signal strengths from sediments and a reference aluminum plate. An iterative algorithm that uses reflection coefficients to optimize the sediment porosity was developed. Once the optimal sediment porosity is obtained, the acoustic and EM wave speeds and then the top-layer thickness were evaluated. In comparison with ground truth data, the measured and estimated sediment porosity and top-layer thickness show differences less than 8.6%. The new integrated method provides an efficient and accurate methodology to obtain

sediment properties under different sediment conditions.

4.2 Introduction

Geophysical instruments based on acoustic and electromagnetic (EM) wave techniques are commonly used to collect sediment properties (Telford et al. 1990; Scholz 2001; Cagatay et al. 2003). Based upon the acoustic wave reflection coefficient, the sediment acoustic speed, porosity, and mean grain size can be estimated (Bachman 1985; Richardson and Briggs 1993; Davis et al. 2002). Similarly, the EM-wave velocity, a function of dielectric permittivity in sediments, can be used to calculate the sediment porosity (Topp et al. 1980; Bristow and Jol 2003). These sediment properties are crucial for quantifying coastal sediment erosion, deposition and redistribution processes (Fukuda and Lick 1980; Teeter et al. 2001; Swenson et al. 2006). However, acoustic wave-based methods have difficulties in penetrating into coarse-grained sediments (e.g., sand and gravel) and glacial till due to low energy transmission and signal scattering (Morang et al. 1997). While EM wave-based methods are limited in high electrical conductivity environments due to high energy attenuation (Annan 2005).

Previous studies showed that combining acoustic and EM wave-based techniques helps interpreting sediment properties under different sediment conditions (Sellmann et al. 1992; Schwamborm et al. 2002; Lin et al. 2009). In recent years, some studies have attempted to numerically or experimentally estimate soil properties by using combined acoustic and EM wave-based geophysical techniques (Mutter and Mutter 1993;

Dannowski and Yaramanci 1999; Garambois et al. 2002; Fratta et al. 2005; Ghose and Slob 2006; Turesson 2006). Nevertheless, quantitative estimations of sediment properties in freshwater environments by fully integrating the two techniques are not yet available. This paper presents a quantitative methodology that integrates acoustic and EM wave-based geophysical methods to accurately quantify subbottom sediment porosity and thickness in shallow low-conductive waters. Using the acoustic wave-based subbottom profiler (SBP) and the EM wave-based ground penetration radar (GPR), the measured reflection coefficients R obtained during simultaneous surveys are incorporated into an iterative algorithm. This algorithm is then used to solve for the sediment porosity. Once the porosity is determined, the acoustic and EM wave speeds are estimated and the thickness of the top sediment layer is therefore obtained.

4.3 Methodology

Geophysical data were collected at the Little Sand Bay Harbor of the Apostle Islands National Lakeshore (Bayfield Peninsula of Lake Superior in the State of Wisconsin, USA – Figure 4.1). The size of the harbor is 60 m by 40 m with rubble mound breakwater structures on the perimeter. The bottom of the harbor is made of poorly graded sandy sediments (over 96% sandy particles with mean grain size D_{50}=0.25 mm and particles sizes ranging from 0.075 to 4.75 mm) as determined from ten in-situ grab samples.

A Tritech SeaKing SBP system with a GPS receiver and a Sensor & Software

EKKO Pulse 1000 GPR system were mounted on a Zodiac boat to simultaneously collect acoustic and EM-wave reflection data (Figure 4.2). The Tritech Seaking SBP is a parametric echo-sounder. Parametric echo-sounders use a high frequency signal and the non-linearity of water to generate a narrow, low frequency beam within the high frequency signal (Schrottke et al., 2006). This is accomplished by emitting two slightly different high frequencies signals (~100 kHz) to create high (i.e., 200 kHz) and low (i.e., 20 kHz) frequency signals. As the high and low frequencies have the same carrier, they yield no side lobes and have similar footprints (Schrottke et al., 2006). The theoretical vertical resolution (i.e., wave velocity over two times the bandwidth) is ~0.00375 m for the high frequency and ~0.0375 m for the low frequency component. The GPR system is equipped with 450 MHz antennae (dominant frequency: 225 MHz) to capture bottom and subbottom reflections with vertical resolution of 0.037 m in water and 0.11 m in sediments (i.e., a quarter of the EM wavelength assuming the EM wave velocity in water and sediments are around 0.33×10^8 m/s and 10^8 m/s).

According to the Fresnel's ellipse, the diameter *d* of the footprint for the SBP or GPR systems can be determined by (Schwamborn et al., 2002):

$$d=V\cdot\sqrt{\frac{t}{f}} \tag{4.1}$$

where V is the wave velocity, t is the two-way travel time, and f is the frequency of the wave. The diameter of the footprints for the SBP and GPR are 0.16 and 0.62 m respectively (for a 2 m depth). The SBP and GPR acquisition parameters are provided in Table 3.1. Even though the footprint diameters are not identical, low frequency SBP and

GPR have similar resolutions; therefore, they are used in the proposed methodology to simultaneously evaluate sediment porosity and layer thickness.

To characterize sediment porosity, the reflection coefficient R (i.e., the ratio of the reflection wave amplitude to the incident wave amplitude) is obtained from both SBP and GPR survey data. The reflected wave strength E for both acoustic and EM waves can be expressed as (Gregoire and Hollender 2004; Robb et al. 2007):

$$E(\mathrm{dB}) = 20\log\left[\frac{A(L)}{A(L_0)}\right] = 20\log\left[T_T \cdot G \cdot T_R \cdot R \cdot e^{-\alpha \cdot L}\right] \tag{4.2}$$

where A is the signal amplitude, L is the reflected distance, L_0 is a reference distance (i.e., a quarter of the acoustic and EM wavelengths in water), T_T and T_R are the responses of the transmitter and receivers, α is the water attenuation coefficient, and $G(=(L_0/L)^{\beta})$ accounts for geometrical spreading where β is the spreading coefficient depending on the geometry of the wavefront (Telford et al. 1990). In this study, the geometric spreading is assumed to be constant and equal to one.

Eq. (4.2) has several unknown parameters and the reflection coefficient cannot be directly calculated from the collected wave strength. To solve this problem, the parameters T_T, T_R, and α must be determined for the SBP and GPR systems by obtaining reflected signals at different depths from an interface with a known reflection coefficient. By using strength ratios of reference signals, the measured reflection coefficient R_{sed} for the SBP or GPR data at water-sediment interface can be evaluated as:

$$E_{ref}-E_{sed}=20\cdot\left[\log\left(T_T\cdot G\cdot T_R\cdot R_{ref}\cdot e^{-\alpha\cdot L}\right)-\log\left(T_T\cdot G\cdot T_R\cdot R_{sed}\cdot e^{-\alpha\cdot L}\right)\right] \quad (4.3)$$

and simplified to:

$$R_{sed}=R_{ref}\cdot 10^{\frac{E_{sed}-E_{ref}}{20}} \quad (4.4)$$

where R_{ref} is the reflection coefficient of the SBP or GPR data from a known reflection interface, E_{sed} is the measured signal strength for the SBP or GPR data from the bottom sediment, and E_{ref} is the reference signal strength for the SBP or GPR data from the known reflection interface.

In this study, the reference responses were collected from a 0.7 m-diameter (smaller than the footprints of the SBP and GPR signals) and 0.02 m-thick aluminum plate. The density and acoustic speed of aluminum are 2700 kg/m^3 and 4915 m/s. The reflection coefficient at the water-aluminum plate-sediment interface range due to the three-media nature of the problem (Fratta and Santamarina 2002). However, reflection coefficients for the 200 kHz incident frequency and different plate thicknesses (i.e., wavelength/plate thickness ratios equal to 0.6 to 2.4) showed constant reflection amplitudes, so the reflection coefficient was assumed constant and equal to the two media reflection (i.e., 0.797). For normal incident EM-waves, the reference reflection coefficient is R_{ref}=-1. To address the effect of geometrical spreading and signal attenuation in Eq. (4.2), the systems were calibrated at four different depths. Then, the unknown parameters of $T_T\cdot T_R$, and α were obtained, and used to evaluate the reference signal strengths at the ranges of water depth tested.

To validate the results, ground truth data were collected using Shelby tube core samples and a hydraulic jetting system. The Shelby tube is a thin-wall tube used to collect sediment samples (Lee et al. 2004). When the sediment core samples were collected, a diver helped covering the end side of the tube with a cap to prevent the sandy sediments from escaping the tube. The collected cores were used to estimate the bottom sediment porosity. In addition, the hydraulic jetting system was used to directly measure the thickness of sandy sediments (Rukavina and Lahaie 1991; Lin et al. 2009). The bottom sediments were fluidized using a high pressure water jet while the jetting pipe was advanced into the sediment layer. Penetration continued until the jet encountered firm glacial sediments. The penetration depth was regarded as the thickness of the top-sandy layer.

4.4 Data Interpretation

For the SBP system, the incident acoustic wave is nearly normal to the water-sediment interface as the same piezocrystal is used to send and receive the acoustic signals. The normal incident wave reflection coefficient from bottom sediments is:

$$R_{sed}^{SBP} = \frac{\rho_{sed} V_{p\_sed} - \rho_{water} V_{p\_water}}{\rho_{sed} V_{p\_sed} + \rho_{water} V_{p\_water}} \tag{4.5}$$

where ρ_{sed} and ρ_{water} are the bulk densities of sediment and water, and V_{p_sed} and V_{p_water} are the acoustic velocities in sediment and water. The bulk density ρ_{sed} and acoustic velocity V_{p_sed} in sediments are both functions of sediment porosity n. Given that the

sediments are fully saturated, the sediment bulk density ρ_{sed} is

$$\rho_{sed} = (1\text{-}n) \cdot \rho_s + n \cdot \rho_{water} \tag{4.6}$$

where ρ_s=2650 kg/m^3 and ρ_{water}=1000 kg/m^3 are the assumed density of the sandy sediment particles and water. The acoustic velocity V_{p_sed} is also a function of the stiffness of the pore water and the sediment skeleton (Santamarina et al. 2001):

$$V_{p\_sed} = \sqrt{\frac{B_{sed} + \frac{4}{3} G_{sed}}{\rho_{sed}}} \tag{4.7}$$

where B_{sed} and G_{sed} are the bulk and shear modulus of the sediment fabric. The sediment bulk modulus is a function of the bulk water B_{water}, sediment solid particles B_s, sediment skeleton B_{sk} and Poisson's ratio ν (Fratta et al. 2005):

$$B_{sed} = \frac{1}{\frac{n}{B_{water}} + \frac{1-n}{B_s}} + B_{sk} = \frac{1}{\frac{n}{B_{water}} + \frac{1-n}{B_s}} + \frac{2}{3}\frac{1+\nu}{1-2\nu} G_{sed} \tag{4.8}$$

The sediment shear modulus G_{sed} is therefore determined as a function of the S-wave velocity: $G_{sed}=(V_{s\_sed})^2 \cdot \rho_{sed}$, where S-wave velocity V_{s_sed} is

$$V_{s\_sed} = \theta \left(\frac{\sigma'_{mean}}{p_r} \right)^{\eta} \tag{4.9}$$

where σ'_{mean} is the average effective stress in the polarization plane, θ and η are sediment-dependent parameters, and p_r=1 kPa is a reference stress (Santamarina et al. 2001).

For the GPR system, the generated EM-wave is a polarized wave that can be divided into perpendicular and parallel polarized waves according to the orientation of the antennas relative to each other and to the transect (Reppert et al. 2000). For low conductivity and non-ferromagnetic materials, the EM wave velocity V_{sed}^{GPR} is:

$$V_{sed}^{GPR} = \frac{c}{\sqrt{\varepsilon_{sed}^{'}}} \tag{4.10}$$

where $c=3\cdot10^8$ m/s is the EM-wave speed in free space and ε_{sed}' is the real relative dielectric permittivity. For incident and reflected angles θ_1 (Figure 3.2a), the parallel polarized reflection coefficient R_{sed}^{GPR} for low conductivity and non-magnetic materials is (Ward and Hohmann 1988; Kraus and Fleisch 1999):

$$R_{sed}^{GPR} = \frac{\cos(\theta_1) - \sqrt{\frac{\varepsilon_{sed}'}{\varepsilon_{water}'} - \sin^2(\theta_1)}}{\cos(\theta_1) + \sqrt{\frac{\varepsilon_{sed}'}{\varepsilon_{water}'} - \sin^2(\theta_1)}} \tag{4.11}$$

where ε_{sed}' and ε_{water}' are the real relative dielectric permittivities of the sediments and the water. The real dielectric permittivity of the ε_{sed}' is related to the saturated sediment porosity:

$$\left(\varepsilon_{sed}^{'}\right)^{\gamma} = (1-n)\left(\varepsilon_{s}^{'}\right)^{\gamma} + n\left(\varepsilon_{water}^{'}\right)^{\gamma} \tag{4.12}$$

where ε_s' (=3 to 10) is the real relative dielectric permittivity of sediment solid particles. Different types of formulation have been proposed for Eq. (3.12) depending on the exponent γ. Looyenga (1965) suggested a value of γ equal to 1/3 while when γ is 0.5, the

equation is known as Complex Refractive Index Method (CRIM - Birchak et al. 1974). When γ is 1.0, the formulation is the volumetric mean of the mixtures (Brown 1956). Roth et al. (1990) suggested γ values of 0.65 and 0.46 for sandy and clayey sediment types. In this study, these different formulas were tested and compared to the ground-truth data.

Finally, combining Eqs. (4.5) to (4.9) with Eqs. (4.10) to (4.12), the reflection coefficients R_{sed}^{SBP} and R_{sed}^{GPR} can be calculated if the porosity is assumed. The measured reflection coefficients for the SBP or GPR data were obtained from Eq. (4.4). Then, the porosity is determined by minimizing the objective function F that consists of difference of measured and estimated reflection coefficients for both SBP and GPR surveys, i.e.,

$$F = \left[\left(R_{sed}^{SBP}\right)^{<measured>} - \left(R_{sed}^{SBP}\right)^{<calculated>}\right]^2 + \left[\left(R_{sed}^{GPR}\right)^{<measured>} - \left(R_{sed}^{GPR}\right)^{<calculated>}\right]^2 \quad (4.13)$$

where <measured> indicates the reflection coefficients measured during the surveys and <calculated> indicates the reflection coefficients calculated using Eqs. (4.5) and (4.11). By setting the derivative of the objective function with respect to the porosity n equal to zero,

$$\left[\left(R_{sed}^{SBP}\right)^{<measured>} - \left(R_{sed}^{SBP}\right)^{<calculated>}\right] \cdot \frac{\partial\left[\left(R_{sed}^{SBP}\right)^{<claculated>}\right]}{\partial n} + \left[\left(R_{sed}^{GPR}\right)^{<measured>} - \left(R_{sed}^{GPR}\right)^{<calculated>}\right] \cdot \frac{\partial\left[\left(R_{sed}^{GPR}\right)^{<claculated>}\right]}{\partial n} = 0 \quad (4.14)$$

the optimal porosity is therefore obtained. The acoustic and EM wave velocities are calculated using the determined optimal porosity. Figure 4.3 summarizes in a flow chart of the inversion procedure.

4.5 Results and Discussions

Reflection calibration. To calibrate the response of the two systems, reference and sediment reflection signatures for the SBP and GPR surveys were measured. The reference reflection signatures were collected from the aluminum plate placed on the bottom sediment underneath the SBP and GPR systems (Figure 4.2b). Data were collected at four different locations with four different depths within the harbor (i.e., 1.6, 2.0, 2.4, and 2.8 m). All these places had sediments with very similar particle size distributions as documented by the collected grab samples. More than 100 traces were captured and then averaged to increase signal-to-noise ratios.

Figures 4.4 and 4.5 present the SBP and GPR reflected signal strengths from the aluminum plate and bottom sediments at a depth of 1.6 m. The SBP system collected the acoustic responses from the aluminum plate and bottom sediments and presented the records in terms of decibels (Figure 4.4a). Figure 4.5 shows the EM wave signal reflected from the aluminum plate and bottom sediments in time and frequency domains. The EM wave responses are plotted in decibels by normalizing the measured amplitude by the minimum voltage the GPR system can resolve (Figure 4.5c).

The reflection coefficient at the water-sediment interface is obtained from the peak of the amplitude spectra of wavelets normalized by the peak of the reflected amplitude spectra of the aluminum plate (using Eq. (4.4), values from Figures. 4.4a and 4.5b, and R_{ref}=0.797 for the SBP and R_{ref}=-1 for the GPR). The reflection coefficients for the SBP and GPR were estimated as 0.372 and 0.281, respectively. Using the algorithm presented in Section 4.3, and setting θ=80 m/s and η=0.25 for loose sand in Eq. (4.9) (Santamarina

et al. 2005), and ε_s' between 3 and 10, the sediment porosity is calculated. For γ values varying between 1/3 and 1 in Eq. (4.12), the calculated sediment porosities vary between 0.38 and 0.43, which all closely match the measured sediment porosity of 0.44 from the sediment core data. Due to very slight variations in the calculated sediment porosity, γ=0.5 as CRIM formula is therefore used in this study.

Then, reflection amplitude collected at four depths were plotted and fitted with a regression curve (Figures. 4.4b and 4.5d) to allow for the estimation of the unknown reflection model parameters. The range for the acoustic wave attenuation coefficient α in freshwater varies between 0.00012 to 0.00058 Np/m (Urick 1976). Based upon data from the US EPA (2009), the electrical conductivity σ of water in Lake Superior was $159 \cdot 10^{-4}$ S/m collected two months later than survey date. The EM wave attenuation factor α is given by:

$$\alpha = \omega \left\{ \frac{\mu\varepsilon}{2} \left[\left(1 + \frac{\sigma^2}{\varepsilon^2 \omega^2} \right)^{1/2} - 1 \right] \right\}^{1/2} \tag{4.15}$$

where ω (=$2\pi f$) is the angular frequency, ε is the dielectric permittivity (F/m), μ is the magnetic permeability (H/m) of the medium. With the parameters listed in Table 4.2, we obtained, according to Eq. (4.15), an attenuation coefficient α - 0.335 Np/m. Due to changes in water temperature and total dissolved salts (Hayashi 2004), the EM wave attenuation coefficient α may vary between 0.100 to 0.500 Np/m. Fitting parameters $T_T \cdot T_R$, and α were varied until a minimum difference between the measured and calculated reflection signal strengths was found. The estimated EM wave attenuation coefficient α was 0.136 Np/m (Figure. 4.5d) that was smaller than the value obtained with

Eq. (4.15) using US EPA data. For acoustic wave, the calculated attenuation coefficient α is very small (~0.00046 Np/m – similar to the value reported by Urick 1976), and therefore it was neglected. The fitting curves and corresponding parameters for the SBP and GPR data are presented in figures 4.4b and 4.5d, and in Table 4.3.

Field Surveys. Two lines, one inside the harbor and another outside the harbor (Lines 1 and 2 in figure 4.1) were surveyed to estimate the sediment porosity and top-layer thickness. A moving average algorithm with data window of 10 traces was used to obtain smooth reflection coefficients. These reflection coefficients were then used to estimate porosity and acoustic and EM speeds in sediments layers. In the SBP survey, no layer structure was observed, while the GPR survey data provided one visible layer (Figure 4.6). The sandy sediments might have prevented the acoustic signals from penetrating into the sublayer while still allowing EM-waves to propagate into the subbottom. At some places, there was no layer visible in the GPR data possibly because of the lateral topographic variations. For example, the V_{sed}^{GPR} value of 0.06 m/ns yields a vertical resolution of 0.067 m; then layer thicknesses smaller than this value would not be detected. Following the proposed procedures, a porosity of 0.42 was estimated, which is close to the ground-truth measured values of 0.39 (difference=7.7 %). The two-way travel time data into the subbottom multiplied by the calculated EM wave speed is used to obtain the sandy layer thickness. A comparison with the hydraulic jetting results indicates that the average difference between measured and calculated layers thickness is only 7.2 % (see figure 4.6).

The survey line outside the harbor shows a sand dune (section D in Figure 4.7). Sand dunes frequently occur along the nearshore of the Great Lakes (Davidson-Arnott and Ollerhead 1995). There is one distinct layer between 10 to 40 m of the survey line (see figure 4.7). The results show that the calculated sediment porosity ranges between 0.3 to 0.45 in the nearshore. These values agree with porosity commonly found in sandy sediments along the nearshore of the Great Lakes (Quigley and Robbins 1984). In these offshore areas, sediment porosities have been documented to be as small as 0.3. When the water depth increases, wave disturbances on the bottom are less significant (Mei 1989) and smaller sediment porosities are typically found. The top-layer thickness in the sand dune varied between 0.1 to 0.6 m. The top-layer sandy sediment thickness was verified using the hydraulic jetting system at three locations along the sand dune (Figure 4.7), and the measured thicknesses are all close to the estimates (average difference = 8.6 %).

Overall, the small differences between the measurements and estimates of sediment porosity and top-layer thickness may be attributed to: (i) errors from the energy loss of reflected signal due to local sediment texture and scattering, (ii) the acoustic and radar speeds may not be constant within the top-layer because of inhomogeneous features (sediment densities always increases with the depth) in sediments, and (iii) spatial variations of sediment properties may lead to different absorptions and reflection of signals. Nevertheless, the integrated acoustic and electromagnetic wave-based technique performs well yielding less than 8.6 % difference between the estimated and measured sediment porosity and top-layer thickness. The combined geophysical techniques indeed reduce the limitations of the single technique applied. That is, when the SBP signals were unable to image the sublayers inside the harbor areas, the GPR signals provided sublayer

data in the sandy sediments. In comparison with the traditional coring method, the integrated acoustic and EM wave techniques eliminate the logistical efforts and obtain in-situ sediment properties efficiently.

4.6 Conclusions

An integrated acoustic and EM-wave based technique to measure sediment properties in freshwater environments is presented. The reflection coefficients of sediments are determined based on the ratios of reflected signal strengths from sediments and an aluminum plate. Based upon the sediment porosity data collected at water depth of 1.6 m, the coefficient γ for different values in the mixture equation showed insignificant effects on porosity estimates. Then, the CRIM formula was adopted in this study for calculating EM wave speed in sediments. After the SBP and GPR reflected signals were calibrated using an aluminum plate at different depths, the sediment reflection coefficients were estimated. An iterative inversion method based on the minimization of the SBP and GPR reflection coefficient objective function was used to calculate the local subbottom sediment porosity and the top layer thickness. In comparison with the ground-truth data, the measured and estimated sediment porosity and top-layer thickness show differences less than 8.6%. In summary, this new integrated methodology provides an effective, non-destructive way to estimate the in-situ sediment porosity and top-layer thickness under different sediment conditions, which is helpful to evaluate nearshore erosion and deposition processes.

4.7 **References**

Annan, A.P. (2005). Ground penetrating radar. In *Near Surface Geophysics*, Edited by K. Butler. Society of Exploration Geophysics. Tulsa, OK: 357-438.

Bachman, R.T. (1985). Acoustic and physical property relationships in marine sediment. *J. Acoust. Soc. Am.*, 78: 616-621.

Birchak, J.R., Gardner, C.G., Hipp, J.E., and Victor, J.M. (1974). High dielectric microwave probes for sensing soil moisture. *Proceedings of the IEEE*, 62, 1, 93-98.

Bristow, C. S and Jol, H. M., Eds. (2003). *An Introduction of Ground Penetrating Radar (GPR) in Sediments*, Geological Society, London, Special Publications, 211: 1-7.

Brown, Jr., W.F. (1956). Dielectrics, in *Encyclopedia of Physics*, 17: Berlin: Springer.

Cagatay, M.N., Gorur, N., Polonia, A., Demirbag, E., Sakinc, M., Cormier, M.-H., Capotondi, L., McHugh C., Emre, O., and Eris, K. (2003). Sea-level changes and depositional environments in the Izmit Gulf, eastern Marmara Sea, during the late glacial-Holocene period. *Marine Geology*, 202(3-4): 159-173.

Dannowski, G. and Yaramanci, U. (1999). Estimation of water content and porosity using combined radar and geoelectrical measurements. *European Journal of Environmental and Engineering Geophysics*, 4, 71-85.

Davis, A., Haynes, R., Bennell, J., and Huws, D. (2002). Surficial seabed sediment properties derived from seismic profiler responses. *Mar. Geol.* 182: 209-223.

Davidson-Arnott, R.G.D. and Ollerhead, F. (1995). Nearshore erosion on a cohesive shoreline. *Mar. Geol*., 122: 349-365.

Fratta, D. and Santamarina, J. C. (2002). Shear Wave Propagation in Jointed Rock: State of Stress. *Geotechnique*. 52(7): 495-505.

Fratta, D., Alshibli, K.A., Tanner, W.M., and Roussel, L. (2005). Combined TDR and P-wave Velocity Measurements for the Determination of in Situ Soil Density. *ASTM Geotechnical Testing Journal*, 28(6): 553-563.

Fukuda, M.K. and Lick, W. (1980). The entrainment of cohesive sediment in freshwater. *J. Geophys. Res.*, 85(C5): 2813-2824.

Garambois, S., Senechal, P., Perroud, H. (2002). On the use of combined geophysical methods to assess water content and water conductivity of near-surface formation. *Journal of Hydrology*, 259, 32-48.

Ghose, R. and Slob, E.C. (2006). Quantitative integration of seismic and GPR reflections to derive unique estimates for water saturation and porosity in subsoil. Geophysical research letter, 33: L05404, doi:10.1029/2005GL025376.

Gregoire, C. and Hollender, F. (2004). Discontinuity characterization by the inversion of the spectral content of ground-penetrating radar (GPR) reflections – Application of the Jonscher model. *Geophysics*, 69(8), 1414-1424.

Hayashi, M. (2004). Temperature-electrical conductivity relation of water for environmental monitoring and geophysical data inversion. Environmental Monitoring and assessment, 96(1-3), 119-128.

Kraus, J.D. and Fleisch, D. (1999). *Electromagnetics*. McGraw-Hill Higher Education. 637 pages.

Lee, C., Wu, C.H. and J.A. Hoopes. (2004). Automated sediment erosion testing system using digital imaging, *J. Hydraulic Engineering - ASCE*, 130, 8, 771-781.

Lin, Y.T., Schuettpelz, C.C., Wu, C.H., and Fratta, D. (2009). A combined acoustic and electromagnetic wave-based technique for bathymetry and subbottom profiling in

shallow waters. *Journal of Applied Geophysics*, 68(2), 203-218. Doi: 10.1016/j.jappgeo.2008.11.010

Looyenga, H. (1965). Dielectric constants of mixtures. *Physica*, 31: 401-6.

Mei, C.C. (1989). The applied dynamics of ocean surface waves. World Scientific. 760 pages.

Morang, A., Larson, R., and Gorman, L. (1997). Monitoring the coastal environment; Part III: Geophysical and research methods. *Journal of Coastal Research*, 13(4): 1064-1085.

Mutter, C.Z. and Mutter, J.C. (1993). Variations in thickness of layer 3 dominate oceanic crustal structure. *Earth and Planetary Science Letters*, 117: 295-317.

Quigley, M.A. and Robbins, J.A. (1984). Silica regeneration processes in nearshore southern Lake Michigan. *Journal of Great Lakes Res*., 10(4), 383-392.

Reppert, P.M., Morgan, F.D., and Toksoz, M.N. (2000). Dielectric constant determination using ground-penetrating radar reflection coefficient. *Journal of Applied Geophysics*, 43: 189-197.

Richardson, M.D. and Briggs, K.B. (1993). On the use of acoustic impedance values to determine sediment properties. *Proc. Inst. Acoustics*, 15(2): 15-24.

Robb, G.B.N., Best, A., Dix, J., White, P., Leighton, T., Bull, J., and Harris. A. (2007). Measurement of the in situ compressional wave properties of marine sediments. *IEEE Journal of Oceanic Engineering*, 32(2):.484-496.

Roth, K., Schulin, R., Fluhler, H., and Atinger, W. (1990). Calibration of time domain reflectometry for water content measurement using a composite dielectric approach. *Water Resource Research*, 26: 2267-2273.

Rukavina, N.A. and Lahaie, G.G. (1991). Measurement of thickness of nearshore sand by hydraulic jetting. *J. Sediment. Petrol*. 62(4): 737-738.

Santamarina, J.C., Klein, K., and Fam, M. (2001). Soils and Waves. Wiley. Chichester, UK, 488 pages.

Santamarina, J.C., Rinaldi, V.A., Fratta, D., Klein, K.A., Wang, Y.H., Cho, G.C., Cascante, G. (2005). A survey of elastic and electromagnetic properties of near-surface soils. In: Buttler, D. (Ed.). Near-Surface Geophysics, pp. 71-87.

Scholz, C.A. (2001). Application of seismic sequence stratigraphy in lacustrine basins. In, *Tracking Environmental Changes Using Lake Sediments*, Edited by W.M. Last and J.P. Smol. Volume 1: Basin Analysis, Coring, and Chronological Techniques. Kulwer Academic Publishers. Dordrecht, The Netherlands: 7-22.

Schrottke, K., Becker, M., Bartholoma, A., Flemming, B.W., and Hebbeln, D. (2006). Fluid mud dynamics in the Weser estuary turbidity zone tracked by high-resolution side-scan sonar and parametric sub-bottom profiler. *Geo-marine letters*, 26(3): 185-198.

Schwamborn, G.J., Dix, J.K., Bull, J.M., and Rachold, V. (2002). High-resolution seismic and ground penetrating radar–geophysical profiling of a thermokarst lake in the western Lena delta, northern Siberia. *Permafrost and Periglacial Processes*, 13(4): 259-269, DOI: 10.1002/ppp.430.

Sellmann, P.V., Delaney, A.J., and Arcone, S.A. (1992). *Sub-bottom surveying in lakes with ground-penetrating radar*. CRREL Report 92-8, U.S. Army Engineering Cold Regions Research and Engineering Laboratory, Hanover, NH.

Swenson, M.J., Wu, C.H., Edil, T.B., and Mickelson, D.M. (2006). Bluff recession rates

and wave impact along the Wisconsin coast of Lake Superior. *J. of Great Lakes Research*, 32(3): 512-530.

Telford, W.M., Geldart, L.P., and Sheriff, R.E. (1990). *Applied geophysics*, Cambridge University Press. Cambridge, UK.

Teeter, A.M., Johnson, B.H., Berger, C., Stelling, G., Scheffner, N.W., Garcia, M.H., and Parchure, T.M. (2001). Hydrodynamic and sediment transport modeling with emphasis on shallow-water, vegetated areas (lakes, reservoirs, estuaries and lagoons). *Hydrobiologia*, 444(1-3): 1-23.

Topp, G.C., Davis, J.L., and Annan, A.P. (1980). Electromagnetic Determination of Soil Water Content: Measurements in Coaxial Transmission Lines. *Water Resources Research*, 16(3): 574–582.

Turesson, A. (2006). Water content and porosity estimated from ground-penetrating radar and resistivity. *Journal of Applied Geophysics*, 58, 99-111.

Urick, R.J. (1976). Principles of underwater sound. 2nd Edition. McGraw-Hill Inc. 320 pages.

US EPA (2009). United States Environmental Protection Agency. URL: http://iaspub.epa.gov/waters10/attains_get_services.storet_station?p_org=WIDNR_WQX&p_station=163221 [Accessed on August 15, 2009].

Ward, S.H. and Hohmann, G.H. (1988). Electromagnetic theory for geophysical applications. In: *Electro-magnetic Methods in Applied Geophysics, Vol. 1, Theory.* M.N. Nabighian, Ed., pp. 130-311. SEG. Tulsa, OK

Table 4.1: SBP and GPR acquisition parameters

	SBP	GPR
System	Tritech Seaking SBP	Sensors and software PE1000
Transmitter	24 V	200 V
Transducer frequency	20 kHz/200 kHz	450 MHz
No. of stacks/trace	NA*	16
Antennas separation	NA*	0.25 m
Trace acquisition rate	7.52 trace / m	1 trace /m

* NA: Not applicable

Table 4.2: Parameters used for estimating EM wave attenuation coefficient α

Frequency of the EM wave field *f*	225 MHz
Dielectric permittivity ε of water	7.08×10^{-10} F/m
Magnetic permeability μ of water	$4\pi\times10^{-7}$ H/m
Electric conductivity σ of water	159×10^{-4} S/m
EM wave attenuation coefficient α of water	0.335 Np/m

Table 4.3: Regression equations for the reference signals from the aluminum plate for the combined SBP and GPR system.

SBP system	$E_{ref}^{SBP}(dB)=20\cdot\log_{10}\left[T_T\cdot T_R\cdot R_{ref}^{SBP}\cdot\left(\frac{L_0^{SBP}}{2d\text{-}2d_0}\right)^{\beta}\cdot e^{-\alpha(2d-2d_0)}\right]$ where d is the water depth and d_0 is the submerged distance of the SBP transducer, L_0^{SBP} is the reference distance for the SBP (in this study, L_0^{SBP} is used as the theoretical resolution in water with 0.0188 m), $T_T\cdot T_R=1.89\cdot10^4$, $R_{ref}^{SBP}=0.93$, $\alpha\approx0$ Np/m, and $\beta=1.0$.
GPR system	$E_{ref}^{GPR}(dB)=20\cdot\log_{10}\left[T_T\cdot T_R\cdot R_{ref}^{GPR}\cdot\left(\frac{L_0^{GPR}}{2d}\right)^{\beta}\cdot e^{-\alpha\cdot2d}\right]$ where L_0^{GPR} is the reference distance for the GPR (in this study, L_0^{GPR} is used as the theoretical resolution in water with 0.0367 m), $T_T\cdot T_R=2.62\cdot10^5$, $R_{ref}^{GPR}=1$, $\alpha\approx0.136$ Np/m, and $\beta=1.0$.

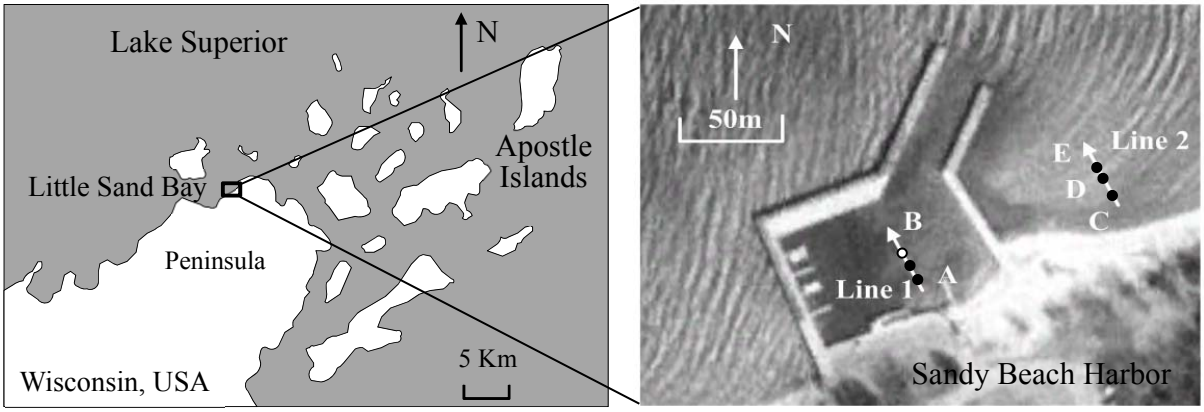

Figure 4.1: Geographic location and survey lines of the testing site at harbor of Sandy Beach (Apostle Islands National Lakeshore, Wisconsin, USA).

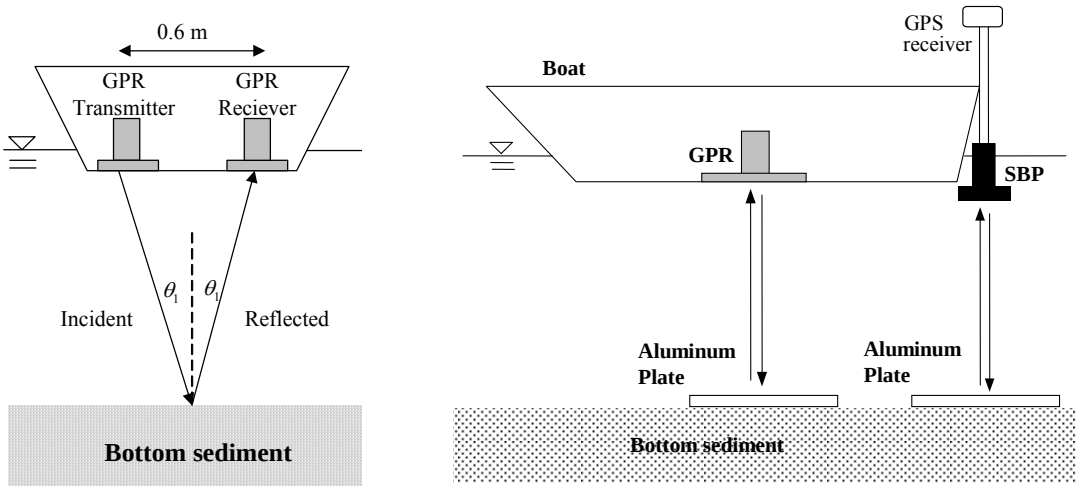

Figure 4.2 Data acquisition system: (a) cross-sectional view of GPR data reflection collection and (b) combined SBP and GPR system setup for the evaluation of the reference reflection signatures.

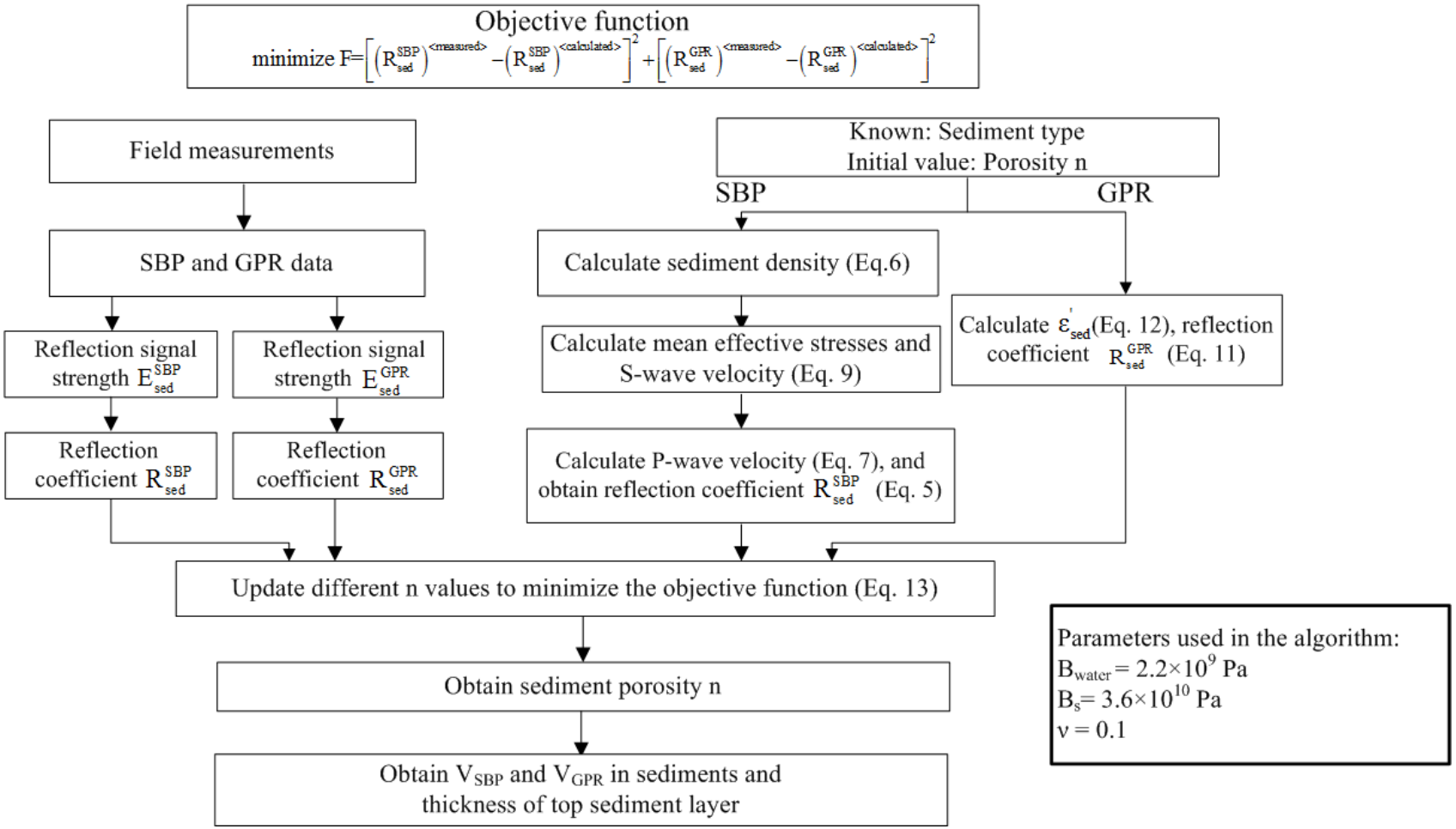

Figure 4.3 Flow chart for GPR and SBP data interpretation and inversion of sediment porosity and top-layer thicknes

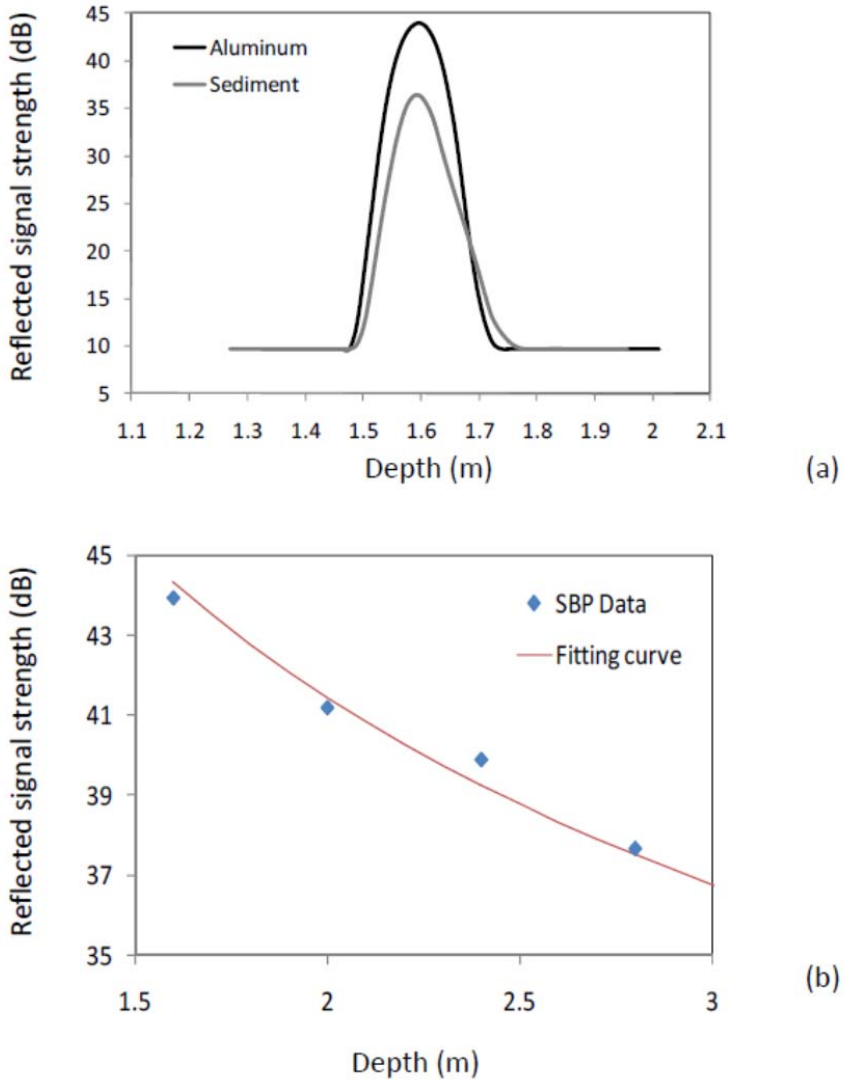

Figure 4.4: Measurements of reflection signal strength for SBP system from the aluminum plate and bottom sediments. (a) Typical SBP reflection trace and (b) SBP attenuation curve with the aluminum plate at four depths.

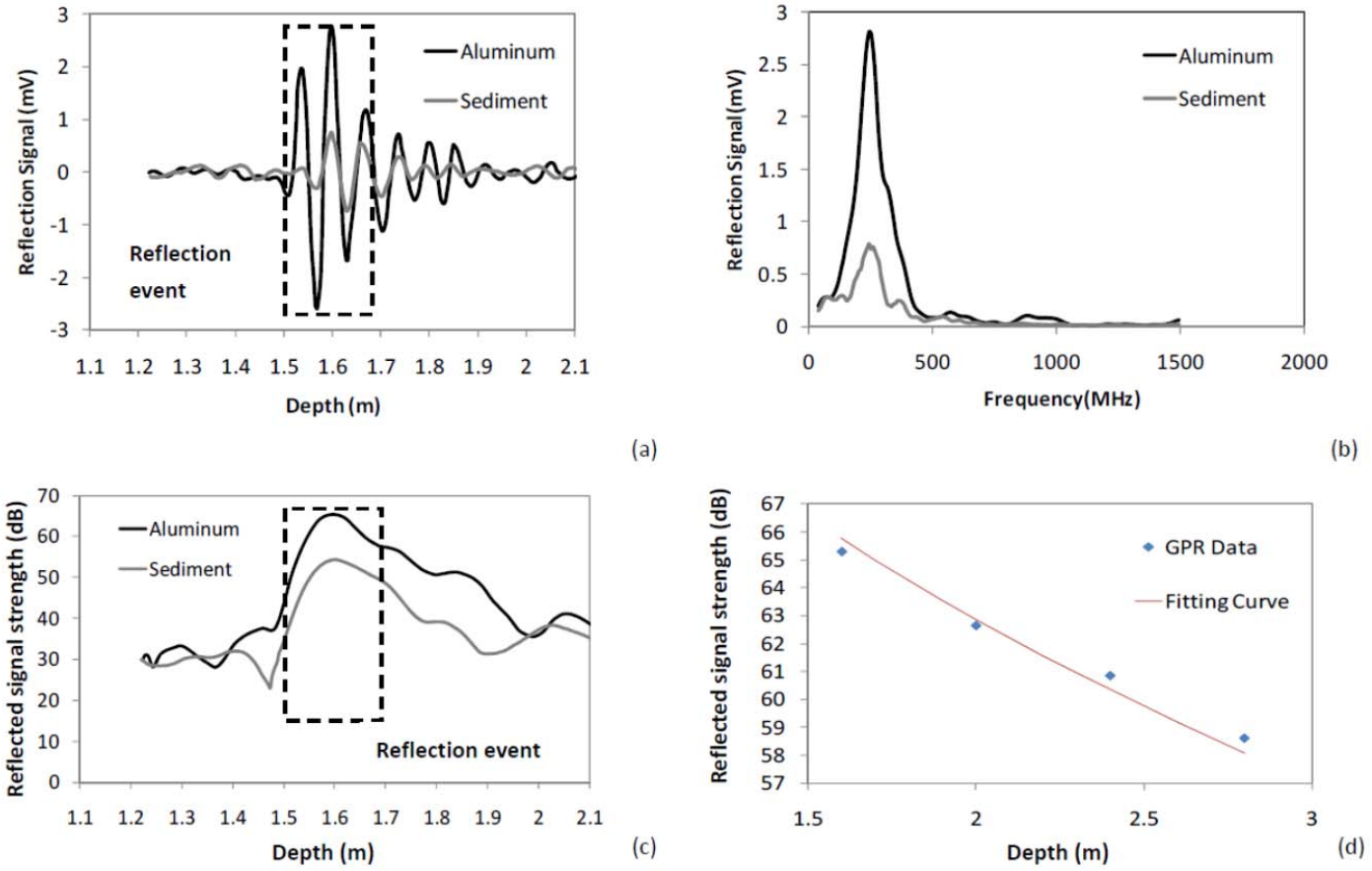

Figure 4.5: Measurements of reflection signal strength for the GPR system from the aluminum plate. Typical GPR reflection trace in (a) time and (b) frequency domains, (c) instantaneous signal strength in dB, and (d) GPR attenuation curves.

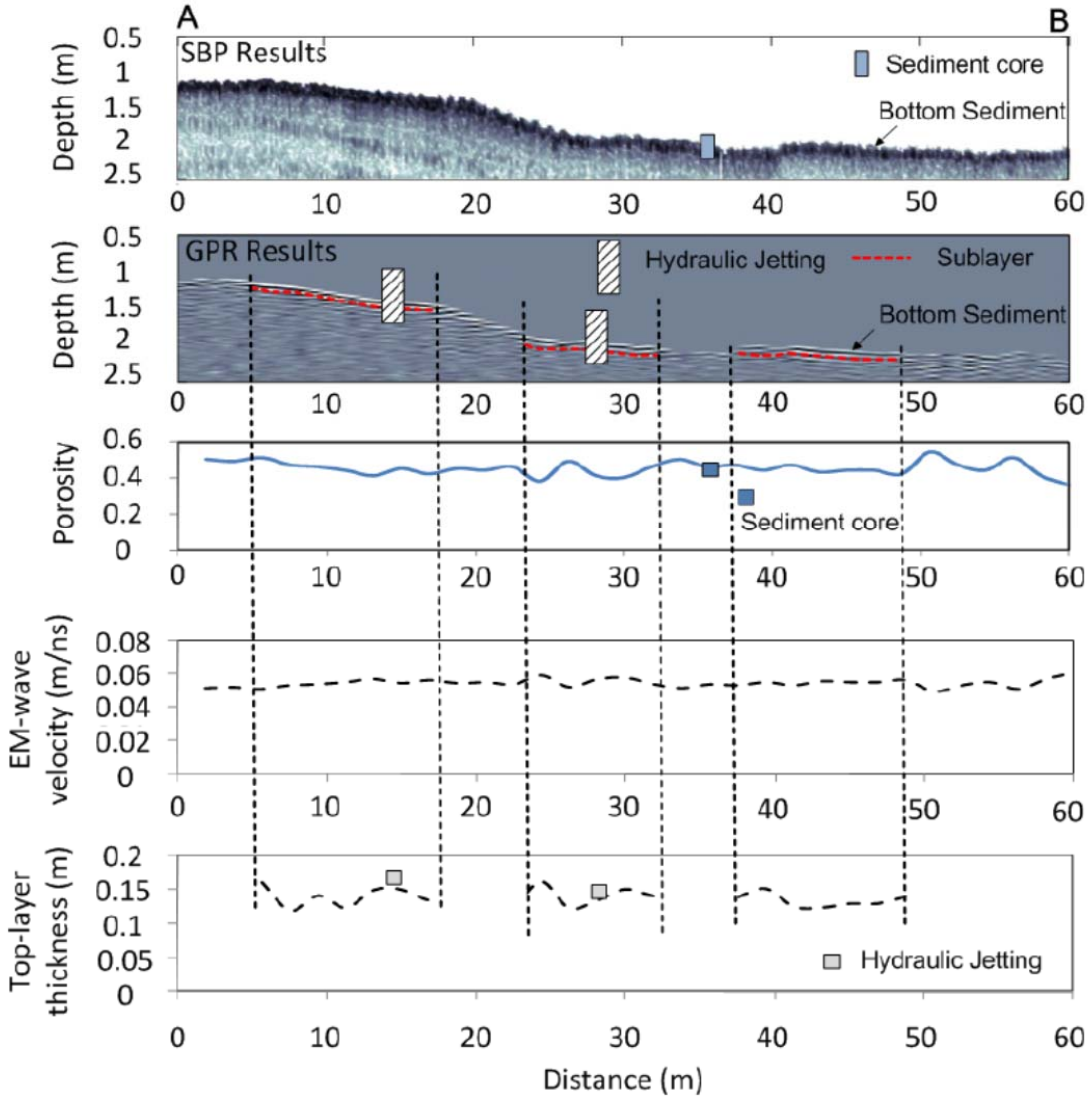

Figure 4.6: Integrated acoustic- and EM-wave profile results inside the Little Sandy Bay harbor (survey line 1).

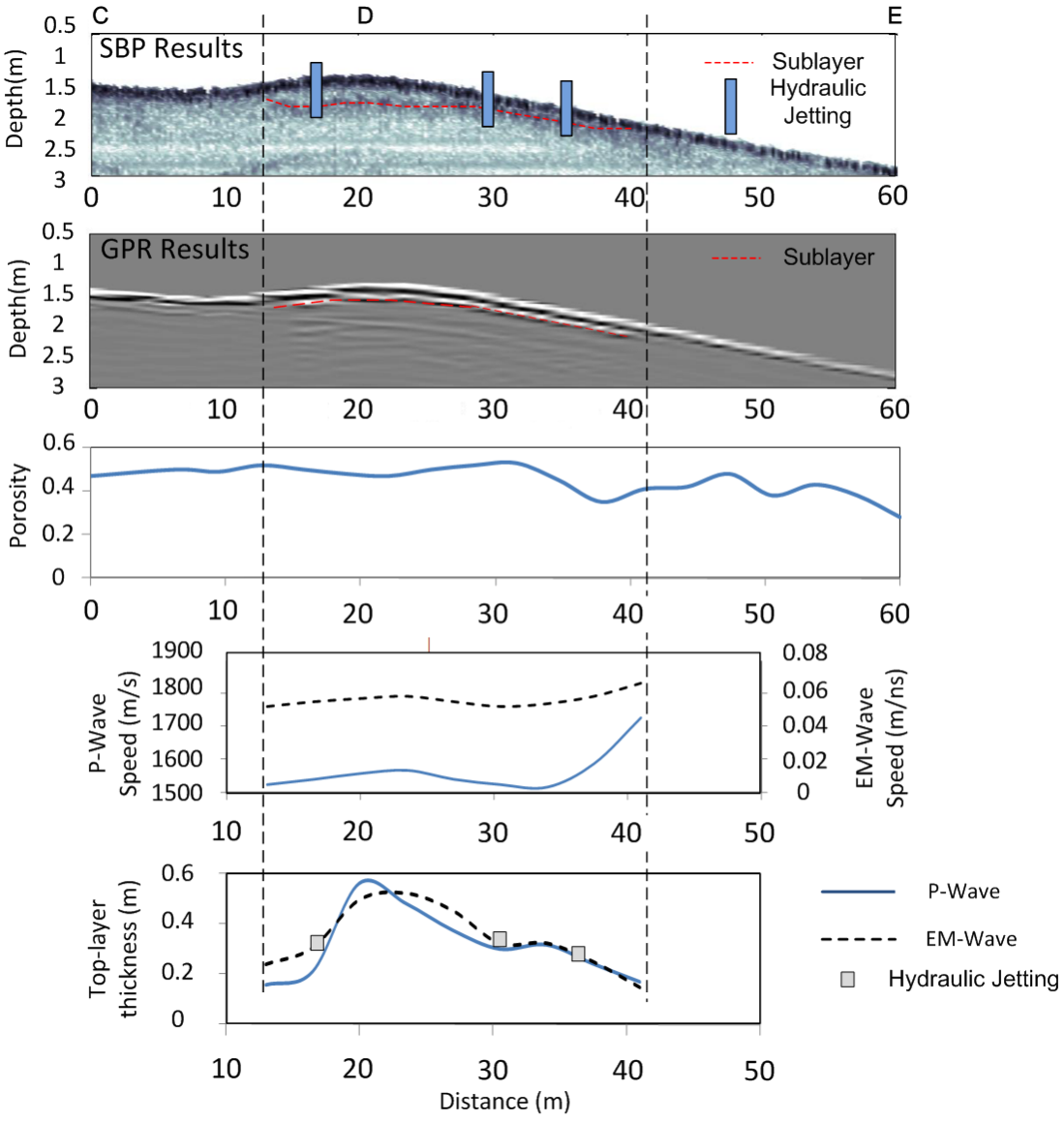

Figure 4.7: Integrated acoustic- and EM-wave profile results outside the Little Sandy Bay harbor (survey line 2).

Chapter 5

Applications of integrated geophysical techniques to monitor nearshore environment changes in response to newly-built coastal structures in Lake Michigan

This chapter is to be submitted to *Journal of Great Lakes*, as "Applications of integrated geophysical techniques to monitor nearshore environment changes in response to newly-built coastal structures in Lake Michigan**.**" by Lin, Y. T., Wu, C.H., Fratta, D., and Clark, G.R.

5.1 Abstract

Coastal bluffs in the Great Lakes are strongly affected by subaqueous physical forces such as winds, waves, and nearshore circulation, as well as any subaerial alteration of coastline. At a site near Concordia University Wisconsin in Lake Michigan, a thousand-meter long coastal revetment structure with pocket beaches was constructed from 2005-2008 to mitigate bluff toe erosion and subsequent bluff failure. Coastal bluffs along shorelines of Lake Michigan are mainly composed of over-consolidated clay, and underwater lakebed downcutting rates have significant impacts on the long-term bluff recession rates. In this study, both subaqueous and subaerial processes were monitored to examine the effects of the newly-built structures on coastal bluffs and lakebed downcutting. Successive aerial photo images and in-situ observations showed that while the bluff toes in front of the coastal revetment were protected, the adjacent bluffs on the northern and southern bluffs still experienced recessions. Notably, excessive slumping occurred on the southern bluffs, in comparison with the northern bluffs. To effectively measure subaqueous bathymetry and the top-layer thickness of substrate sediments, we integrated three geophysical techniques: subbottom profiler (SBP), ground-penetrating radar (GPR), sidescan sonar (SSS), and validated the survey results with in-situ observations. Results showed that

bathymetry erosion and lakebed dowcutting were larger in front of the coastal structures than the adjacent areas. The bathymetry profiles in southern areas performed oscillated patterns in five-year surveys possibly because the southern areas are located between two coastal structures, which resulted in complicated hydrodynamic features, i.e. currents and waves. The lakebed downcutting in northern and southern areas were similar. The coastal structures intercepted sediment supplies, caused beach disappearance, and finally led to severe bluff slumping in southern shores of the coastal structures.

5.2 Introduction

Nearshore environment, located at the interface between the terrestrial bluffs and open-water, plays an important role for ecosystem functions in the Great Lakes (Brazner and Beals, 1997; Meadows et al., 2005). Nearshore environment is susceptible to physical forcing like waves, currents, and water level fluctuations (Amin, 1991; Jibson and Odum, 1994; Brown, et al., 2005) as well as coastal protection structures like breakwaters, jetties, groins, and harbors (USACE, 2002). Physical features of nearshore environment such as bathymetry and sediment properties (composition, porosity and top-layer thickness) can affect habitats and biological communities (Fukuda and Lick, 1980; Teeter et al., 2001; Mackey and Liebenthal, 2005; Goforth and Carman, 2005). For instance, bottom bathymetry controls the nearshore wave climates and circulation patterns, which in turn affect sediment fluxes and redistribute biota populations (Chapelle et al., 2000; James et al., 2002). Sediment substrates like composition and porosity are closely related to the species of fish and benthic macroinvertebrates (Robillard and Mardsen, 2001; Hayes et al., 2009). The top-layer of the bottom sediments can store nutrients and organic matters (Balzer, 1984; Chapelle, 1995). Changes of the top-layer thickness of bottom

sediments thereby alter the distributions of the biota biomass (Graf et al., 1982; Herman et al., 2001). Of importance the balance of sediment in nearshore environment can dictate the stability of bluffs along the shoreline, which can cause great concerns of the safety of human lives and properties (Edil and Haas, 1980; Platt, 1994; Heinz Center, 2000).

Coastal structures are commonly used to stabilize bluff and prevent further bluff erosion or slumping to nearshore environment (USACE, 2002). To date the effects of the coastal structures on beach profiles are still controversial. Kraus (1988), Plant and Griggs (1992), Kraus and McDougal (1996), and McDougal et al. (1996) found that beach profiles were not significantly affected by the presence of the coastal structures. On the contrary, some studies showed that the “hard” coastal structures can cause larger waves due to reflection and in turn induce additional sediment resuspension and transport (Miles et al., 2001), leading to excessive bottom erosion in nearshore (Dean, 1987; Lee and Ryu 2008). Komar and McDougal (1988) suggested that the beaches adjacent to the coastal structures could experience excessive erosion, which is so-called end-of-wall or flanking effects (Dean, 1987; Basco, 2006). Possible mechanisms for the flanking effects can be due to sand trapping (Dean, 1987), rip currents and seaward return flows (McDougal et al., 1987), and blockage of littoral drift (Griggs and Tait, 1988). Recent studies suggest at a certain distance from gaps, rip currents can even occur and bend back towards the structures, joining the inshore flux over the structure crest. Furthermore, apparent changes can occur at spatial scales exceeding the structure dimensions and can be interpreted as a long-term trend in morphological evolution due to the disturbance of the shore-parallel net sediment flux (Kraus and McDougal, 1996). The interruption of

longshore sediment movement by coastal structures may result in down-drift shoreline erosion over hundreds of meters or kilometers, affecting bluff stability and accelerating bluff recession rates to considerable distances from the structures (Dean and Dalrymple, 2002). While we have gained a good understanding on the role of coastal structures in eroding lake-bottom along non-cohesive nearshore environment, very few studies have documented the elevated cohesive lakebed erosion (also called downcutting), one of the important factors to determine the long-term bluff recession rate in the Great Lakes (Davidson-Arnott and Ollerhead, 1995).

In order to measure thickness of sandy layer, monitor sediment substrate and estimate downcutting rates, sediment cores collected by divers are usually applied (Davidson-Arnott and Ollerhead, 1995). However, limited number of samplings due to intensive logistic efforts cannot fully map the spatial variation of downcutting (Davidson-Arnott and Langham, 2000). In addition, disturbances of sediment cores inevitably can occur during collection, transport, or laboratory testing processes (Wheatcroft, 2002). Therefore, efficient and accurate monitoring techniques on the changes of large-scale nearshore environment are highly desired. Recent advancements of geophysical techniques makes repeatable survey of bottom substrate and bathymetry feasible (Scholz, 2001; Cagatay et al., 2003; Bradford et al., 2005). Generally, two kinds of geophysical techniques have been applied to the nearshore areas mapping. First, acoustic wave-based techniques are based upon changes in mechanical impedance, which is related to the product of acoustic speed and the density of the medium (Schock, 2004). Second, electromagnetic (EM) wave techniques measure reflections created at interfaces with contrasting dielectric permittivity (Annan and Davis, 1992). Both acoustic and EM

signals reflect any abrupt changes of physical properties, that is, the interface of different mediums (water-sediment, or sand layer-clay layer). Water depths and sediment layer structures thereby can be estimated and delineated. Nevertheless, the two techniques have their limitations. Acoustic signals have difficulty in penetrating through coarse-grained sediments (e.g., sand and gravel) and glacial till due to low energy transmission and signal scattering (Morang et al., 1997). EM signal strength attenuates quickly in high conductivity materials, penetrating only a few centimeters in clayey sediments and sea water (Annan, 2005).

In Lake Michigan, sediment compositions of nearshore environment are extremely diverse. Types of sediment bottom consist of cohesive clay, silt, sand, gravel, cobble, boulder, and bed rock (Waples, et al.; 2005; Brown et al., 2005). Previous studies obtained sediment porosity or layer thickness using either acoustic or EM techniques (Topp et al., 1980; Richardson and Briggs, 1993; Davis et al., 2002), depending on the prior knowledge of sediment types on the sites. Difficulties in mapping a mixed type of sediment properties have been recognized (Morang et al., 1997). Recently Lin et al. (2009) developed a combined acoustic and electromagnetic technique to effectively monitor the diverse types of nearshore bathymetry and bottom substrate in Lakes Michigan and Superior. Employing an iterative inversion algorithm that integrates acoustic and electromagnetic geophysical measurements, the error of the estimated porosities and top-layer thickness in sediments is found to be no more than 10% for each survey (Lin et al., 2010). While this integrated acoustic and electromagnetic technique is promising, no results on monitoring the changes of nearshore sediment properties in front of newly-built coastal structures have been reported yet.

The objectives of the paper are two folds. First using the integrated geophysical instrument we monitor the nearshore bathymetry and sediment substrate, especially top-layer thickness of sediments, in newly-built coastal structures in Lake Michigan for the last five-year periods. Second we aim to compare the nearshore bathymetry after newly built coastal structures with the equilibrium beach profile. In addition we examine lakebed downcutting adjacent to the newly-built coastal structures with the purpose of addressing long-term implication of the bluff recession in Lake Michigan. Nearshore environment and bluff profile in responses to interactions between physical drivers and newly built structures will be discussed. The information would be valuable for considering future coastal development and management in the Great Lakes.

5.3 Methods

Study site

Figure 5.1 shows the study site, the Concordia University Wisconsin (CUW), Mequon, Wisconsin, which sits on 45 m (~ 135 ft) high bluff extending 1 km (~1.6 mi) along the shoreline of Lake Michigan. The bluff materials consist of clay, ripple-marked sand, cobble, and boulder. The material in the foreshore is mainly sand (Brown et al., 2005). The underlying glacial till is composed primarily of silty-clay lacustrine deposits that are susceptible to lakebed downcutting, a common process along cohesive coastal bluffs in the Great Lakes (Davidson-Arnott and Ollerhead, 1995). Based upon analysis of aerial photographs, the bluff recession rate before the coastal construction was 0.34 m/year (Brown et al., 2005). To mitigate continuous bluff slumping hazards, a bluff stabilization and enhancement project was undertaken in 2005. The coastal structures

including revetment and rubble mounts serve to protect the bluff toe erosion on the CUW campus, and were constructed and completed in 2008. Coastal revetments were also constructed on several individual land owners to prevent erosion of bluff toes in south of the CUW campus (see figure 5.1).

Bluff recession rates

Recession rates of bluff crests and toes were obtained using aerial photos methods. We briefly describe the method here and the details of procedures to estimate bluff recession rates can be found in Hatch (2004) and Swanson et al. (2006). Aerial photos in 2000, 2005, and 2010 were digitized and processed to be orthophotos with the resolutions of 1 m/pixel. Following suggestions from previous studies (Zuzek et al., 2003; Swanson et al., 2006), Figure 5.2 shows that the bluff crest and toe locations are obtained using a sampling interval of 10 m transect with 920m for the CUW and ± 500m northern and southern sides of the CUW, yielding the accuracy of ±1~2m (Hatch 2004). By averaging the locations of the bluff crests and toes for the northern sides, CUW, and southern sides, the errors can be reduced to ~10 cm. Some limitations also affect the accuracy of the bluff recession rates. For example, trees on the bluff top and high reflectance of some air photos can reduce the visibility of the bluff lines. Following Hatch's suggestions (2004), histogram stretch enhancements were utilized to improve the visibility of the bluff top.

Integrated geophysical techniques and ground-truth measurements

To map nearshore bathymetry and substrate, the combined geophysical technique (Lin et al., 2009) with a subbottom profiler (SBP) and a ground penetrating radar (GPR)

system was employed (figure 5.3). The SeaKing parametric SBP, manufactured by Tritech International Limited, transmits two similar frequencies (~100 kHz) to generate high (200 kHz) and low frequencies (20 kHz) to map the substrate with the vertical resolution of 0.3 cm in water and sediment. The pulseEkko 100 GPR system (Sensor and Software, Ontario, Canada) with 400V transmitter are equipped with a 200 MHz antennas, which has a vertical resolution of 8 cm in water and 15 cm in sediment (assuming that the EM wave speed in sediments is 0.06 m/ns). Bathymetry was obtained by processing data based upon the acoustic signal travel time between the transducer and lake bottoms. The bathymetry was then mapped to 2 m x 2 m grids interpolated by using the Kriging method. The water level data from NOAA station (ID: 9087057) in Milwaukee, WI (24 km away from the Concordia University site) was used to correct the water level differences in each study year. To map both clay/fine-grained sediments and boulder/sand materials, we employ an inversion algorithm to estimate sediment porosity, speed of acoustic and EM waves, and the top-layer thickness in bottom sediments. Details of the inversion algorithm can be found in Lin et al. (2010). In this study, a side-scan sonar (SSS) was also attached to the zodiac boat below 0.5 m of the water surface (see figure 5.3). The SSS emits acoustic signals at a frequency of 675 KHz, with 30 m range on each side, i.e. a swath of 60 m, giving a sampling resolution (range/sampling points=(2x30)/1396) of ~4.3 cm and the boat coverage area of 60 m^2/sec. The strength of acoustic backscattered signals can reveal the hardness of bottom substrates (Blondel and Murton, 1996) with the purpose of distinguishing the hard (glacial tills) and soft (sand) bottom textures.

Errors of geophysical measurements are from wave motions and instrument resolutions. Wave motions displace traces of geophysical data depending whether traces were collected in a wave crest, trough or somewhere in between. The error due to wave motions was removed by employing moving average over the measurements. Detailed procedures can be referred to Lin et al. (2009). The final instrument resolution would be determined from the combined effects of GPS, SBP, and GPR. Nominal horizontal resolution of GPS is 1m, which yields a vertical error of 0.02 m with the slope of ~0.02 in survey areas. The SBP with resolution of 0.003 m is used to obtain bathymetry profiles. Therefore, error bounds of bathymetry profiles are approximately equal to ±0.024m. For thickness of sublayers, the GPR with resolution of 0.15m needs to be taken into consideration, yielding the error bounds of layer thickness, ±0.171 m. We further averaged the measurements over the three sub-regions (i.e., north, middle CUW campus, and south) to reduce the error bounds of layer thickness and locations of lakebed. Based upon 2 m x 2 m grids, number of grids in the north, middle and south regions are ~4000, ~25000, and ~2500, respectively. The maximum error bound for the top-layer thickness obtained in south regions is thereby $\sim \pm \frac{0.171}{\sqrt{2500}} = \pm 3.42 \times 10^{-3} m$. By considering error propagation, maximum error bound for locations of lakebed found in south regions is $\pm \sqrt{\left(\frac{0.024}{\sqrt{2500}}\right)^2 + \left(3.42 \times 10^{-3}\right)^2} = 3.45 \times 10^{-3} m$.

To obtain ground truth measurements, a Shelby tube, an aluminum rod coring sampler, and a hydraulic jetting system were used. For silty and clay sediments we used Shelby tubes, made of a thin galvanized wall with a 7.6 cm outer diameter. To facilitate underwater sampling, a lighter and extendable aluminum rod, instead of a traditional steel

rod, was specially made to take sediment cores from shallow (2 - 3 m) to intermediate (5 ~ 7m) water depth. After the sediment core was collected, both ends of the core were covered by plastic caps and carefully transported back to the laboratory for data analysis (Lee et al., 2004). For sandy sediments, the hydraulic jetting system (Rukavina and Lahaie 1991; Lin et al., 2009) was operated from a boat to directly measure the thickness of sandy sediments. The pipe of the jetting system assembled in the field was attached to a water pump through a flexible hose. The water jet from a pump fluidized the sandy sediment when the jetting pipe was advanced into the sediment column. Penetration depth was read using a graduated marking on the pipe until the jet met bedrock or firm glacial sediments. The depth of jetting pipe penetration was the thickness of the soft sandy sediment layer. At last an underwater camera attached to a towing side scan sonar (SSS), shown in figure 5.3, was utilized to take images with the purpose of confirming remote geophysical observations of bottom sediment morphology and composition.

Equilibrium beach profile

The equilibrium beach profile, the mean profile of measured profiles over a period of several years, is the result of the balance between destructive forces and constructive forces (Bruun 1954). Generally, the beach profile follows a simple relationship (Dean, 1991):

$$h(x) = Ax^n , \tag{5.1}$$

where h is the water depth, x is the distance along the beach profile, and A is a scale factor, which can be related to the sediment characteristics and wave conditions (Moore, 1982; Kriebel et al., 1991; Komar and Willaims, 1994). The most common expressions

for beach profiles are with n=2/3 (two-third power law), obtained from Bruun (1954) and Dean (1977) analysis. Dean (1991) also applied the shallow-water linear waves theory to derive the n values by the following dominant forces: (i) for wave energy dissipation per unit volume of the water column with n of 2/3; (ii) for the longshore component of radiation stress with n of 2/5; and (iii) for the wave energy dissipation per unit bed area s with n of 2/5. In this study, the equilibrium beach profiles in the structured and unstructured areas from Lake Michigan are analyzed and compared.

Cumulative wave impact height

To account for wave impacts on bluff recession, wave impact height (WIH) defined as the elevation of wave runup minus the elevation of a bluff toe is usually adopted (Ruggiero et al. 2001). Brown et al. (2005) used averaged monthly WIH to explain temporal variations in bluff recession on the Lake Michigan coastlines. Swenson et al. (2006) included the magnitude, frequency, and duration of all waves to develop a new wave-bluff interaction index, cumulative wave impact height (CWIH), which can better perform wave impacts on bluff recession. In this study, CWIH is adopted to correlate the waves with bluff recession. Due to lack of hindcast of wave data, historical data including wind speeds and directions gathered from adjacent NOAA stations, and fetches are used to estimate the wave height. Because only storm events can generate waves large enough to cause erosion of a bluff toe (Amin, 1991), we only consider wave height induced by storm events. Following the criteria suggested by Amin (1991) and Davidson-Arnott and Pollard (1980), if the wind speed over 4.5m/s lasts for 6 hours, wind occurring within the range of directions affecting the study areas, and changes of wind direction is less than 45

degrees, it is regarded as a storm event. The water level data is from Milwaukee, WI (28 km, south of the study site), and the wind data is obtained from Port Washing, WI (15 km, north of the study site). The water levels at survey days from 2007 to 2011 are listed in Table 5.1. The data shows that the water level was lowest in 2007 and reached the peak in 2009. Due to the lack of wave observations at the study site, we estimate the wave climate using the available wind data. Based upon the orientation of the study site, the range of wind directions affecting the study areas is 45^{o} (northeastern) to 135^{o} (southeastern) degrees. Following the hindcast procedure (CERC, 1984), the deep-water wave height and wave period during 2007 to 2011 were obtained (see Table 5.2). The information of wind data, cumulative wave impact height (CWIH), number, durations, and total hours of storm events are listed in Table 5.2.

Lakebed downcutting

Lakebed downcutting, equal to bathymetry subtracted by sandy layer thickness (Davidson-Arnott 1995), is the erosion of cohesive materials (glacial tills) in nearhsore areas. In this study, SBP due to better resolution was used to acquire the bathymetry elevation using water level adjacent to the NOAA station (Milwaukee) with the reference datum of IGLD 85. The thickness of top sediment layer, i.e. sand, was obtained using the inversion algorithm (Lin et al., 2010). Elevation of lakebed (glacial tills) was obtained by subtracting the thickness of sand layer thickness from bathymetry. Lakebed downcutting, elevation decrease of glacial tills locations, is thereby calculated through the difference of annual lakebed change over the study period. Furthermore the study site was divided into

north (unstructured), middle (structured) and south (unstructured) areas to provide the spatially arithmetic-mean elevation of bathymetry and lakebed.

For the lake bottom, the resolution due to the SBP system is 0.003m, whereas the resolution for the sublayer can be calculated from the GPR (~0.15m) and SBP (~0.003m) system, which yield the combined error of $\pm\sqrt{0.15^2 + 0.003^2} = \sim \pm 0.15\,\text{m}$. The spatial-averaged of lake bottom and lake bed in three regions can further improve the error bound. Based upon 2 m x 2 m grids, number of grids (data points) in the north, middle and south regions are ~4000, ~25000, and ~2500, respectively. The maximum error bounds for the lake bathymetry and lake bed are found in south regions, which are: $\pm\sqrt{\frac{0.003^2}{2500}} = \pm 6\times 10^{-5}\,(m)$, and $\pm\sqrt{\frac{0.15^2 + 0.003^2}{2500}} = \pm 3\times 10^{-3}\,(m)$, respectively.

5.4 Results

Bluff recession

Table 5.3 lists recession rates of bluff crests and toes over the study areas from 2000 to 2010. The results show that bluff recessions at toes were accelerated in southern sides, while decreased in northern sides after completeness of coastal structures. On the contrary, recession rates of bluff crest were accelerated in northern sides. Because larger bluff recessions and lakebed downcutting in south side were found from 2005 to 2010, it is suggested that the coastal structures pose negative impacts on bluff stability in south sides. Figure 5.4 shows photos taken in the south and north shores of the coastal revetments from 2008 to 2011. In 2008, vegetation covers were visible along the south

shore of structured areas. In 2009, bluff failure occurred, the vegetation rooted on the bluff slid into water, and the vegetation line moved up. According to visual observations, the toe of bluff was retreated by ~1m from 2008 to 2009, which is larger than average 0.34m/year reported in Brown et al. (2005). The erosion rates of bluff toes also corresponded to the results from aerial photos (see Table 5.3). In 2010 and 2011, the locations of vegetation line were stable, and no more bluff slump was observed. For the northern unstructured areas, bluff conditions are stable, and no bluff slump or upwards of vegetation line was observed from 2008 to 2011. According to the erosion rates of bluff crests and toes, and bluff height of 45 m over a 100-meter-long south shore, volumes of sediment materials from bluffs can be estimated, which are 1845 and 2970 m^3 / yr before and after the coastal structures were built. The coastal structures led to ~61% increases of sediment materials into the water body, and these materials mainly consisting of clay particles were brought to the offshore.

Bathymetry

All surveys were conducted in summer season from 2007 to 2011 to minimize seasonal nearshore morphology changes. Figure 5.5a shows the bathymetry contours were collected in 2011. The water depth is deeper in front of coastal revetments than the areas near the natural beaches. According to the wave information from NOAA (station ID: 45007), averaged wave period in Lake Michigan from 2007 to 2011 is 3.7 sec, the depth for wave breaking is approximately between 2~2.5m. The wave-breaking line is defined as the limit of nearshore regions in this study. Due to the limitation of data, bathymetry changes from 2008 to 2011 over the entire study areas are provided in figure

5.5b. The areas where most erosion and deposition occurring are very scattered. Severe erosion is mainly observed in the nearshore and the areas in front of coastal revetments.

In order to compare with 2007 data, coordinates of survey lines from 2007 were input into the 2008, 2009 2010, and 2011 2m x 2m grids to searching for minimum distances between the coordinates from 2007 survey lines and 2008, 2009, 2010 and 2011 bathymetry grids. By using this method, the errors of coordinates matched among 2007 to 2011 data are no more than $\frac{\sqrt{8}}{2} \approx 1.414$ m, approximately the same as the resolution of the GPS receiver. The comparisons of bathymetry profiles in four selected survey lines are shown in figure 5.6. The slope of the front side of the coastal revetment is ~45 degrees (visual observation, see Lines *C1*, and *C2*). Lines *C1*, and *C2* located at the regions off the coastal structured areas showed that bathymetry profiles became smoother, and uneven features had been flattened from 2007 to 2008 between 30 to 70 m from the shore. For line *C1*, the bathymetry profiles were decreased, i.e. erosion, from 2007 to 2008, and were filled with sediments from 2008 to 2009, and then the bottom kept being eroded afterwards. The significant erosion of line *C1* was observed in the regions with depth between 1.8 to 2.5 m after 5-year period. For the line *C2*, in front of the submerged breakwater, it exhibited significant bottom erosion (maximum is ~0.5 m from 2007 to 2009) occurring at around 40 to 80 m from the shoreline. From 2009 to 2011, the bathymetry was filled back to the level in 2007, and the eroded areas were filled with sediments. The net erosion of Line *C2* was observed in the areas with depth less than 2m. In the areas with depth larger than 2m, the sediment depositions were observed in 5-year period.

For line *S1*, near the edge of coastal revetment, the bathymetry profiles oscillated on yearly basis, and the node of the oscillations is located at 80 m from the shoreline (depth of 2m). After 5-year period, bathymetry erosion and deposition showed scattered patterns along the survey line, but the net changes of bathymetry profiles were close to zero, i.e. the sediment-in and -out of the region were approximately in balance. The bathymetry profiles of line *N1* in the nearshore showed small changes (~less than 0.15m/year) in comparison with Lines *S1*, *C1*, and *C2*, but the bathymetry profiles kept being eroded. Therefore, the sediments out from the survey line were more than the sediments into the survey line.

Equilibrium beach profile

Figure 5.7 shows the equilibrium beach profiles that were fitted eq.(5.1) for the mean natural beaches adjacent to the coastal revetment structures areas over the 5-year study period. It is found that *n* values of the northern and southern beaches are 0.65 and 0.61, respectively, close to the mean values 0.63 reported by Wood et al. (1994) for southern Lake Michigan profiles and similar to the mean value 0.67 reported by from Bruun (1954) on the west coast and Dean (1977) on the east coast to the Texas-Mexico border. The *A* values, related to the sediment characteristics and wave conditions (Moore, 1982; Kriebel et al., 1991; Komar and Willaims, 1994), of the northern and southern beaches are 0.11 to 0.14, respectively, which are also within the ranges reported by Moore (1982) and Wood et al. (1994). For the nearshore profile in front of coastal revetment, the significant deviations are found within 70 m, in comparisons with the natural beaches. The water depth is deeper and bottom is relatively flat in the structured areas, consistent to the

descriptions by Dean (1987) and McDougal et al. (1996). Interestingly the mean beach profiles beyond 70m away from the structure areas resemble to the mean nature beach profiles, suggesting that the beach profiles become less influenced by the presence of the coastal structures. Similar observations were reported by Kraus (1988), Plant and Griggs (1992), and McDougal et al. (1996).

Sediment substrates

An example for SBP, GPR and SSS of 2009 survey results along the line *C2* is shown in figure 5.8. The first reflections from SBP (figure 5.8a) and GPR (figure 5.8b) delineate the location of sediment bottom and the subsequent reflections denote the sediment sublayer. The SSS data (see figure 5.8c) qualitatively depicts the soft (hard) bottoms with weak (strong) signal reflections (Stanic, et al. 1989). Strong relationships between reflection strengths and sediment types are found here. For example the areas between 25 to 45 m (see the rugged images, i.e. Area 1 in SSS data and the ground-truth picture in figure 5.9a), the SBP signals failed to reveal any substrate because of the strong scattering of acoustic signals by the boulders, while the GPR signals were able to penetrate through these boulders. In the range of 45 to 85 m, the weak reflections were due to the overlying soft sands (see Area 2 in SSS data and ground-truth sand dunes in figure 5.9b). Both GPR and SBP provide the sub-layer information on the areas between 85 m and 105 m (see the ground-true picture in figure 5.9c), composed of hard glacial tills (strong reflection and rugged images, i.e. Area 3 in SSS data) and soft sand (weak reflection and smooth images in SSS data). GPR and SPB data shows the sublayers for the weak reflection areas, also support by the ground-truth measurements obtained by

sediment cores. For the areas covered by glacial tills commonly found in the Great Lakes (USACE 2002), there is no layer observed both on GPR and SBP data. After the distance beyond 110 m, the thin sand layer appeared again on both SBP and GPR graphs.

To quantify geophysical substrate results, the iterative inversion algorithm (Lin et al., 2010) on signals of SBP and GPR was used to sediment top-layer thickness. Figure 5.8d shows the good comparisons between the estimated top-layer thickness and the ground-truth measurements based upon sediment coring and hydraulic jetting techniques. The discrepancy of the top-layer thickness is 6.7%. Overall the results demonstrate that the remote integrated geophysical method can effectively provide accurate "spatial" sediment substrate measurements in comparison with traditional point measurements.

Figure 5.10a shows the contours of mean sand layers from 2009 to 2011 over the study areas. The sandy layers were distributed sporadically over the glacial tills, and the mean thickness could vary up to 0.3m. We further subtract the sandy layer thickness from the measured bathymetry to obtain actual lakebed composed of mainly glacial tills. Fig. 5.10b shows the changes of the lakebed from 2008 to 2011. Sandy layer thickness is an important parameter on lakebed downcutting rates. A thick sandy layer can protect the lakebed from being eroded, while a thin sandy layer can promote lakebed downcutting because of sandy particle abrasion (USACE, 2002). For the places with sever lakebed erosion (darker color in figure 5.10b), only some specific locations follow the above-mentioned principle. The dash circle shows the lakebed downcutting due to lack of sand protection, and the solid circle denotes effect of the sand particle abrasion process on lakebed erosion. Because the thickness of the sandy layer obtained from four times surveys in Fig. 10a is a snap shot, it may not be able to represent the averaged-yearly

sandy layer thickness. Therefore, not every scenario of lakebed erosions can be only explained by the sandy layer thickness. Instead, the spatially averaged the lakebed downcutting is applied to discuss the variations of lakebed downcutting in three subregions, i.e., north, middle and south regions.

5.5 Discussion

The following sections discuss the climate-driven factors such as waves, water level fluctuations (Amin, 1991, Fuller, 2002) and coastal structures like shore-protection structure (Dean, 1987; Ranasinghe and Turner, 2006) on nearshore environment changes. The integrated geophysical techniques can estimate the top-layer thickness (sandy layer), and therefore the changes of lakebed as well as (nearshore lowering) downcutting rate can be determined. Figure 5.11 provides information of lake level, mean bathymetry, mean sandy layer thickness and mean lake bed in three regions: north part of unstructured regions, coastal structured regions, and south part of unstructured regions to discuss the effects of physical drivers. Due to lack of the data in the whole survey areas in 2007, the measurements of individual lines in the structured and south areas were used and adjusted based upon the mean bathymetry differences in 2007 and 2008 (see figure 5.6).

Effects of water level fluctuations and storm events

The rises of water level may result in the erosion of upper beach and deposition of the offshore (Bruun, 1962; Schwartz, 1987). The water level increases from 2007 to 2009, and therefore the bathymetry and lake bottom erosion were observed. The

maximum lake bottom erosion was observed in the structured areas from 2007 to 2008. The water level was increased, but the CWIH and total storm hours (storm event times mean duration of storm events) were both small in comparison with the data from 2009 to 2011. The possible reasons to cause largest lake bottom erosion may be due to the coastal structures. The next section will discuss the effects of coastal structures. From 2009 to 2010, the lake level was decreased, but the lake bottom erosion became larger than previous year. The CWIH and storm events reached maximum from 2009 to 2010, which explains the larger lake bottom erosion from 2009 to 2010. From 2010 to 2011, the water level was approximately the same as previous year, but the CWIH became smaller, and thus the lake bottom erosion became smaller. The distributions and thickness of sandy layer are sensitive and dynamic to the weather conditions, i.e. shore-term variations, and therefore did not show apparent correlations to long-term parameter such as yearly water level, CHIW and storm events.

Following Wood et al. (1994), the equilibrium beach profiles can be used to check the response of beach morphology to the lake-level change. Because the relatively narrow range of n values, it is reasonable to fix n at a value of 0.67 and to consider A as the only free variable as Dean (1977) and Wood et al. (1994) assumed. By fixing the n values, the results of A values from 2008 to 2011 are shown in Table 5.4. The A values fall in a very small range from 0.098 to 0.105, and are not related to lake-level change (see table 5.1). As Wood et al. (1994) indicated, the approximately constant A values mean that the beach profiles are in an equilibrium state and respond on a similar time scale to the lake-level changes.

Effects of coastal structures

In this study site, constructions of coastal revetments began from 2005 and finished in 2008. The largest bottom erosion in the structured areas was observed from 2007 to 2008. In addition, the lake bottom erosion in the structured areas was larger than unstructured areas for all survey years. This may be due to wave reflection and dissipations in front of coastal srtructures are larger and would significantly increase suspended sediment concentrations and bottom sediment resuspensions. The results also show that the sandy layer thickness is thinner in the structured areas than that in unstructured areas (see figure 5.11). Dean (1987) mentioned that “hard” coastal structures such revetments can induce frontal effects, leading to toe scouring, and depth increases. Lee and Ryu (2008) have also shown that sediment transports were altered greatly by the presence of coastal structures. The interactions between the wave motions and the coastal structures increase wave heights and in turn induce additional sediment resuspensions and transports (Miles et al., 2001).

The coastal revetments protect the shoreline from being eroded; whereas the shorelines without coastal revetments are still receded, and thus the toe of bluffs is still attacked by wave motions. In the south shore adjacent to the coastal revetments (approximately at the edge of structured and unstructured areas), significant changes of bluff conditions were observed from 2008 to 2009. The phenomena of excessive erosion in the nearshores close to coastal structures is so-called called end-of-wall or flanking effects, and may be attributed to the adjacent coastal revetments (Dean, 1987; Basco, 2000). Based upon the field and laboratory data from seawall, Komar and McDougal (1988) also showed that the excess erosion in the adjacent beaches of the seawall may be

related to the length of seawall. The possible mechanism for the flanking effects may be due to sand trapping (Dean, 1987), rip currents and seaward return flows (McDougal et al., 1987), and blockage of littoral drift (Griggs and Tait, 1988). Sediment budget is critical to shoreline erosion (Allen, 1981), and for analyzing sediment budget, sediment transport due to cross-shore and longshore currents are taken into consideration. The intensity of the currents increases with increasing incident wave (Masselink and Hughes, 2003), and the currents in the structured areas are larger than the adjacent areas. Figure 5.12 shows the schematic of sediment budgets in the north, middle, and south regions. Sediment fluxes with cross-shore currents in and out between nearshore and offshore were in balance because of beach profiles approximately in equilibrium states. In this study site, from 2008 to 2011, the averaged wind direction was 80 to 85 degrees (see table 5.2), shoreline was 8 degree toward to the north, and therefore a southward lognshore current was generated. The sediment transport rate Q_ℓ due to longshore currents can be estimated by using the so-called CERC equation (CERC, 1984):

$$Q_\ell = \frac{K}{(\rho_s - \rho) g (1-n)} \left(\frac{\rho g^{\frac{3}{2}}}{16\kappa^{\frac{1}{2}}} \right) H_b^{\frac{5}{2}} \sin(2\alpha_b), \tag{5.2}$$

where Q_ℓ is the volumetric transport rate in $m^3 day^{-1}$, K is a coefficient related to median grain size d_{50} (del Valle, Medina, and Losada, 1993), $\rho_s \left(= 2650 kg/m^3\right)$ and $\rho \left(= 1000 kg/m^3\right)$ are mass density of sediment grain and water, n is the sediment porosity, H_b and α_b are the wave breaker height and angle, and κ is the breaker index $\left(= H_b / d_b = 1 \text{ for simplicity}, d_b \text{ is the wave breakign depth}\right)$. Based upon the field data shown in table 5.2, and in-situ measurements, the following values,

$H_b = 1.3m,\ n = 0.4,\ d_{50} = 0.33mm,\ K = 0.6,$ and $\alpha_b = 15^{\circ}$ were used to estimate sediment transport rate Q_ℓ, finally yielding Q_ℓ of $0.115m^3/s \approx 9900m^3/day$. In the middle regions (structured areas), coastal structures intercepted sediment supplies, and no sediment from land sites was brought into the water body. Therefore, in the south regions, less sediment fluxes from the north were into the water body. The sediment flux in and out between the nearshore and offshore in south regions were still the same. As a result, sediments deposited along the shoreline were less than those eroded from the shoreline, i.e. sediment depletion. Once sand beach covered along the shoreline were disappeared, the exposed toes of bluffs possibly kept being attacked by the wave motions, and finally bluff failure occurred and significant slumps were observed (see the picture in figure 5.12). In addition, the south regions are located between two coastal structures (see figure 5.1), the complicated hydrodynamic features may lead to stronger circulations and more sediment losses. The coastal structures protect the shoreline as well as bluff, but bluffs in the adjacent regions still keep being eroded and receded.

Capability and limitations

In this study, based upon available datasets and previous studies, we suggested that erosion in southern shore are due to the unbalance sediment budget caused by the new-built coastal structures. In order to confirm our suggestions, investigations such as sediment transport due to longshore currents, ground-water level, geological stratigraphy, soil strength of bluffs are required, especially their differences between northern and southern shores. Secondly, this study applied geophysical techniques to obtain the bathymetry and substrates information are in the nearshores of Lake Michigan on

multiple-year measurements. For the sediment layer thickness, the SBP and GPR are alternative techniques based upon the sediment types on the lake bottoms. In the study site, there are soft sand layers existing sporadically on lake bottoms. The SBP and GPR system both can provide soft sandy layer information in this study site (Lin et. al. 2010). However, larger sediment particles may prevent the SBP signals from penetrating. Although the GPR system is a good alternative to image the substrate with overlying soft sand, the theoretical resolution for assumed EM speed of 0.06 m/ns in sediments). Sometimes there is still missing substrate and top-layer thickness information due to the thin top-layer in sediments. Secondly, the calculations of layer thickness stand on the product of wave travel time and wave speeds. In this study, we assumed the wave speeds are constant in the same sublayer. The inhomogeneous layer structures (sediment densities always increase with the depth) result in the variations of wave speeds even in the same layer. Therefore, the small differences inevitably exist between the estimated and measured top-layer thickness. Due to lack of water level gauge in the study site, the adjacent water level data are needed when the bathymetry differences are compared. The discrepancy of the water level between the study site and adjacent water gauges would lead to over- or underestimate the bathymetry changes. Also, because the nearshore environment is dynamic, yearly measurements may lost many precious information.

5.6 Conclusions

In this study, by employing aerial photos, in-situ observations, and an integrated geophysical method, bluff recession rates, bluff failures, and spatial and temporal deposition and erosion patterns in subaqueous sites were delineated in a five-year period.

Erosion rates of bluff toes in southern shores were increased to ~1 m/year after the coastal structures were finished. Accordingly, several bluff slumps in southern shore were observed from 2008 to 2009, and meanwhile, lakebed downcutting also reached its maximum among five-year data. According to the available data, it is suggested that bluff failures in southern shore may arise from the unbalanced sediment budget because the coastal structures intercept sediment supplies into the water body, and lead to the disappearance of beach in southern shores. Also, the southern regions are located between two adjacent coastal structures, and complicate circulation may result in excessive lakebed and bluff erosion.

The mean bathymetry and lakebed experienced largest erosion from 2007 to 2008 when the coastal structures were finished. In front of the coastal structures, water depth reaches ~1m, but after 80m from the structures, the beach profiles gradually become similar to those in unstructured areas, i.e. reaching an equilibrium state. Because of larger wave motions in structured areas, erosion of bathymetry and lakebed was larger than southern and northern regions without coastal structures. The sandy layer thicknesses in structured areas were generally thinner than that in unstructured areas. After 2008, changes of bathymetry and lakebed erosion increased with increasing of the CWIH and numbers of storm events.

The build of coastal structures makes habitats in nearshores undergo significant changes in terms of water depth, redistributions of sandy particles and resulting bluff recession in five-year period. These changes in nearhsores are possibly critical to animal, biota, and human activities. The quantitative methods and analysis tools developed in this

study are valuable and useful for spatial and temporal monitoring on nearshore environment in the Great Lakes.

5.7 Acknowledgement

This research was funded by the Wisconsin Coastal Management Program (WCMP). Specifically we thank Mr. Michael Friis and Miss Angel Kathleen at the WCMP for their continuous support. We also thank Mr. Bruce Bessert at the Concordia University, Wisconsin for providing the access to the study site.

5.8 References

Amin, S.M.N. (1991). Bluff toe erosion along a section of the Lake Erie South shore, Ph.D. thesis, Kent State University, Kent, Ohio, U.S.A. Kent, Ohio.

Annan, A.P. and Davis, J.L., (1992). Design and development of a digital ground penetrating radar system. In: Ed. J. Pilon, Ground Penetrating Radar*, Geol. Surv. Can. Pap*. 90-4, 15-23.

Annan, A.P. (2005). Ground penetrating radar. In *Near Surface Geophysics*, Edited by K. Butler. *Society of Exploration Geophysics*. Tulsa, OK: 357-438.

Aubrey, D.G. (1979). Seasonal patterns of onshore/offshore sediment movement. *Journal of Geophysical Research*, 84(C10), 6347-6354.

Bachman, R.T. (1985). Acoustic and physical property relationships in marine sediments. *J. Acoust. Soc. Am*, 78(2), 616-621.

Balzer, W. (1984). Organic matter degradation and biogenic clement cycling in a nearshore sediment (Kiel Bight). *Limnol. Oceanogr*., 29(6), 1231-1246.

Bano, M., and Girard, J.F. (2001). Radar reflections and water content estimation of Aeolian sand dune. *Geophys. Res. Lett.*, 28(16), 3207-3210.

Basco, D.R. (2006). Seawall impacts on adjacent beaches: separating fact from friction. *Journal of coastal research*, SI39, 741-744.

Beach, R.A., and Sternberg, R.W. (1992). Suspended sediment transport in the surf zone: response to incident wave and longshore current interaction. *Marine Geology*, 108, 275-294.

Bishop, C., Skafel, M. and Nairn, R., (1992). Cohesive profile erosion by waves. Proc. 23rd Int. Conf. Coastal Eng., ASCE, pp. 2976-2989.

Bradford, J.H., McNamara, J.P., Bowden, W., Gooseff, M. (2005). Measuring thaw depth beneath peat-lined arctic streams using ground-penetrating radar. *Hydrol Process*. 19, 2689-2699.

Bray, M.J., and Hooke, J.M. (1997). Prediction of soft-cliff retreat with accelerating sea-level rise. *Journal of Coastal Research*, 13(2), 453-467.

Brazner, J.C., and Beals, E.W. (1997). Patterns in fish assemblages from coastal wetland and beach habitats in Green Bay, Lake Michigan: a multivariate habitats of abiotic and biotic forcing factors. *Can. J. Fish. Aquat. Sci.* 54: 1743-1761.

Brown, E.A., Wu, C.H., Michelson, D.M., and Edil, T.B. (2005). Factors controlling rates of bluff recession at two sites on Lake Michigan. *J. Great Lakes Res.* 31:306-321.

Bruun, P. (1954). Coast erosion and the development of beach profiles. Technical Memorandum, No.44, Becah Erosion Board, US Army Corps of Engineers, Water Experiment Station, Vicksburg, MS.

Bruun, P. (1962). Sea level rise as a cause of shore erosion. *Journal of Waterways and Harbors Division*, ASCE, 88, 117-130.

Butt, T., and Russell, P. (2000). Hydrodynamics and cross-shore sediment transport in the swash-zone of natural beaches: A review. *Journal of Coastal Research*, 16(2), 255-268.

Cagatay, M.N., Gorur, N., Polonia, A., Demirbag, E., Sakinc, M., Cormier, M.-H., Capotondi, L., McHugh C., Emre O., and Eris K., (2003). Sea-level changes and depositional environments in the Izmit Gulf, eastern Marmara Sea, during the late glacial-Holocene period. *Marine Geology*: 202(3-4), 159-173.

CERC. (1984). *Shore Protection Manual* (4th Edition). Coastal Engineering Research Center, Waterway Experiment Station, Corps of Engineers, Vicksburg.

Chapelle, A. (1995). A preliminary model of nutrient cycling in sediments of a Mediterrean lagoon. *Ecological Modeling*, 80, 131-147.

Chapelle, A., Menesguen, A., Deslous-Poali J-M., Souchu, P., Mazouni, N., Vaquer, A., and Millet, B. (2000). Modeling nitrogen, primary production and oxygen in a Mediterranean lagoon. Impact of oysters farming and inputs from the watershed. *Ecological modeling*, 127, 161-181.

Davidson-Arnott, R.G.D. (2005). Conceptual model of the effects of sea level rise on sandy coasts. *Journal of Coastal Research*, 21(6), 1168-1172.

Davidson-Arnott, R.G.D., and Ollerhead, F. (1995). Nearshore erosion on a cohesive shoreline. *Mar. Geol*., 122, 349-365.

Davis, A., Haynes, R., Bennell, J., and Huws, D. (2002). Surficial seabed sediment properties derived from seismic profiler responses. *Marine Geology*, 182, 209-223.

Dean, R.G. (1977). Equilibrium beach profiles: U.S. Atlantic and Gulf coasts, *Ocean Eng. Rep.* 12, 45 pp. +appendix, Univ. of Del., Newark, 1977.

Dean, R.G. (1987). Coastal Armoring: Effects, Principles and Mitigation. Proceedings of the 20st International Conference on Coastal Engineering (Taiwan) (2), pp. 1843-1857.

Dean, R.G. (1991). Equilibrium beach profiles: Characteristics and applications, *J. Coastal Res*., 7(1), 53-84.

Dean, R.G., and Dalrymple, R.A. (2002). Coastal processes with engineering applications. Cambridge university press, 475pp.

Del Valle, R., Medina, R., and Losada, M.A. (1993). "Dependence of the coefficient *K* on the grain size." *J. Waterway, Port, Coastal and Ocean Eng*., 118(6), 568-574.

Fairley, I., Davidson, M, Kingston, T., Dolphin, T., and Phillips, R. (2009). Empirical orthogonal function analysis of shoreline changes behind two different designs of detached breakwaters. *Coastal Engineering*, 56, 1097-1108.

FitzGerald, D.M., Fenster, M.S., Argow, B.A., and Buynevich, I.V. (2008). Coastal impacts due to sea-level rise. *Annu. Rev. Earth Planet Sci.* 36, 601-647.

Fukuda, M.K., and Lick, W. (1980). The entrainment of cohesive sediment in freshwater. *J. Geophys. Res*. 85(C5), 2813-2824.

Fuller, J.A. (2002). Bank recession and lakebed downcutting: response to changing water levels at Maumee bay state park, Ohio. *J. Great Lakes Res*., 28(3), 352-361.

Gallagher, E.L., Elgar, S., and Guza, R.T. (1998). Observations of sand bar evolution on a natural beach. *J. Geophys. Res*. 103, 3203-3215.

Goforth, R.R. and Caram. S.M. (2005. Nearshore community characteristics related to shoreline properties in the Great Lakes, *J. Great Lakes Res*., 31(Supplement 1), 113-128.

Graf, G., Bengtsson, W., Diesner, U., Schulz, R., and Theede, H. (1982). Benthic response to sedimentation of a spring phytoplankton bloom – process and budget. *Marine Biology*, 67(2), 201-208.

Griggs, G.B., and Tait, J.F. (1988). The effects of coastal protection and structures on beaches along northern Monterey Bay, California. *Journal of Coastal Research*, Special Issue, No.4, 93-111.

Hayes, D., Jones, M., Lester, N., Chu, C., Doka, S., Netto, J., Stickwell, J., Thompson, B., Minns. C.K., Shuter, B., and Collins, N. (2009). Linking fish population dynamics to habitat conditions: insights from the application of a process-oriented approach to several Great Lake Species. *Rev. Fish Biol. Fisheries*, 19, 295-312.

Hakanson, L. (1981). A manual of Lake Morphometry. Berlin: Springer-Verlag.

Herman, P.M.J., Middelburg, J.J., and Heip, C. (2001). Benthic community structure and sediment processes on an intertidal flat: results from the ECOFLAT project. *Continental Shelf Research*, 21, 2055-2071.

Hoefel, F., and Elgar, S. (2003). Wave-induced sediment transport and sandbar migration. *Science*, 299(5614), 1885-1887.

Ishimaru, A. (1977). Theory and application of wave-propagation and scattering in random media. *Proceedings of the IEEE*, 65(7), 1030-1061.

James, M.K., Armsworth, P.R., Mason, L.B., and Bode, L. (2002). The structure of reef fish metapopulations: modeling larval dispersal and retention patterns. *Porc. R. Soc. Lond. B.* Vol. 269., No. 1505, 2079-2086.

Jibson, R.W., and Odum, J.K. (1994). Rates and processes of bluff recession along the Lake Michigan shoreline in Illinois. *J. Great Lakes Res*. 20:135-152.

Kalff, J. (2002). Limnology. Prentice-Hall. 592 pp.

Komar, P.D. (1998). Beach processes and sedimentation. 2nd. Prentice, New Jersey, 354pp.

Komar, P.D., and Mcdougal, W.G. (1988). Coastal erosion and engineering structure: the Oregon experience. *Journal of coastal research*, SI4, 77-92.

Komar, P.D., and William, G.M. (1994). The analysis of exponent beach profiles. *Journal of Coastal Res*., 10, 59-69.

Kraus, N.C. (1988). The effects of seawalls on the beach: an extended literature review. *J. Coastal Res*., 4, Special Issue, 1-28.

Kraus, N.C., and McDougal, W.G. (1996). The effects of seawalls on the beach: Part 1. An updated literature review. *J. Coastal Res*., 12(3), 691-701.

Kriebel, D.L., Kraus, N.C., and Larson, M. (1991). Engineering methods for predicting beach profile response. *Coastal Sediments* 91, 557-571.

Lee, C., Wu, C.H., and Hoopes, J.A. (2004). Automated sediment erosion testing system using digital imaging. *J. Hydraulic Engineering* – ASCE, 130, 8,771-781.

Lee, G.H., Nicholls, R.J., and Birkmeier, W.A. (1998). Storm-driven variability of the beach-nearshsore profile at Duck, North Carolina, UAS, 1981-1991.*Marine Geology*, 148, 163-177.

Lee H.J., and Ryu, S.O. (2008). Changes in topography and surface sediments by the Saemangeum dyke in an estuarine complex, west coast of Korea. *Continental shelf research*, 28(9), 1177-1189.

Lin, Y.T., Schuettpelz, C.C., Wu, C.H., and Fratta, D. (2009). A combined acoustic and electromagnetic wave-based techniques for bathymetry and subbottom profiling in shallow waters. *Journal of Applied Geophysics*, 68, 203-218.

Lin, Y.T., Wu, C.H., Fratta, D. and Kung, K.-J.S. (2010). Integrated acoustic and electromagnetic wave-based technique to estimate subbottom sediment properties. *Near Surface Geophysics*, 8(3), 213-221.

Lou, J., and Schwab, D.J. (2000). A model of sediment resuspension and transport dynamics in south Lake Michigan. *Journal of Geophysical Res*., 105(C3), 6591-6610.

Mackey, S.D., and Liebenthal, D.L. (2005). Mapping changes in Great Lakes nearshore substrate distributions. *J. Great Lakes Res*. 31:75-89.

McDougal, W.G., Kraus, N.C., and Ajiwibowo, H. (1996). The effects of seawalls on the beach: Part 1I. Numerical modeling of SUPERTANK seawall tests. *J. Coastal Res*., 12(3), 702-713.

McDougal, W.G., Sturtevant, M.A., and Komar, P.D. (1987). Laboratory and field investigations of shoreline stabilization structures on adjacent property. *Coastal Sediments'87*, 961-973.

Miles, J.R., Russel, P.E., and Huntley, D.A. (2001). Field measurements of sediment dynamics in front of a seawall. *J. Coastal Res*., 17(1), 195-206.

Meadows, G. A., Mackey, S.D., Goforth, R.R., Mickelson, D.M., Edil, T.B., Fuller, J., Guy Jr, D.E., Meadows, L.A., Brown, E., Carman, S.M., and Liebenthal, D.L. (2005).

Cumulative habitat impacts of nearshore engineering, *Journal of Great Lakes Research*, 31(Supplement 1): 90-112.

Mei, C.C. (1989). The applied dynamics of ocean surface waves. World Scientific. 760 pages.

Moore, B. (1982). Beach profile evolution in response to changes in water level and wave height. M.S. Thesis, University of Delaware, Newark.

Morang, A., Larson, R., and Gorman, L., (1997). Monitoring the coastal environment; Part III: Geophysical and research methods. *Journal of Coastal Research* 13(4), 1064-1085.

Palmer, M.A., Covich, A.P., Lake, S., Biro, P., Brooks, J.J., Cole, J., Dahm, C., Gibert, J., Goedkoop, W., Martens, K., and Verhoeven. (2000). Linkages between aquatic sediment biota and life above sediments as potential drivers of biodiversity and ecological processes. BioScience, 50(12), 1062-1075.

Pilkey, O.H., Young, R.S., Riggs, S.R., Smith, A.W. (1993). The concept of shoreface profile of equilibrium: a critical review. *Journal of Coastal Research*, 9, 255-278.

Plant, N.G., and Griggs, G.B. (1992). Interaction between neashore processes and beach morphology near a seawall. *Journal of Coastal Research*, 8(1), 183-200.

Ranasinghe, R. and Turner, I.L. (2006). Shoreline response to submerged structures: A review. *Coastal Engineering*, 53, 65-79.

Reppert, P.M., Morgan, F.D., and Toksoz, M.N. (2000). Dielectric constant determination using ground-penetrating radar reflection efficient. *Journal of Applied Geophysics*, 43, 189-197.

Richardson, M.D., and Briggs, K.B. (1993). On the use of acoustic impedance values to determine sediment properties. *Proc. Inst. Acoustics*., 15(2), 15-24.

Robillard, S.R., and Marsden, J.E. (2001). Spawning substrate preference of yellow perch along a sand-cobble shoreline in southwestern Lake Michigan. *N AM J FISH Manag.,* 21, 208.215.

Roshanka, R., and Turner, I.L. (2006). Shoreline response to submerged structures: A review. *Coastal Engineering*, 53, 65-79.

Rodriguez, J.F., Admiraal, D.M., Garcia, M.H., and Lopez, F. (2002). Unsteady bed stresses induced by navigation: laboratory observations. *J. Hydr. Eng., ASCE*, 128(5), 515-526.

Rukavina, N.A. and Lahaie, G.G. (1991). Measurement of thickness of nearshore sand by hydraulic jetting. *J. Sediment. Petrol.* 62(4): 737-738.

Russink, B.G., Kuriyama, Y., Reniers, A.J.H.M., Roelvink, J.A., and Walstra, D.J.R. (2007). Modeling cross-shore sandbar behavior on the timescale of weeks. . *J. Geophys. Res*. 112, F03010, doi:10.1029/2006JF00730.

Schock, S.G., (2004). A method for estimating the physical and acoustic properties of the sea bed using chirp sonar data. *IEEE J. of Oceanic Engineering* 29(4), 1200-1217.

Scholz, C.A., (2001). Application of seismic sequence stratigraphy in lacustrine basins. In Last W.M. and Smol J.P., eds), Tracking Environmental Changes Using Lake Sediments, vol. 1, Basin Analysis, Coring, and Chronological Techniques. Kulwer Academic Publishers, Dordrecht, The Netherlands, pp.7-22.

Schwartz, M.L. (1987). The Bruun Rule-twenty years later. *Journal of Coastal Research*, 3, ii-iv.

Stockberger, M.T., and Wood, W.L. (1990). Applications of equilibrium beach concepts to sandy Great Lakes shores. Proceedings of the 22nd Coastal Engineering Conference (American Society of Civil Engineering), 3, 2291-2303.

Swenson, M.J., Wu, C.H., Edil, T.B., and Mickelson, D.M. (2006). Bluff recession rates and wave impact along the Wisconsin coast of Lake Superior. *J. of Great Lakes Research* 32(3), 512-530.

Teeter, A.M., Johnson, B.H, Berger, C., Stelling, G., Scheffner, N.W., Garcia, M.H., and Parchure, T.M. (2001). Hydrodynamic and sediment transport modeling with emphasis on shallow-water, vegetated areas (lakes, reservoirs, estuaries and lagoons). *Hydrobiologia*, 444(1-3), 1-23.

Topp, G.C., Davis, J.L., and Annan, A.P. (1980). Electromagnetic Determination of Soil Water Content: Measurements in Coaxial Transmission Lines. *Water Resources Research*, 16(3): 574–582.

USACE, (2002). Coastal Engineering Manual, Part III, EM1110-2-1100. US Army Corps of Engineers, April.

Wheatcroft, R.A. (2002). In situ measurements of near-surface porosity in shallow-water marine sands. *IEEE Journal of Oceanic Engineer*, 27(3), 561-570.

Waples, J.T., Paddock, R., Janssen, J., Lovalvo, D., Schulze, B., Kaster, J., and Klump, J.V. (2005). High resolution bathymetry and lakebed characterization in the nearshore of western Lake Michigan. *J. Great Lakes Res*. 31:64-74.

Wood, L.W., Stockberger, M.T., and Madalon, L.J. (1994). Modeling beach and nearshore profile response to lake level change. *J. Great Lakes Res*. 20(1):206-214.

Table 5.1

Water level records for corresponding survey days from NOAA Milwaukee station (datum: IGLD85).

Year	2007	2008	2009	2010	2011
Water level (m)	176.072	176.25	176.43	176.304	176.292

Table 5.2

Wind data, storm events, wave climate, and cumulative wave impact height from 2007 to 2011.

	2007 2008	2008 2009	2009 2010	2010 2011
Percentage of wind exceeding 4.5 m/s from 45° to 135°(%)	4.51	4.36	6.80	5.40
Mean wind speed U_{10} exceeding 4.5 m/s from 45° to 135° (m/s)	6.15	7.10	7.42	7.80
Storm events	43	34	41	31
Mean duration of storm events (hrs)	16.0	19.0	21.1	23.2
Total hours of storm events (hrs)	688	646	865	713
Mean wave height in deep water (m)	1.05	1.18	1.28	1.38
Mean wave period (sec)	4.41	4.63	4.79	5.00
CWIH (m)	0.045	0.052	0.098	0.07

Table 5.3

Bluff crest and toe recession rates at the study site for two different epochs, before (2000-2005) and after (2005-2010) coastal bluff enhancement.

Area \ Epoch	2000-2005 (before construction)		2005-2010 (after construction)	
	bluff crest (m/year)	bluff toe (m/year)	bluff crest (m/year)	bluff toe (m/year)
North	0.14	0.55	0.46	0.51
Middle	0.63	0.41	~0	~0
South	0.40	0.42	0.29	1.03

Table 5.4

A, n values in northern and southern regions.

A, *n* values	North			South		
	n is not a constant		*n*=0.67	*n* is not a constant		*n*=0.67
	A	*n*	*A*	*A*	*n*	*A*
2008	0.114	0.648	0.099	0.124	0.628	0.099
2009	0.108	0.652	0.098	0.136	0.606	0.099
2010	0.137	0.613	0.103	0.177	0.562	0.105
2011	0.098	0.677	0.100	0.118	0.641	0.100

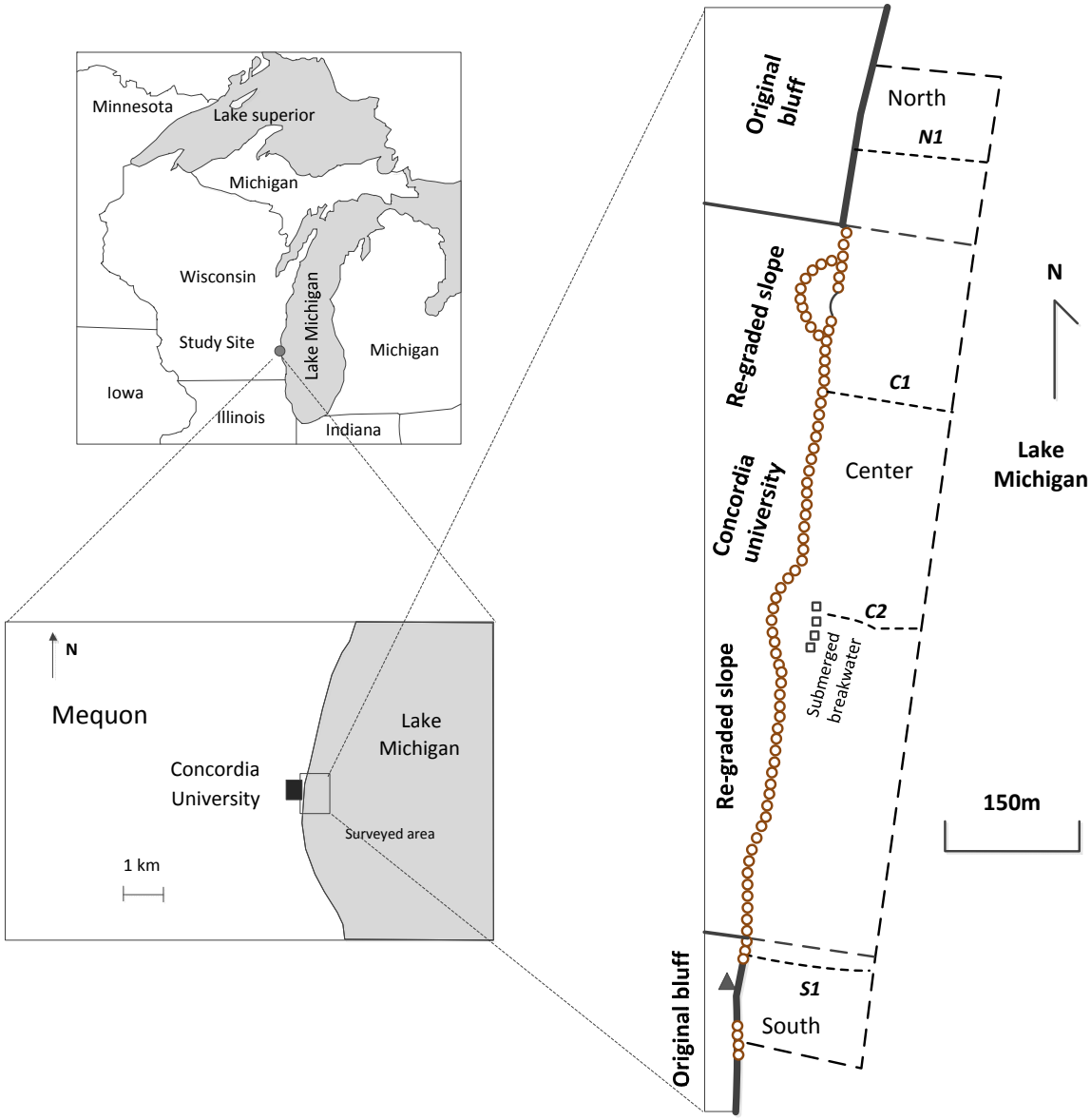

Figure 5.1 Location of the study site, Concordia University Wisconsin, with symbols ○ for coastal revetment; □ for the submerged breakwater; and ▬ for natural beaches. The bluffs at CUW were regarded and planted with grass. Dashed lines, N1, C1, C2, and S1 were survey transects.

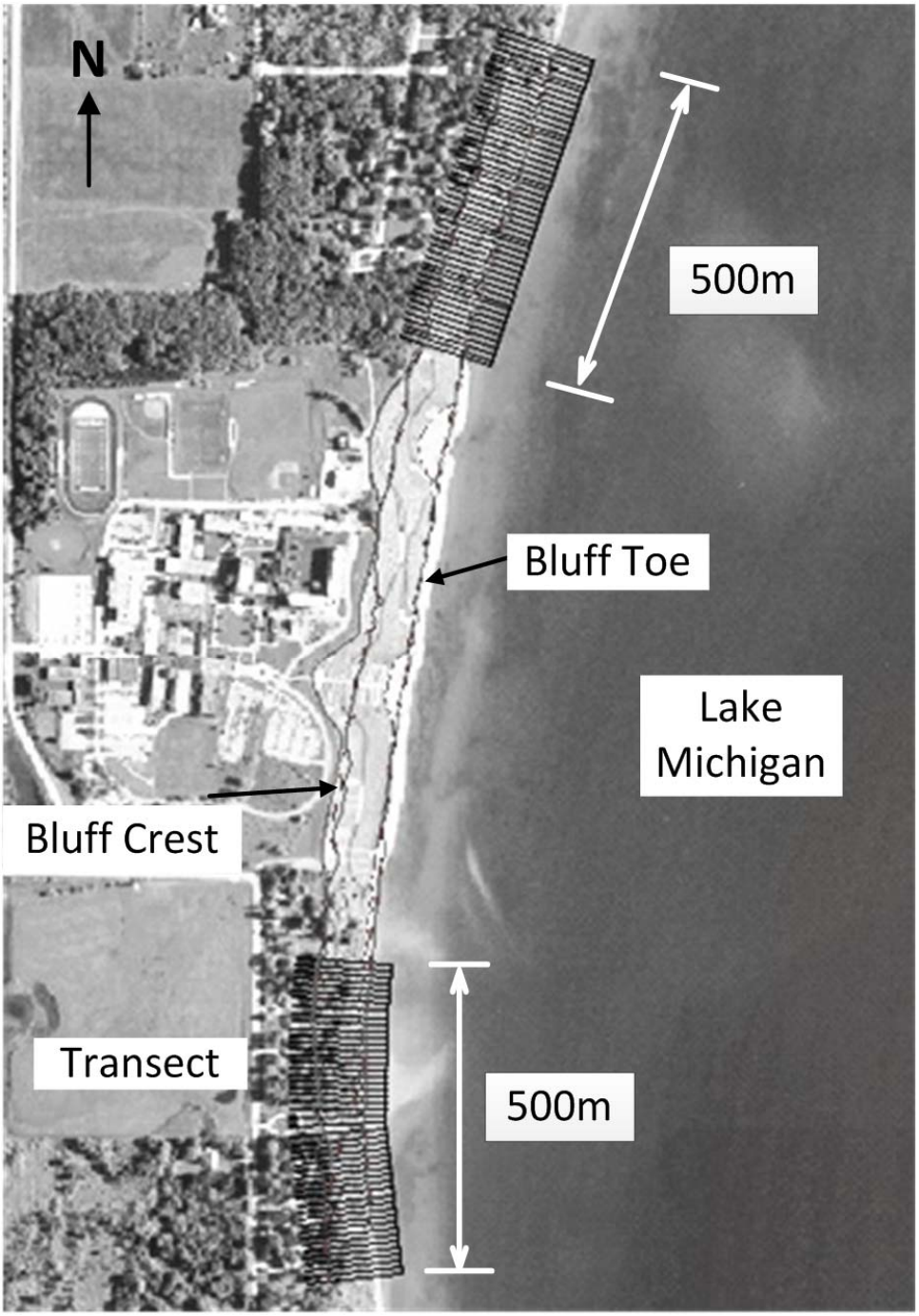

Figure 5.2 Transects for bluff recession measurements. Note transects in the structured areas are not shown for brevity.

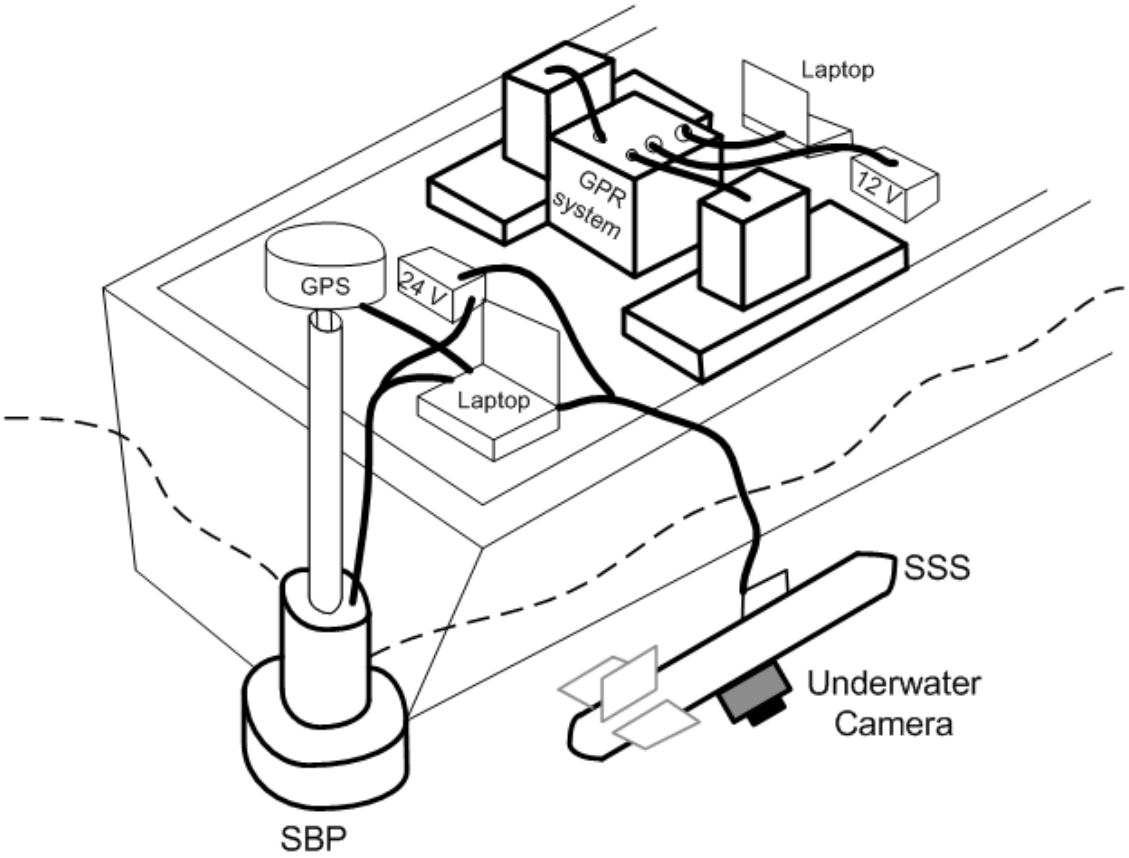

Figure 5.3 Sketch of the combined geophysical instrument techniques including SBP and GPR in a zodiac boat with SSS and an underwater camera system at the side.

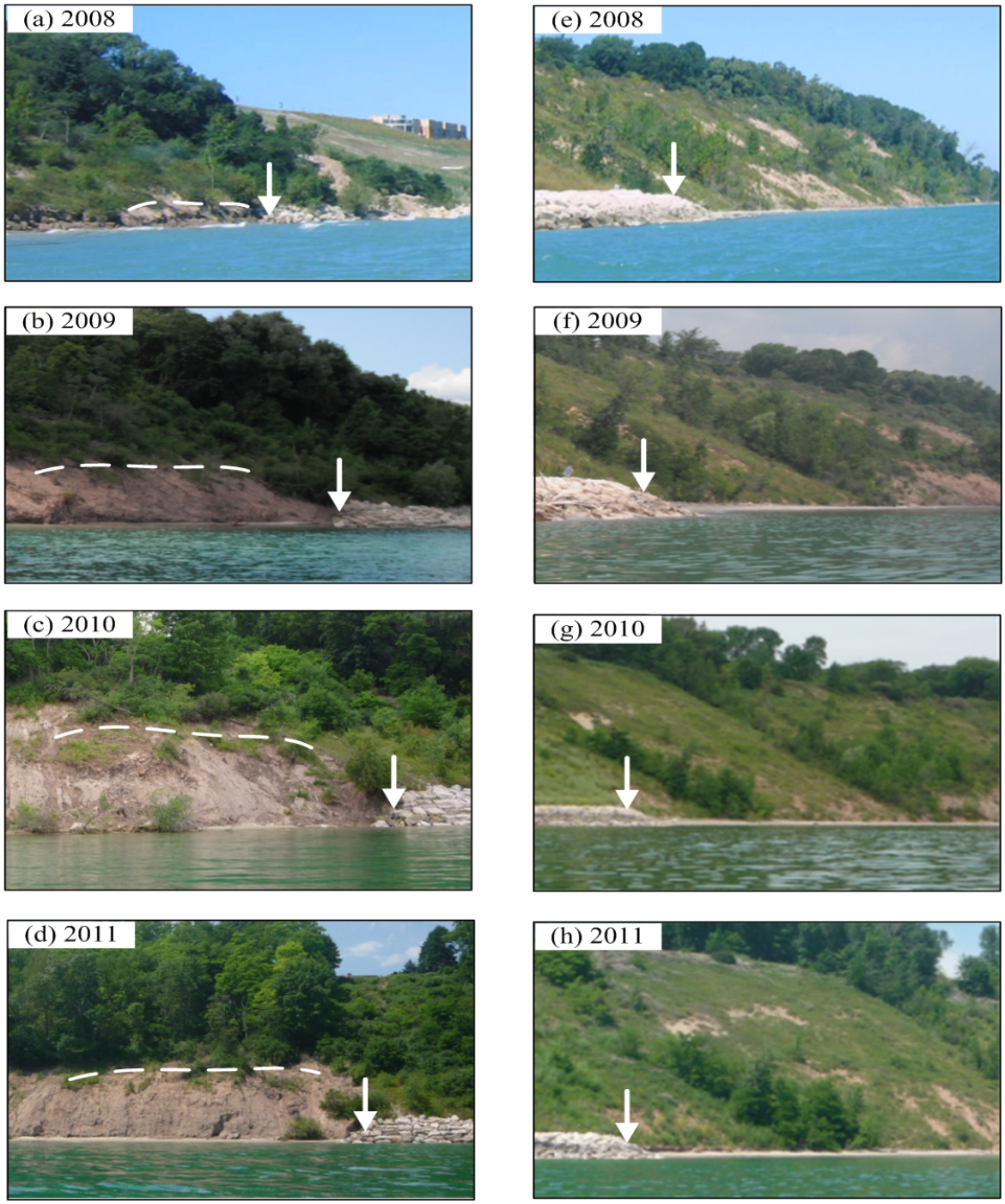

Figure 5.4 Oblique photos of the bluff on the north (a) ~ (d) and the south (e) ~ (h) at the study site taken from 2008 to 2011. Arrows show the edge of newly built coastal structures. Dash-lines in (a) to (d) denote the tip of vegetation on the bluff at the southern areas. Vegetation cover visible in 2008 disappeared in 2009 as severe slumping occurred. In the northern areas, no apparent change on bluffs was observed during the study period.

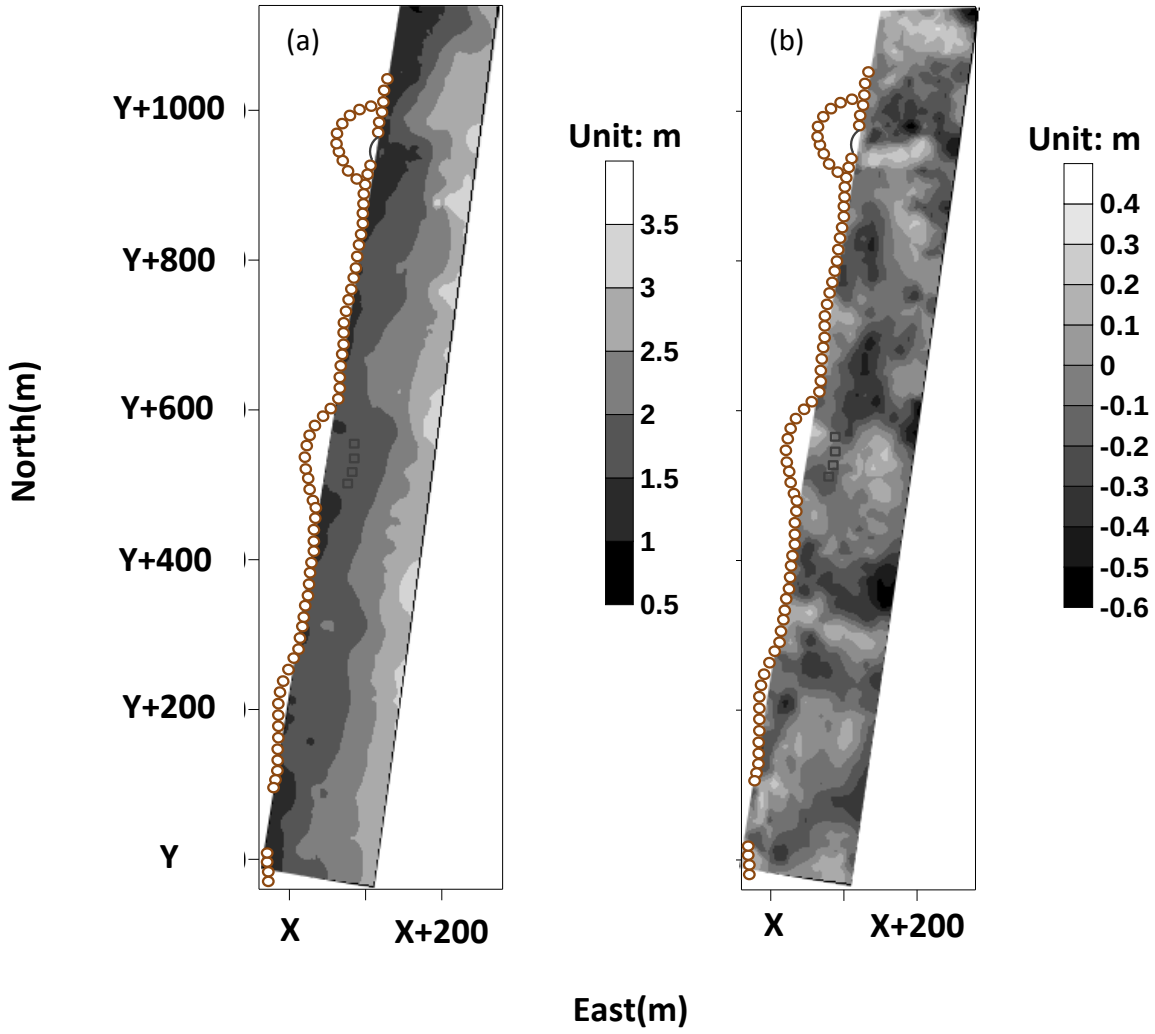

Figure 5.5 (a) Bathymetry of 2011 in reference to the IGLD85 datum and (b) bathymetry changes between 2008 and 2011, where X=426000, and Y=4788800 in the UTM system. Positive and negative values denote deposit and erosion, respectively of the bathymetry.

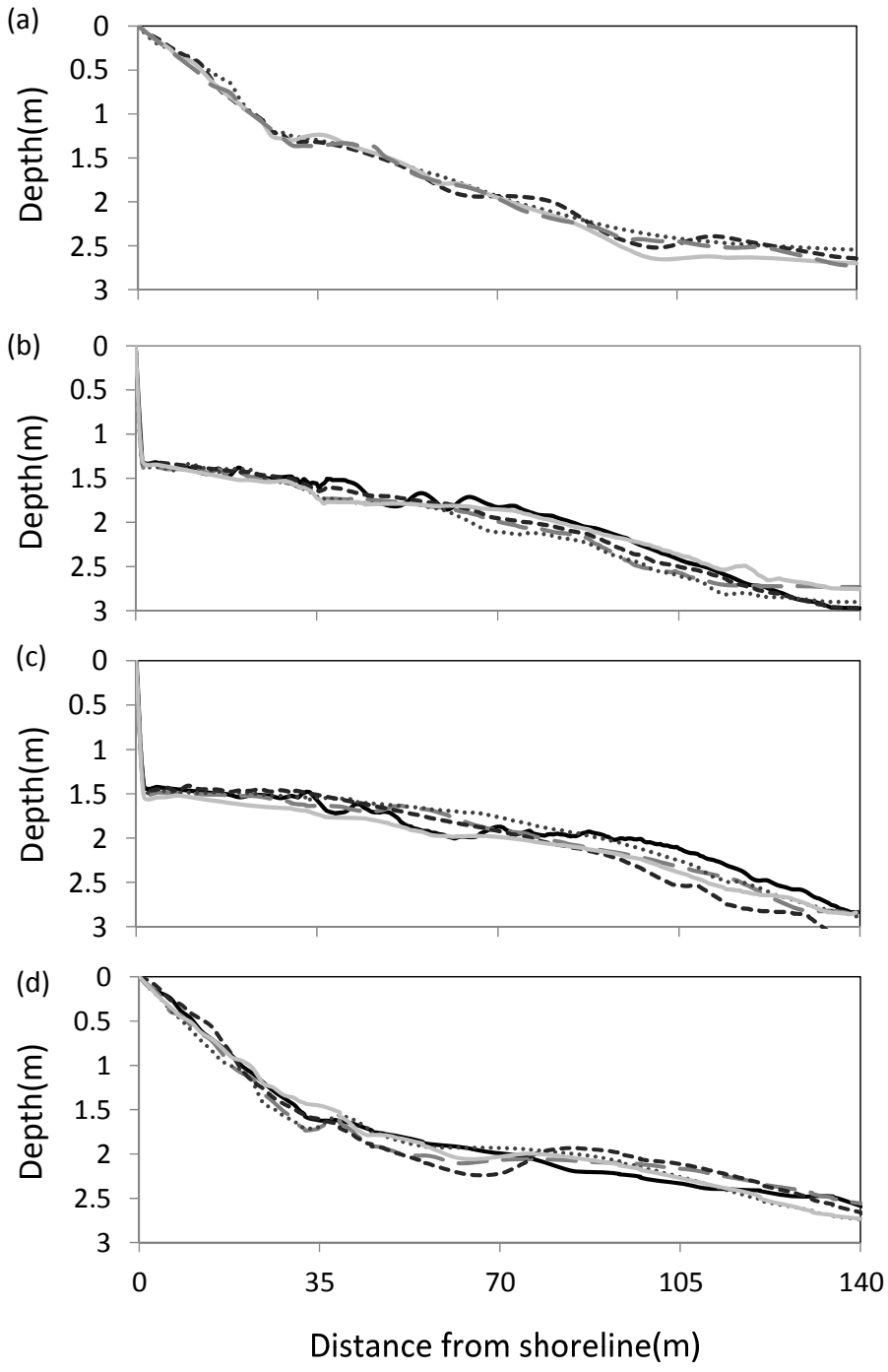

Figure 5.6 Comparison of bathymetry from 2007 to 2011 along the four survey lines: (a) Line *N1*, (b) Line *C1* (the front side is due to the slope~45 degree of the coastal revetment), (c) Line *C2*, and (d) Line *S1*. (:2007; :2008; :2009; : 2010; : 2011).

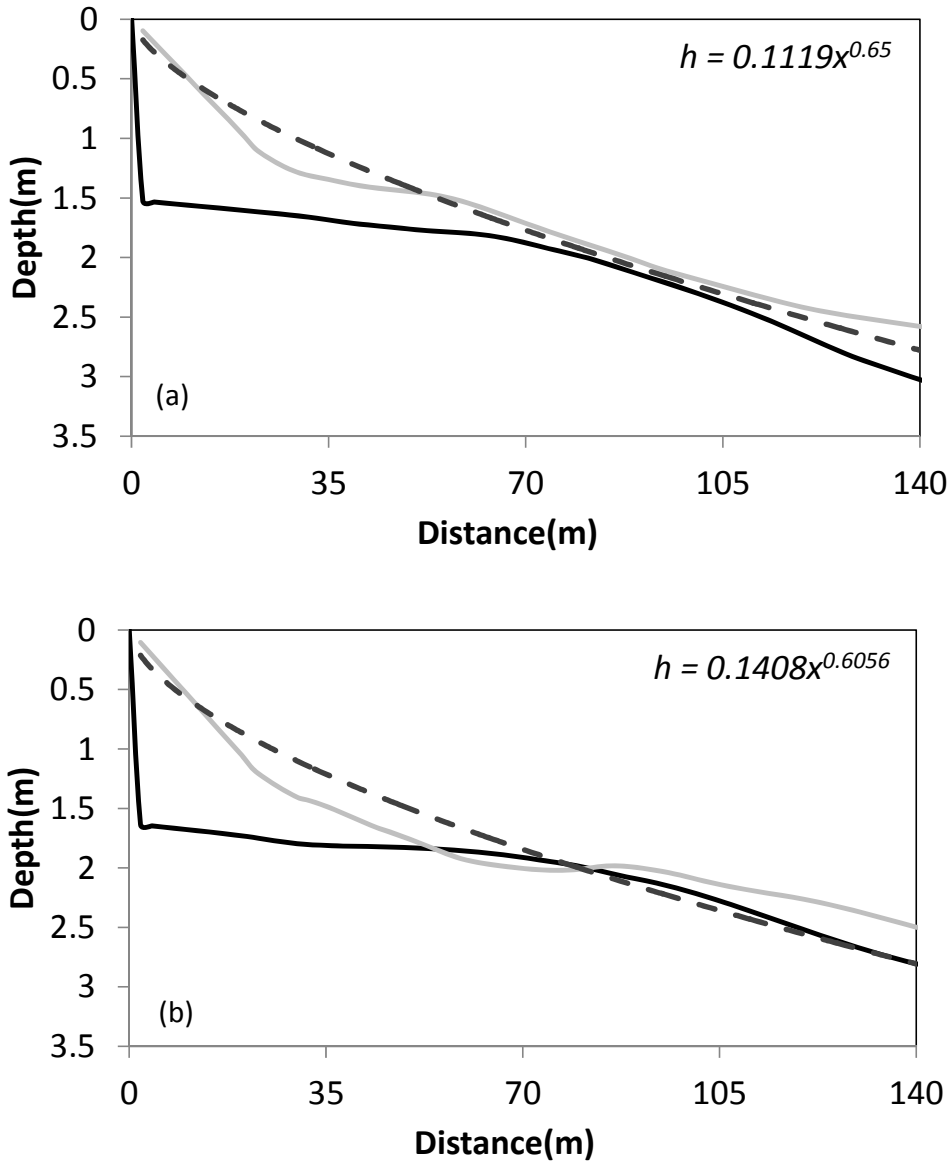

Figure 5.7 Mean beach profile and equilibrium beach profile. (a) North areas (grey-line), North zones of structured areas (black-line), and the equilibrium beach profile (dash-line) based upon the mean profiles in north areas; and (b) South areas (grey-line), South zones of structured areas (black-line), and the equilibrium beach profile (dash-line) based upon the mean profiles in south areas. The equations denote the equilibrium beach profiles, and 0 m at the *x*-axis is the edge of land and water.

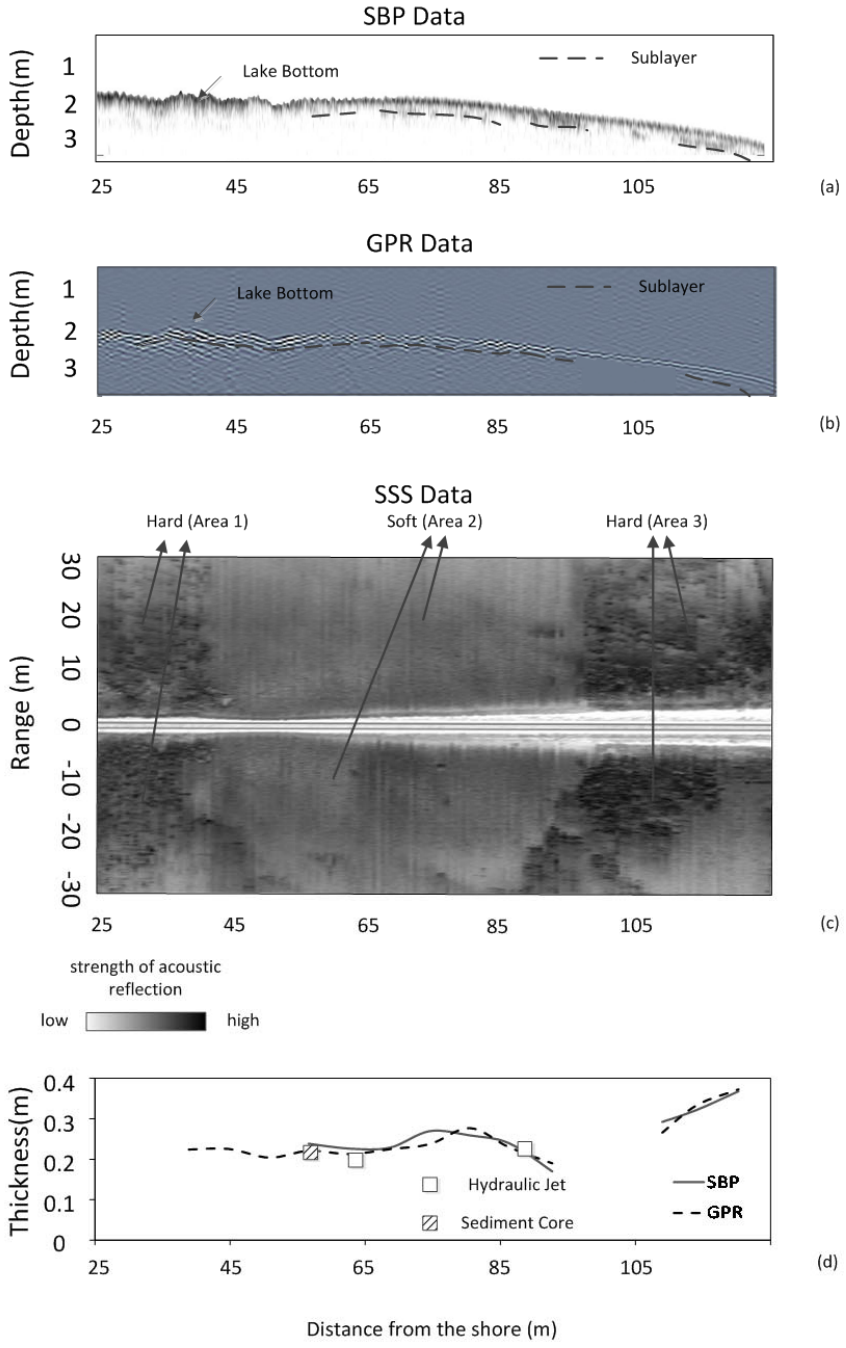

Figure 5.8 SBP, GPR and SSS profiling results for Line *C2*: (a) SBP data, (b) GPR data and (c) SSS data, and (d) Top-layer thickness.

(a)

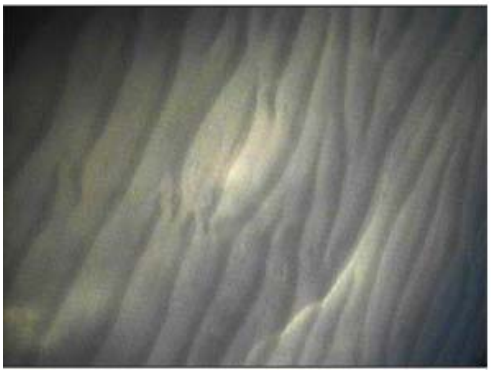

(b)

(c)

Figure 5.9 Pictures from underwater camera in the nearshores of Concordia University: (a) Area 1 (boulders), (b) Area 2 (sand dunes), and (c) Area 3 (glacial tills-hard clay)

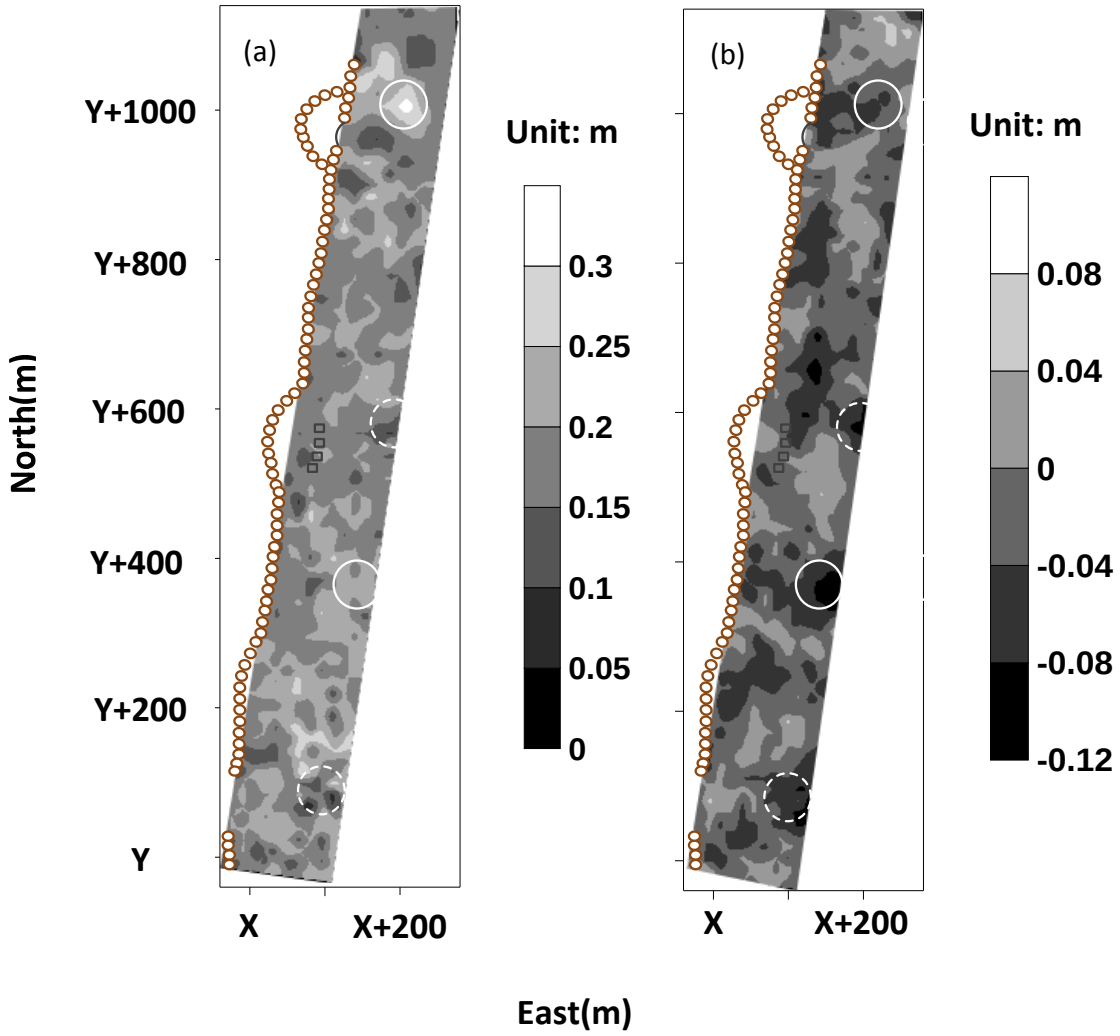

Figure 5.10 (a) Mean sandy layer thickness and (b) lakebottom changes from 2009 to 2011 (Solid-circle: bottom erosion due to sandy particle abrasion, dash-circle: bottom erosion due to lack of sand protection).

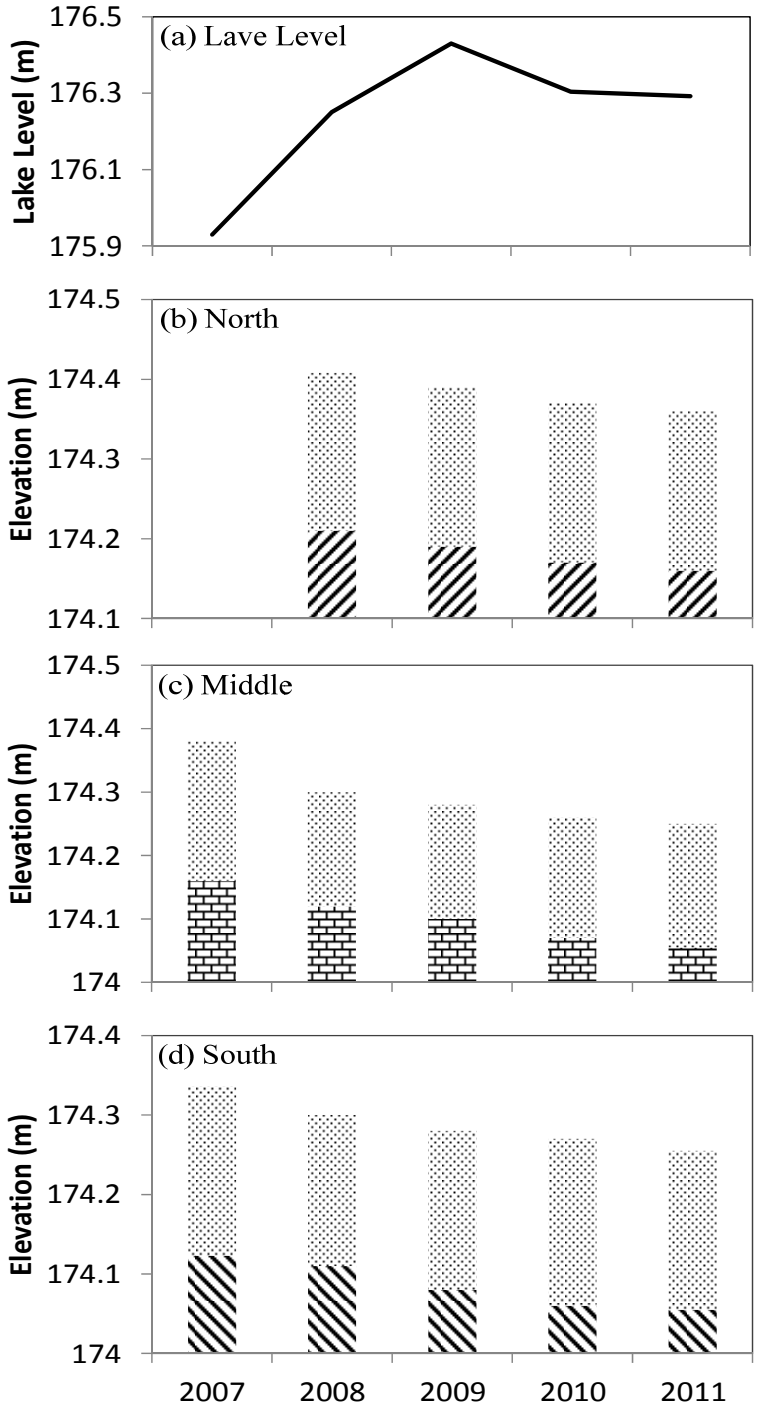

Figure 5.11 Lake level, bathymetry, and lake bottom elevation from 2007 to 2011. Note: lake bottom elevation for south areas (▨), structured areas (▤), and north areas (▨), and thickness of sandy layer(▩). Datum: IGLD85.

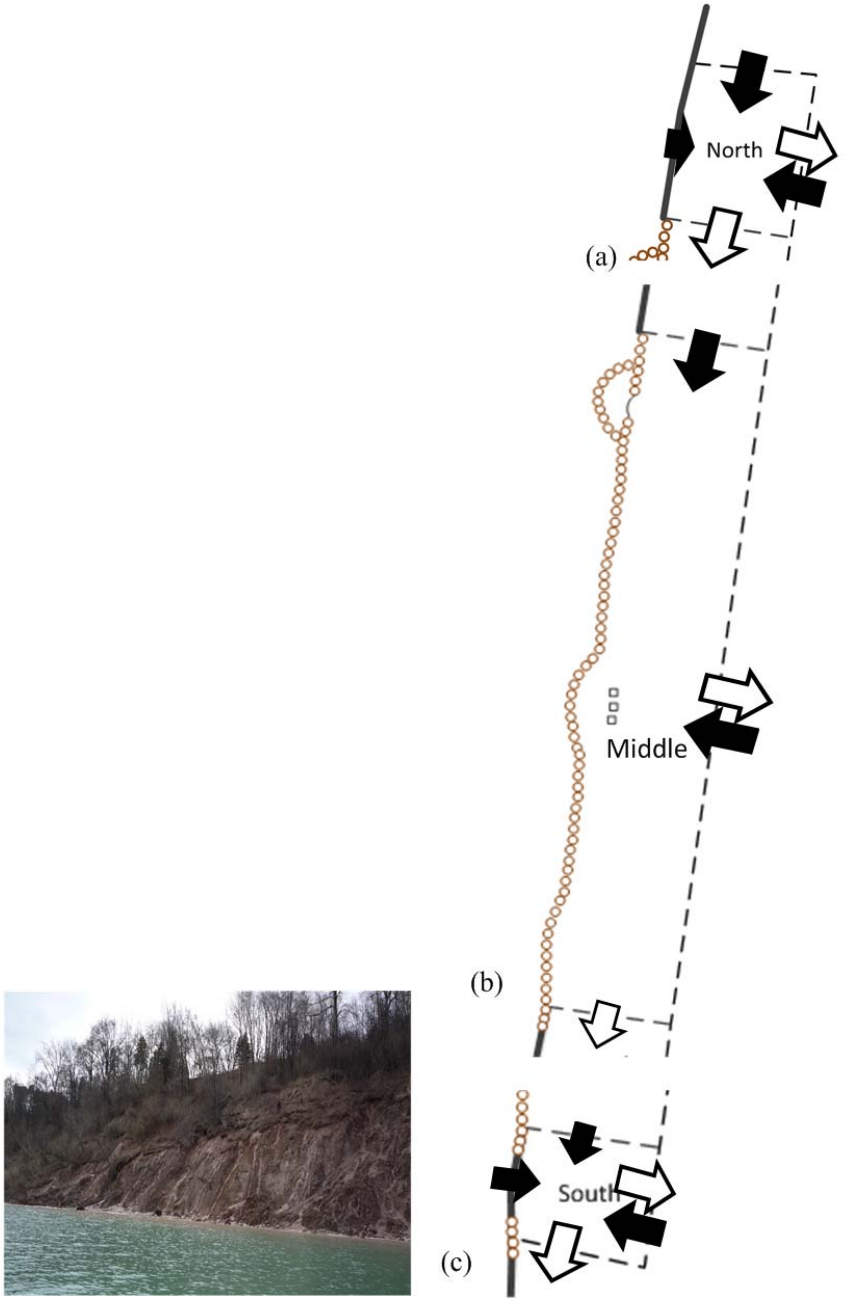

Figure 5.12 Schematic of sediment budget in north (a), middle (b), and south regions (c). Note: black arrow-sediment flux into the region; white arrow-sediment flux out of the region, and the length of the arrow denotes the magnitude of the sediment flux. Pictures show the disappearance of beach and erosion of bluff toes.

Chapter 6 Conclusions and future work

6.1 Conclusions

The overall aims of my thesis are to understand physical mechanisms of thermal-driven flow within emergent vegetation, and coastal processes, specifically changes of bathymetry and downcutting rates around newly-built coastal structures in shallow water. For the first topic, two analytic models related to heat input and output from the water columns have been developed to examine physical processes of thermal-driven circulation. By assuming small bottom slopes, convective terms in governing equations are second-order and thus neglected, and asymptotic solutions can be found. In both models, horizontal velocity is significantly reduced by the presence of vegetation. For the first model of heat uniformed-distribution over the water columns, i.e. unstratified temperature structures, viscosity is balanced with the pressure gradient in shallow water same as the case without vegetation; whereas in deep water, vegetative drag becomes more important rather than the inertia. Time lags between reversal of horizontal velocity and pressure gradient are reduced. Vegetative drag can regulate circulation as the same phase as the pressure gradient. Because of vegetative drag, locations of the maximum and minimum horizontal velocity move closer to the tip of the domain. Regarding to the second model, a light extinction coefficient is included, i.e. stratified temperature structures. During the daytime, solar radiation exponentially decays with the water depth, and residual heat reaching bottom is assumed to reemit as a bottom heat flux. On the other hand, during the nighttime, heat dissipates through the water surface. The asymptotic solutions show that bottom heating is an important mechanism to drive

horizontal exchange flow. As a result, for clearer water, i.e. smaller light extinction coefficients, it leads to greater thermal-driven flow than that of turbid water (larger light extinction coefficients). In very shallow water, both asymptotic solutions found in unstratified and stratified models are approximately the same since heat diffuses over the entire water columns, and vegetative drag reduces same percentages of the circulation. For deep water, horizontal velocity is not reversed for clearer water due to relatively stronger pressure gradient generated during the heating period. Vegetative drag changes the phases of the circulation for turbid water rather than clear water. Also, vegetation distribution can alter temperature structures and subsequently changes the circulation patterns in both models. At the extreme cases, i.e., vegetation occupies half of the domain, and open water in the other half domain, vegetation shading can surpass topographic effects, and leads to opposite circulation patterns as the no vegetation case. For turbid water, circulation is more easily affected by the vegetation distributions because of the weaker driving pressure gradient.

Second part of my thesis is to study nearshore environment changes and downcutting processes after newly-built coastal structures. First, a combined geophysical technique including acoustic-basis SBP and electromagnetic-wave basis GPR were developed to map bathymetry and substrates under different sediment features. The advantages of the combined techniques can reduce limitations from single technique, and obtained information of substrates in diverse sediment environments. Second, acoustic and electromagnetic signals reflected from sediment bottom were integrated, and an algorithm was developed to estimate sediment porosity and top-layer thickness in bottom sediments. The integrated algorithm was then applied to monitor nearshore environment

changes and estimate downcutting rates in new-built coastal structures at the Concordia site of Lake Michigan. Five-Year successive measurements (2007 to 2011) suggest that bathymetry profiles outside structured areas experience significant erosions in the first two years after the coastal structure was finished. Afterward, bathymetry profiles in structured and unstructured areas became similar and approach an equilibrium state. Although the downcutting rates were larger in the structured areas than the unstructured areas, the coastal structure prevented the coastal line being eroded, and protected the coastal bluffs. From 2008 to 2009, in the southern shore of the study site, the lakebed lowering (downcutting) rates were greater than the average downcutting rate. Meanwhile, serious bluff slumps in the south shores were also observed. The presence of coastal structures may intercept the sediment supplies to the southern regions under prominent southward longshore currents. Once the sediment supplies are short, sediment materials keep being removed from southern regions, sandy beaches are lost, and the exposed bluff toes under wave attacks may finally fail. In addition, the southern regions are located between two coastal structures. As a result, wave and circulation patterns may be complicated, and are responsible for excessive erosion in the southern regions. The results suggest that the coastal structure pose negative impacts on bluff stability in southern shores.

6.2 Future works

In the first part of theoretical derivations of natural convection over a vegetated slope, laboratory experiments are necessary to reveal the underlying physics and compare with the asymptotic solutions. So far, only shading effects of vegetation are considered to

induce temperature gradients over a flat bottom in the laboratory experiments. As far as the author's best understanding, laboratory tests combing vegetation shading and topographic effects are not reported yet. The laboratory experiments can be used to examine results from the asymptotic and numerical results.

In addition, in theoretical derivations, vegetation is assumed to be uniformly distributed along the vertical directions, which may not be true in the field conditions. In the future, the vertical distributions of vegetation could be included into drag terms in stream functions, and be solved by using power series functions. Also, surface shear stress such as the mild wind could be considered in the model by adjusting surface boundary conditions. Within emergent vegetation, wind-induced shear stresses should be small enough, and convective terms could be still neglected. On the other hand, present analytical methods that neglect convective term and consider two-dimensional flows may not meet with the field conditions. Therefore, it is worth and necessary to develop numerical approaches to understand new physical insights. The numerical model can also cover effects of the submerged vegetation on thermal-driven flows.

For the second part of the thesis, i.e. applications of geophysical techniques on monitoring environmental changes, successful measurements have been conducted on sandy, silty and clayey environments with low water conductivity. By using the integrated geophysical techniques, downcutting rates can be estimated over a substantial area. In addition to downcutting processes, neashore sediment budget plays a key role in beach revolutions and bluff responses. If more sediment is deposited than removed, the sediment budget is in a surplus, the beach grows seaward, and the bluff toe is hardly attacked by wave motions. On the contrary, when the sediment removed exceeds than

deposited, the sediment budget has a deficit, the beach retreats landward, and the bluff easily suffers by the wave attacks. For conducting analysis of sediment budget in nearshore, field observations to obtain wave climates, circulations, wave breaking depth, bottom slopes, and bottom sediment properties are necessary. The data can be then combined with numerical simulations to predict shoreline evolutions due to any addition of coastal structures, which can be an effective tool to address the guideline of the integrated bluff management (IBM).